FUNDAMENTAL APPROACH TO PRACTICAL CORROSION PROBLEMS

By

MEI-WEN HUANG

A DISSERTATION PRESENTED TO THE GRADUATE SCHOOL
OF THE UNIVERSITY OF FLORIDA IN PARTIAL FULFILLMENT
OF THE REQUIREMENTS FOR THE DEGREE OF
DOCTOR OF PHILOSOPHY

UNIVERSITY OF FLORIDA

2007

To my parents in Taiwan, who, always support all my efforts especially for my PhD

ACKNOWLEDGMENTS

I sincerely express my gratitude to my advisor, Professor Mark E. Orazem, for his technical guidance throughout my graduate research. I will always be grateful for his patience and encouragement. I also thank Professor Kevin Ogle, Dr. Christian Alley, Dr. Bernard Tribollet, Dr. Vincent Vivier, and Dr. Nadine Pébère for their expertise in electrochemistry. I express my appreciation to my committee members, Professor Jason Butler, Professor Kirk Ziegler, Professor Charles Martin, Professor Chung-Won Park, and Professor Darryl Butt for their contribution to my proposal presentation and dissertation defense.

I thank our group members, Patrick McKinney, Sunil Roy, Shaoling Wu, and Bryan Hirschorn. Special appreciation goes to the former group members Kerry Allahar and Nellian Perez-Garcia for their support. I was very fortunate to be a member of this group.

I wish to acknowledge IRSID, Arcelor Innovation in France, for funding the project and for giving me a chance to perform experiments in their laboratories in 2006. I also express appreciation to my friends in Arcelor, Yannick Lerous, Taigo Machado, and Aurelie Felten for their friendship and for their assistance in life and work.

Finally, and most importantly, I express my thanks and gratitude to my parents and my friends in Taiwan, who have always supported me in spirit along this journey. They gave me the courage to pursue my dreams, and I am always going to be grateful for having them by my side.

TABLE OF CONTENTS

LIST OF TABLES

LIST OF FIGURES

Abstract of Dissertation Presented to the Graduate School
of the University of Florida in Partial Fulfillment of the
Requirements for the Degree of Doctor of Philosophy

FUNDAMENTAL APPROACH TO PRACTICAL CORROSION PROBLEMS

By

Mei-Wen Huang

August 2007

Chair: Mark E. Orazem
Major: Chemical Engineering

My study covers two important research topics that are relevant to corrosion of metal. The first project involved developing a mathematical model for delamination of polymeric coating from active materials. The model described simultaneously the coupled phenomena of mass transfer, electroneutrality, loss of interfacial adhesion, and propagation of delamination during the delamination process. The key to this work included the use of pH-dependent porosity and pH-dependent polarization kinetics to simulate implicitly the bond-breaking reactions that occurred during the delamination process.

The computational results predicted from the model, under the assumption of equilibrium pH-porosity relation, concluded the overall delamination process is limited by the transport of cations from defect to delaminated zone, and the rate of the delamination process scales with the mobility and ionic strength of cations. This conclusion is in good agreement with the interpretation obtained from experiments. The consistency with experiments supported the pH-dependent hypotheses employed in the model.

The equilibrium pH-porosity relation becomes invalid when time constants for the bond-breaking reactions are large compared to those for the diffusion and migration processes. The investigation of kinetic pH-porosity relation showed that when the bond-breaking reactions occur in a sufficiently small rate, the delamination mechanism shifts from a mass-transfer-limited mechanism to a mixed-controlled mechanism. A similar mechanism transition was also observed in experiments.

The second project presented in this document explored, by theoretical calculations, the role of current and potential distributions associated with disk electrodes on impedance response. It has known that the geometry-induced current and potential distributions lead to a high-frequency dispersion on impedance response of a disk electrode. The contribution of the work was to express the geometric effect on impedance response in terms of constant-phase element (CPE) and to use both global and local impedances to study this geometric effect. A coherent notation was proposed for global and local impedances which accounted for global, local, local interfacial, and both global and local Ohmic impedances.

The electrochemical systems under study in the second project included an ideally-polarized blocking electrode, an electrode exhibiting a local CPE behavior, and an electrode exhibiting a single Faradaic reaction. The calculation results from these systems showed that the global impedance of a disk electrode is influenced by the current and potential distributions at high frequencies. While the local interfacial impedance exhibits the expected behavior for a given system, the local impedance shows inductive behavior at high frequency and ideal behavior at low frequency. The local impedance is influenced by the Ohmic impedance, which has complex behavior at intermediate frequencies. The representation of an Ohmic impedance as a complex number represents a departure from standard practice. This complex character is believed to be the origin of the inductive features seen in the local impedance and the origin of the CPE-like behavior found in the global impedance.

CHAPTER 1
INTRODUCTION

This dissertation covers two research topics that are important to corrosion of metal. The first research topic involves developing a mathematical model for delamination of polymeric films from active metals. The delamination of paint from metal surface, also known as cathodic delamination, is a major problem for automotive and building applications. Experimental findings demonstrated that the cathodic delamination process involved coupling of mass transfer, electrochemical reactions, loss of interfacial adhesions, and propagation of the delamination along the metal-coating interface. These experiments, in principle, are useful for identifying the phenomena occurring in the delamination systems. However, it is difficult to verify that a proposed mechanism does indeed give observed experimental results. Therefore, a quantitative approach was taken to simulate the transit, propagation phase of the delamination process on coated metals.

The second project presented in this document explored, by theoretical calculations, the role of current and potential distributions associated with disk electrodes on impedance response. Electrochemical impedance spectroscopy (EIS) is often applied as a tool to investigate the rate of corrosion. Impedance spectra, however, are often influenced by the current and potential distributions on electrode surfaces. This work investigates the influence of the geometric effect associated with disk electrodes on impedance responses and describes this effect in terms of constant phase element (CPE).

The introduction for the cathodic delamination model is presented in Section 1.1. Section 1.2 presents the introduction for the impedance calculation.

1.1   Mathematical Models for Cathodic Delamination of Coated Metal

Reactive metals in applications such as automotive and architecture are often protected by covering their surfaces with a micron-thick layer of organic/polymeric coatings. The organic coating provides a matrix in which anticorrosive pigments and/or inhibitors are dispersed [1] and forms a physical barrier between metal and atmosphere.

While additives are introduced into polymeric coatings, the detachment of polymers from metal surface reduces significantly the efficiency of the corrosion protection.

The adhesive strength between the metal and the coating plays an essential role on determining the rate of corrosion. Sugama et al. [2] demonstrated that thermoplastic polymers such as poly(ethylene) exhibit a poor adherence to the metal surface due to the lack of functional groups. George et al. [3] and Sugama et al. [2] showed that the incorporation of functional groups, for example, methacrylic acid (MA) and -COOH, onto the thermoplastic polymers improved the bond strength and further reduced the corrosion rate. Despite the fact that the functional groups on the coating lead to a strong adhesion, the experimental results by Leidheiser et al. [4, 5] indicated that the bond structure is vulnerable to alkaline environment created by oxygen reduction underneath the coating.

Yasuda et al. [6, 7] found that small molecules with high permeability, such as water and oxygen, can penetrate through a defect-free coating and be reduced at the metal-coating surface. So long as the cathodic reaction began to occur underneath the paint, the OH$^-$ ions produced in the interfacial layers promoted the decomposition of polymers, resulting in a delamination of the polymer film from the metal surface. Hammond [8] and Sugama [2] verified the bond-breakage phenomenon by a reduction of the bonding energy for -COOH group and an increase in the bonding energy for -COONa group.

Stratmann et al. [9–18] investigated experimentally the cathodic delamination for coated steel and coated electrogalvanized steel. Following the interpretation reported by Stratmann et al. [9–11, 13–16], the cathodic delamination system consists of a defect where the bare metal is exposed to atmosphere, and a delaminated zone where the interfacial bonding is partially damaged due to the delamination process. Exposure of the metal surface to atmosphere favors metal dissolution at the defect. Along the delaminated zone where the anodic reactions are prohibited because of the presence of the coating, oxygen and water penetrate the coating and react at the interface. Due to the nature of

the configuration, the early stage of the cathodic delamination is often described as the formation of an electrochemical cell with distinct anodic and cathodic zones.

The later stage of the delamination becomes complicated when corrosion products are formed underneath the paint. Furbeth and Stratmann [10] reported that the precipitation of $ZnCO_3$, under a high CO_2 concentration in atmosphere, inhibited the oxygen reduction and led to a pure anodic delamination for a coated electrogalvanized steel. Ogle et al. [19, 20] studied the cathodic delamination on galvanized steel and found that the chemical stability of the interfacial oxide layers plays a critical role on determining the propagation rate and the delamination mechanism. [19, 20]

It is difficult to demonstrate that a proposed mechanism suggested based on experimental work does indeed give the observed experimental results. Interpretation is often limited to qualitative and subjective observations. Therefore, a quantitative approach is necessary. Allahar [21, 22] developed the first mathematical model for the cathodic delamination of coated metal. The key to his work involved applying the concept that the porosity and the polarization kinetics at the metal-coating interface were pH dependent. The simulation results provided qualitative agreements with the experimental observations reported by Stratmann et al. [9–11, 14–16], which supported the hypotheses employed in the model. The model developed by Allahar, however, did not incorporate chemical reactions that take place at the later stage of the delamination process.

The objective of the work was to develop, from first principles, a mathematical model that simulates the propagation of delamination in the presence of electrochemical and chemical reactions. The chemical reactions included homogeneous reactions in the interfacial oxidized layer and formation of corrosion product underneath the coating. A second objective was to examine whether the delamination rate and the delamination mechanism predicted from the model agree with the experimental results.

1.2 Influence of Geometry-Induced Current And Potential Distribution of Disk Electrodes on Impedance Response

Electrochemical impedance spectroscopy (EIS) is a powerful technique that has been used extensively in interfacial electrochemistry to study electrochemical kinetics [23, 24] and to determine interfacial capacitance. [25, 26] The impedance response of an electrode is generated by measuring the ratio of applied potential to surface-averaged current as a function of frequency. The influence of a particular phenomenon on the impedance response is determined by the time constant of that process. [27] Mass transfer effects are usually apparent at low frequencies because the diffusivity of ionic species in aqueous medium is small. Kinetic and double-layer effects are more important at high frequencies. An important advantage of EIS is that the influence of governing chemical and physical phenomena can be distinguished with a single experimental procedure encompassing a sufficiently broad range of frequency.

The critical issue of EIS is the ambiguity associated with the interpretation of impedance results. [25, 28, 29] A common approach of interpreting impedance data is to compare experimental spectra with that of known electrical circuit elements such as resistors, capacitors, and inductors. [28] The circuit analog models are found useful for understanding the physical processes that contribute to impedance responses; however, experimental data rarely show the ideal response expected for electrochemical reactions. The impedance response typically reflects a distribution of reactivity that is commonly represented in equivalent circuits as a constant-phase element (CPE). [29, 30]

The dispersion leading to CPE behavior can be attributed to distributions of time constants along either the area of the electrode (a two-dimensional surface) or along the axis normal to the electrode surface (a three-dimensional aspect of the electrode). A 2-D distribution might arise from surface heterogeneities such as grain boundaries, crystal faces on a polycrystalline electrode, variations in surface properties, or geometry-induced current and potential distributions. [31–34] A 3-D distributions may be attributed to

22

changes in the conductivity of oxide layers [35, 36] or from porosity or surface roughness. [37, 38] This CPE behavior can be described as arising from a 3-dimensional distribution, with the third direction being the direction normal to the electrode surface. [39, 40] Jorcin et al. [40] demonstrated that the use of local electrochemical impedance spectroscopy (LEIS) makes it possible to distinguish the CPE behavior that has an origin with a 3-D distribution from one that arises from a 2-D distribution of properties along the surface of the electrode.

The disk electrode geometry is well-defined and amenable to numerical calculation of the impedance response. Newman [41, 42] calculated the current and potential distributions on disk electrodes and developed both numerical and analytical treatments for the impedance response of a blocking electrode and an electrode subject to a Faradaic reaction. The results demonstrated that geometry-induced current and potential distributions cause a time-constant dispersion that distorts the impedance response. Nisancioglu [43–45] showed the extent to which this frequency dispersion causes an error in the values for charge-transfer resistance and interfacial capacitance obtained from impedance data. The discussion by Nisancioglu and by Newman, however, did not address the common practice of describing non-ideal impedance response in terms of constant-phase elements.

The first objective of this research topic was to calculate, from first principles, the influence of non-uniform current and potential distributions associated with a disk electrode on impedance response. The second objective of the work was to describe the role of the time-constant dispersion in terms of CPE behavior and to relate global impedance response with local impedance. The impedance calculations were performed for an ideally-polarized blocking electrode, a blocking disk electrode with a local CPE behavior, and a disk electrode subject to a simple Faradaic reaction.

The structure of the dissertation is divided according to the two research topics. The first part of the dissertation, presented from Chapter 2 to Chapter 6, deals with

fundamental electrochemical concepts, theoretical development, simulation results, and discussions that are associated with the cathodic delamination system. The objective of this part was to gain an understanding of the phenomena that may contribute to the delamination process through developing a mathematical model for cathodic delamination.

The fundamental electrochemical concepts relevant to the cathodic delamination system, such as electrode kinetics and transport in dilute solutions, are presented in Chapter 2. Experimental and simulation work associated with the cathodic delamination system are reviewed in Chapter 3. The constructions of the pH-dependent porosity and pH-dependent polarization kinetics are also presented in Chapter 3.

The model developed by Allahar did not include chemical reactions that become important at the later stage of the delamination. In the present work, multiple homogeneous reactions and precipitation of corrosion products were considered in the oxidized layer. The theoretical development of the present model followed the approaches taken by Allahar [22]. The development of the model is presented in Chapters 4 and 5. The computational results are presented in Chapter 6.

The second part of this dissertation, presented in Chapters 7 to 10, explores the influence of geometry-induced current and potential distributions on the impedance response of a disk electrode. Electrochemical impedance spectroscopy (EIS) is a rapid and convenient technique that provides electrochemical properties of tested systems over a wide range of frequencies. A brief introduction to EIS and issues encountered in EIS are presented in Chapter 7.

The current and potential distributions associated with a disk electrode embedded in an insulating plane are reviewed in Chapter 7. The theoretical development and calculation results for the ideally-polarized blocking electrode are presented in Chapter 8, the results for the blocking electrode with a local CPE behavior are presented in Chapter 9, and the results for the disk electrode exhibiting a Faradaic reaction are presented in Chapter 10.

CHAPTER 2
BACKGROUND ELECTROCHEMISTRY

The fundamental electrochemical concepts relevant to the cathodic delamination system, such as mass transport of ionic species in dilute solutions and electrode kinetics, are presented in this chapter. A detailed treatment of electrochemistry in electrolyte from a mathematical perspective has been presented by Newman. [46]

2.1 Mass Transport

In an electrochemical system, conservation of mass restricts the governing equation for the concentration of a species i to [46]

$$\frac{\partial c_i}{\partial t} = -\nabla \cdot N_i + R_i \qquad (2\text{--}1)$$

where the terms on the right side represent the net input due to the flux N_i and the net rate of production due to homogeneous reactions R_i, respectively. In dilute electrochemical systems, N_i is given by the Nernst-Planck equation [46]

$$N_i = -z_i c_i F u_i \nabla \Phi - D_i \nabla c_i + c_i v \qquad (2\text{--}2)$$

where Φ is the local solution potential, u_i is the mobility, D_i is the diffusion coefficient, z_i is the charge number, v is the mass average velocity of the electrolyte, and F is Faraday's constant. The terms on the right side of equation $(2\text{--}2)$ represent the contributions by migration, diffusion, and convection to the flux of a species, respectively.

Combination of equations $(2\text{--}1)$ and $(2\text{--}2)$, under the assumption that the electrolyte is incompressible ($\nabla \cdot v = 0$), yields the governing equation for c_i in a stagnant electrochemical system

$$\frac{\partial c_i}{\partial t} = z_i u_i F \nabla \cdot (c_i \nabla \Phi) + D_i \nabla^2 c_i + R_i \qquad (2\text{--}3)$$

where convective contributions to the flux of a species are negligible. The Nernst-Einstein equation [46]

$$u_i = D_i/RT \tag{2–4}$$

is generally applicable to dilute electrochemical systems where R is the molar gas constant and T is the absolute temperature. Combination of equations (2–2) and (2–4) yields the flux of a species

$$N_i = -z_i c_i F \frac{D_i}{RT} \nabla \Phi - D_i \nabla c_i \tag{2–5}$$

Equations (2–3) is rewritten as

$$\frac{\partial c_i}{\partial t} = D_i \left[z_i \nabla \cdot (c_i \nabla \Phi) + \nabla^2 c_i \right] + R_i \tag{2–6}$$

by employing the Nernst-Einstein equation.

2.2   Solution Potential

The governing equation for the solution potential in an electrochemical system is Poisson's equation [46]

$$\nabla^2 \Phi = -\frac{F}{\varepsilon} \sum_i z_i c_i \tag{2–7}$$

where ϵ is the permittivitty of the medium. An expression based on the concept of electroneutrality at a point, *i.e.*

$$\sum_i z_i c_i = 0 \tag{2–8}$$

has been used as the governing equation for Φ. Newman has shown that equation (2–8) provides a very good approximation to Poisson's equation outside the thin double charge layer near electrodes. [46] It is important to note that the assumption of electroneutrality does not imply that Lapalace's equation holds for the potential, because this approximation is made on the basis of a large value of F/ϵ in equation (2–7). [46]

The conservation of charge is given by

$$\nabla \cdot i = 0 \tag{2--9}$$

The ionic current density due to the motion of charged particles in an electrolytic solution is calculated by [46]

$$i = F \sum_i z_i N_i \tag{2--10}$$

Combination of equations (2--5) and (2--10), in the absence of convection, yields

$$i = -\kappa \nabla \Phi - F \sum_i z_i D_i \nabla c_i \tag{2--11}$$

where the conductivity κ is defined as

$$\kappa = \frac{F^2}{RT} \sum_i z_i^2 D_i c_i \tag{2--12}$$

The ionic current density in equation (2--11) can be divided into migration and diffusion contributions. The driving force for the migration and diffusion current densities are potential and concentration gradients, respectively. [46]

In the absence of concentration gradients, equation (2--11) reduces to an expression of Ohm's law

$$i = -\kappa \nabla \Phi \tag{2--13}$$

Combination of equation (2--13) with equation (2--9) yields Laplace's equation

$$\nabla^2 \Phi = 0 \tag{2--14}$$

for the solution potential Φ.

2.3   Electrochemical Kinetics

The rate of charge-transfer or Faradaic reactions taking place at electrode surface is important in corrosion systems. The reaction rate, characterized by current density, depends on the composition of the electrolytic solution adjacent to the electrode. [46]

Consider a simple heterogeneous electrochemical conversion of A to B on an electrode surface

$$A \rightleftarrows B^+ + e^- \qquad (2\text{--}15)$$

For the reaction described by equation (2–15), the forward reaction is anodic and the backward reaction is cathodic. The overall rate of the reaction r is given

$$r = r_f - r_b \qquad (2\text{--}16)$$

where r_f and r_b are the forward and backward rates, respectively.

Under the assumption that each reaction is first order, the overall rate can be written as

$$r = k_f c_A - k_b c_B \qquad (2\text{--}17)$$

From activated complex theory, equation (2–17) can be recast as

$$r = k_a \exp\left(\frac{(1-\beta)nF}{RT}V\right) c_A - k_c \exp\left(\frac{-\beta nF}{RT}V\right) c_B \qquad (2\text{--}18)$$

where V is the interfacial potential, β (known as the symmetry factor) is the fraction of the applied potential that favors the cathodic reaction, and n is the number of electrons transferred. Equation (2–18) can be written in terms of current density i as [46]

$$\frac{i}{nF} = k_a \exp\left(\frac{(1-\beta)nF}{RT}V\right) c_A - k_c \exp\left(\frac{-\beta nF}{RT}V\right) c_B \qquad (2\text{--}19)$$

The interfacial potential V is defined as

$$V = \Psi - \Phi \qquad (2\text{--}20)$$

where Ψ is the potential of the metal and Φ is the potential in electrolytic solution adjacent to the electrode.

When the anodic and cathodic reactions in equation (2–15) reach the same rate, a zero current is obtained under the condition of reaction equilibrium. At the equilibrium potential V_0, the net rate of the reaction is zero; however, the individual rates of the

reactions are non-zero. The current density at the equilibrium potential is defined as exchange current density i_0 and is calculated using either

$$\frac{i_0}{nF} = k_a \exp\left(\frac{(1-\beta)nF}{RT}V_0\right)c_A \tag{2-21}$$

or

$$\frac{i_0}{nF} = k_c \exp\left(\frac{-\beta nF}{RT}V_0\right)c_B \tag{2-22}$$

Substitution of i_0 into equation (2–19) yields the Butler-Volmer equation [46]

$$i = i_0\left[\exp\left(\frac{\alpha_a F}{RT}\eta_s\right) - \exp\left(\frac{-\alpha_c F}{RT}\eta_s\right)\right] \tag{2-23}$$

where the surface overpotential η_s is given by $\eta_s = V - V_0$, the anodic transfer coefficient α_a is given by $\alpha_a = (1-\beta)n$, and the cathodic transfer coefficient is given by $\alpha_c = \beta n$. The surface overpotential η_s represents the departure from an equilibrium potential such that, at $\eta_s=0$, the total current $i = i_a$ - i_c is equal to zero.

The exponential behavior of the Butler-Volmer equation results in a characteristic feature of electrochemical reactions. In the limit of $\alpha_a F\eta_s \gg RT$, equation (2–23) can be reduced to

$$i = i_0\exp\left(\frac{\alpha_a F}{RT}\eta_s\right) \tag{2-24}$$

Solving for η_s in equation (2–24) gives

$$\eta_s = \frac{RT}{\alpha_a F}\ln\left|\frac{i}{i_0}\right| \tag{2-25}$$

or

$$\eta_s = 2.303\frac{RT}{\alpha_a F}\log_{10}\left|\frac{i}{i_0}\right| \tag{2-26}$$

The Tafel slope for the anodic reaction β_a is given by the expression in front of the log term in equation (2–26)

$$\beta_a = 2.303\frac{RT}{\alpha_a F} \tag{2-27}$$

The corresponding Tafel slope for the cathodic reaction is given as

$$\beta_c = 2.303 \frac{RT}{\alpha_c F} \tag{2–28}$$

The Butler-Volmer equation, equation (2–23), can be recast using these Tafel slopes into

$$i = 10^{(V-E_a)/\beta_a} - 10^{(V-E_c)/\beta_c} \tag{2–29}$$

where E_a and E_c are the effective equilibrium potentials given by

$$E_a = V_0 - \beta_a \log_{10} i_0 \tag{2–30}$$

for the anodic reaction and

$$E_c = V_0 - \beta_c \log_{10} i_0 \tag{2–31}$$

for the cathodic reaction, respectively. [47]

2.3.1 Kinetic Control

In electrochemical systems, multiple Faradaic reactions often occur simultaneously on an electrode surface. For example, zinc dissolution

$$\mathrm{Zn} \rightarrow \mathrm{Zn}^{+2} + 2\mathrm{e}^- \tag{2–32}$$

and hydrogen evolution reaction

$$2\mathrm{H_2O} + 2\mathrm{e}^- \rightarrow \mathrm{H_2} + 2\mathrm{OH}^- \tag{2–33}$$

may both occur in a corrosion system. Under such circumstance, the individual electrochemical reactions can be treated independently. Therefore, a Butler-Volmer equation such as equation (2–23) can be written for each of these reactions.

The current density due to the reversible corrosion reaction i_{Zn}

$$\mathrm{Zn} \rightleftarrows \mathrm{Zn}^{2+} + 2\mathrm{e}^- \tag{2–34}$$
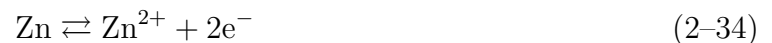
can be calculated by

$$i_{\mathrm{Zn}} = 10^{(V-E_{\mathrm{a,Zn}})/\beta_{\mathrm{a,Zn}}} - 10^{(V-E_{\mathrm{c,Zn}})/\beta_{\mathrm{c,Zn}}} \qquad (2\text{--}35)$$

In most corrosion systems, metal dissolution is considered to be an irreversible reaction. Thus, the current density due to the zinc dissolution i_{Zn} is given by

$$i_{\mathrm{Zn}} = 10^{(V-E_{\mathrm{Zn}})/\beta_{\mathrm{Zn}}} \qquad (2\text{--}36)$$

where $E_{\mathrm{a,Zn}}$ and $\beta_{\mathrm{a,Zn}}$ are replaced by E_{Zn} and β_{Zn}, respectively. Similarly, the current density $i_{\mathrm{H_2}}$ due to the hydrogen evolution in reaction (2–33) is given by

$$i_{\mathrm{H_2}} = -10^{-(V-E_{\mathrm{H_2}})/\beta_{\mathrm{H_2}}} \qquad (2\text{--}37)$$

under the assumption that the reaction is irreversible. The total current density for the given system is the sum of the individual current density

$$i_{\mathrm{net}} = i_{\mathrm{Zn}} + i_{\mathrm{H_2}} \qquad (2\text{--}38)$$

The polarization behavior of the corrosion and the hydrogen evolution are termed activation polarization because the rates of the electrochemical reactions are driven by the surface overpotential η_s.

2.3.2   Mass Transfer Control

The rate of electrochemical reactions can also be limited by the rate at which reacting species are carried to the electrode surface. An example of such a case is illustrated in Figure 2-1 for an oxygen reduction reaction. The polarization behavior of the oxygen reduction contains activation and concentration components. The current densities is a function of potential in the activation polarization part, but is independent of potential in the concentration polarization part. The reaction rate in the concentration polarization regime is limited by the rate of transport of oxygen to the metal surface. The mass-transfer-limited current density, symbolized as $i_{\mathrm{lim,O_2}}$, depends on solution agitation, temperature and concentration of the limiting species. [48] The numerical value of the
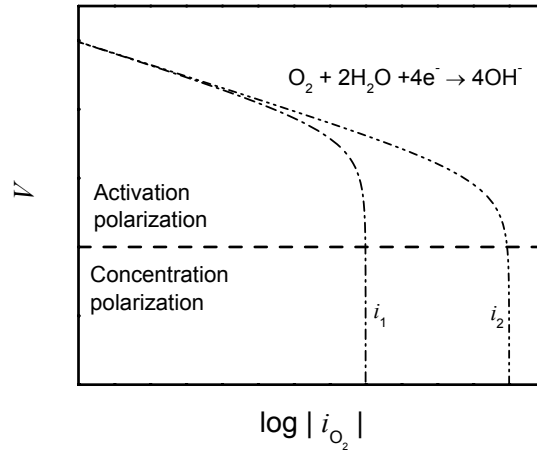
Figure 2-1. Polarization plots for oxygen reduction at two values of mass-transfer-limited current density labelled as i_1 and i_2. The horizontal dashed line separates the activation potential and concentration polarization parts of the plots.

limiting current density is given by

$$i_{\mathrm{lim,O_2}} = \frac{-nFD_{O_2}c_{O_2,\infty}}{x} \qquad (2\text{--}39)$$

where x and c_{O_2} are the distance that oxygen diffuses through and the oxygen concentration in the bulk, respectively. The current density due to the oxygen reduction $i_{\mathrm{O_2}}$ is given by the mathematical expression

$$i_{O_2} = -\left[\frac{1}{i_{\mathrm{lim,O_2}}} + 10^{(V-E_{O_2})/\beta}\right]^{-1} \qquad (2\text{--}40)$$

to account for both activation and concentration regimes.

CHAPTER 3
LITERATURE REVIEW ON CATHODIC DELAMINATION

As described in literature, the delamination of paint under humid and corrosive environment involves a coupling of mass transfer, electrochemistry, loss of adhesion at the metal-coating interface, and propagation of a moving front along the interface. Experimental and simulation work associated with the cathodic delamination system are reviewed briefly in this chapter.

3.1 Experimental Observation

The kinetics and the mechanisms of the delamination process have been investigated experimentally for coated steel and coated electrogalvanized steel using local electrochemical and physical techniques. Stratmann et al. [9–18, 49] employed a scanning Kelvin probe to measure potential distributions at buried polymer/metal interfaces. They performed the experiments under accelerated corrosive conditions and minimized surface treatments, thus the delamination rate predicted from their samples were larger than that observed from commercial technical samples. [19] William et al. [50, 51] also employed the scanning Kelvin probe technique to study the influence of inhibitors on the delamination mechanism of coated galvanized steel.

A new technique based on Fourier transform infrared-multiple internal reflection (FTIR-MIR) allowed in-situ measurements of the thickness of water layer at metal-coating interface. [52, 53] This technique provided a means to determine the rate of water transport through the coating and to calculate the diffusion coefficient of water through the polymer film. Jorcin *et al.* [54] explored the delamination phenomena at a steel/epoxy-vinyl prime interface using local electrochemical impedance mapping. The results showed that the delaminated area measured by visual observations after the removal of the coating were approximately three times smaller than that determined by the local electrochemical impedance mapping.

The samples used in delamination experiments are typically made by applying a micro-thick polymer layer on a metal substrate using a roll coat procedure. [19] After few days of curing, the samples are scribed to create a defect area. This well-defined defect serves as a reservoir for electrolyte when the coated samples are placed into a controlled-humidity and subjected to intermittent salt sprays. Depending upon whether the metal dissolution occurs at the defect or under the paint, the electrochemical mechanisms of the delamination can be divided into two broad categories: anodic and cathodic delamination. As reported in the literature, the delamination often begins in a condition where the uncoated area plays a role of a local anode, and the coated part represents a local cathode.

Furbeth and Stratmann [9–11] reported that the cathodic delamination process on a coated metal with a coating defect was the result of a galvanic couple formed between the defect and the intact zone. Cathodic reactions at the metal-coating interface were balanced by anodic reactions at the bare metal exposed by the defect. A schematic diagram of a delamination system, following the interpretation obtained by Stratmann et al., is presented in Figure 3-1. The system consists of a defect where the bare metal is exposed to an electrolyte of NaCl, and a delaminated zone where the interfacial adhesive bonding between the substrate and the paint is partially damaged due to the delamination process. The exposure of the metal to the electrolyte initiates an anodic reaction at the defect. On the delaminated zone where the metal dissolution is limited due to the presence of the coating, small molecules such as water and oxygen diffuse through the polymer film and are reduced at the interface. [6, 7, 12, 16] The cathodic delamination process is driven by the formation of an electrochemical cell formed between the anodic and the cathodic sites.

Leng and Stratmann [15] suggested that, after the delamination began to occur, the intact coating-substrate interface was replaced gradually by two new interfaces: a substrate-electrolyte layer and electrolyte-polymer layer. The electrochemical reactions,

34
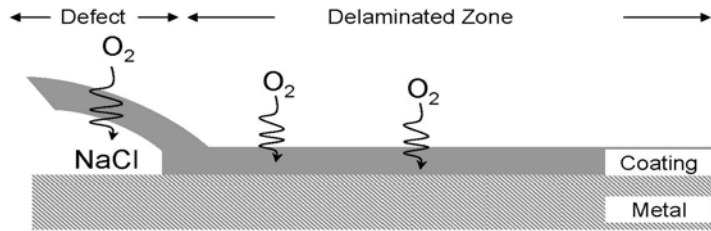
Figure 3-1. Schematic representation of cathodic delamination of a coated metal, following the interpretation obtained by Stratmann et al. [9–11] The system consists of a defect where the metal is exposed to an electrolyte, and a delaminated zone where the interface adhesive strength is partially broken.

therefore, expanded from the scratch and propagated away from the defect with a well-defined delamination front. The OH^- ions produced in the cathodic reaction mechanism promoted coating disbondment through polymer decomposition and hydrolysis of interfacial bonds. [51] Leng and Stratmann [14] found that the reduction of oxygen partial pressure decreased significantly the delamination rate, concluding that the oxygen reduction was important in the delamination process. Other radical peroxide intermediates generated in the oxygen reduction have also been proposed as possible aggressive species during the delamination process. For a case of an ultrathin plasma polymer layer, Grundmeier [55, 56] suggested that the metal-coating interface was destroyed by the attack of the intermediates formed in the cathodic reaction mechanism.

The potential distributions obtained from the scanning Kelvin probe were used to interpret the delamination mechanism for coated zinc and coated steel. [9–18, 50, 51] A schematic representation of a potential distribution, following the experimental results reported by Stratmann et al., is given in Figure 3-2(a) as a function of position with elapsed time as a parameter. The zero position in the figure represents the boundary between the defect and the delaminated zone. Three different regions are observed in Figure 3-2(a). The interfacial potential shows a gradual increase with position in the delaminated region, an abrupt increase in the front region, and approximately a constant value in the intact region. As observed in Figure 3-2(a), the shape of the potential
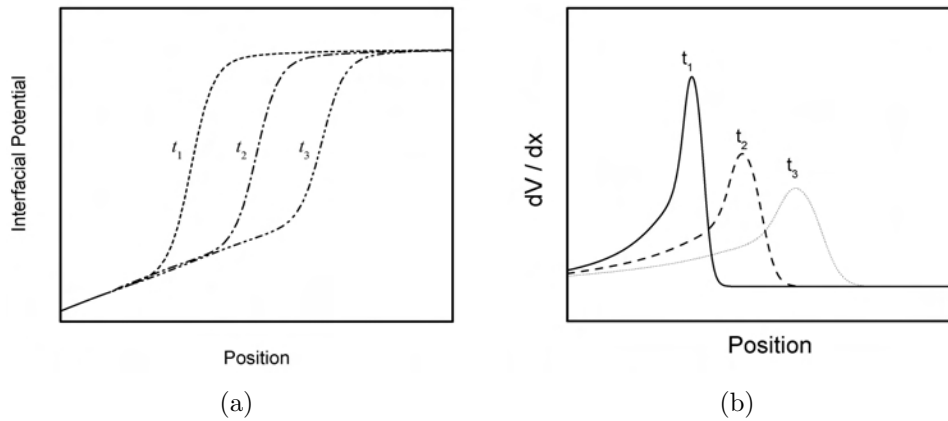
Figure 3-2. Schematic representation of experimental interfacial potential distribution. a) interfacial potential distribution as a function of position with elapsed time as a parameter; and b) dV/dx distribution as a function of position with elapsed time as a parameter.

distributions is maintained throughout the experiments. The length of the intact region decreases with increasing time. William et al. [50, 51] also obtained a similar transition in the potential measurements for a coated electrogalvanized steel pigmented with CrO_4^{2-} and Ce^{3+} ions.

The interfacial potential distribution was differentiated with respect to position to yield dV/dx distributions, shown in Figure 3-2(b), as a function of position with elapsed time as a parameter. The peak marked the deflection point of the abrupt increase observed in Figure3-2(a). The position of the peak, recognized as the delamination front, represented a region where the reaction of breaking bonds is ongoing. The peak height corresponding to the value of dV/dx was observed to decease with delamination time. Leng and Stratmann [15] suggested that, with increasing time, there was a more gradual change in the electrochemical potential across the front region.

The delamination kinetics can be determined by plotting the delaminated distance calculated from the dV/dx curve as a function of time. Leng [15] and William [51] employed a general power law

$$x_{del} = kt_{del}^a \qquad (3\text{--}1)$$

to describe the delamination mechanism, where x_{del}, k, and t_{del} are delaminated distance, rate constant, and delamination time, respectively. Furbeth and Stratmann [11] reported a value of $a = 0.55$ from coated steel with minimized surface treatments, which concluded that the overall delamination process was governed primarily by the transport of cations from the defect to the delaminated zone. Their results also demonstrated that, for non-pigmented samples and a short-time exposure, the rate of the delamination depended strongly on the ionic strength and the mobility of cations. [11]

Experimental observations have shown that the later stage of the delamination becomes more complicated when passive films or corrosion products are formed underneath the coating. [10, 19] Furbeth and Stratmann [10] reported that the formation of $ZnCO_3$, under a high CO_2 concentration in the atmosphere inhibits the electron transfer of oxygen reduction, resulting in a pure anodic delamination for coated electrogalvanized steel. The precipitation of $Zn(OH)_2$ or ZnO at the defect prevents corrosion of the uncoated area, therefore, the cathodic reaction becomes dominating on the scratch for coated zinc samples. Moreover, after longer-time exposure, as the delamination front moves further away the defect, both anodes and cathodes can appear under the paint and it becomes difficult to distinguish whether the moving front is anodic or cathodic.

Numerous research efforts have been made to study the influence of inhibitors and surface treatments on the delamination rate and the delamination kinetics. Hernandez et al. [57] indicated that the zinc-aluminum phosphate pigments reduced the delamination rate by forming a phosphate layer underneath the paint. Ogle et al. [19] tested various surface treatments under both anodic and cathodic delamination conditions. The results were interpreted in terms of the differing chemical stability of the conversion layers toward OH^- ions generated by oxygen reduction.

3.2 Mathematical Models

It is difficult to demonstrate that a proposed mechanism suggested based on experimental work does indeed give the observed experimental results. Interpretation

is often limited to qualitative and subjective observations. Therefore, a mathematical model is necessary to identify the phenomena and mechanisms that contribute to the delamination process.

To date, there are not many mathematical models that simulate explicitly the propagation of front along the metal-coating interface during the cathodic delamination of a coated metal. Yet, the occluded environment underneath the paint have been modeled extensively in terms of crevice corrosion models [58–61] or disbonded coating models. [62, 63] These models are often used to calculate the spatial distributions of c_i, Φ, and the current density along the metal surface.

3.2.1   Crevice and Disbonded Coating Models

The crevice system, given in Figure 3-3, has been approximated by a geometry that consists of a disbonded region adjacent to a defect. The boundary located at the plane of symmetry represents an impermeable wall. The thickness of the disbondment, termed the gap, is assumed uniform along the metal-coating interface. In disbonded coating systems, the length of the system in the direction parallel to the substrate is often assumed to be large as compared to the gap. This facilitates the assumption that variations in the direction normal to the metal surface are negligible.

Chin and Sabde [62] developed a steady-state model for a disbondment system under cathodic protection. The model accounted for oxygen reduction but neglected corrosion and hydrogen evolution under the cathodic protection. The ionic species considered were Na^+, Cl^-, and OH^-, and no other homogeneous chemical reactions were included. The diffusion and migration of species were considered; however, the diffusion coefficients were treated as $D_i = 10^{-5}$ cm^{2}s^{-1} for all ionic species.

Following the development presented by Chin and Sabde [62], Allahar [22] established a two-dimensional disbondment model in the presence of multiple electrochemical reactions and one homogeneous reaction. In his work, the assumption that D_i was equal for all species was relaxed. [22] A quasipotential transformation was introduced
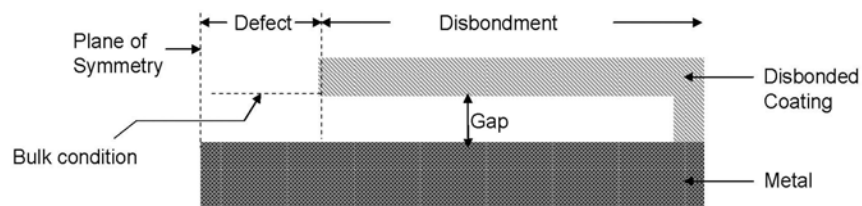
Figure 3-3. Schematic diagram of a disbonded coating system on a coated metal.

to solve the system of coupled equations that described the transport of species and the electroneutrality condition. The application of the transformation increased computational accuracy and overcame the numerical difficulties arose from the inclusion of homogeneous reactions.

Sridhar [63] developed a transient model for disbonded coating system to simulate the evolution of the disbondedment. The species considered in the model were separated into primary and secondary species. The concentration distributions of the primary species were calculated using given potential distributions and conservation relationships. The concentration distributions of the secondary species were calculated using the concentration of the primary species and the equilibrium relationships associated with homogeneous reactions. The computational results showed that the pH and potential gradients in the disbonded region were the consequences of the competition between anodic dissolution and cathodic reactions. Exposure time, applied potential, solution conductivity, and crevice geometry were the factors that influenced the pH and potential gradients.

3.2.2 Cathodic Delamination Model

Based upon the experimental observations reported by Stratmann et al. [9–18], Allahar [21, 22] developed the first mathematical model for the cathodic delamination of coated metal. The model accounted for the coupling of mass transfer of species, electrochemical kinetics, bond-breakage phenomena, and the propagation of the front along the metal-coating interface. The key to the development of the model involved

applying the concept that the porosity and the polarization kinetics at the interface were pH dependent. These pH-dependent hypotheses provided an approach to simulate the growth of the delamination within a fixed domain. The development of Allahar's work served to guide that of the present work.

3.2.2.1 pH-Dependent Porosity

Furbeth and Stratmann [9] reported that, during the cathodic delamination process, the coating degraded into a gel-type medium and the adhesive bond between the coating and the metal was weakened. The OH^- ions produced in the oxygen reduction underneath the paint were linked to the coating degradation and the loss of adhesion. In the mathematical model developed by Allahar, [21, 22] the transition from the degraded region to the intact region was characterized by the change in porosity. Under the assumption that the oxidation of the coating was due to the attack of OH^- ions, the interfacial porosity was treated as a function of pH.

The transition of the porosity in the delaminated zone was constructed based upon the de-adhesion experiments performed by Furbeth and Stratmann. [9] From the tensile force distributions, Allhar [22] proposed that the porosity was somewhat larger in the delaminated region due to the interfacial bonds being partially broken. In the intact region where the delamination has not occurred, the porosity was somewhat smaller. Thus, the porosity made a transition from the value associated with the delaminated region to that associated with the intact region. A mathematical formula was then constructed to describe the the distribution of the porosity in the delaminated domain.

Experimental results revealed that in the delaminated and front regions the concentrations of the two major species, OH^- and Na^+, were approximately equal. [9] Therefore, the pH distribution was constructed according to the observed c_{Na^+} distribution. The expression for the porosity-pH relation,

$$\varepsilon = \frac{b_{\varepsilon,1}}{1 + \exp[b_{\varepsilon,2}(pH - b_{\varepsilon,3})]} + \frac{b_{\varepsilon,4}}{1 + \exp[b_{\varepsilon,5}(pH - b_{\varepsilon,6})]} + b_{\varepsilon,7} \qquad (3\text{--}2)$$

was obtained by coupling the porosity and the pH distributions, where $b_{\varepsilon,1}$ to $b_{\varepsilon,7}$ were fitting parameters.

The use of the pH-dependent interfacial porosity represented a novel approach to account implicitly for the bond-breaking process during the cathodic delamination. As proven by Allahar, no propagation was observed when the pH-porosity relation was not incorporated in the model. [22]

3.2.2.2   pH-Dependent Polarization Kinetics

Due to the presence of the coating, the polarization behavior of electrochemical reactions at the metal-coating interface is different from that at the metal-electrolyte interface. Allahar [22] derived expressions for the polarization kinetics at the metal-coating interface based upon expressions applicable to a bare metal surface.

The current density due to zinc dissolution and oxygen reduction at the zinc-coating interface were calculated using [22]

$$i_{\mathrm{Zn}}^{coat} = w_{\mathrm{A}}w_{\mathrm{Zn}}i_{o,Zn}10^{\left(\frac{V-E_{\mathrm{Zn}}}{\beta_{\mathrm{Zn}}}\right)} \tag{3-3}$$

and

$$i_{\mathrm{lim},O_2}^{coat} = -w_{\mathrm{A}}w_{O_2}nFD_{O_2}c_{O_2,\infty}\frac{\varepsilon_g^{1.5}\varepsilon_c^{1.5}}{\varepsilon_g^{1.5}g_c + \varepsilon_c^{1.5}g_m} \tag{3-4}$$

The surface coverage w_{A} represented the surface area available for electrochemical reactions. The poisoning parameter w_{Zn} considered the influence of surface on the exchange current density of zinc dissolution. The effect of the coating or other formed deposits on the transport of oxygen through the gel medium was included by a blocking parameter w_{O_2}. As the effect of these parameters varied according to the local pH, the parameters were linked to pH with the same manner described in the porosity-pH relation.

The use of porosity to represent the bond-breaking process occurring during the cathodic delamination process provided a mathematical framework for the development of advanced models. The numerical approach employed by Allhar was not able to include

homogeneous or other chemical reactions due to the ill-conditioned coefficient matrix generated from governing equations. In the present work, a series of homogeneous reactions and formation of corrosion products were considered. A different numerical approach using Newman's BAND algorithm [46] was employed in order to incorporate these chemical reactions into the model.

3.3 Objective

The objective of the work was to develop a mathematical model that simulates the cathodic delamination of a coated metal in the presence of multiple electrochemical reactions, homogeneous reactions and formation of corrosion products. The electrochemical reactions considered along the metal-coating interface were zinc dissolution and oxygen reduction. Water dissociation and a series of reactions associated with Zn^{2+} hydrolysis were treated as homogeneous reactions in the model. The corrosion product $ZnOH_2$ was assumed to precipitate along the metal-coating interface. The concepts of pH-dependent porosity and pH-dependent polarization kinetics remained in the model, but modifications were made to reduce the number of the fitting parameters used in the program.

The second objective was the use of the developed model to predict the delamination rate and the delamination kinetics for non-pigmented coated samples. As addressed earlier, the rate and the mechanism of the delamination system depend strongly on the application and the property of inhibitors and/or pigments. The chemical variations associated with these surface treatments, however, are not the major focus of the present work.

CHAPTER 4
THEORETICAL DEVELOPMENT OF DELAMINATION MODEL

The propagation model simulated the evolution of the delamination process from given initial conditions. The propagation of front and the bond-breakage reactions accompanying the delamination process were modeled through the hypotheses that porosity and the polarization kinetics at the coating-metal interface were pH dependent. Mathematical constructions for the initial conditions and the pH-dependent hypotheses followed the development by Allhar. Modifications were made to reduce the number of the fitting parameters used in the program.

4.1   Porosity-pH Relation

In the present model, the delaminated zone was considered to be a porous medium. The flux in a dilute, porous electrochemical system N_i^* was expressed as [46]

$$N_i^* = -z_i c_i F \frac{D_i^*}{RT} \nabla \Phi - D_i^* \nabla c_i \qquad (4\text{–}1)$$

where c_i is the concentration in the aqueous phase. The effective diffusion coefficient D_i^* in a porous medium was related to the porosity ε by [64]

$$D_i^* = \varepsilon^{1.5} D_i \qquad (4\text{–}2)$$

where D_i is the diffusivity in an aqueous medium. Equation (4–1) was recast in terms of D_i using equation (4–2) as

$$N_i^* = \varepsilon^{1.5} (-z_i c_i F \frac{D_i}{RT} \nabla \Phi - D_i \nabla c_i) \qquad (4\text{–}3)$$

The conservation of a species i in a porous medium was expressed in terms of N_i as

$$\frac{\partial (\varepsilon c_i)}{\partial t} = -\nabla \cdot (\varepsilon^{1.5} N_i) + \varepsilon R_i \qquad (4\text{–}4)$$

where N_i was the flux in the solution phase.
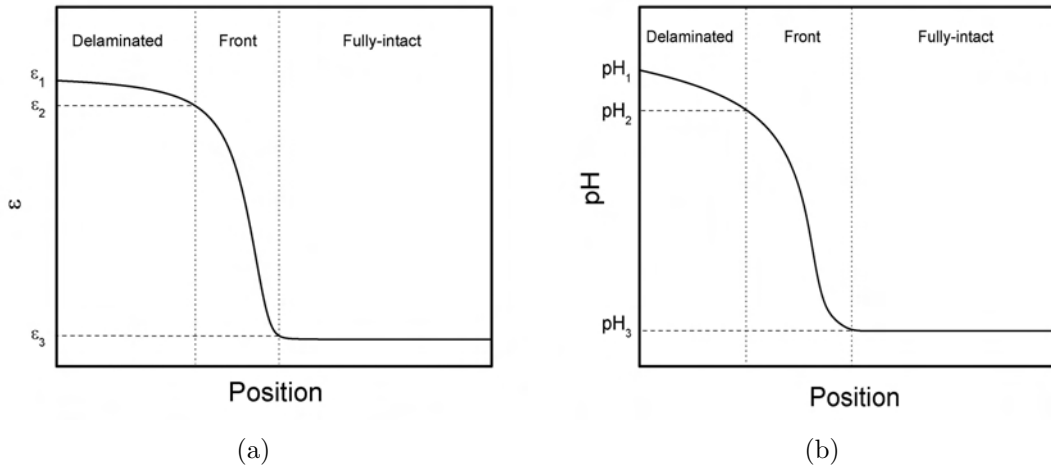
Figure 4-1. Schematic diagrams for interfacial porosity ε and pH as functions of position in the delaminated zone. The dashed lines separate the domain into the delaminated, front, and fully-intact regions: a) interfacial porosity; and b) local pH.

Following the approach taken by Allahar, [22] interfacial porosity was used to characterize the transition from a degraded region to an intact region in the delaminated zone. An assumed porosity transition in the delaminated domain, shown in Figure 4-1(a), was constructed according to the de-adhesion tests conducted by Stratmann et al. [9]. Three transition regions are observed in Figure 4-1(a). The porosity decreases gradually with position in the delaminated region. In the front region where the delamination is ongoing, the porosity shows an abrupt decrease with position. The porosity remains unchanged in the intact region where the delamination has not yet occurred.

Experimental results revealed that in the delaminated and front regions the concentrations of the two major species, Na^+ and OH^-, were approximately equal. [9] Thus, the pH distribution in the delaminated domain was constructed based upon the observed c_{Na^+} distributions. [9] An assumed pH distribution is given in Figure 4-1(b) where the pH value decreases with position in the delaminated and front regions. As the OH^- ions produced in the oxygen reduction underneath the paint were linked to the
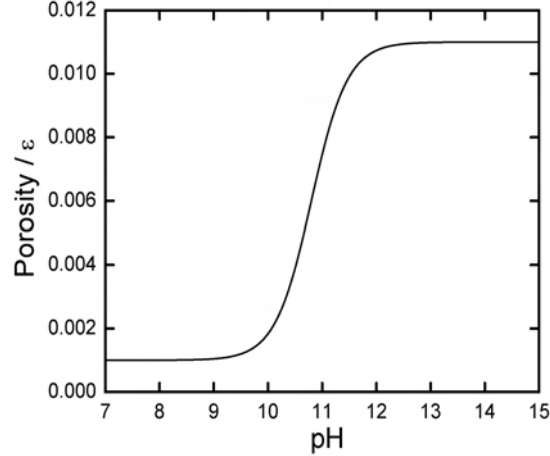
Figure 4-2. Schematic diagram for distribution of interfacial porosity ε as a function of local pH.

coating degradation and the loss of adhesion, [9–18] the porosity used to represent the adhesion between the metal and the coating was treated as a function of pH.

The porosity-pH relation was obtained by combining Figures 4-1(a) and 4-1(b) to yield the ε distribution as a function of pH shown in Figure 4-2. The mathematical expression for the ε-pH relationship was obtained by fitting an equation of the form

$$\varepsilon(pH) = \frac{b_{\varepsilon,1}}{1 + \exp(b_{\varepsilon,2}(pH - b_{\varepsilon,3}))} + b_{\varepsilon,4} \qquad (4\text{–}5)$$

to the plot in Figure 4-2 where $b_{\varepsilon,1}$ to $b_{\varepsilon,4}$ were fitting parameters. The porosity was assumed to reach the value given by equation (4–5) instantaneously; thus the ε-pH relationship represents an equilibrium condition between ε and pH.

4.2 Polarization Kinetics

The electrochemical reactions of interest in the cathodic delamination model involved zinc dissolution

$$\text{Zn} \rightarrow \text{Zn}^{2+} + 2\text{e}^- \qquad (4\text{–}6)$$

and oxygen reduction

$$\text{O}_2 + 2\text{H}_2\text{O} + 4\text{e}^- \rightarrow 4\text{OH}^- \qquad (4\text{–}7)$$

The polarization kinetic at the metal-coating interface was derived from that applicable to the metal-electrolyte interface.

4.2.1 Zinc Dissolution

In an aqueous environment with a bare metal surface, the current density due to zinc dissolution i_{Zn} follows the Bulter-Volmer equation [48]

$$i_{\text{Zn}} = i_{o,\text{Zn}} 10^{(\frac{V - E_{\text{Zn}}}{\beta_{\text{Zn}}})} \qquad (4\text{--}8)$$

where β_{Zn}, E_{Zn}, $i_{o,\text{Zn}}$ are the Tafel slope, equilibrium potential, and exchange current density, respectively, for the zinc dissolution. A poisoning factor ζ was employed to calculate the current density due to the zinc dissolution at the metal-coating interface, *i.e.* [22]

$$i_{\text{Zn}}^{coat} = \zeta i_{o,Zn} 10^{(\frac{V - E_{\text{Zn}}}{\beta_{\text{Zn}}})} \qquad (4\text{--}9)$$

The poisoning factor ζ considered the effect of coating, the availability of surface area to zinc dissolution during the delamination. The factor also accounted implicitly for the presence of passive films formed on the metal surface. The poisoning factor ζ was assumed to be a function of pH, and the construction of the ζ-pH relationship was performed in a manner similar to the construction of the ε-pH relationship.

4.2.2 Poisoning-pH Relation

Experimental observations indicated that, during the cathodic delamination process, anodic dissolution along the metal-coating interface is poisoned due to the presence of the coating. [9, 16] Thus, the zinc dissolution was considered unfavorable in the delaminated zone by assigning $\zeta \ll 1$. An hypothesized distribution of ζ as a function of position is presented in Figure 4-3(a). In the delaminated region, the poisoning parameter ζ is approximately a constant, indicating that the surface availability to the zinc dissolution is independent of position in this region. The poisoning parameter decreases exponentially with position in the front region, demonstrating that the anodic reaction is unfavorable in the front. In the fully-intact region the value of ζ is held as a constant.
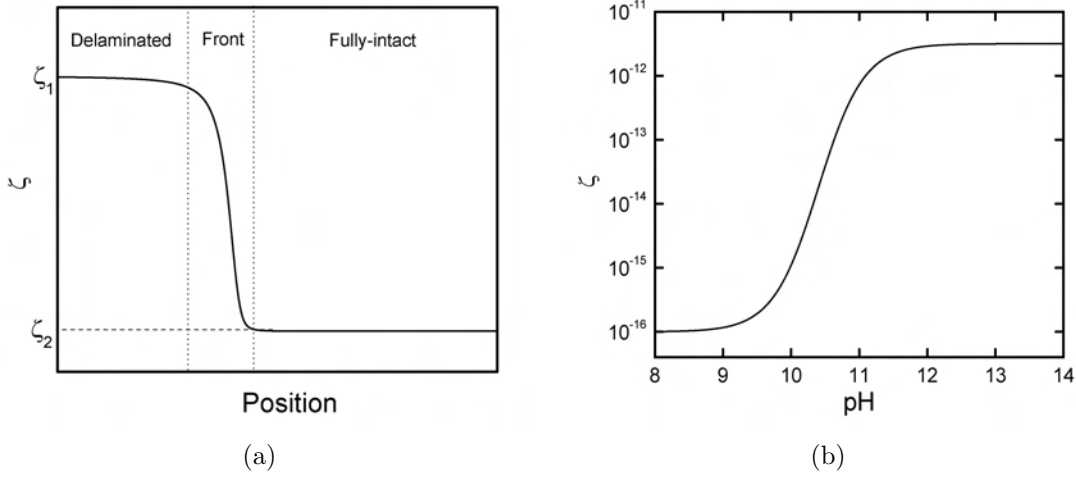
Figure 4-3. Schematic diagram for distribution of poisoning factor ζ: a) as a function of position; and b) as a function of local pH.

The relationship between ζ and pH, given in Figure 4-3(b), was constructed by coupling the distributions shown in Figures 4-3(a) and 4-1(b). The mathematical expression for the ζ-pH relationship was obtained by fitting an equation of the form

$$\zeta(pH) = \frac{b_{\zeta,1}}{1 + \exp(b_{\zeta,2}(pH - b_{\zeta,3}))} + b_{\zeta,4} \tag{4–10}$$

to the plot in Figure 4-3(b) where $b_{\zeta,1}$ to $b_{\zeta,4}$ were fitting parameters.

4.2.3 Oxygen Reduction

Under the assumption that oxygen reduction is mass-transfer-limited at the metal-electrolyte interface, the limiting current density is given as [48, 65]

$$i_{\lim,O_2} = \frac{-nFD_{O_2}c_{O_2,\infty}}{x} \tag{4–11}$$

where x is the distance that oxygen diffuses through and $c_{O_2,\infty}$ is the oxygen concentration in the bulk. In the presence of coating and interfacial oxidized layer, the mass-transfer-limited current density due to oxygen reduction was calculated using [22]

$$i_{\lim,O_2}^{\text{coat}} = -\alpha_{O_2}nFD_{O_2}c_{O_2,\infty}\frac{\varepsilon_g^{1.5}\varepsilon_c^{1.5}}{\varepsilon_g^{1.5}g_c + \varepsilon_c^{1.5}g_m} \tag{4–12}$$

47
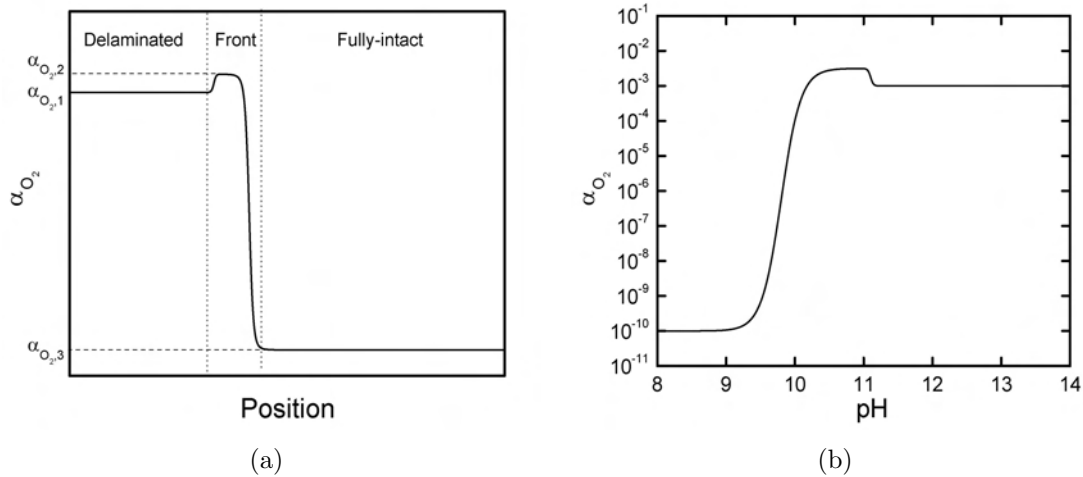
Figure 4-4. Schematic diagram for distribution of blocking factor α_{O_2}: a) as a function of position; and b) as a function of local pH.

where g_m and g_c were the thickness of the gel-medium and the coating, respectively, and ε_c and ε_g were the porosity of the un-degraded coating and the gel-medium, respectively. The complex term seen at the right side of equation (4–12) was derived by solving the concentration distribution of oxygen in the direction normal to the metal surface. The blocking factor α_{O_2} accounted for the influence of the coating and the oxidized layer on the transport of oxygen to the metal surface. The blocking factor α_{O_2} was assumed to be a function of pH and the construction of the α_{O_2}-pH relationship was performed in a manner similar to the construction of the ε-pH relationship.

4.2.4 Blocking-pH Relation

An assumed distribution of α_{O_2} as a function of position along the metal-coating interface is presented in Figure 4-4(a). The blocking factor is a constant in the delaminated region, indicating that the transport of oxygen is independent of position in this region. A largest electrochemical reactivity for oxygen reduction is expected across the front region; thus, the blocking factor increases in the front. The blocking factor decreases to a minimum to represent a smallest reactivity in the intact region.

The α_{O_2}-pH relation was constructed by coupling Figures 4-4(a) and 4-1(b) to yield the α_{O_2} distribution as a function of pH given in Figure 4-4(b). The mathematical

Table 4-1. Fitting parameters used in the expressions of pH-dependent interfacial porosity, blocking, and poisoning parameters.

k.	ε	ζ	α_{O_2}
b1	0.01	4.50	7.50
b2	-3.00	-3.30	-7.00
b3	10.8	10.4	9.80
b4	0.001	-16.0	-0.50
b5	-	-	-50.0
b6	-	-	11.10
b7	-	-	-10.0

expression for the α_{O_2}-pH relation was obtained by fitting an equation of the form

$$\alpha_{O_2}(pH) = 10^{\left(\frac{b_{\alpha,1}}{1+\exp(b_{\alpha,2}(pH-b_{\alpha,3}))} + \frac{b_{\alpha,4}}{1+\exp(b_{\alpha,5}(pH-b_{\alpha,6}))} + b_{\alpha,7}\right)} \tag{4--13}$$

to the plot in Figure 4-4(b) where $b_{\alpha,1}$ to $b_{\alpha,7}$ were fitting parameters.

The values of the fitting parameters used in equations (4–5), (4–10) and (4–13) are listed in Table 4-1. The choice of the values of these parameters might play an important role on the computational results. Thus, a systematic sensitivity analysis was performed and the results are reported in Appendix E.

4.3 Chemical Reactions

The oxygen reduction taking place underneath the coating results in an increase of pH in the interfacial degraded layer. For zinc, a series of chemical reactions associated with Zn^{2+} hydrolysis and formation of corrosion product $Zn(OH)_{2(s)}$ are possible in alkaline solutions. [66, 67] In the presented model, multiple homogeneous reactions, including water dissociation and a series of reactions associated with Zn^{2+} hydrolysis, were considered. The mechanisms and equilibrium conditions of these chemical reactions are summarized in Table 4-2. [67] All the homogeneous reactions were assumed to be equilibrated because the time constants for reaching the equilibrium conditions are much smaller than that for the diffusion of the limiting reactant. [68, 69]

The precipitated corrosion product $Zn(OH)_{2(s)}$ is thermodynamically stable within the pH ranging from 8.5 to 11. [66, 67] The reaction mechanism of forming solid $Zn(OH)_{2(s)}$

Table 4-2. Reaction mechanism and equilibrium condition for homogeneous reactions
included in the model. [66, 67]

Reaction NO.	Chemical Reaction	Equilibrium Condition
1	$H_2O \longleftrightarrow OH^- + H^+$	$K_w = c_{OH^-}c_{H^+}$
2	$Zn^{2+} + OH^- \longleftrightarrow ZnOH^+$	$\log \frac{c_{ZnOH^+}}{c_{Zn^{2+}}} = -9.67 + pH$
3	$ZnOH^+ + 2OH^- \longleftrightarrow HZnO_2^- + H_2O$	$\log \frac{c_{HZnO_2^-}}{c_{ZnOH^+}} = -17.97 + pH$
4	$HZnO_2^- + OH^- \longleftrightarrow ZnO_2^{2-} + H_2O$	$\log \frac{c_{ZnO_2^{2-}}}{c_{HZnO^{2-}}} = -13.17 + pH$

was assumed to be

$$Zn^{2+} + 2OH^- \rightarrow Zn(OH)_{2(s)} \tag{4–14}$$

The rate of production of $Zn(OH)_{2(s)}$ depends strongly on the concentrations of Zn^{2+} and
OH^-; thus, the precipitation rate was related to $c_{Zn^{2+}}$ and c_{OH^-} by

$$r_{pre} = k[c_{OH^-}^2 c_{Zn^{2+}} - Ksp] \tag{4–15}$$

where k is a rate constant and K_{sp} is the standard solubility product of $Zn(OH)_{2(s)}$
at room temperature. [70] The difference between the two terms in the bracket at
the right side of equation (4–15) represents the driving force for forming $Zn(OH)_{2(s)}$.
Equation (4–15) provides an approach, in terms of the concentrations of Zn^{2+} and OH^-
ions, to incorporate the solid species $Zn(OH)_{2(s)}$ in the complex model. However, this
approach is different from that employed in thermodynamic calculations in which the total
concentrations of Zn^{2+} and OH^- ions were held as constants. [71, 72]

CHAPTER 5
CATHODIC DELAMINATION MODEL

The development of the mathematical model is presented in this chapter. The model simulated the propagation of the front along the metal-coating interface during the cathodic delamination of a coated zinc.

5.1   Governing Equations

Under the assumption that the thickness of the coating is much smaller than the length of the domain, the mathematical model was developed focusing on a one-dimensional delaminated zone. The significance of the defect was included implicitly at the boundary sharing with the defect. The dependent variables considered in the model were potential Φ and concentrations of OH^-, Na^+, Cl^-, H^+, Zn^{2+}, $ZnOH^+$, $HZnO_2^-$, ZnO_2^{2-}, and $Zn(OH)_{2(s)}$.

The governing equation for the solution potential was derived from the electroneutrality condition

$$\sum_{i=1}^{i=9} z_i c_i = 0 \tag{5–1}$$

The governing equation for c_i in a 1-D domain was

$$\frac{\partial\left(\varepsilon c_i\right)}{\partial t} \;=\; -\frac{\partial\left(\varepsilon^{1.5} N_i\right)}{\partial x} + R_i + S_i \tag{5–2}$$

where S_i represented the rate of production per unit volume by electrochemical reactions. The conservation equations for the chemically inert species, Na^+ and Cl^-, were obtained by assigning $S_{Na^+} = 0$, and $S_{Cl^-} = 0$. The governing equations for the species participating in heterogeneous reactions, Zn^{2+} and OH^-, were formulated as

$$\frac{\partial\left(\varepsilon c_{Zn^{2+}}\right)}{\partial t} \;=\; -\frac{\partial\left(\varepsilon^{1.5} N_{Zn^{2+}}\right)}{\partial x} + R_{Zn^{2+}} + \frac{i_{Zn}^{coat}}{2F} \tag{5–3}$$

and

$$\frac{\partial\left(\varepsilon c_{OH^-}\right)}{\partial t} \;=\; -\frac{\partial\left(\varepsilon^{1.5} N_{OH^-}\right)}{\partial x} + R_{OH^-} + \frac{i_{lim,O_2}^{coat}}{-F} \tag{5–4}$$

respectively. The net production of Zn^{2+} and OH^- by the homogeneous reactions at any position was equal to zero, *i.e.*

$$R_{Zn^{2+}} + R_{ZnOH^+} + R_{HZnO_2^-} + R_{ZnO_2^{2-}} = 0 \tag{5–5}$$

and

$$R_{OH^-} - R_{H^+} - R_{Zn^{2+}} + 2R_{HZnO_2^-} + 3R_{ZnO_2^{2-}} = 0 \tag{5–6}$$

Substitution of R_i into equation (5–5) yielded the governing equations for $c_{Zn^{2+}}$ and c_{OH^-}, respectively, *i.e.*

$$G_{Zn^{2+}} - \frac{i_{Zn}^{coat}}{2F} + G_{ZnOH^+} + G_{HZnO_2^-} + G_{ZnO_2^{2-}} = 0 \tag{5–7}$$

and

$$G_{OH^-} + \frac{i_{lim,O_2}^{coat}}{-F} - G_{H^+} - G_{Zn^{2+}} + \frac{i_{Zn^{2+}}^{coat}}{2F} + 2G_{HZnO_2^-} + 3G_{ZnO_2^{2-}} = 0 \tag{5–8}$$

where

$$G_i = \frac{\partial\left(\varepsilon c_i\right)}{\partial t} + \frac{\partial\left(\varepsilon^{1.5} N_i\right)}{\partial x} \tag{5–9}$$

The equilibrium conditions listed in Table 4-2 were applied as the governing equations for H^+, $ZnOH^+$, $HZnO_2^-$, and ZnO_2^{2-}. [66] The rate of formation of the corrosion product $Zn(OH)_{2(s)}$ was associated with $c_{Zn^{2+}}$ and c_{OH^-} by

$$\frac{\partial c_{Zn(OH)_{2(s)}}}{\partial t} = k[c_{Zn^{2+}} \cdot c_{OH^-}^2 - K_{sp}] \tag{5–10}$$

where the standard solubility product K_{sp} has a value of 3×10^{-17} (mol/liter)^3 at room temperature. [10]

The phenomena of bond-breakage and coating degradation involve chemical reactions. Equation (4–5) governs the equilibrium relationship between interfacial porosity and local pH. The equilibrium ε-pH relation is valid under the assumption that the time constants of bond-breakage reactions are sufficiently small. When the time constants for these phenomena are large compared to those for the processes of diffusion and migration, the equilibrium assumption becomes invalid. A non-equilibrium relationship between ε and pH

was assumed to follow

$$\frac{\partial \varepsilon}{\partial t} = -k_{neq} \left(\varepsilon - \varepsilon_{eq} \right) \qquad (5\text{--}11)$$

where the equilibrium porosity ε_{eq} is obtained in equation (4–5) and k_{neq} is the rate constant for the bond-breakage reactions. In the limit that $k_{neq} \to \infty$ the value of ε attains its equilibrated value $\varepsilon = \varepsilon_{eq}$.

5.2   Boundary Condition

At the boundary with the defect, the solution potential and concentrations of chemical species were fixed at a bulk condition Φ_∞ and $c_{i,\infty}$, respectively. The boundary condition for the solution potential Φ at the fully-intact region remained as the electroneutrality condition. A zero-flux boundary condition $N_i = 0$ was used for each species at the boundary in the fully-intact region.

5.3   Solution Method

The system of coupled equations consisted of four equations written in the form of equation (5–2) for OH^-, Na^+, Cl^-, and Zn^{2+}, respectively, equation (5–1) for the electroneutrality condition, equilibrium conditions for H^+, $ZnOH^+$, $HZnO_2^-$, and ZnO_2^{2-}, equation (5–10) for the corrosion product, and an equation for the porosity-pH relationship. When the porosity was assumed to reach its equilibrium value instantaneously, the equilibrium ε-pH relationship, equation (4–5), was used as the governing equation for ε. When the non-equilibrium ε-pH relationship was applied, equation (5–11) was used as the governing equation for ε.

The derivative terms were discretized at each node in the domain using Taylor series approximation. The first-order temporal derivative was given by

$$\frac{\partial \left(\varepsilon c_i \right)}{\partial t} = \frac{\left(\varepsilon c_i \right)^{n+1} - \left(\varepsilon c_i \right)^n}{\triangle t}$$

where the superscripts in brackets n and $n + 1$ represented the conditions at a given time t and a time one time step ahead, $t + \triangle t$. Terms of the order $(\triangle t)$ and higher were neglected in the temporal derivative. The spatial derivatives for a non-boundary node m

were approximated using the central finite difference equations [73], *i.e.*

$$\frac{\partial f_m}{\partial x} = \frac{f_{m+1} - f_{m-1}}{2\Delta x} + O(\Delta x)^2 \tag{5-12}$$

$$\frac{\partial^2 f_m}{\partial x^2} = \frac{f_{m+1} - 2f_m + f_{m-1}}{(\Delta x)^2} + O(\Delta x)^2 \tag{5-13}$$

where f was a generic variable for c_i, Φ, and ε. Terms of the order $(\triangle x)^2$ and higher were neglected in the spatial derivatives. A quarter-point method was used to approximate the derivative term in the boundary conditions. The approximation of m-$\frac{1}{4}$ was obtained using

$$\left(\frac{\partial f}{\partial x}\right)_{m+\frac{1}{4}} = \frac{f_m - f_{m-\frac{1}{2}}}{\left(\frac{\Delta x}{2}\right)} + O(\Delta x^2) \tag{5-14}$$

where

$$f_{m-\frac{1}{2}} = \frac{f_m + f_{m-1}}{2} \tag{5-15}$$

The resulting system of algebraic equations was accurate to the order of $(\triangle x)^2$.

The system of coupled, non-linear, partial differential equations required an iterative method to converge on a solution starting from an initial guess. A tri-diagonal method, BAND algorithm, coupled with time step was chosen to calculate the distribution of c_i, Φ, and ε in the delaminated domain. The mathematical model was developed using *Microsoft Visual Fortran, Version 9.0* with double precision accuracy. [74]

CHAPTER 6
RESULTS AND DISCUSSION FOR DELAMINATION MODEL

The present mathematical model simulated the evolution of a cathodic delamination system from a set of given initial conditions. The resulting distributions satisfied the coupled phenomena of mass transfer, electroneutrality, and disbondment reactions during the delamination process. The calculated results and discussions are presented in this chapter.

6.1   Initial Conditions

The geometric parameters used in the model included a coating thickness $g_c = 45$ μm, a gel-medium thickness $g_c = 5$ μm, and a net length of 0.8 cm for the delaminated, front and intact regions. The initial lengths of these regions were 0.1 cm, 0.05 cm, and 0.65 cm, respectively.

The input parameters for the simulation included the grid size $\triangle x = 4 \times 10^{-4}$ cm , the time step $\triangle t = 0.1$ s, and the total time $t = 60$ min. The potential on the metal was chosen as V = -0.95 V_{SHE}. The polarization parameters for zinc dissolution included β_{Zn} =0.04 $V/decade$, $i_{0,\text{Zn}}$ =0.008 A/cm^2, and $E_{0,\text{Zn}}$ =- 0.763 V_{SHE}. The diffusion coefficients D_i for the chemical species are given in Table 6-1.   The concentration of dissolved oxygen at the surface of the coating was 1.26 $\times$ 10^{-3} M. [46]

Table 6-1. Diffusion coefficients of chemical species[46, 75]

Chemical Species	D_i in bulk electrolyte (cm^2/s)
O$_2$	1.90$\times 10^{-5}$
OH$^-$	5.25$\times 10^{-5}$
Na$^+$	1.47$\times 10^{-5}$
Cl$^-$	2.03$\times 10^{-5}$
Zn^{2+}	0.71$\times 10^{-5}$
H$^+$	9.32$\times 10^{-5}$
ZnOH$^+$	1.00$\times 10^{-5}$
HZnO$_2^-$	1.00$\times 10^{-5}$
ZnO$_2^{2-}$	1.00$\times 10^{-5}$
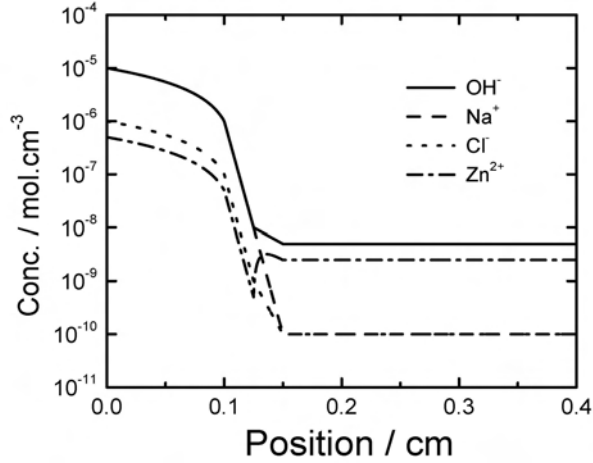
Figure 6-1. Initial concentration distributions of OH^-, Na^+, Cl^-, and Zn^{2+} ions along the metal-coating interface.

6.1.1   Initial Concentration Distributions

The objective of this work was to explore the propagation phase of the delamination process. Thus, an initial condition was established which reflected a system after the delamination had begun. The initial concentration distributions presented in Figure 6-1 were constructed based on the experimental data reported by Leng and Stratmann [14–16] The initial concentrations of Na^+ and OH^- ions were equal at any position in the delaminated domain. The shape of the c_{Cl^-} distribution followed that of c_{Na^+} distribution. The concentrations of Na^+, Cl^-, and OH^- ions decreased monotonically with position in the delaminated and front regions. In the intact region, the concentrations of all species reached asymptotic values. The distribution of $c_{Zn^{2+}}$ was obtained by satisfying electroneutrality at a given position. The concentrations of the corrosion product and the species produced in the homogeneous reactions were assumed to be zero at $t=0$.

6.1.2   Initial Distribution of Porosity

The construction of the relation between porosity and pH is given in Section 4.1. The fitting parameters used in the equilibrium ε-pH relationship (equation (4–5)) are given in Table. The initial porosity distribution is shown in Figure 6-2(a) as a function of position and in Figure 6-2(b) as a function of pH. As seen in Figure 6-2(a), the porosity decreases
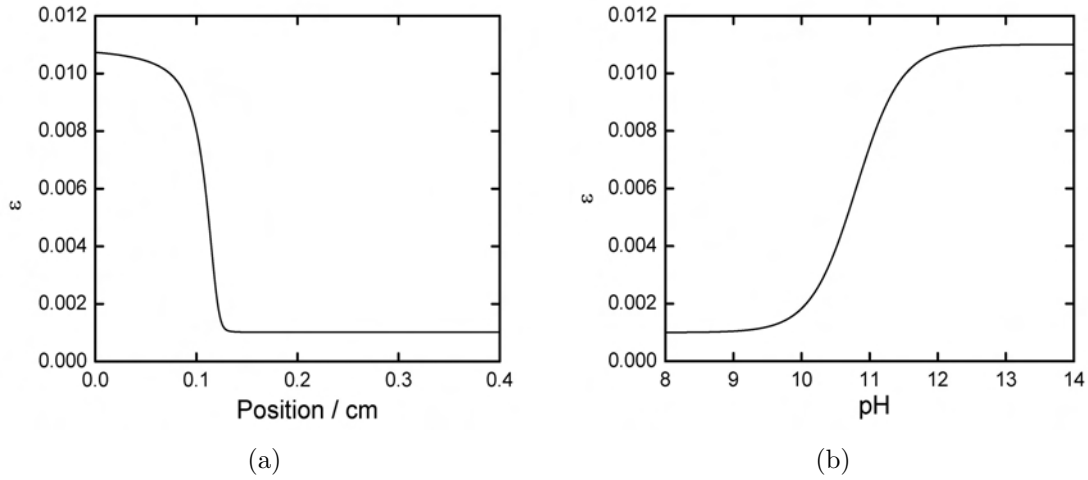
Figure 6-2. Calculated initial porosity distribution: a) as a function of position; and b) as a function of pH.

non-linearly in the delaminated and the front regions. The porosity maintains a uniform value in the intact region. The porosity-pH plot (Figure 6-2(b)) presents the concept that at a high pH the adhesive strength is low and that at a low pH the adhesive strength is high.

6.1.3 Initial Distribution of Polarization Parameters

The polarization parameters α_{O_2} and ζ were used to calculate the current densities due to the zinc dissolution and oxygen reduction at the metal-coating interface. Equations (4–10) and (4–13) govern the ζ-pH and α_{O_2}-pH relations. The fitting parameters used in the equations are given in Table 4-1. The initial distributions of ζ are presented in Figure 6-3(a) as a function of position and in Figure 6-3(b) as a function of pH. Figures 6-4(a) and 6-4(b) present the initial distributions of α_{O_2} as a function of position and pH, respectively.

The current density expressions given in equations (4–9) and (4–12) were applied to generate the polarization plot at the metal-coating interface as a function of pH presented in Figure 6-5. The pH value of 8.7 corresponds to the positions in the intact region where local anodic reactions are balanced by local cathodic activities. The corrosion current density at the metal-coating interface, therefore, is approximately equal to zero in the
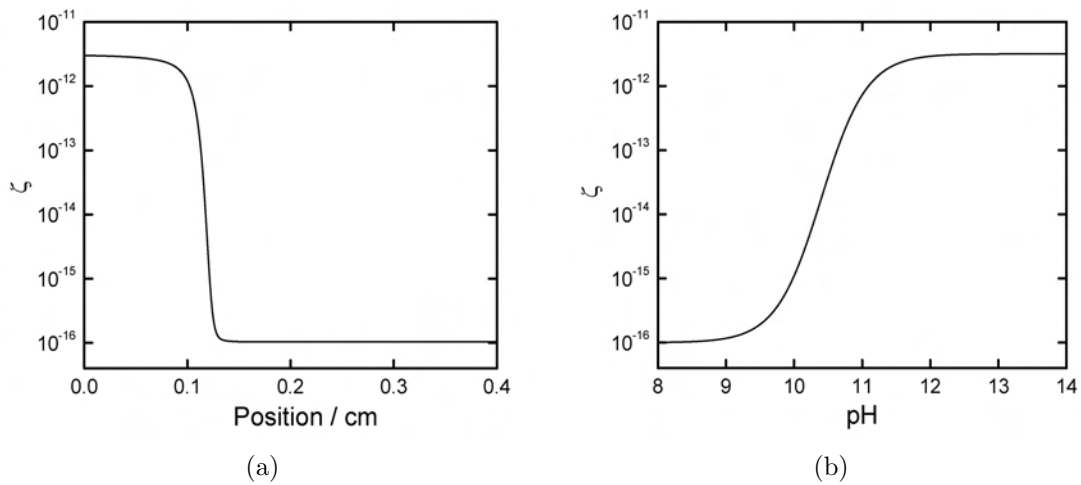
Figure 6-3. Calculated initial distribution of poisoning factor: a) as a function of position; and b) as a function of pH.
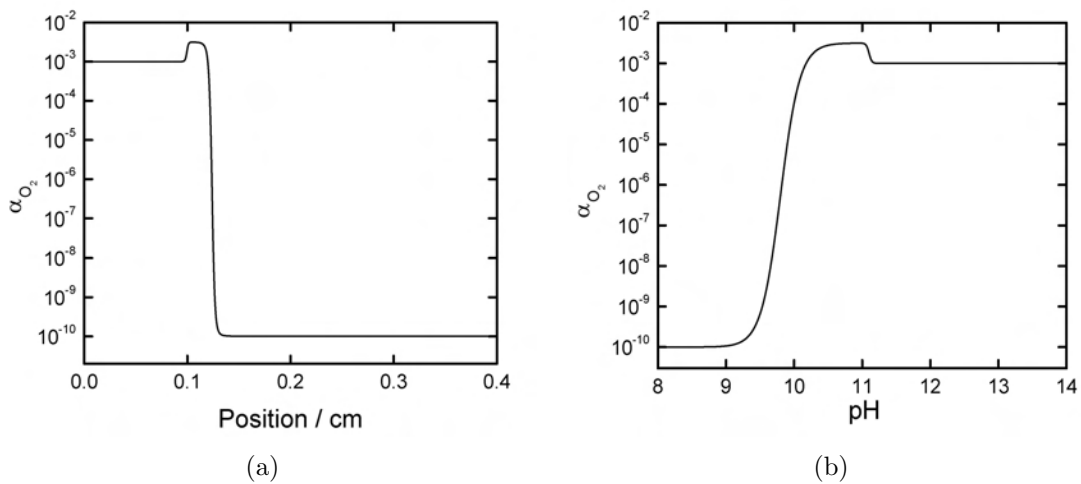
Figure 6-4. Calculated initial distribution of blocking factor: a) as a function of position; and b) as a function of pH.
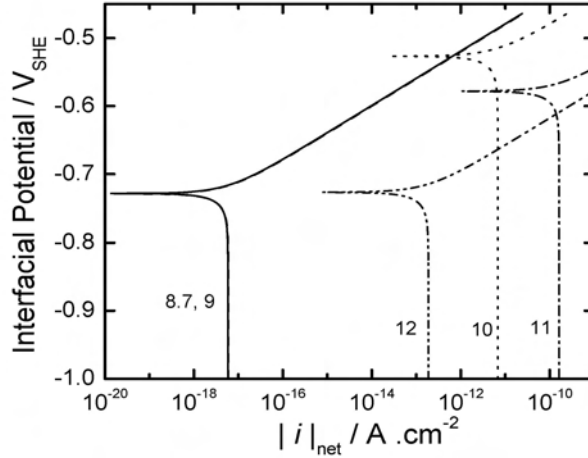
Figure 6-5. Interfacial potential as a function of absolute net current density with local pH as a parameter. The distributions associated with the pH values of 8.7 and 9 are superimposed.

intact region. As seen in Figures 6-3(b) and 6-4(b)), the magnitudes of ζ and α_{O_2} do not change over the pH range 8 to 9. Thus, the polarization curves associated with pH 8.7 and 9 superimpose as observed in Figure 6-5.

The pH ranging from 9 to 11 corresponds to the moving front in which the bond-breaking reactions are ongoing. As shown in Figures 6-3(b) and 6-4(b), both ζ and α_{O_2} show an increase from pH 9 to 11; consequently, the anodic and cathodic current densities in the front region are larger than those in the intact region. The increase in the current densities reflects physically an enhanced electrochemical reactivity in the front region.

The curve of pH 12 in Figure 6-5 corresponds to the delaminated region in which the interfacial bonds are partially broken due to the delamination process. As the polarization parameters ζ and α_{O_2} account implicitly for the influence of passive films or deposits on the electrochemical reactions, both anodic and cathodic current densities in the delaminated region are smaller than those in the front region.

6.2   Equilibrium Porosity-pH Relationship

The simulation results obtained using the equilibrium ε-pH relationship are presented in this section. The results using the kinetic ε-pH relationship are presented in Section 6.3.
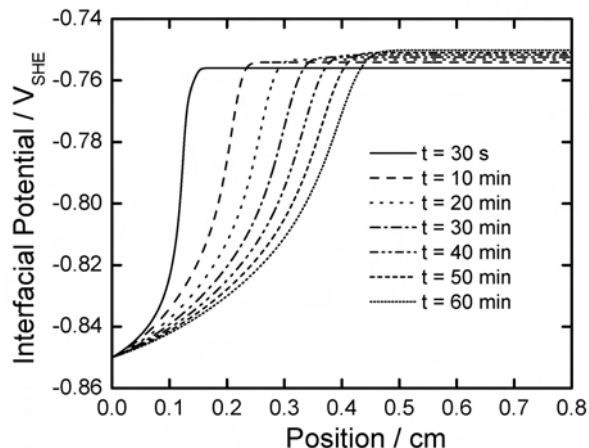
Figure 6-6. Calculated distributions of interfacial potential along the metal-coating
interface with elapsed time as a parameter.

6.2.1 Interfacial Potential Distribution

The calculated distribution of interfacial potential V is presented in Figure 6-6 with
elapsed time as a parameter. In the graphical presentations in the subsequent sections,
$t = 30$ s was chosen as the initial condition to avoid the artificiality at $t = 0$. At a given
time, the interfacial potential increases with distance away from the scratch and reaches
a constant value in the intact region. The constant plateau seen in Figure 6-6 represents
the intact region and is observed to shorten with elapsed time. The shape of the potential
distribution is maintained throughout the simulation, indicating that the phenomena and
the hypotheses considered in the model sustains the profile of V while the delamination
front propagates along the metal-coating interface. These features are consistent with the
experimental results of coated electrogalvanized reported by Stratmann *et al.* [10] and
Williams et al.. [50]

Following the analysis reported by Leng and Stratman, [15] the interfacial potential
distributions were differentiated with respect to position to yield distributions of $\mathrm{d}V/\mathrm{d}x$
as a function of position with elapsed time as a parameter given in Figure 6-7. The
sharp peak marks the deflection point of the sharp increase observed in Figure 6-7. The
position of the peak, identified as the delamination front, propagates away from the
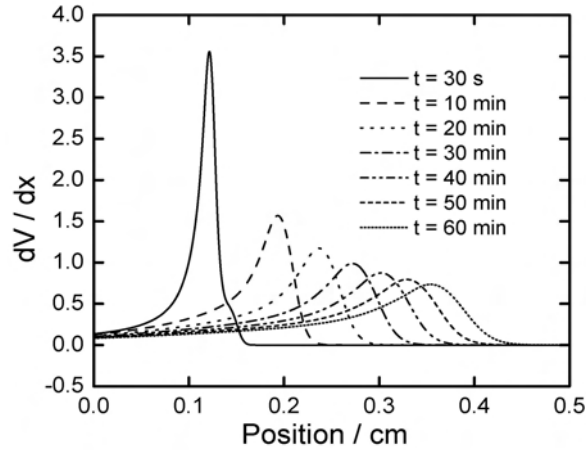
Figure 6-7. Calculated distributions of dV/dx along the metal-coating interface with elapsed time as a parameter.

defect with increasing time. The peak height corresponding to the magnitude of dV/dx deceases with increasing delamination time. The decreasing trend is in agreement with the experimental results reported by Leng and Stratmann. [15] The explanation given by Leng and Stratmann was that, with time, a more gradual change in electrochemical potential in the front region. [15] The agreement with the experiments demonstrates that the hypotheses of the pH-dependent interfacial porosity and pH-dependent polarization kinetics were reasonable for the front propagation during the delamination process.

The rate of propagation of the potential front, calculated from the maxima peak given in Figure 6-7, is presented in Figure 6-8. The rate initially is large but exponentially decreases with elapsed time. After a long-time extrapolation, the delamination rate determined by the potential front is 1.66 mm/hr, approximately two times larger than the experimental rate for coated steel observed by Leng and Stratmann. [14] The discrepancy between the theoretical and experimental work can be attributed to the use of the equilibrated pH-porosity relation in the model. The phenomena of bond breakage and coating degradation involve chemical reactions. The application of the equilibrium pH-porosity relation assumes instantaneously that the time constants associated with breaking bonds are small. When time constants for bond-breakage phenomena are large
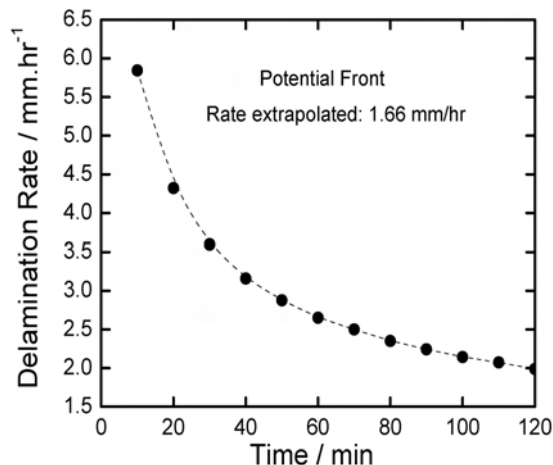
Figure 6-8. Instantaneous velocity of potential front, calculated from the time-dependent position of the maxima given in Figure 6-7.

compared to those for the diffusion and migration, the assumption of the equilibrium pH-porosity relation becomes invalid. An investigation for non-equilibrium pH-porosity will be addressed in Section 6.3.

6.2.2 Concentration Distributions

The distribution of pH in the delaminated zone is presented in Figure 6-9 as a function of position with elapsed time as a parameter. The calculated results show that the pH in the delaminated and front regions increases with time and remains unchanged in the intact region. The increase in pH in the delaminated and front regions is attributed to the OH^- ions produced by oxygen reduction underneath the coating and by diffusion from the boundary with the defect. The shape of the pH distribution is maintained throughout the simulation, which again, demonstrates that the hypotheses and physical phenomena considered in the model are able to sustain the profile of pH while the delamination front propagates along the interface.

The calculated distributions of c_{Na^+} and c_{Cl^-} are presented in Figure 6-10 as a function of position with elapsed time as a parameter. The trends associated with the c_{Na^+} and c_{Cl^-} distributions are similar with those seen in the pH distribution. A slight decrease in the c_{Cl^-} distribution is observed in the front region. This decreasing
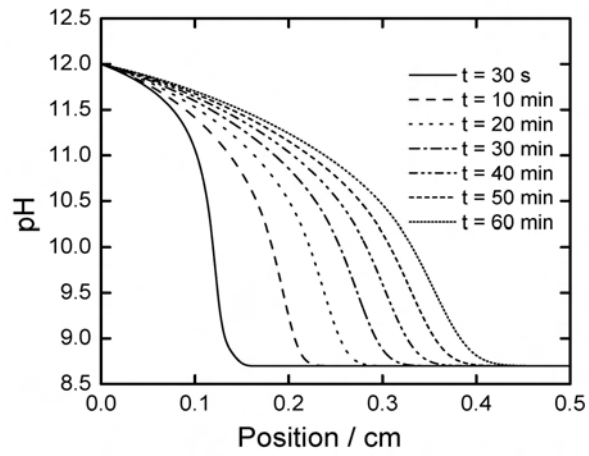
Figure 6-9. Calculated distributions of pH along the metal-coating interface with elapsed time as a parameter.

(a)   (b)
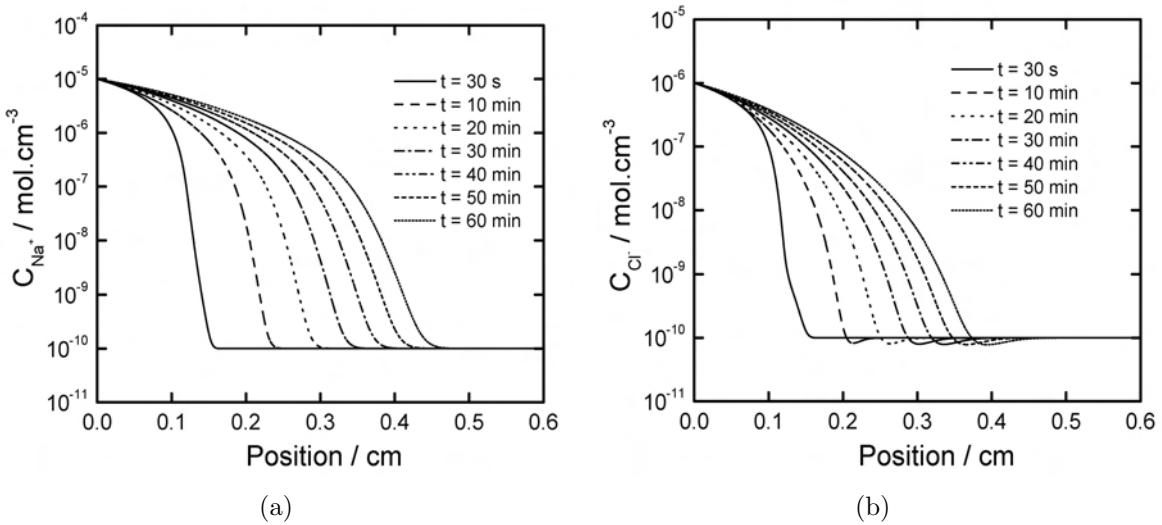
Figure 6-10. Calculated concentration distributions along the metal-coating interface with elapsed time as a parameter. a) Na^+ ions; and b) Cl^- ions.
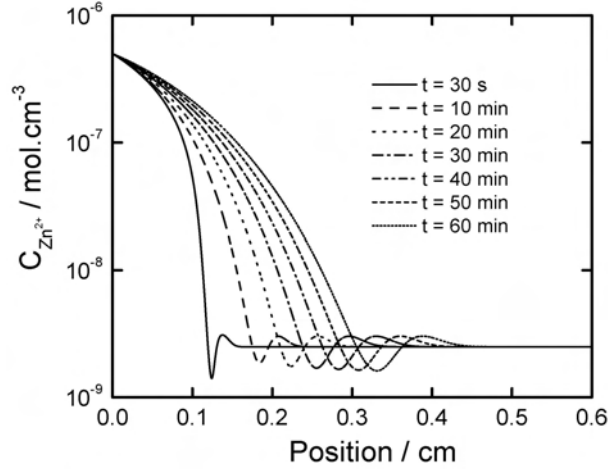
Figure 6-11. Calculated concentration distributions of Zn^{2+} ions along the metal-coating interface with elapsed time as a parameter.

feature demonstrates that the Cl^- ions are expelled from the front region because of the production of OH^- ions by oxygen reduction.

The calculated distribution of $c_{Zn^{2+}}$ is given in Figure 6-11 as a function of position with elapsed time as a parameter. The shape of the distribution is maintained throughout the simulation. In the front region the concentration of Zn^{2+} ions increases with position at part of the region and decreases with position at the other part of the region. This feature shows that the distribution of $c_{Zn^{2+}}$ is constrained by the electroneutrality condition applied in the model.

The concentration distributions of the species produced in the homogeneous reactions ($ZnOH^+$, $HZnO_2^-$, and ZnO_2^{2-}) are presented in Figure 6-12 as a function of position with elapsed time as a parameter. For all three species, the concentrations decrease with position in the delaminated and the front regions. During the course of simulation, the changes in concentration across the delaminated and the front regions become more gradual as the delamination propagates into the fully-intact region.

6.2.3 Precipitated Corrosion Product

The precipitation of corrosion products $Zn(OH)_{2(s)}$ has been observed in delamination systems and cut-edge corrosion systems. [19, 76] The distribution of $c_{Zn(OH)_{2(s)}}$ calculated
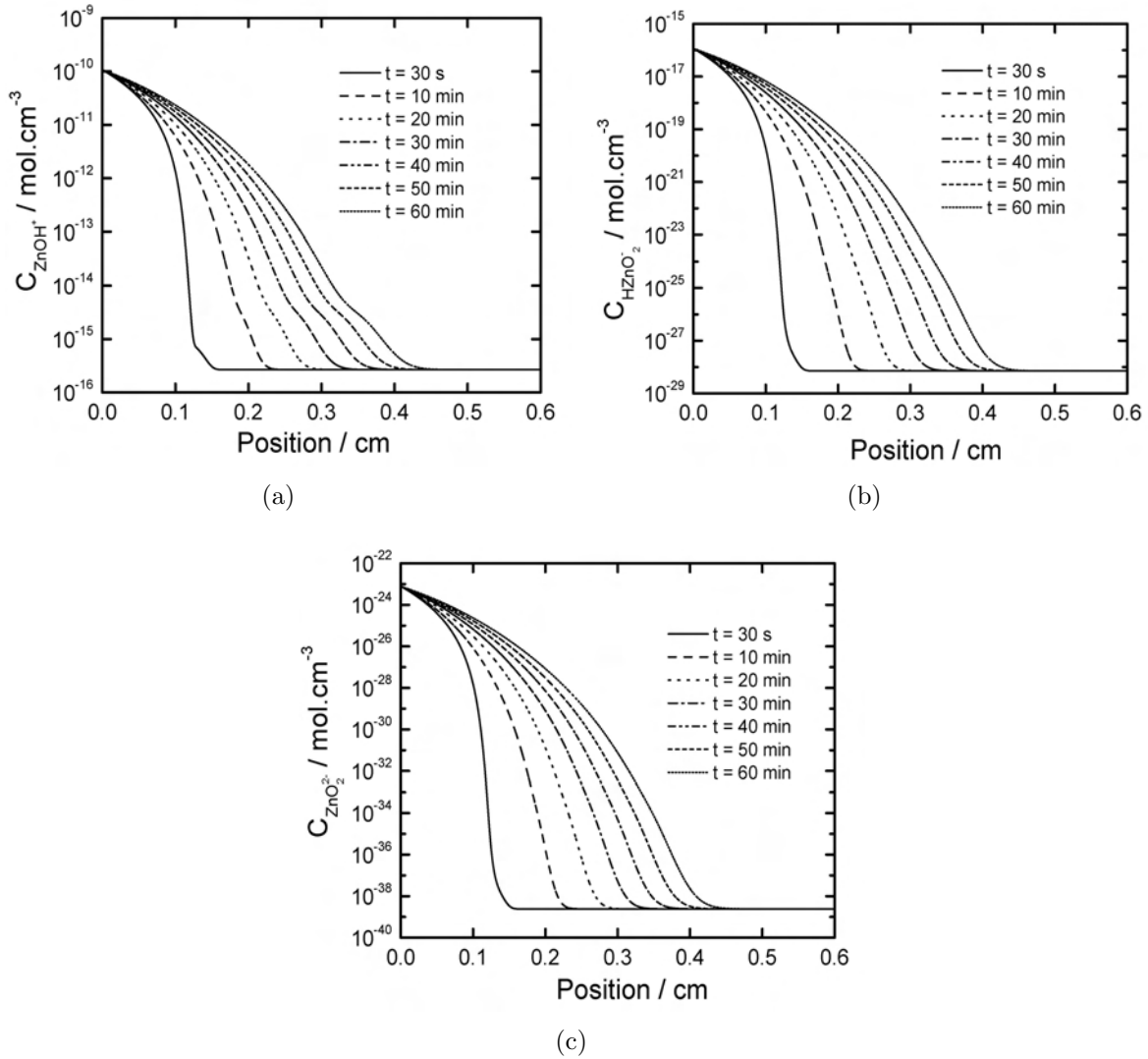
Figure 6-12. Calculated concentration distributions along the metal-coating interface with elapsed time as a parameter. a) $ZnOH^+$ ions; b) $HZnO_2^-$ ions; and c) ZnO_2^{2-} ions.
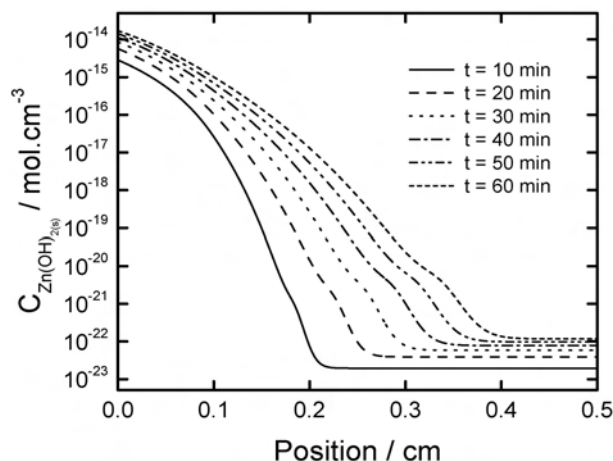
Figure 6-13. Calculated concentration distributions of precipitated corrosion product $Zn(OH)_{2(s)}$ along the metal-coating interface with elapsed time as a parameter.

from the presented model is given in Figure 6-13 as a function of position with elapsed time as a parameter. The concentration of $Zn(OH)_{2(s)}$ increases with time in the delaminated, front and intact regions. At a given time, the concentration of $Zn(OH)_{2(s)}$ decreases with position in the delaminated and front regions, and maintains a constant in the intact region.

It has been known that the formation of passive layer $Zn(OH)_{2(s)}$ on electrode surface protects materials from corrosion and moderates the corrosion rate. [19] This inhibitive feature, in the model presented here, was included implicitly through the use of the poisoning factor, but not related quantitatively with the local concentration of $Zn(OH)_{2(s)}$. The solubility of $Zn(OH)_{2(s)}$, as indicated in the Purbaix diagram, [66] has a minimum around pH 9 and increases with increasing pH. This transition feature is not observed in Figure 6-13. The inconsistency with the literature might be due to that the approach taken in the model to incorporate the solid species $Zn(OH)_{2(s)}$ (equation (4–14)) is different from that employed in the Purbaix diagram in which the total concentrations of Zn^{2+} and OH^- ions were held as constants. [71, 72].
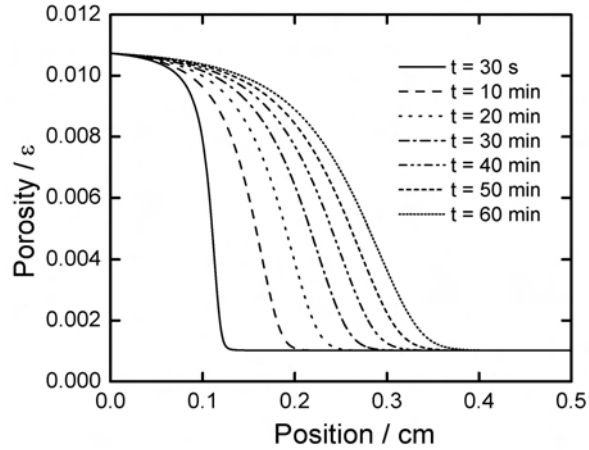
Figure 6-14. Calculated distributions of porosity along the metal-coating interface with elapsed time as a parameter.

6.2.4   Porosity Distribution

The calculated porosity distribution is presented in Figure 6-14 as a function of position with elapsed time as a parameter. The shape of the porosity distribution remains the same with the initial distributions throughout the simulation. As the delamination front propagates into the intact region, the interfacial porosity increases to satisfy the equilibrium ε-pH relationship. At a given position, the increase in the porosity with time is reflected by the increase in pH observed in Figure 6-9. The trends associated in the porosity distribution are similar with those observed in the pH distributions, confirming that the destruction of the interfacial adhesions is related to the generation of OH^- ions during the delamination process.

In experiments, the delamination front, where the delamination is ongoing, is often determined by the potential distributions measured using the scanning Kelvin probe. In the mathematical model presented here, however, it is more reasonable to define the delamination front by the porosity gradients, because the porosity is the key to represent the adhesive strength between the metal and the coating. [21, 22]

The distribution of $d\epsilon/dx$ along the metal-coating interface is presented in Figure 6-15 as a function of position with elapsed time as a parameter. The sharp peak characterizes a

67
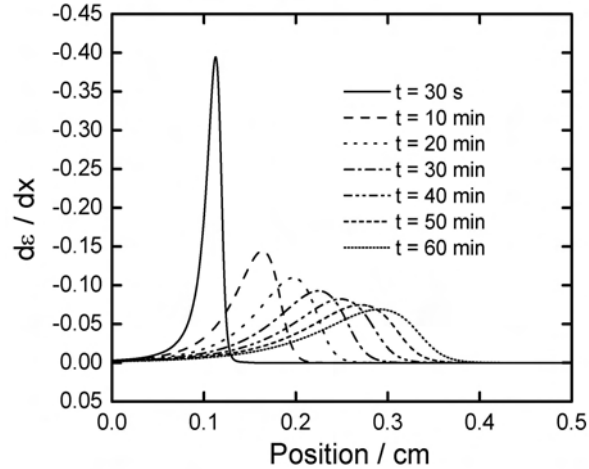
Figure 6-15. Calculated distributions of $d\epsilon/dx$ along the metal-coating interface with elapsed time as a parameter.

porosity front that moves toward the intact region during the delamination process. The velocity of the porosity front corresponds to the rate of breaking the interfacial bonds and is approximately 1.50 mm/hr after extrapolated to a longer time (see Figure 6-16). This value is slightly smaller than that of the potential front, but still larger than the experimental result of coated steel. [14] The discrepancy between the simulation and experimental rates can be attributed to the use of the equilibrium pH-porosity relation, which yields to the upper limit to the propagation rate.

6.2.5 Delamination Kinetics

Following the approach taken by Leng [15] and William [51], the delamination kinetics was analyzed by plotting the delaminated distance as a function of elapsed time. The propagation distances determined by the potential and the porosity fronts are presented in Figures 6-17(a) and 6-17(b), respectively, as a function of time in a double-logarithmic plot with cation type as a parameter. The calculated reaction order is approximately 0.56 for the potential front and 0.6 for the porosity front. The slopes seen in Figures 6-17(a) and 6-17(b) are independent of the cation types, and the values are in close agreement with the reaction order of 0.52 to 0.59 determined by Stratmann *et al.* [10] for polymer coated electrogalvanized steel (Figure 6-17(c)). These results indicate that the overall
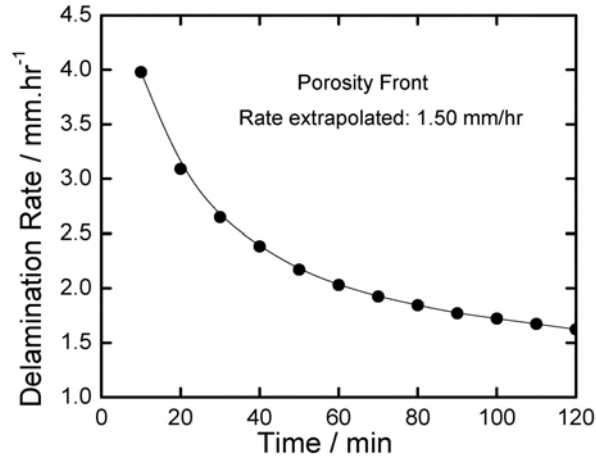
Figure 6-16. Instantaneous velocity of porosity front, calculated from the time-dependent position of the maxima given in Figure 6-15.

Table 6-2. Diffusion coefficients of cations [70, 75]

Type of cation	D_i in bulk electrolyte (cm^2/s)
Li$^+$	1.25×10^{-5}
Na$^+$	1.47×10^{-5}
K$^+$	1.84×10^{-5}
Cs$^+$	2.10×10^{-5}

delamination process is primarily limited by the mass transport of ions from the defect to the delamination front. Due to the co-existence of the potential and concentration gradients, the transport of ions represents the contributions by migration as well as diffusion.

6.2.5.1   Influence of Cation Type on Delamination Rate

The influence of cation type on the delamination rate can be seen in Figure 6-18, where the delaminated distance calculated based on the potential and porosity fronts are plotted as a function of square root of time. A linear relation between the delaminated distance and $\sqrt{\text{time}}$ is observed for all of the cation types. The rate of the propagation decreases in the order of Cs$^+$ > K$^+$ > Na$^+$ > Li$^+$ for both potential and porosity fronts, and this result is correlated to the mobility of the cations in an aqueous medium (Table 6-2).   The result indicates that, with the chemical and physical assumptions, the

69

(a)

(b)

(c)
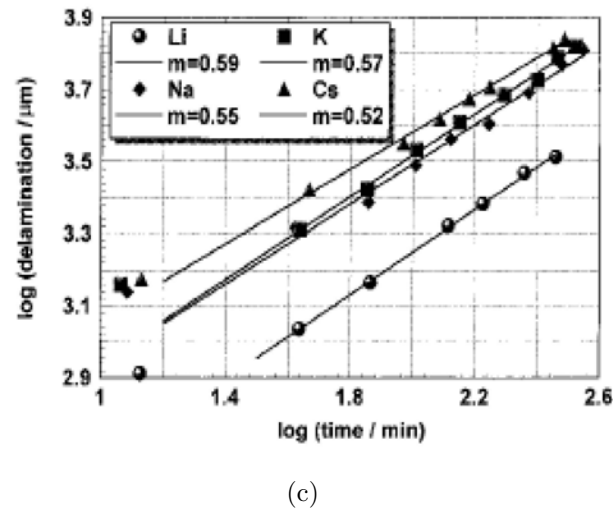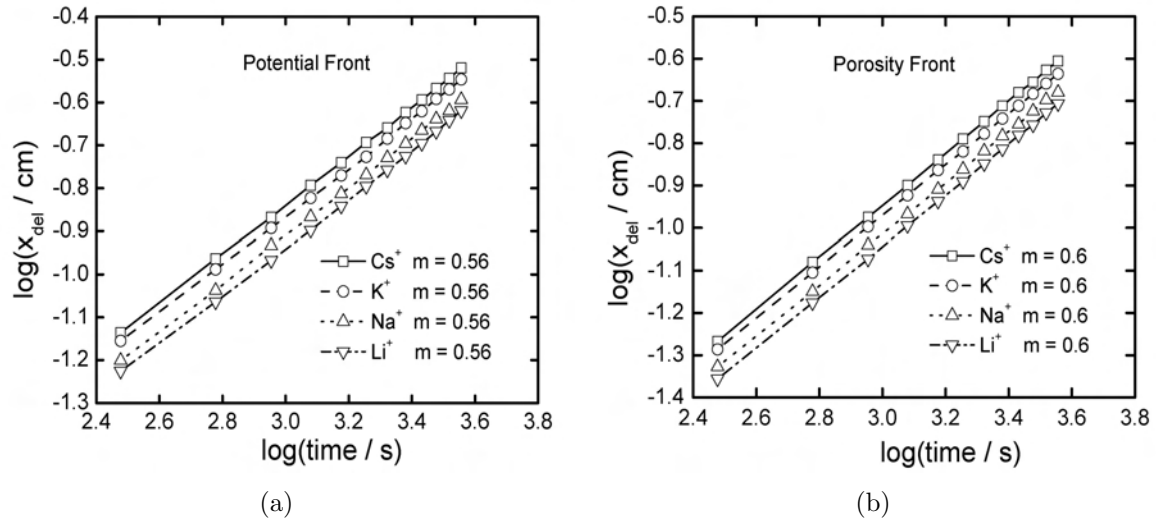
Figure 6-17. Delaminated distance as a function of elapsed time in double-logarithmic scale with cation type as a parameter. The concentration of the electrolyte at the defect is 0.5 M. a) Delaminated distance determined by potential front; b) Delaminated distance determined by porosity front; and c) Experimental results obtained from coated electrogalvanized steel samples. Data taken from Stratmann et al. [11] with permission of Corrosion Science.
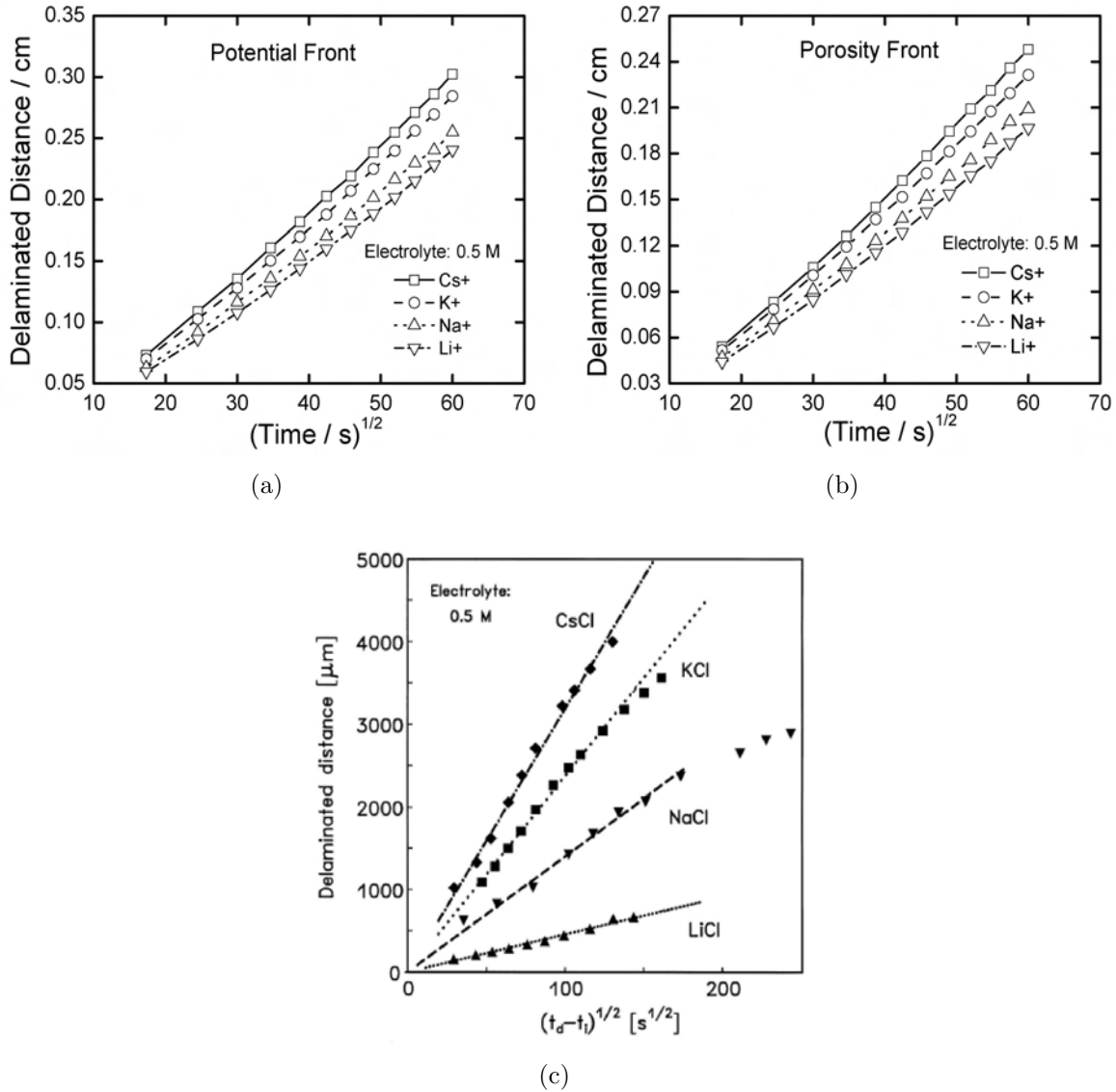
Figure 6-18. Delaminated distance as a function of square root of time with cation type as a parameter. The concentration of the electrolyte at the defect is 0.5 M. a) Delaminated distance determined by potential front; b) Delaminated distance determined by porosity front; and c) Experimental results obtained from coated steel samples. Data taken from Stratmann et al. [15] with permission of Corrosion Science.

Table 6-3. Diffusion coefficients of anions [75]

Type of anion	D_i in bulk electrolyte (cm^2/s)
Br$^-$	1.25×10^{-5}
Cl$^-$	1.47×10^{-5}
F$^-$	1.84×10^{-5}
ClO$_4^-$	2.10×10^{-5}

delamination predicted from the model is principally controlled by the transport of cations along the metal-coating interface and the rate of this process scales with the mobility of the cations. This result is qualitatively consistent with experimental measurements reported for coated steel and coated zinc systems (Figure 6-18(c)). [10, 15]

6.2.5.2 Influence of Anion Type on Delamination Rate

The influence of anion type on the delamination rate was also examined in the simulation. The resulting propagation distances determined by both potential and porosity fronts are presented in Figure 6-19 as a function of square root of time. It is clear that the delamination rate does not vary with the anion types even though their mobilities in aqueous electrolyte are different (Table 6-3). The production of OH$^-$ ions under the degraded coating attract the cation at the defect, resulting in movements of the cation from the defect toward the intact region. Consequently, the cathodic delamination is more sensitive to the cation type than the anion type. The experimental observations by Leng and Stratmann [11, 15], given in Figure 6-19(c), shows that the anion types influence slightly on the delamination rate, but the variations of the propagation rate between the anion types is much less significant than those between the cation types.

6.2.5.3 Influence of Electrolyte Concentration on Delamination Rate

As reported by Leng and Stratmann [15], the concentration of the electrolyte placed at the defect is also a factor that influences the delamination rate. Figure 6-20 gives the delaminated distance as a function of square root of time with electrolyte concentration as a parameter. The higher concentration at the threshold provides a larger driving force to couple galvanically the intact and the defect zones; therefore, the propagation

(a)

(b)

(c)
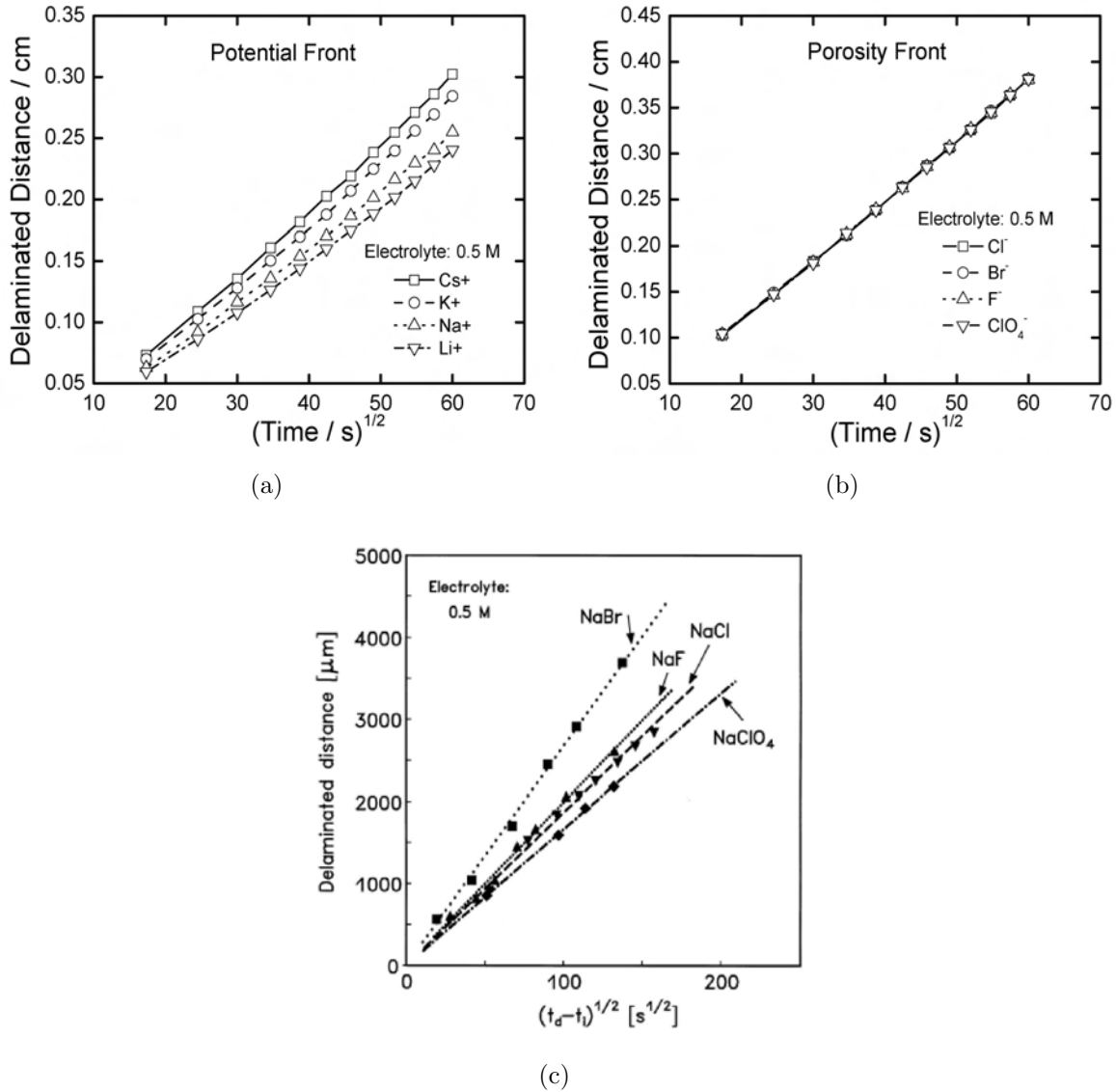
Figure 6-19. Delaminated distance as a function of square root of time with anion type as a parameter. The concentration of the electrolyte at the defect is 0.5 M. a) Delaminated distance determined by potential front; b) Delaminated distance determined by porosity front; and c) Experimental results obtained from coated steel samples. Data taken from Stratmann et al. [15] with permission of Corrosion Science.
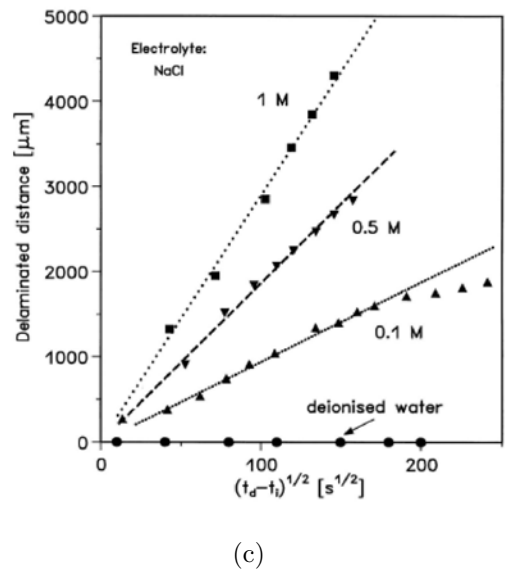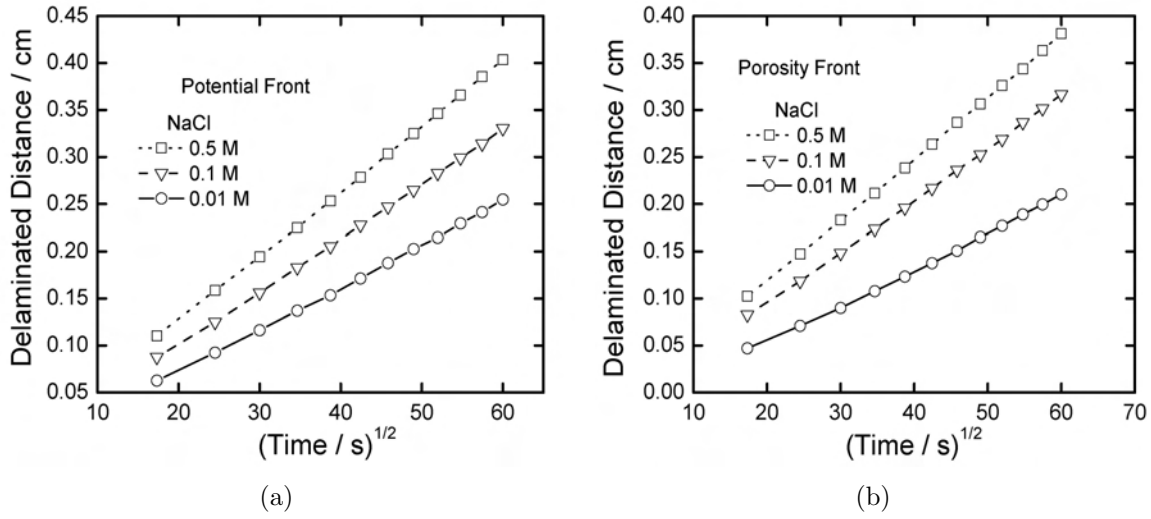
Figure 6-20. Delaminated distance as a function of square root of time with electrolyte concentration as a parameter. a) Delaminated distance determined by potential front; b) Delaminated distance determined by porosity front; and c) Experimental results obtained from coated steel samples. Data taken from Stratmann et al. [15] with permission of Corrosion Science.

rates determined by both potential and porosity fronts increase with the electrolyte concentration. From the kinetic analysis presented above, one important conclusion is that the rate-determining step of the cathodic delamination is driven by the transport of the cations from the defect to the front region, and that the propagation rate scales with the ionic strength and the mobility of the cations. This conclusion is in agreement with the interpretation published by Leng and Stratmann for coated steel. [15]

6.3   Kinetic Porosity-pH Relationship

The use of the equilibrium pH-porosity relation presented above assumed spontaneously that the chemical reactions associated with breaking interfacial bonds occur rapidly. This assumption becomes invalid when the time constants for the bond-breaking reactions are large compared to those for diffusion and migration processes. The investigation for non-equilibrium pH-porosity relation is necessary.

6.3.1   Potential Front and Porosity Front

To explore the role of finite rates of bond breakage, the equilibrium relationship between porosity and pH, given as equation (4–5), was replaced by

$$\frac{\partial \varepsilon}{\partial t} = k_{neq}(\varepsilon - \varepsilon_{eq}) \qquad (6\text{–}1)$$

where k_{neq} is a rate constant that reflects the time constants of bond-breakage reactions, and ε_{eq} is obtained from equation (4–5). Different values of k_{neq} were examined in the simulations, but only the results for $k_{neq} = 0.1$ and 0.001 s^{-1} are presented here.

The resulting distributions of interfacial potential for $k_{neq} = 0.1$ and 0.001 s^{-1} are shown in Figure 6-21 as a function of position with elapsed time as a parameter. The features seen in Figure 6-21 were similar to those observed in Figure 6-6, which were obtained using the equilibrium pH-porosity relation. The distributions of the potential gradient dV/dx for $k_{neq} = 0.1$ and 0.001 s^{-1} are shown in Figure 6-22 as functions of position with elapsed time as a parameter. Again, the trends associated with the dV/dx plot for non-equilibrium pH-porosity relation are similar to those found using the
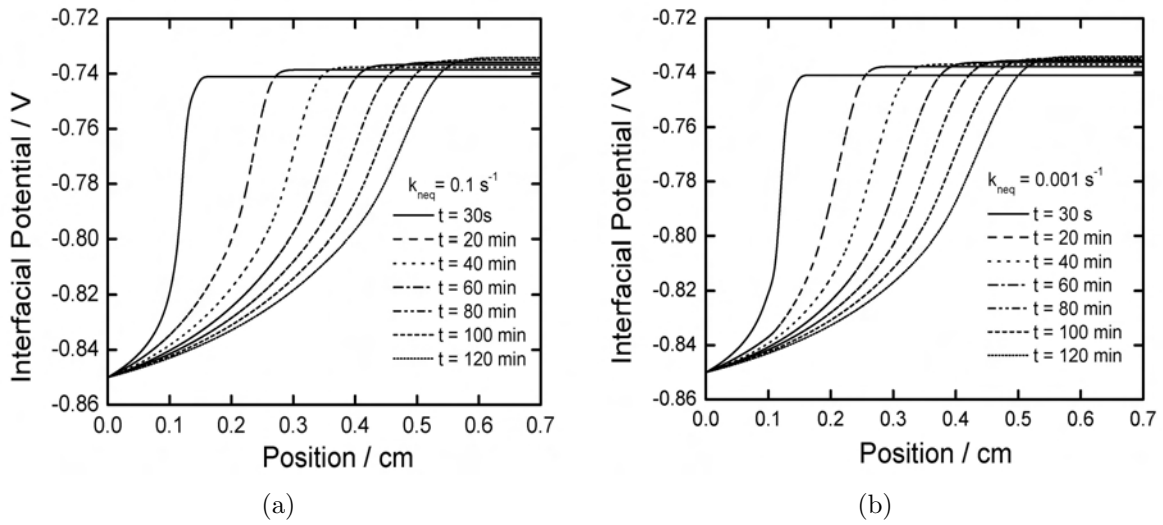
Figure 6-21. Calculated distribution of interfacial potential along the metal-coating interface a) $k_{neq} = 0.1\ s^{-1}$; and b) $k_{neq} = 0.001\ s^{-1}$.
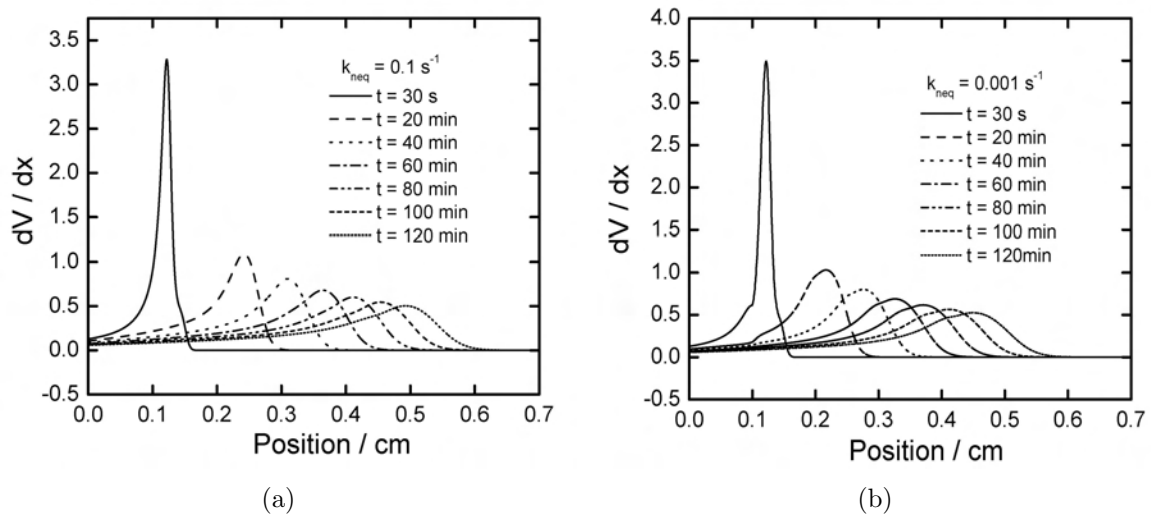
Figure 6-22. Calculated distribution of interfacial potential gradient dV/dx along the metal-coating interface a) $k_{neq} = 0.1\ s^{-1}$; and b) $k_{neq} = 0.001\ s^{-1}$.
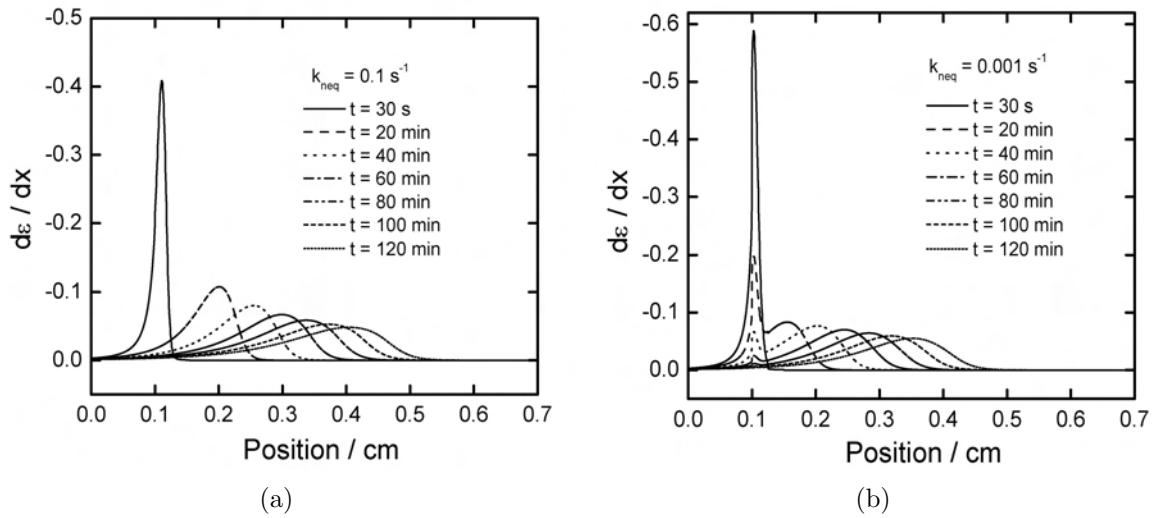
Figure 6-23. Calculated distribution of porosity gradient $d\varepsilon/dx$ along the metal-coating interface a) $k_{neq} = 0.1\ s^{-1}$; and b) $k_{neq} = 0.001\ s^{-1}$.

equilibrium relation. The delamination rate determined by Figures 6-22(a) and 6-22(b), after extrapolated to longer time, were 1.63 mm/hr and 1.55 mm/hr for $k_{neq} = 0.1$ and $0.001\ s^{-1}$, respectively. These values are slightly smaller than the equilibrium delamination rate (1.66 mm/hr), indicating that the use of the kinetic pH-porosity relation within the model influenced the velocity of the potential front.

The propagation of the potential front is then compared with that of the porosity front. The resulting distributions of $d\varepsilon/dx$ for $k_{neq} = 0.1$ and $0.001\ s^{-1}$ are presented in Figure 6-23 as functions of position with elapsed time as a parameter. The trends associated with in Figure 6-23 are similar to those observed in Figure 6-15, which were obtained using the equilibrium pH-porosity relation. The velocity of the porosity front evidently decreases from 1.37 mm/hr for k_{neq}=0.1 s^{-1} to 0.93 mm/hr for k_{neq}=0.001 s^{-1}. The propagation rate for k_{neq}=0.001 s^{-1} is much smaller than the equilibrium porosity front rate (1.5 mm/hr) and the value is in good agreement with the experimental observation of 0.8 mm/hr for coated galvanized steel. [15]

From the analysis presented above, it is evident that the rate of breaking interfacial bonds in the cathodic delamination process is controlled by the rate constant k_{neq}, but
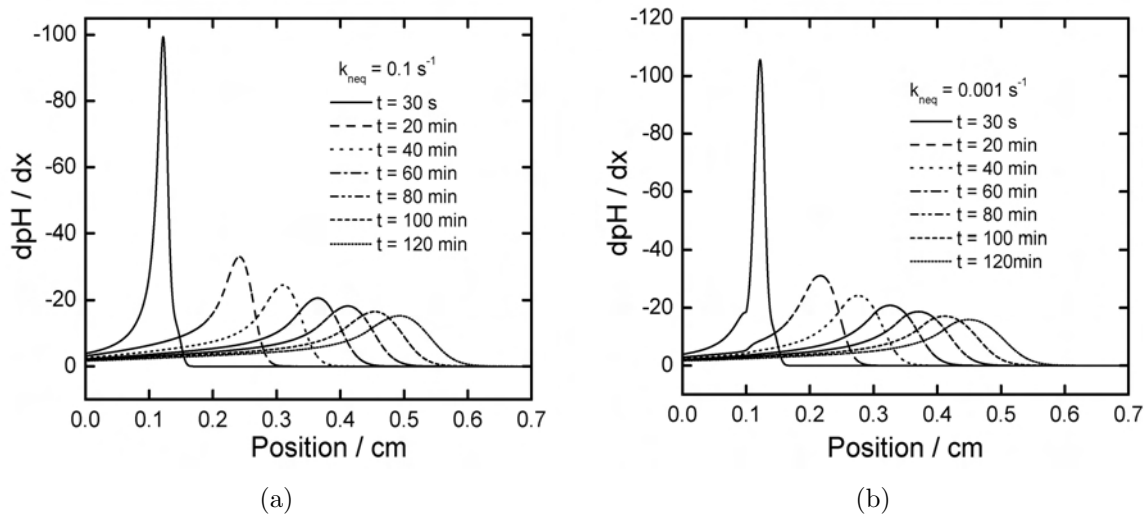
Figure 6-24. Calculated distribution of pH gradient along the metal-coating interface a) $k_{neq} = 0.1\ s^{-1}$; and b) $k_{neq} = 0.001\ s^{-1}$.

the velocity of the potential front is not. Thus, the next question to be addressed is; what properties can be correlated to the propagation of the potential front? Figure 6-24 gives the pH gradient distributions for $k_{neq} = 0.1$ and $0.001\ s^{-1}$ as functions of position with elapsed time as parameter. The shape and the features within the pH gradient distributions are similar to those seen in dV/dx and $d\varepsilon/dx$ plots. The location of the deflection point in Figures 6-24(a) and 6-24(b), termed pH front, are approximately equal to the position of the potential fronts in Figures 6-22(a) and 6-22(b), respectively. The velocity of the pH front changes from 1.63 mm/hr to 1.55 mm/hr when k_{neq} decreases from 0.1 to 0.001 s^{-1}. This result suggests that the change of pH along the metal-coating interface is an important factor that influences the movement of the potential front.

The influence of the rate constant k_{neq} on the velocity of potential front, porosity front and pH front is summarized in Table 6-4. When k_{neq} decreased from infinity to $10^{-4}\ s^{-1}$, the rate of the potential front decreased from 1.66 mm/hr to 1.26 mm/hr, and the rate of the porosity front decreases from 1.50 mm/hr to 0.73 mm/hr. The comparison between the potential and pH front rates confirms that the movement of the potential front depends on the pH front. The change of the front velocities indicates that the values

Table 6-4. Calculated velocities of potential, porosity and pH front

rate constants (k_{neq} / s^{-1})	velocity of potential front mm/hr	velocity of porosity front mm/hr	velocity of pH front mm/hr
∞	1.66	1.50	1.69
10^{-1}	1.63	1.37	1.61
10^{-2}	1.60	1.26	1.60
10^{-3}	1.55	0.93	1.55
10^{-4}	1.26	0.73	1.25
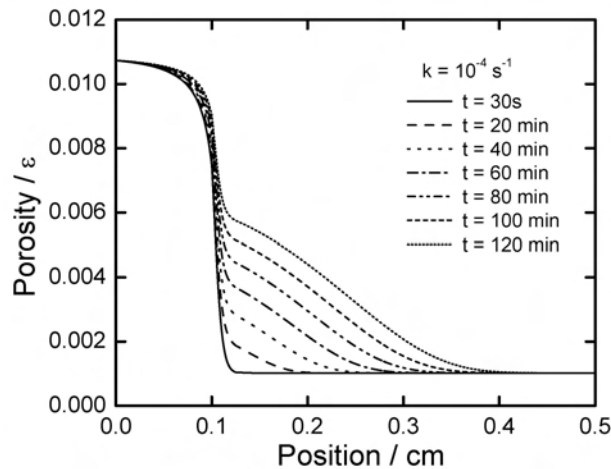
Figure 6-25. Calculated distributions of dϵ/dx along the metal-coating interface with elapsed time as a parameter.

of k_{neq} influence the propagation of all fronts, but the influence is much more evident on the porosity front.

As observed in Table 6-4, the velocity difference between the potential and porosity fronts increases with decreasing k_{neq}. The production of OH$^-$ ions in the faster potential front creates a driving force for the bond-breakage reactions that are limited by the finite rate constant. As a result, the disbondment occur in a broad region when the bond-breakage reactions are sufficiently slow. The distribution of porosity for $k_{neq} = 10^{-4}$ s^{-1} is presented in Figure 6-25 as a function of position with elapsed time as a parameter. Due to the limitation of the finite rate constant, the well-defined porosity front seen in Figure 6-14 becomes less distinguishable in Figure 6-25. Instead, the change of the porosity takes place in a broad region and this region expands with increasing time.
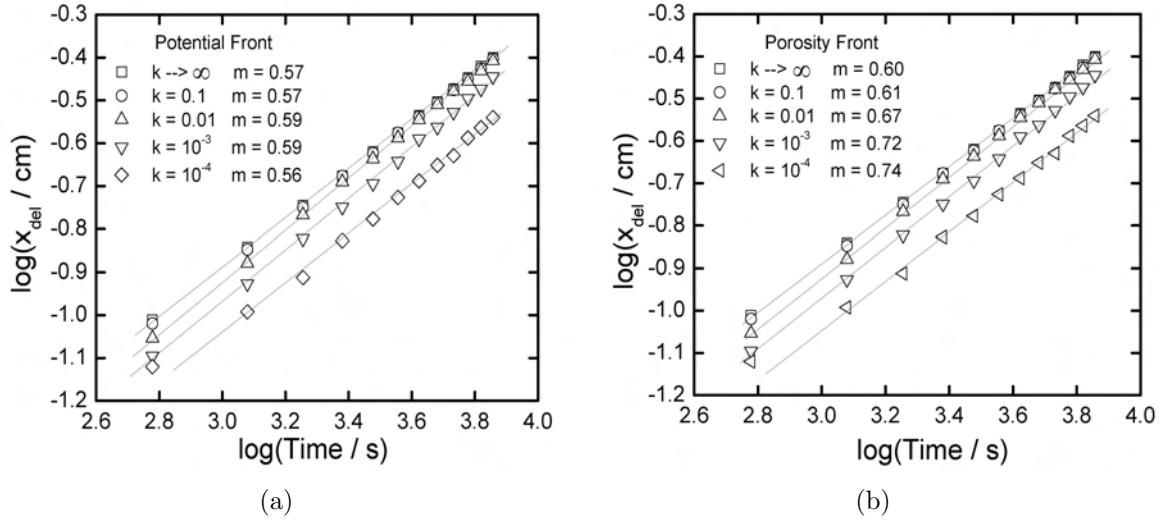
Figure 6-26. Delaminated distance as a function of delamination time in double-logarithmic scale with cation type as a parameter. a) Delaminated distance determined by the potential front; and b) Delaminated distance determined by the porosity front.

6.3.2 Delamination Kinetics

Figure 6-26(a) gives the propagation distance determined by the potential front as a function of time with k_{neq} as a parameter. When the rate constant k_{neq} changes from infinity to 10^{-4} s^{-1}, the slopes of the lines change slightly from 0.57 to 0.59. The slight change in the slope demonstrates that the rate constant k_{neq} does not have significant impacts on the rate-determining step of the overall delamination process. Figure 6-26(b) gives propagation distance determined by the porosity fronts as a function of time with k_{neq} as a parameter. The slope is approximately equal to 0.6 for the equilibrium pH-porosity relation but increases to 0.74 for $k_{neq}=10^{-4}$ s^{-1}. The change in the slope is an indication that the delamination mechanism shifts from a mass-transfer controlled to a mixed-control mechanism when the bond-breakage reactions are sufficiently slow. The transition is consistent with the experimental results reported by Stratmann et al. [10] that the overall delamination process is limited by kinetics when the delamination rate is sufficiently small.

CHAPTER 7
ELECTROCHEMICAL IMPEDANCE SPECTROSCOPY

Electrochemical Impedance Spectroscopy (EIS) is a small-signal technique in which a sinusoidal current or potential perturbation is imposed on tested systems and the corresponding potential or current response is measured (see Figure 7-1). Comparison of the input and output signals provides the impedance at a given perturbation frequency.

The influence of a particular phenomenon on impedance response is, in principle, determined by the time scale of that process. [27] For example, the time constant for mass-transfer effects is relatively large because the diffusivity of ionic species in aqueous medium is small. Therefore, mass-transfer effects are usually apparent at low frequencies; whereas kinetic and double-layer effects are more important at high frequencies. An advantage of EIS is that, with a single experimental procedure encompassing a sufficiently broad range of frequency, the governing chemical and physical phenomena can be distinguished at a given potential.
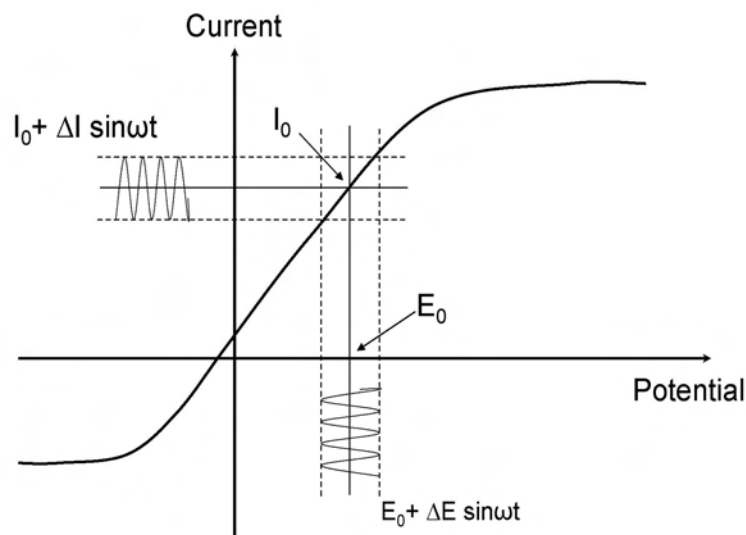
Figure 7-1. Schematic representation for theory of Electrochemical Impedance Spectroscopy (EIS) where E is potential and I is area-averaged current. Impedance is defined as the ratio of potential difference between working and reference electrodes to surface-averaged current.

Experimental impedance spectra are typically interpreted in terms of circuit models that consist of combinations of passive circuit elements. While equivalent circuit models are useful for understanding the physical processes or chemical mechanisms that occur in electrochemical systems, observed impedance spectra frequently show a dispersion that cannot be fitted using simple elements. The dispersion typically reflects a distribution of reactivity that is commonly represented in equivalent electrical circuits as a constant-phase element (CPE). The distributed reactivity may arise from variation of properties either along the area of electrode (2-D) or along the axis normal to electrode surface (3-D). A 2-D distribution could be associated with geometry-induced current/potential distributions or surface heterogeneity such as grain boundaries, crystal faces or other variations in surface properties. A 3-D distribution may arise from changes in the conductivity of oxide layer [35] or from porosity or surface roughness. [37, 38]

The recent development of local electrochemical impedance spectroscopy (LEIS) [54, 77] makes it possible to distinguish CPE behavior that has an origin with a 3-D distribution from one that arises from a 2-D distribution of properties along the surface of the electrode. [40] In LEIS, similar with traditional impedance methods, a sinusoidal current or potential perturbation is imposed on tested systems and the corresponding potential or current response is measured. The local impedance technique consists of a probe with two micro-electrodes allowing measurements of potential at two positions. Under the assumption that the Ohmic impedance between the two probes is given by a constant, the current density at the probe can be estimated from the measured potential difference $\triangle V_{\text{probe}}$ by

$$i_{\text{probe}} = V_{\text{probe}} \frac{\kappa}{d} \tag{7--1}$$

where d is the distance between the potential sensing electrodes and κ is the conductivity of the electrolyte. The local impedance can then be calculated from the ratio of the electrode potential measured relative to a reference electrode far away from the surface to the local current density i_{probe}.

(a)   (b)   (c)
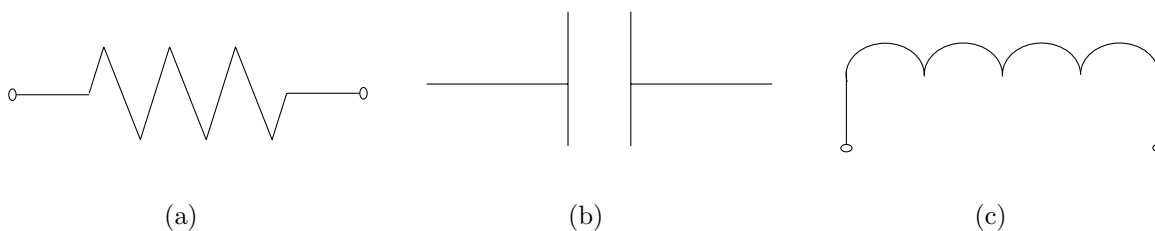
Figure 7-2. Passive elements that serve as components of an electrical circuit. a) Resistor; b) Capacitor; and c) Inductor.

The subsequent sections provide basic concepts involved in electrochemical impedance spectroscopy. Detailed discussions of technical and theoretical issues associated with EIS is available elsewhere. [25, 28, 29, 78]

7.1   Passive Electrical Circuits

Experimental impedance spectra are typically compared to that of known electrical circuits. Electrical circuits can be constructed from the passive elements shown in Figure 7-2. [25, 28, 29]

The impedance of a passive circuit element is defined as the ratio of the potential difference between the element clamps to the current flowing through the element, *i.e.*

$$Z = \frac{\triangle V}{\triangle I} \tag{7–2}$$

and has units Ohms Ω. For a pure resistor, equation 7–2 yields

$$Z_{\text{resistor}} = R \tag{7–3}$$

whereas, for a capacitor

$$Z_{\text{capacitor}} = \frac{1}{j\omega C} \tag{7–4}$$

and for an inductor, the impedance is

$$Z_{\text{inductor}} = j\omega L \tag{7–5}$$
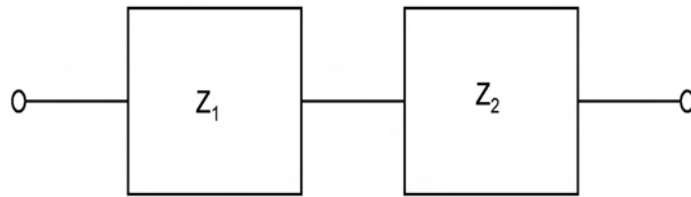
(a)
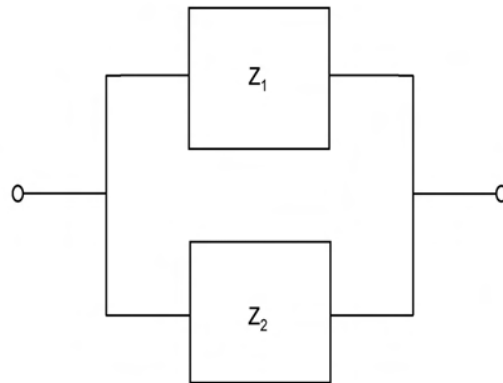
(b)

Figure 7-3. Combinations of passive elements that serve as components of an electrical circuit: a) in series b) in parallel.

For two passive elements in series, the same current must flow through the two elements, and the overall potential difference is the sum of the potential difference for each element. Thus, the impedance for the series arrangement shown in Figure 7-3(a) is given by

$$Z = Z_1 + Z_2 \tag{7--6}$$

For two passive elements in parallel, the overall current is the sum of the current flowing in each element, and the potential difference is the same for each dipole. Therefore, the overall impedance for the parallel arrangement shown in Figure 7-3(b) is given by

$$Z = [\frac{1}{Z_1} + \frac{1}{Z_2}]^{-1} \tag{7--7}$$

Impedance contributions are additive for elements in series; whereas, the inverse of the impedance is additive for elements in parallel.

It is important to note that different circuit analog models possessing the same number of time constants can yield a mathematically equivalent frequency response. [25, 28, 29] The lack of uniqueness of the circuit models creates ambiguity when interpreting impedance results. A good fit to experimental data does not guarantee that the model describes correctly the physics of the given system. Additional experimental observations are needed to verify a proposed model and to avoid ambiguities when interpreting impedance data.

7.2 Constant-Phase Element (CPE)

Experimental impedance results for a solid electrode/electrolyte interface often revel a time-constant dispersion that cannot be described by simple elements. To characterize this time-constant dispersion, the interfacial capacitance is often expressed in equivalent circuits in terms of a constant-phase element (CPE). [25, 28, 29]

CPE typically reflects a non-ideal double-layer capacitance and is usually related to a pure capacitor by

$$Q = C_0(j\omega)^{1-\alpha} \tag{7–8}$$

where the parameters α and Q are constants. When $\alpha = 1$, Q has units of a capacitor and represents the capacity of the interface. When $\alpha \neq 1$, the system shows behavior that can be attributed to distributed properties on electrode surface. The value of α may change from -1 to +1; in this sense, the CPE is treated as an extremely flexible fitting element and its meaning in terms of a distribution of time constants is less clear.

7.2.1 Origin of CPE

Numerous research efforts have been made in literature to study the origin of the CPE behavior. Pajkossy [38, 79] modeled rough electrodes by surfaces of fractal geometry with processes dilatational symmetry. The theoretical calculations yielded CPE behavior with a fractional exponent depending on the fractal dimension. The experiments by

Pajkossy and Kerner [38, 79] showed that the time-constant dispersion on solid electrode was due to surface disorder (on the atomic scale) rather than geometric roughness (larger than atomic scale).

De Levie [80, 81] modeled the impedance of porous electrodes under the assumption that the concentration was uniform and the pores were ideal cylinders. Lasia [82] later replaced the double layer capacitance on pore walls with a CPE. The results reported by Lasia [82] showed that mass transfer and pore geometry influenced the shape of impedance spectrum. The models proposed by de Levie and Lasia considered only a single pore dimension. Song et al. [83] developed a model to predict the effect of pore size distribution on the impedance response of porous electrodes.

Pajkossy et al. [84–87] proposed that the time-constant dispersion arose from the adsorption of molecules or anions on gold electrodes. The capacitance dispersion observed in the presence of specific adsorption can be assigned to either a slow diffusion or slow adsorption processes within the double layer or electrode surface.[87]

Newman and Nisancioglu [41, 42, 45] studied the influence of nonuniform current and potential distribution on the impedance response of a disk electrode. Their results indicated the geometry-induced potential and current distribution induced a high-frequency dispersion that distorted the impedance response. Nisancioglu [45] showed the extent to which this frequency dispersion leads to an error in the values for charge-transfer resistance and interfacial capacitance obtained from impedance data.

7.2.2 2-D and 3-D Distributions

The explanations of CPE behavior presented above suggest that two kinds of distributions can be distinguished. A 2-D distribution could be associated with geometry-induced current/potential distributions or surface heterogeneity such as grain boundaries, crystal faces or other variations in surface properties. CPE behavior may also arise from changes in the conductivity of oxide layer [35] or from porosity or surface roughness. [37, 38] This
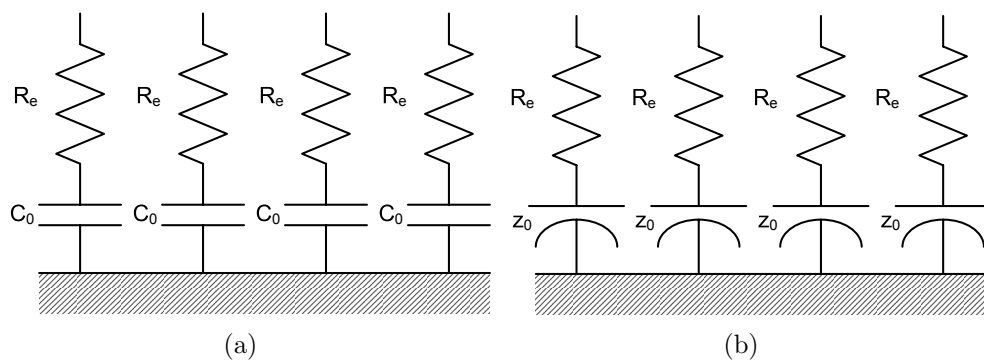
Figure 7-4. Schematic representation of an impedance distribution for a blocking disk electrode where R_e represents the Ohmic resistance, C_0 represents the interfacial capacitance, and z_0 represents an interfacial impedance corresponding to CPE a) 2-dimensional distribution of blocking components in terms of resistors and capacitors; and b) 3-dimensional distribution of blocking components in terms of resistors and constant-phase elements.

can be described as being associated with a 3-D distribution, with the third direction being the direction normal to the electrode surface.

A schematic representation of a 2-D distribution for an ideally-polarized blocking disk electrode is presented in Figure 7-4(a). For a 2-D distribution, the capacitance and Ohmic resistance could be a function of radial position along the electrode. Integration of the admittance associated with these circuit elements would yield a global admittance with a CPE behavior,

$$Y = Z^{-1} = \int_A z^{-1} dA \qquad (7\text{–}9)$$

where A is the electrode area, Y is the global admittance, Z is the global impedance, and z is the local impedance. The local impedance, in the case of a 2-D distribution would, however, show ideal behavior. A 3-D distribution of blocking components in terms of resistors and constant-phase elements is presented in Figure 7-4(b). Such a system will yield a local impedance with a CPE behavior, even in the absence of a 2-D distribution of surface properties. If the 3-D system shown schematically in Figure 7-4(b) is influenced by a 2-D distribution, the local impedance should reveal a variation of CPE coefficients along the surface of the electrode. Thus, local impedance measurements can be used to

distinguish whether the origin of the CPE behavior arises from a 2-D distribution, from a 3-D distribution, or from a combined 2-D and 3-D distribution.

7.3 Current and Potential Distributions on Disk Electrode

Current and potential distributions on electrode surface play an essential role in electrochemical fabrication technologies [88] and in interpretation of electrochemical processes. [89] The geometry of an electrode often constrains the distributions of current and potential on the electrode surface in such a way that both cannot be simultaneously uniform. Newman [46] developed analytical solutions for current and potential distributions on a disk geometry, and the development is reviewed in this section.

In a bulk of a well-stirred electrolytic solution where concentration gradients are negligible within the electrolyte, potential is governed by Laplace's equation, *i.e.*[46]

$$\nabla^2 \Phi = 0 \qquad (7\text{--}10)$$

where Φ is the solution potential. The current density i can then be expressed as

$$i = -\kappa \nabla \Phi \qquad (7\text{--}11)$$

Under the assumption that concentrations are uniform in the electrolyte, the passage of current through the interface is limited by Ohmic resistance in the electrolyte and by charge-transfer resistance associated with reaction kinetics. The primary distribution applies when the flow of current is dominated by the Ohmic resistance and kinetic resistance can be neglected. The secondary distribution applies when both Ohmic and kinetic resistances are controlling.

7.3.1 Primary Current Distribution

In the absence of mass-transfer limitations and Faradaic reactions, the primary current distribution of a disk electrode requires solution of Laplace's equation with a charging boundary condition at the electrode surface. The primary resistance can be

expressed in the form of [46]

$$R_e = \frac{\pi r_0}{4\kappa} \tag{7–12}$$

The primary current density distribution associated with a disk electrode surface follows [46]

$$\frac{i}{<i>} = \frac{1}{2\sqrt{1 - \left(\frac{r}{r_0}\right)^2}} \tag{7–13}$$

where r_0 is the radius of the disk and $<i>$ is the area-averaged current density on the electrode. A graph of $i/<i>$ as a function of dimensionless position r/r_0 is presented in Figure 7-5. The normalized current density is fairly well behaved near the center of the electrode, but it approaches infinity at the edge of the electrode. As a result, the primary current distribution is highly non-uniform for a disk electrode.

7.3.2 Secondary Current Distribution

The secondary current distribution is a consequence of the balance between electrolyte resistance and charge-transfer resistance. For this case, the distribution requires solution of Laplace's equation with a boundary condition at the electrode surface that is associated with both Faradaic reactions and charge of double-layer capacity. The ratio of these two contributions is, in general, expressed in terms of a dimensionless parameter J

$$J = \frac{4}{\pi}\frac{R_e}{R_t} \tag{7–14}$$

Large values of J are seen when the Ohmic resistance dominates over the charge-transfer resistance, and small values of J are seen when the charge-transfer resistance is more important. The secondary current density distribution on a disk electrode is presented in Figure 7-6 as a function of the normalized position with J as a parameter. The current is uniformly distributed when J is sufficiently small and the distribution becomes more nonuniform as J increases. The curve for $J=\infty$ represents the primary distribution seen in Figure 7-5 in which the current distribution is primarily controlled by Ohm's law.
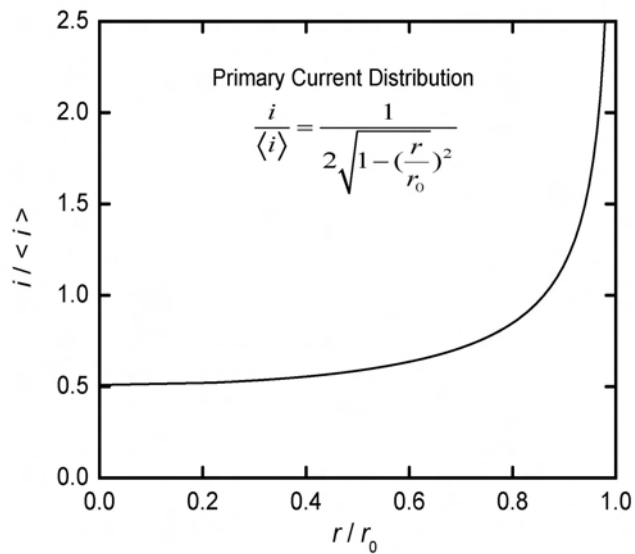
Figure 7-5. Primary current distribution at a disk electrode.
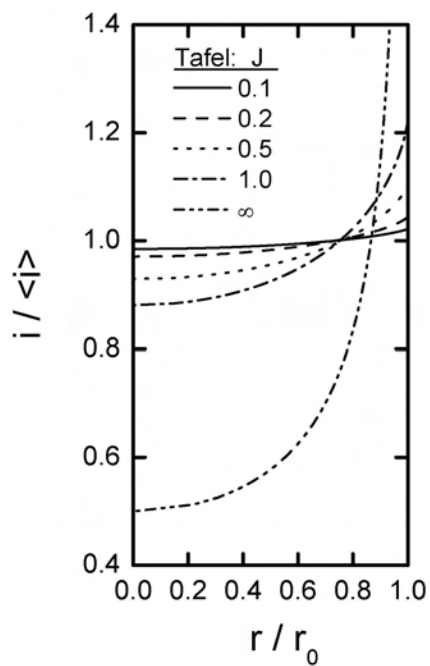
Figure 7-6. Secondary current density distribution at a disk electrode with J as a parameter.

7.4 Objective

The studies by Nisancioglu [45] and by Newman [41, 42] demonstrated that the geometry-induced current and potential distributions cause a high-frequency dispersion that distorts the impedance response on a disk electrode. However, their discussions did not address the dispersion in terms of CPE. Moreover, none of the work developed to date addresses the coupling of 2-D and 3-D distributions, and none of the previous work relates global impedance response with local impedance.

The objective of this work was to explore, from first principle, the role of nonuniform current and potential distributions on the global and the local impedance response of a disk electrode. The electrochemical systems under study included an ideally-polarized blocking electrode, an electrode exhibiting a local CPE behavior, and an electrode exhibiting a single Faradaic reaction. The theoretical development and calculation results of the work are presented in Chapter 8, Chapter 9, and Chapter 10, respectively.

CHAPTER 8
IDEALLY POLARIZED BLOCKING DISK ELECTRODE

This chapter presents the theoretical development and calculation results for the impedance response of an ideally-polarized blocking electrode. [32] There are several types of impedance at play; their definitions and notations are also provided in this chapter.

8.1 Theoretical Development

In the absence of mass-transfer effects, the transient response of a disk electrode requires Laplace's equation with flux conditions at the electrode surface. Following Newman's approach, [42] Laplace's equation in cylindrical coordinates was expressed in rotational elliptic coordinates, i.e.

$$y = r_0 \xi \eta \tag{8–1}$$

and

$$r = r_0 \sqrt{(1 + \xi^2)(1 - \eta^2)} \tag{8–2}$$

where $0 \leq \xi \leq \infty$ and $0 \leq \eta \leq 1$. The coordinate transformation can be seen more clearly in Figure 8-1. Within the rotational elliptic coordinate system, the electrode surface at y = 0 and $r \leq r_0$ can be found at $\xi = 0$ and $0 \leq \eta \leq 1$. The reference electrode and counter electrode located at $y \to \infty$ can be found at $\xi \to \infty$. The insulating surface of the disk at y = 0 and $r > r_0$ is located at $\eta = 1$ and $0 < \xi \leq \infty$, and the center line at y > 0 and $r = 0$ is located at $\eta = 0$ and $0 < \xi \leq \infty$.

Lapace's equation can be expressed in rotational elliptic coordinates as

$$\frac{\partial}{\partial \xi}\left[(1 + \xi^2)\frac{\partial \Phi}{\partial \xi}\right] + \frac{\partial}{\partial \eta}\left[(1 - \eta^2)\frac{\partial \Phi}{\partial \eta}\right] = 0 \tag{8–3}$$

The potential was separated into steady and oscillating parts as

$$\Phi = \bar{\Phi} + \tilde{\Phi}\exp(j\omega t) \tag{8–4}$$
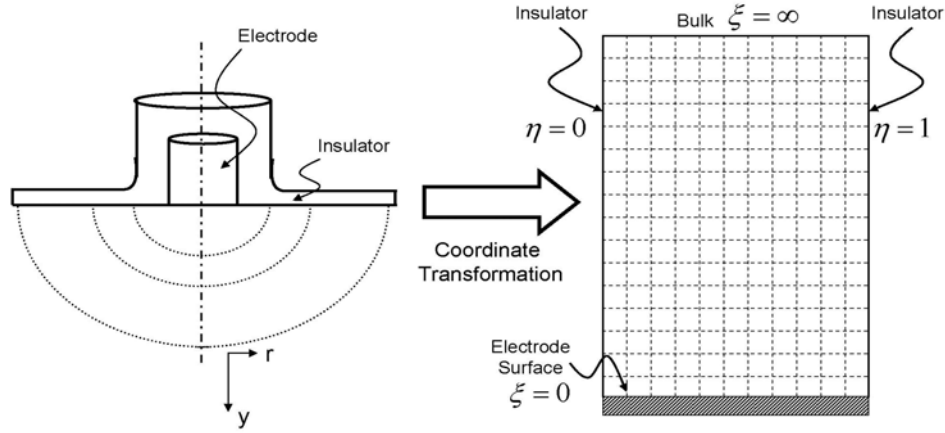
Figure 8-1. Coordinate transformation from a cylindrical coordinate to a rotational elliptic coordinate. The griding in the rotation epiotic coordinate is not drawn to scale.

where $\bar{\Phi}$ is the steady-state solution for potential and $\tilde{\Phi}$ is the complex oscillating potential. Thus, equation (8–3) could be written as

$$2\xi\frac{\partial\tilde{\Phi}_r}{\partial\xi} + (1+\xi^2)\frac{\partial^2\tilde{\Phi}_r}{\partial\xi^2} - 2\eta\frac{\partial\tilde{\Phi}_r}{\partial\eta} + (1-\eta^2)\frac{\partial^2\tilde{\Phi}_r}{\partial\eta^2} = 0 \tag{8–5}$$

and

$$2\xi\frac{\partial\tilde{\Phi}_j}{\partial\xi} + (1+\xi^2)\frac{\partial^2\tilde{\Phi}_j}{\partial\xi^2} - 2\eta\frac{\partial\tilde{\Phi}_j}{\partial\eta} + (1-\eta^2)\frac{\partial^2\tilde{\Phi}_j}{\partial\eta^2} = 0 \tag{8–6}$$

where $\tilde{\Phi}_r$ and $\tilde{\Phi}_j$ refer to the real and imaginary parts of the complex potential, respectively.

For a blocking electrode, the current passes from the electrode to the electrolyte by a means of charging the double-layer capacity. The flux boundary condition at the electrode surface ($\xi = 0$ and $0 \leq \eta \leq 1$) was expressed as

$$i = C_0\frac{\partial(V-\Phi_0)}{\partial t} = -\kappa\left.\frac{\partial\Phi}{\partial y}\right|_{y=0} = -\frac{\kappa}{r_0\eta}\left.\frac{\partial\Phi}{\partial\xi}\right|_{\xi=0} \tag{8–7}$$

where C_0 is the interfacial capacitance and κ is the electrolyte conductivity. Equation (8–7) was written in frequency domain as

$$\mathrm{K}\tilde{\Phi}_j = -\frac{1}{\eta}\left.\frac{\partial\tilde{\Phi}_r}{\partial\xi}\right|_{\xi=0} \tag{8–8}$$

and

$$\mathrm{K}\tilde{V}_r - \mathrm{K}\tilde{\Phi}_r = -\frac{1}{\eta}\left.\frac{\partial\tilde{\Phi}_j}{\partial\xi}\right|_{\xi=0} \tag{8–9}$$

where $\tilde{V}_r$ represents the imposed perturbation in the electrode potential referred to an electrode at infinity and K is the dimensionless frequency

$$\mathrm{K} = \frac{\omega C_0 r_0}{\kappa} \tag{8–10}$$

At $\eta = 0$ and $\eta = 1$, for all $\xi > 0$, zero-flux conditions impose that

$$\frac{\partial\tilde{\Phi}_r}{\partial\eta} = 0 \tag{8–11}$$

and

$$\frac{\partial\tilde{\Phi}_j}{\partial\eta} = 0 \tag{8–12}$$

At the far boundary condition ($\xi \to \infty$ and $0 \le \eta \le 1$),

$$\tilde{\Phi}_r = 0 \tag{8–13}$$

and

$$\tilde{\Phi}_j = 0 \tag{8–14}$$

The equations were solved under the assumption of a uniform capacitance C_0 using the collocation package PDE2D developed by Swell. [90] To ensure the accuracy of the calculations, a series of error analysis was performed to verify that the mesh size used in the program was sufficiently small and the domain size is sufficiently large. Calculations were performed for different domain sizes, and the results presented here were obtained by extrapolation to an infinite domain.
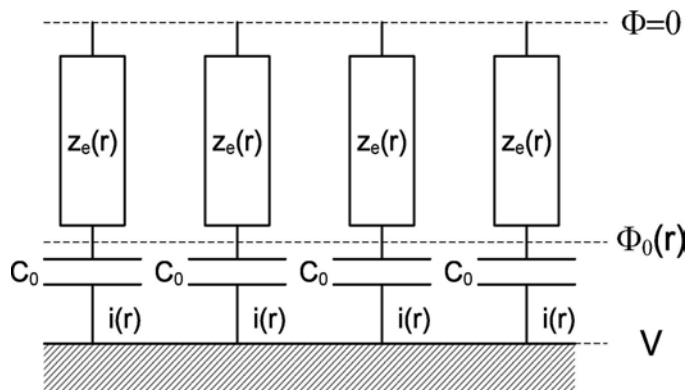
Figure 8-2. The location of current and potential terms that make up definitions of global and local impedance.

8.2 Definition of Impedance

The calculation results presented in the subsequent sections involve several type of impedance. The notations and the definitions of the impedance are presented in this section.

A schematic representation of the electrode-electrolyte interface for an ideally-polarized blocking electrode is given as Figure 8-2, where the block used to represent the Ohmic impedance reflects the complex character of the Ohmic contribution to the local impedance response. The impedance definitions presented in Table 8-1 differ in the potential and current used to calculate the impedance. To avoid confusion with local impedance values, the symbol y is used to designate the axial position in cylindrical coordinates.

8.2.1 Global Impedance

The global impedance is defined to be

$$Z = \frac{\tilde{V}}{\tilde{I}} \tag{8–15}$$

where the complex current contribution is given by

$$\tilde{I} = \int_0^{r_0} \tilde{i}(r) 2\pi r \, dr \tag{8–16}$$

Table 8-1. Notation proposed for local impedance variables[39]

Symbol	meaning	units
Z	global impedance	Ω or Ωcm^2
Z_r	real part of global impedance	Ω or Ωcm^2
Z_j	imaginary part of global impedance	Ω or Ωcm^2
Z_0	global interfacial impedance	Ω or Ωcm^2
$Z_{0,r}$	real part of global interfacial impedance	Ω or Ωcm^2
$Z_{0,j}$	imaginary part of global interfacial impedance	Ω or Ωcm^2
Z_e	global Ohmic impedance	Ω or Ωcm^2
$Z_{e,r}$	real part of global Ohmic impedance	Ω or Ωcm^2
$Z_{e,j}$	imaginary part of global Ohmic impedance	Ω or Ωcm^2
z	local impedance	Ωcm^2
z_r	real part of local impedance	Ωcm^2
z_j	imaginary part of local impedance	Ωcm^2
z_0	local interfacial impedance	Ωcm^2
$z_{0,r}$	real part of local interfacial impedance	Ωcm^2
$z_{0,j}$	imaginary part of local interfacial impedance	Ωcm^2
z_e	local Ohmic impedance	Ωcm^2
$z_{e,r}$	real part of local Ohmic impedance	Ωcm^2
$z_{e,j}$	imaginary part of local Ohmic impedance	Ωcm^2
$\langle\Phi\rangle$	spatial average of potential	V
$\overline{\Phi}$	time average or steady-state value of potential	V
$\langle i\rangle$	spatial average of current density	A/cm^2
$\bar{\imath}$	time average or steady-state value of current density	A/cm^2
y	axial position variable	cm

The use of an upper-case letter signifies that Z is a global value. The global impedance has real and imaginary components designated as Z_r and Z_j, respectively. The total current can also be represented by $\tilde{I} = \pi r_0^2 < \tilde{i}(r) >$ where the brackets signify the area-average of the current density. [39]

8.2.2 Local Impedance

The term local impedance traditionally involves the potential of the electrode measured relative to a reference electrode far from the electrode surface. [91, 92] Thus, the local impedance is given by

$$z = \frac{\tilde{V}}{\tilde{i}(r)} \tag{8–17}$$

The use of a lower-case letter signifies that z is a local value. The local impedance may have real and imaginary values designated as z_r and z_j, respectively. [39]

The global impedance can be expressed in terms of the local impedance as

$$Z = \left\langle \frac{1}{z} \right\rangle^{-1} \tag{8–18}$$

Equation (8–18) is consistent with the treatment of Brug et al. [30] in which the admittance of the disk electrode was obtained by integration of a local admittance over the area of the disk.

8.2.3 Local Interfacial Impedance

The local interfacial impedance involves the potential of the electrode measured relative to a reference electrode $\Phi_0(r)$ located at the outer limit of the diffuse double layer. Thus, the local interfacial impedance is given by

$$z_0 = \frac{\tilde{V} - \tilde{\Phi}_0(r)}{\tilde{i}(r)} \tag{8–19}$$

The use of a lower-case letter again signifies that z_0 is a local value, and the subscript 0 signifies that z_0 represents a value associated only with the surface. The local interfacial impedance may have real and imaginary values designated as $z_{0,r}$ and $z_{0,j}$, respectively. [39]

8.2.4 Local Ohmic Impedance

The local Ohmic impedance involves the potential of a reference electrode $\Phi_0(r)$ located at the outer limit of the diffuse double layer and the potential of a reference electrode located far from the electrode $\tilde{\Phi}(\infty) = 0$ (see Figure 8-2). Thus, the local Ohmic impedance is given by

$$z_e = \frac{\tilde{\Phi}_0(r)}{\tilde{i}(r)} \tag{8–20}$$

The use of a lower-case letter again signifies that z_e is a local value, and the subscript e signifies that z_e represents a value associated only with the Ohmic character of the electrolyte. The local Ohmic impedance may have real and imaginary values designated as $z_{e,r}$ and $z_{e,j}$, respectively. The local impedance

$$z = z_0 + z_e \tag{8–21}$$

can be represented by the sum of local interfacial and local Ohmic impedances. [39]

8.2.5 Global Interfacial Impedance

The global interfacial impedance is defined to be

$$Z_0 = 2\pi \left[\int_0^{r_0} \frac{1}{z_0(r)} r d(r) \right]^{-1} \tag{8–22}$$

or

$$Z_0 = \langle \frac{1}{z_0(r)} \rangle^{-1} \tag{8–23}$$

The use of an upper-case letter signifies that Z_0 is a global value. The global interfacial impedance may have real and imaginary values designated as $Z_{0,r}$ and $Z_{0,j}$, respectively.

8.2.6 Global Ohmic Impedance

The global Ohmic impedance is defined to be

$$Z_e = Z - Z_0 \tag{8–24}$$
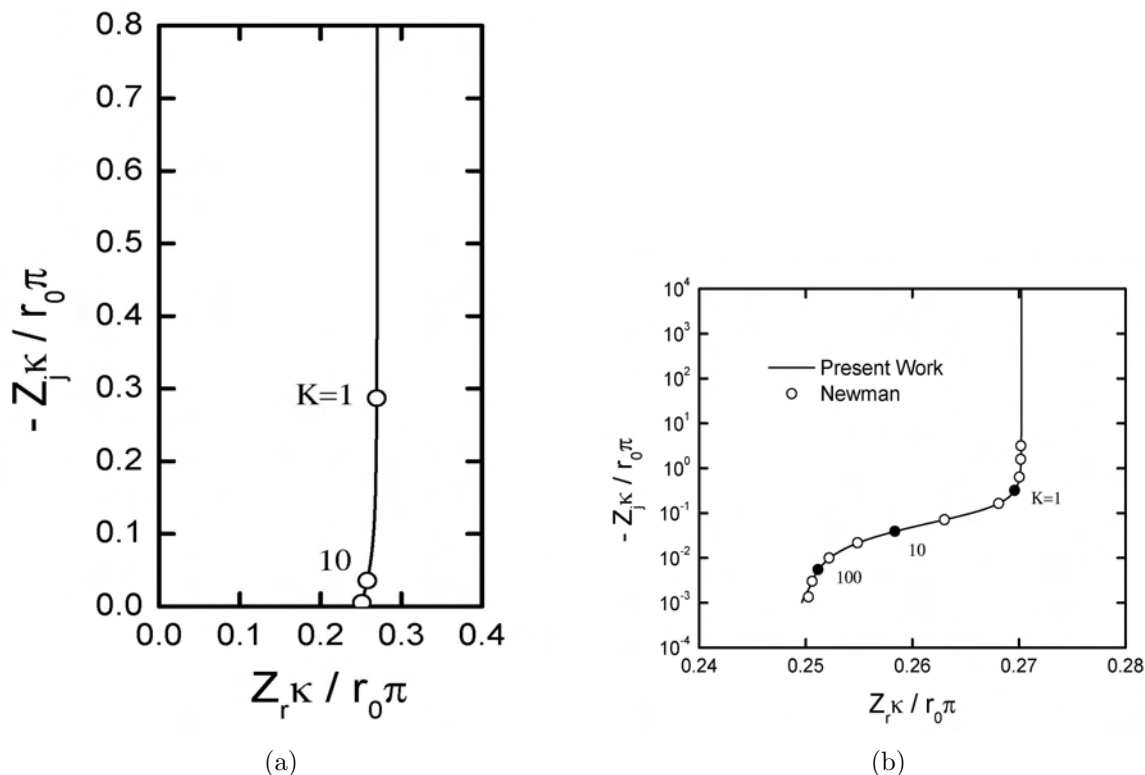
Figure 8-3. Calculated Nyquist representation of the impedance response for an ideally polarized disk electrode. a) linear plot showing effect of dispersion at frequencies K>1; and b) logarithmic scale showing agreement with the calculations of Newman.

The use of an upper-case letter signifies that Z is a global value. The global Ohmic impedance may have real and imaginary values designated as $Z_{e,r}$ and $Z_{e,j}$, respectively.

8.3   Results and Discussion

The calculated results for global, local, local interfacial, and both local and global Ohmic impedance are presented in this section. The results are believed to be incorrect for frequencies K > 100 due to the presence of a singular perturbation problem that arises at the periphery of the electrode at high frequencies. [42]

8.3.1   Global Impedance

The global impedance response presented in Figure 8-3(a) in Nyquist format shows the influence of time-constant dispersion at frequencies K > 1. The impedance was made dimensionless according to $Z\kappa/r_0\pi$ in which the units of impedance Z were scaled by unit
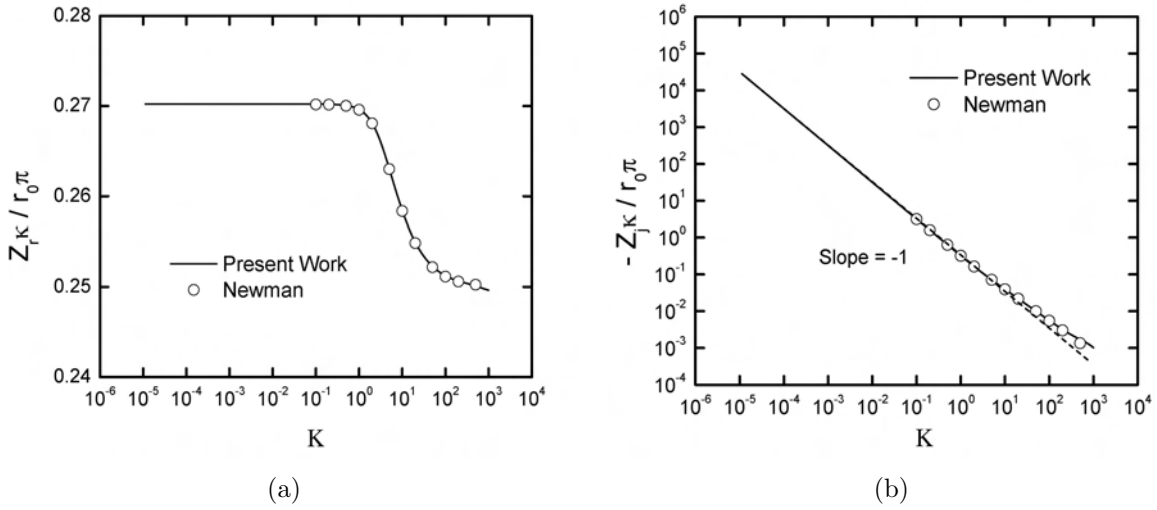
Figure 8-4. Calculated representation of the impedance response for an ideally polarized disk electrode. a) real part; and b) imaginary part showing agreement with the calculations and asymptotic formula of Newman.

area, Ωcm^2. The expanded logarithmic representation presented in Figure 8-3(b) shows good agreement with the numerical solutions presented by Newman. [42]

The comparison with Newman's calculations is seen more clearly in the representation of the real and imaginary parts of the impedance response shown in Figures 8-4(a) and 8-4(b), respectively. As stated by Orazem et al. [78], the slope of $\log(Z_j\kappa/r_0\pi)$ with respect to $\log(K)$ gives the exponent of the CPE, $-\alpha$. The change in the slope of the lines presented in Figure 8-4(b) shows that the impedance response transitions from ideal R_eC_0 behavior at low frequencies to a CPE-like behavior at frequencies $K > 1$. A deviation from Newman's results is seen for frequencies $K > 100$. This error is attributed to a singular perturbation problem, identified by Newman, that arises at the periphery of the electrode at high frequencies. [42]

The change of $-\alpha$ is presented in Figure 8-5 as a function of dimensionless frequency K. The system behaves as an ideal capacitor at low frequencies with $\alpha = 1$. At frequencies $K > 1$, the value of α changes to roughly $\alpha = 0.85$ at $K > 10$. As the
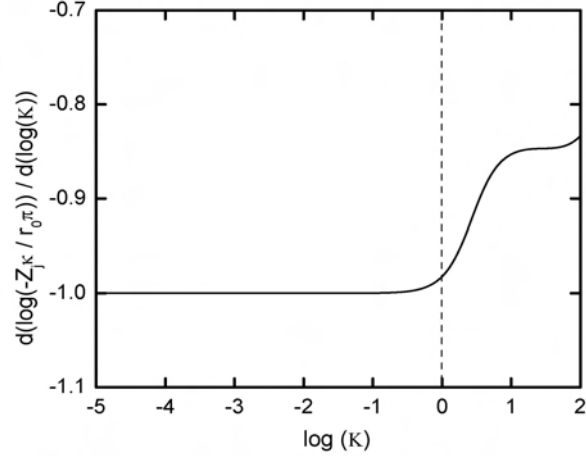
Figure 8-5. The slope of $\log(Z_j\kappa/r_0\pi)$ with respect to $\log(K)$ (Figure 8-4(b)) as a function of $\log(K)$. The results were calculated by the collocation method. The value of this slope is equal to $-\alpha$.

slope is not independent of frequency, the frequency dispersion seen at $K > 1$ does not represent true CPE behavior.

The frequency $K = 1$ at which the current distribution influences the impedance response can be expressed as

$$f = \frac{\kappa}{2\pi C_0 r_0} \tag{8–25}$$

As shown in Figure 8-6, this characteristic frequency can be well within the range of experimental measurements. The value $\kappa/C_0 = 10^4$ cm/s can be obtained for a capacitance $C_0 = 1$ μF/cm^2 (corresponding to an oxide layer) and conductivity $\kappa = 0.01$ S/cm (corresponding to a 0.1 M NaCl solution). The value $\kappa/C = 10^3$ cm/s can be obtained for a capacitance $C_0 = 10$ μF/cm^2 (corresponding to the double layer on an inert metal electrode) and conductivity $\kappa = 0.01$ S/cm (corresponding to a 0.1 M NaCl solution). Figure 8-6 can be used to show that, by using an electrode that is sufficiently small, the experimentalist may be able to avoid the frequency range that is influenced by current and potential distributions.

8.3.2 Local Interfacial Impedance

The calculated local interfacial impedance is presented in Figure 8-7(a) as a function
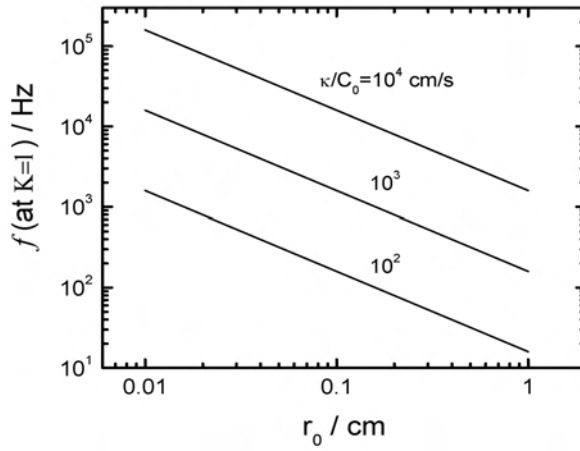
Figure 8-6. The frequency K=1 at which the current distribution influences the impedance response with κ/C_0 as a parameter.
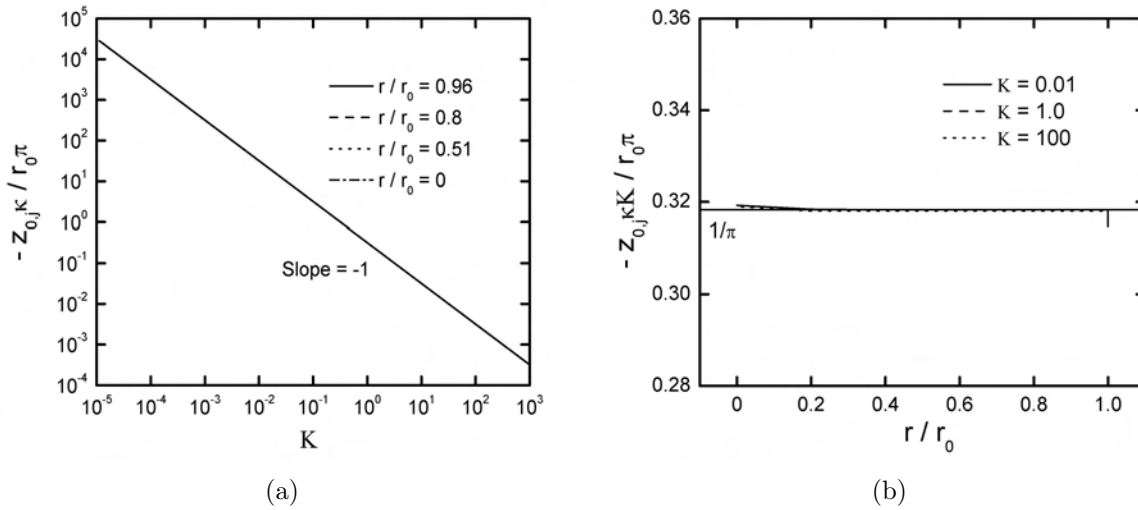
Figure 8-7. Calculated imaginary part of the local interfacial impedance: a) as a function of frequency with position as a parameter; and b) as a function of position with frequency as a parameter.
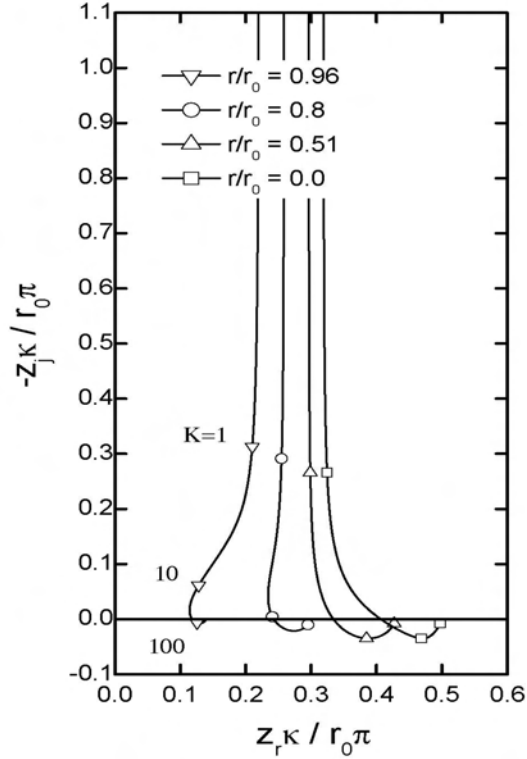
Figure 8-8. The local impedance in Nyquist format with radial position as a parameter.

of frequency with position as a parameter and in Figure 8-7(b) as a function of position with frequency as a parameter. The results presented in Figure 8-7 show that the local interfacial impedance is purely associated with a capacitive behavior. At all frequencies, $z_{0,j}\kappa K/r_0\pi = 1/\pi$ as is expected for an ideal capacitance. The real part of the local interfacial impedance, not shown here, was equal to zero within computational accuracy.

8.3.3 Local Impedance

The calculated local impedance response is presented in Figure 8-8 in Nyquist format with normalized radial position as a parameter. The dimensionless impedance is scaled to the disk area πr_0^2 in order to compare with the asymptotic value of 0.25 for the real part of the dimensionless global impedance. The impedance is largest at the center of the disk and smallest at the periphery, reflecting the greater accessibility of the periphery of the disk electrode. Inductive loops, which are not shown in the global impedance, are seen at high frequencies in local impedance.
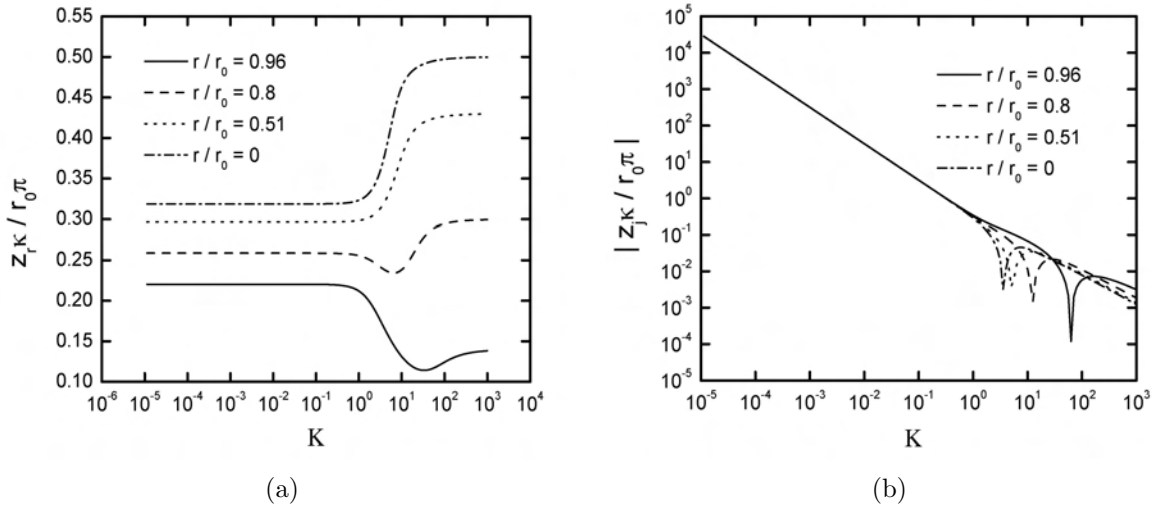
Figure 8-9. Calculated local impedance with radial position as a parameter: a) real part; and b) imaginary part.

The real and imaginary parts of the local impedance are presented in Figures 8-9(a) and 8-9(b), respectively, with radial position as a parameter. The real part of the local impedance presented in Figure 8-9(a) reaches asymptotic values at $K \to 0$ and $K \to \infty$. The imaginary part presented in Figure 8-9(b) shows the change of sign associated with the inductive features in Figure 8-8. The changes in sign occur at frequencies below $K = 100$, showing that the inductive loop cannot be attributed to calculation artifacts.

The radial distribution of the real and imaginary impedance is presented in Figures 8-10(a) and 8-10(b), respectively, with dimensionless frequency K as a parameter. At high frequencies, e.g. $K = 100$, the calculated radial distribution of the real part of the local impedance follows the expression

$$\frac{z_r \kappa}{r_0 \pi}(r) = 0.5 \sqrt{1 - \left(\frac{r}{r_0}\right)^2} \tag{8-26}$$

derived from equation (8–27) using the expression for the primary resistance

$$R_e = \frac{\pi r_0}{4\kappa}$$
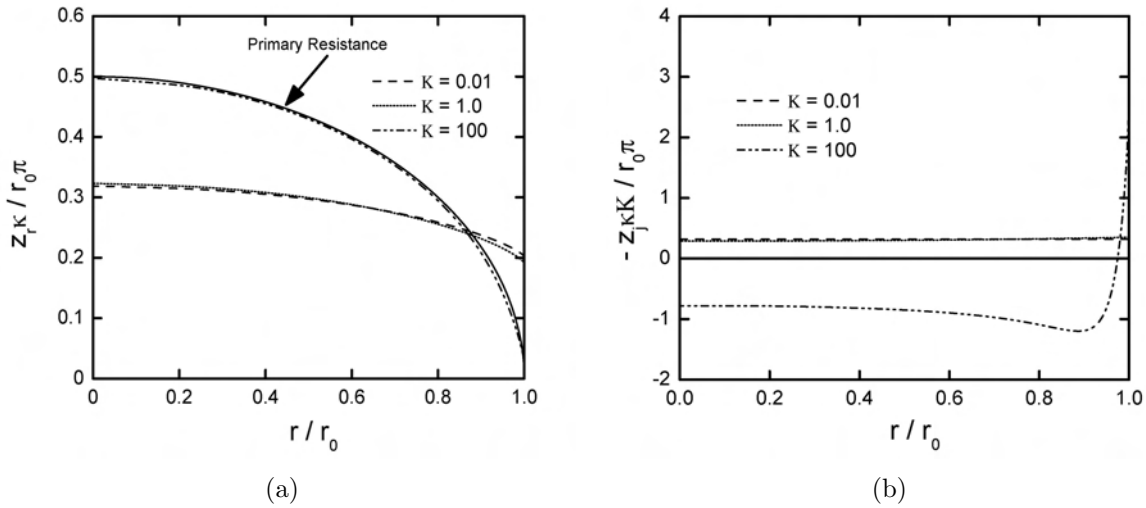
Figure 8-10. Calculated local impedance as a function of radial position: a) real part; and b) imaginary part multiplied by dimensionless frequency K.

Similarly, for frequencies K > 1 the imaginary part of the local impedance deviates from that expected for an ideal capacitive electrode.

8.3.4   Local Ohmic Impedance

Following equation (8–21), the local Ohmic impedance z_e accounts for the difference between the local interfacial and local impedances. The calculated local Ohmic impedance is presented in Figure 8-11 in Nyquist format with radial position as a parameter. The shape of the diagrams are strongly dependent on the position on the electrode. At the periphery of the electrode, two time constants (inductive and capacitive loops) are seen; whereas, at the electrode center only an inductive loop is evident. These loops are distributed around the asymptotic value of 1/4. The calculated values for real and imaginary parts of the local Ohmic impedance are presented in Figures 8-12(a) and 8-12(b), respectively, as a function of frequency with radial position as a parameter. The local Ohmic impedance has only real values at K → 0 and K → ∞, but in the frequency range 10^{-2} < K < 100, z_e has both real and imaginary components. Figure 8-12(a) clearly shows the asymptotic behavior in the low frequency range with values distributed around 1/4.
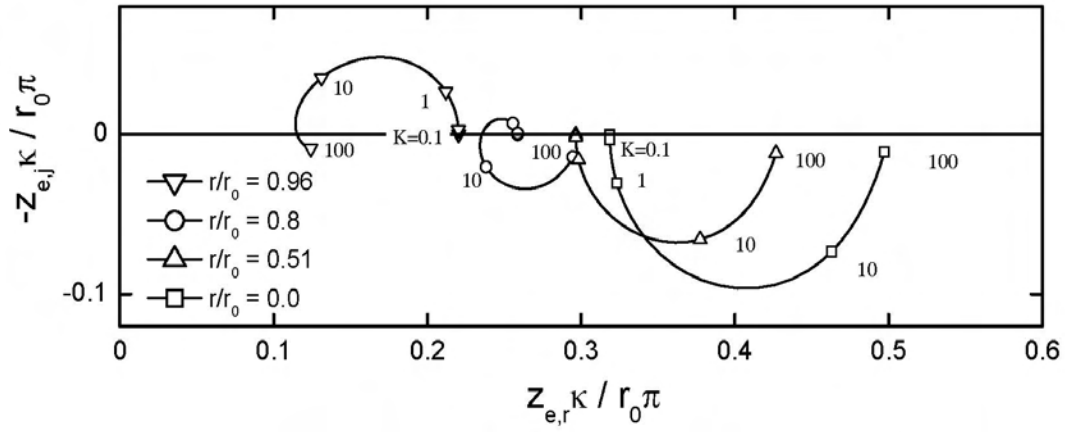
Figure 8-11. The local Ohmic impedance in Nyquist format with radial position as a parameter.

<div align="center">(a)</div>

<div align="center">(b)</div>
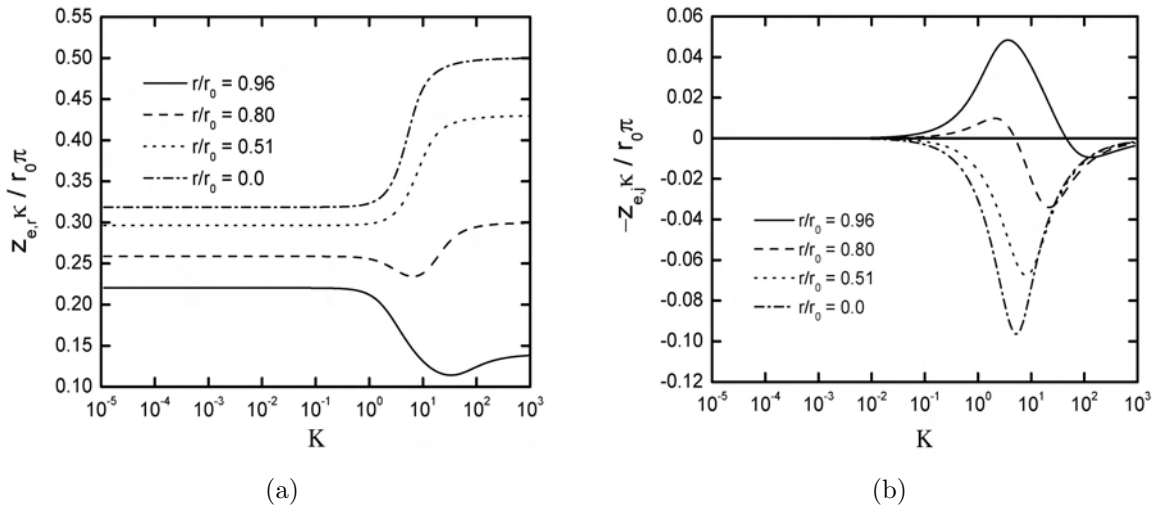
Figure 8-12. Calculated values for local Ohmic impedance as a function of frequency with radial position as a parameter: a) real part; and b) imaginary part.
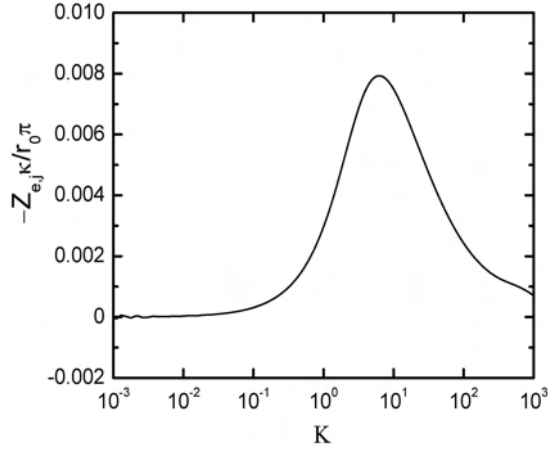
Figure 8-13. The imaginary part of the global Ohmic impedance, calculated from equation (8–28), as a function of dimensionless frequency.

8.3.5   Global Interfacial and Global Ohmic Impedance

The local interfacial impedance is associated with a pure capacitance that is independent of radial position. Thus, the global interfacial impedance should also be a pure capacitance C_0 in units of $\mu F/cm^2$. The global Ohmic impedance Z_e is obtained from the global impedance Z by the expression

$$Z_e = Z - \frac{1}{jC_0\omega} \tag{8–27}$$

or, in the dimensionless terms used in the present work,

$$\frac{Z_e\kappa}{r_0\pi} = \frac{Z\kappa}{r_0\pi} - \frac{1}{j\pi K} \tag{8–28}$$

The real part of Z_e is equal to the real part of Z as given in Figure 8-4(a). The imaginary part of Z_e is given in Figure 8-13 as a function of dimensionless frequency K. In the low frequency range Z_e is a pure resistance equal to $1.08R_e$, and, in the high frequency range, Z_e tends towards R_e. The imaginary part of the global Ohmic impedance shows a non-zero value in the frequency range that is influenced by the current and potential distributions. Figures 8-4(a) and 8-13 show that all the effect of the current and potential distribution appears in the global Ohmic impedance.

107

CHAPTER 9
BLOCKING DISK ELECTRODE WITH LOCAL CPE

In Chapter 8, it has been shown that the nonuniform current and potential distributions influence the global and local impedances of an ideally-blocking disk electrode. The objective of this chapter is to explore the influence of current and potential distribution on the impedance responses of a blocking electrode exhibiting a local CPE behavior. In this sense, the goal is to explore the role of coupled 2D and 3D distributions on the impedance responses of a disk electrode. This chapter presents the theoretical development and results for the impedance calculations. [39] Experimental validation provided by Vivier is also presented in this chapter. [39, 93]

9.1   Theoretical Development

The mathematical development presented in this chapter followes that presented in Chapter 8. Laplace's equation in cylindrical coordinates was expressed in rotational elliptic coordinates as equations (8–5) and (8–6) for real and imaginary parts, respectively. The modification made here was the substitution of the capacitor at electrode surface (ξ=0) by a constant phase element CPE, *i.e.*

$$i = Q\frac{\partial(V - \Phi_0)}{\partial t} = -\kappa \left.\frac{\partial\Phi}{\partial y}\right|_{y=0} = -\frac{\kappa}{r_0\eta}\left.\frac{\partial\Phi}{\partial\xi}\right|_{\xi=0} \tag{9–1}$$

where Q can be related to the interfacial capacitance C_0 by equation (7–8). The flux boundary condition at the electrode surface $\xi = 0$ was written in frequency-domain as

$$\mathrm{K}\left\{(\tilde{V}_r - \Phi_r)\cos\frac{\alpha\pi}{2} + \Phi_j\sin\frac{\alpha\pi}{2}\right\} = -\frac{1}{\eta}\left.\frac{\partial\Phi_r}{\partial\xi}\right|_{\xi=0} \tag{9–2}$$

and

$$\mathrm{K}\left\{\tilde{V}_r\sin\frac{\alpha\pi}{2} - \Phi_j\cos\frac{\alpha\pi}{2} - \Phi_r\sin\frac{\alpha\pi}{2}\right\} = -\frac{1}{\eta}\left.\frac{\partial\Phi_j}{\partial\xi}\right|_{\xi=0} \tag{9–3}$$

where $\tilde{V}_r$ represents the imposed perturbation in the electrode potential and K is the dimensionless frequency

$$\mathrm{K} = \frac{Q\omega^\alpha r_0}{\kappa} \tag{9–4}$$

As seen in equation (9–4), the dimensionless frequency K includes the CPE coefficient Q, the frequency ω raised to the power of the CPE exponent α, the disk radius r_0, and the electrolyte conductivity κ.

At $\eta = 0$ and $\eta = 1$, zero-flux conditions impose that

$$\frac{\partial \tilde{\Phi}_r}{\partial \eta} = 0 \tag{9–5}$$

and

$$\frac{\partial \tilde{\Phi}_j}{\partial \eta} = 0 \tag{9–6}$$

At the far boundary condition $\xi \to \infty$,

$$\tilde{\Phi}_r = 0 \tag{9–7}$$

and

$$\tilde{\Phi}_j = 0 \tag{9–8}$$

The equations were solved under assumption of uniform CPE parameters Q and α. The simulations were performed using the collocation package PDE2D developed by Sewell. [90] The calculations were performed for differing domain sizes and the results reported here were obtained by extrapolation to an infinite domain size. As discussed in the previous chapater, the calculated results are believed to be incorrect for frequencies K $>$ 100 due to the presence of a singular perturbation problem that arises at the periphery of the electrode at high frequencies. [42]

9.2 Results and Discussion

The calculated results for global, local, local interfacial, and both local and global Ohmic impedances are presented in this section. A list of symbols for the impedance used in the subsequent sections is provided in Table 8-1.

9.2.1 Global Impedance

The calculated dimensionless impedance response is presented in Figure 9-1 in Nyquist format with α as a parameter. The representation given in Figure 9-1 applies for

109
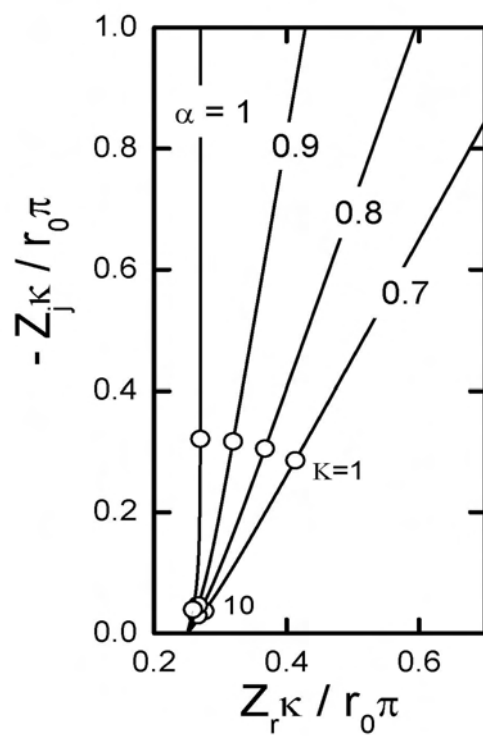
Figure 9-1. Nyquist representation for the calculated impedance response of a blocking disk electrode with a local CPE with α as a parameter.
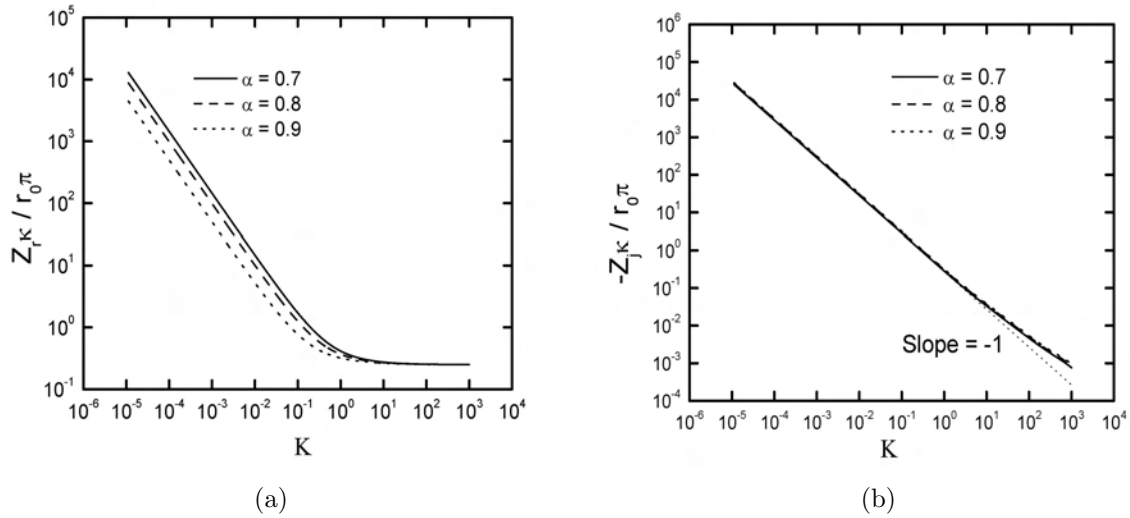
Figure 9-2. Calculated impedance response for a blocking disk electrode with a local CPE as a function of dimensionless frequency K: a) real part; and b) imaginary part.

all values of electrolyte conductivity κ and disk radius r_0, but different values are obtained for different values of α. The impedance was made dimensionless according to $Z\kappa/r_0\pi$ in which the units of impedance Z are assumed to be scaled by area and having units of Ωcm^2.

The frequency dependence of the impedance response can be seen more clearly in Figures 9-2(a) and 9-2(b), where the real and imaginary parts of the impedance, respectively, are presented as functions of dimensionless frequency K with α as a parameter. The real part of the dimensionless impedance, plotted in Figure 9-2(a), approaches the expected theoretical value of 1/4 at high frequency. [42] The low-frequency behavior depends slightly on the value of α. When plotted against dimensionless frequency K, the values of the dimensionless imaginary impedance in Figure 9-2(b) superpose for all values of α. This superposition is made possible by the inclusion of α in the definition of frequency K in equation (9–4).

Orazem et al. [78] cited the utility of logarithmic plots of imaginary impedance as a function of frequency to identify CPE behavior. The calculated slope of $\log(Z_j\kappa/r_0\pi)$ with
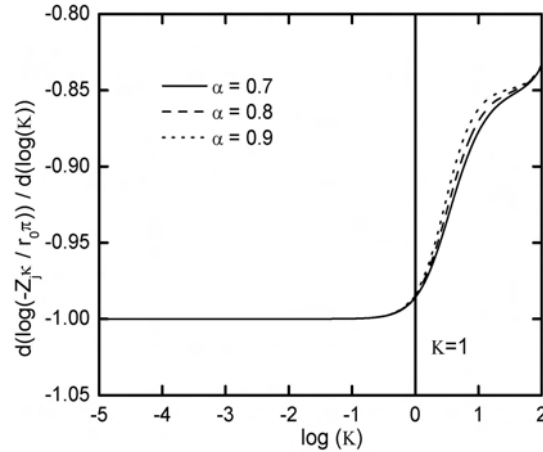
Figure 9-3. The calculated slope of $\log(Z_j\kappa/r_0\pi)$ with respect to $\log(K)$ (Figure 9-2(b)) as a function of $\log(K)$ with α as a parameter.

respect to $\log(K)$ (Figure 9-2(b)) is presented in Figure 9-3. with α as a parameter. Due to the definition of K, the slope at low frequencies of the logarithmic plots of imaginary impedance as a function of K is equal to -1. At frequencies K > 1, the slope increases to approximately -0.85. When expressed in terms of these dimensionless parameters, the low-frequency response is independent of α, but the results obtained at higher frequencies depend on α.

The calculation of effective CPE coefficient Q_{eff} provides further evidence that the low-frequency behavior is unaffected by the current and potential distribution. The effective CPE coefficient Q_{eff} for an electrochemical system can be obtained from the imaginary part of the impedance by

$$Q_{\text{eff}} = \sin\left(\frac{\alpha\pi}{2}\right)\frac{-1}{Z_j(\omega)\omega^\alpha} \qquad (9\text{--}9)$$

The effective CPE coefficient obtained from equation (9–9) scaled by the input value is presented in Figure 9-4 as a function of frequency with α as a parameter. Equation (9–9) yields the input value for the CPE coefficient at low frequencies, but this calculation is influenced by the current distributions at frequencies K > 1.

112
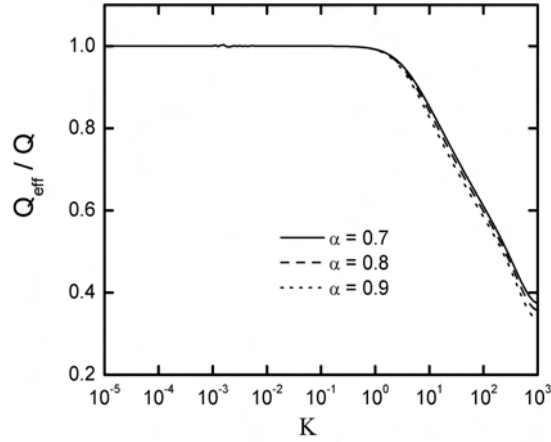
Figure 9-4. Effective scaled CPE coefficient as a function of frequency with α as a parameter.

9.2.2 Local Interfacial Impedance

The calculated local interfacial impedance at $\alpha = 0.8$ is presented in Figure 9-5 in Nyquist format with normalized position as a parameter. All of the lines are superposed indicating that the local interfacial is independent of position. The real and imaginary of the local interfacial impedance at $\alpha = 0.8$ are presented, respectively, in Figures 9-6(a) and 9-6(b) as a function of frequency with normalized radial position as a parameter. All the lines are superposed and the slopes seen in both real and imaginary impedance plots are equal to -1. This idealized character of the local interfacial impedance is seen more clearly in Figure 9-7 in which the impedance is scaled by the dimensionless frequency and given as a function of radial position with frequency as a parameter. At all frequencies, the scaled real part of the local interfacial impedance follows

$$\frac{z_{0,r}\kappa K}{r_0 \pi} = \frac{1}{\pi}\cos(\alpha\pi/2) \tag{9--10}$$

and the imaginary part of the local interfacial impedance follows

$$\frac{-z_{0,j}\kappa K}{r_0 \pi} = \frac{1}{\pi}\sin(\alpha\pi/2) \tag{9--11}$$

113
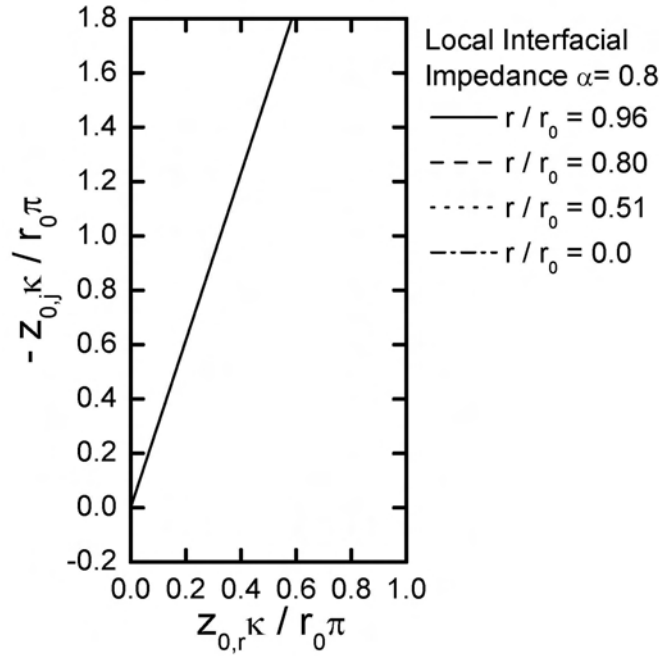
Figure 9-5. Nyquist representation for the calculated local interfacial impedance response of a blocking disk electrode with a local CPE with normalized radial position as a parameter.

(a)   (b)
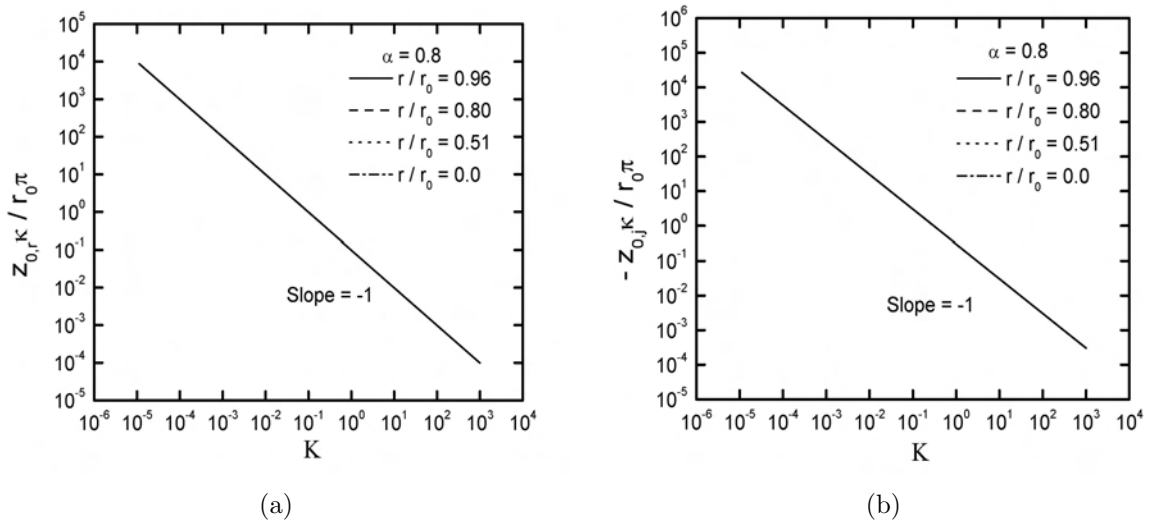
Figure 9-6. Calculated local interfacial impedance as a function of frequency with position as a parameter: a) imaginary part; and b) real part.

114
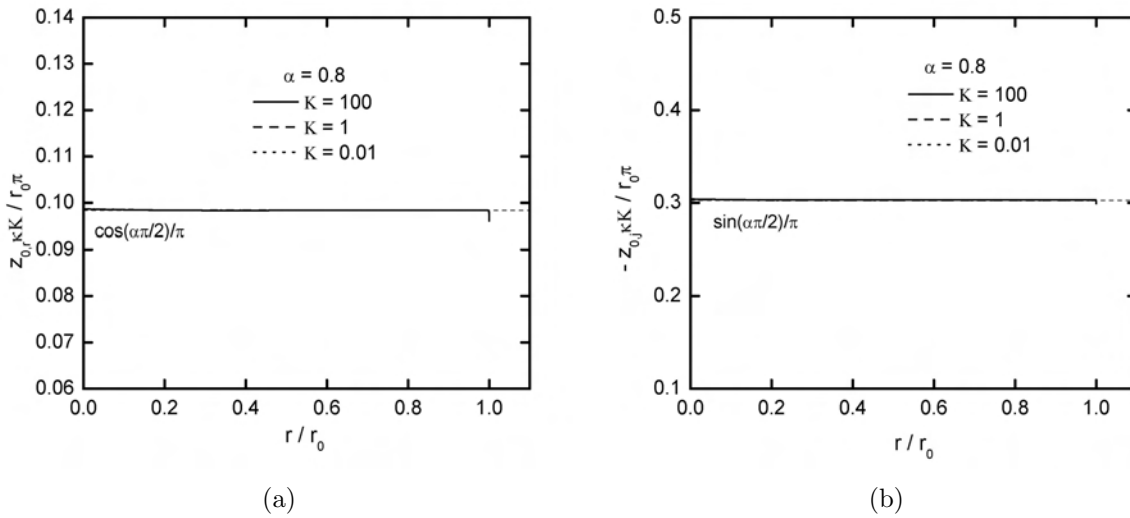
Figure 9-7. Calculated local interfacial impedance as a function of position with frequency as a parameter: a) imaginary part; and b) real part.

The results presented in Figures 9-6 and 9-7 show that the calculated local interfacial impedance is independent of 2-D distributions.

9.2.3 Local Impedance

The calculated local impedance response for $\alpha = 0.8$ is presented in Figure 9-8 with normalized radial position as a parameter. The dimensionless impedance is scaled to the disk area πr_0^2 to show the comparison with the high-frequency asymptotic value in Figure 9-1. The impedance is largest at the center of the disk and smallest at the periphery, reflecting the greater accessibility of the periphery of the disk electrode. Inductive loops, which are not shown in the global impedance, are seen at high frequencies in local impedance for all the radial positions.

The real and imaginary parts of the local impedance are presented in Figures 9-9(a) and 9-9(b), respectively, with radial position as a parameter. The real and imaginary parts of the local impedance presented in Figure 9-9 show a pure CPE behavior at low frequencies and a geometry-induced dispersion at high frequencies. The imaginary part presented in Figure 9-9(b) shows the change of sign associated with the inductive features
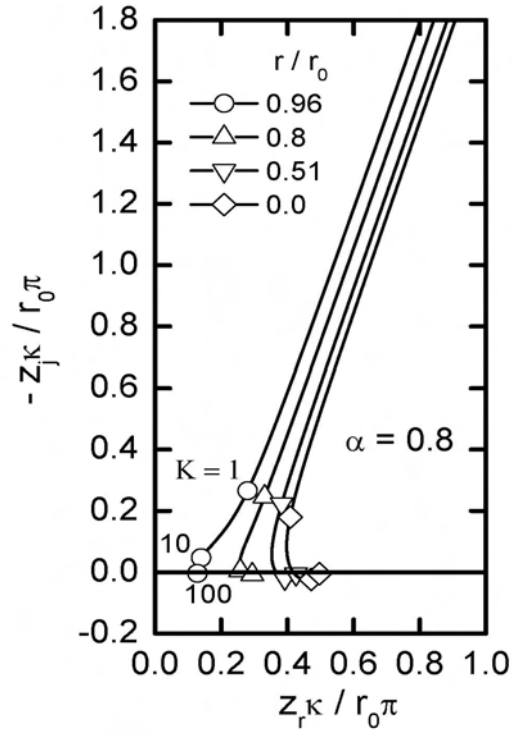
Figure 9-8. The local impedance in Nyquist format with radial position as a parameter.
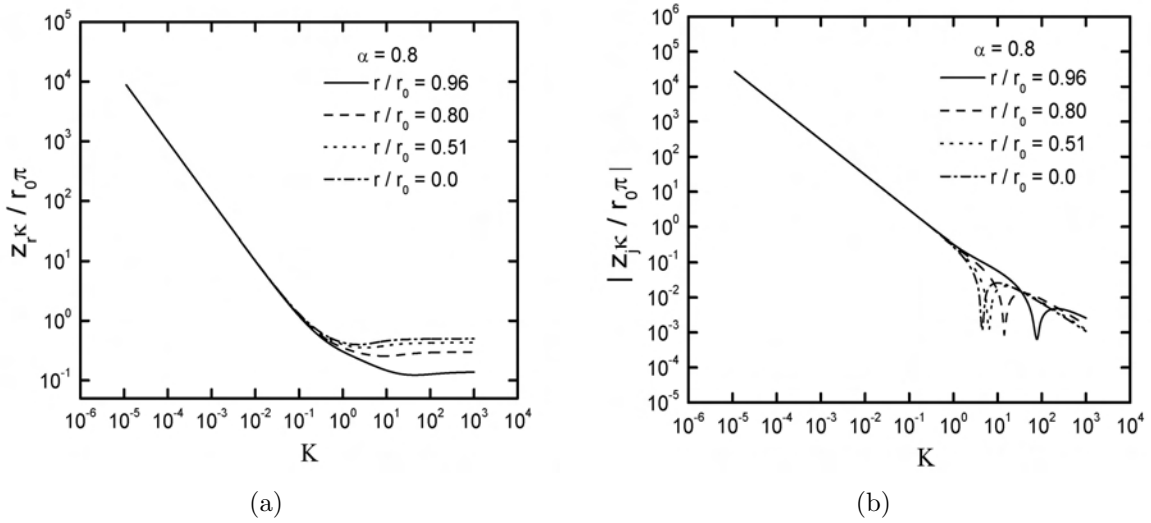
Figure 9-9. Calculated local impedance: a) real part; and b) imaginary part.

116
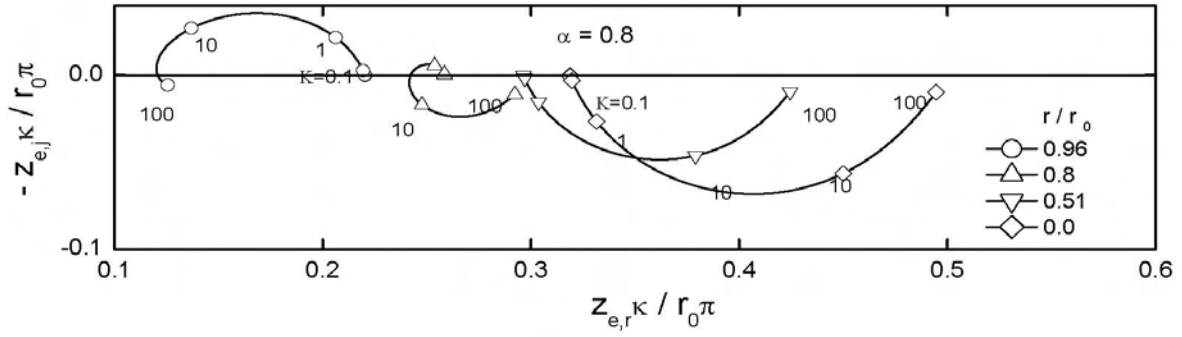
Figure 9-10. The local Ohmic impedance in Nyquist format with radial position as a parameter.

seen in Figure 9-8. The changes in sign occur at frequencies well below $K = 100$, showing that the inductive loop cannot be ascribed to calculation artifacts.

9.2.4 Local Ohmic Impedance

The local Ohmic impedance z_e accounts for the difference between the local interfacial and the local impedances. The calculated Ohmic impedance for $\alpha = 0.8$ is presented in Figure 9-10 in Nyquist format with radial position as a parameter. The results obtained here for the local Ohmic impedance are very similar to those reported for the ideally polarized electrode. At the periphery of the electrode, two time constants (inductive and capacitive loops) are seen; whereas, at the electrode center only an inductive loop is evident. These loops are distributed around the asymptotic real value of 1/4.

9.2.5 Global Interfacial and Global Ohmic Impedance

The local interfacial impedance has shown to be associated with an ideal CPE behavior and to be independent of radial position. Thus, the global interfacial impedance is given by

$$Z_0 = \frac{1}{(j\omega)^\alpha Q} \tag{9-12}$$

The global Ohmic impedance Z_e is obtained from the global impedance Z by the expression

$$Z_e = Z - Z_0$$

117
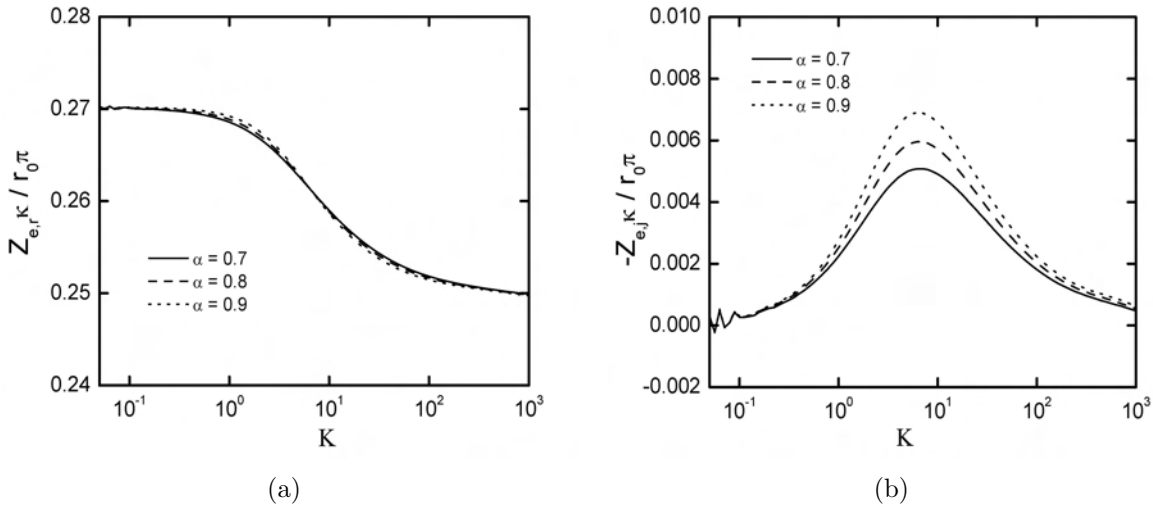
Figure 9-11. Calculated values for global Ohmic impedance as a function of frequency with α as a parameter: a) real part; and b) imaginary part.

or, in the dimensionless terms used here,

$$\frac{Z_e \kappa}{r_0 \pi} = \frac{Z \kappa}{r_0 \pi} - \frac{1}{j^\alpha \pi \mathrm{K}} \tag{9–13}$$

The real part of Z_e is given in Figure 9-11(a), and the imaginary part of Z_e is given in Figure 9-11(b) as functions of dimensionless frequency K with α as a parameter. In the low frequency range $Z_e \kappa / r_0 \pi$ is a pure resistance equal to 0.27, and, in the high frequency range, $Z_e \kappa / r_0 \pi$ tends towards 1/4. The imaginary part of the global Ohmic impedance shows a non-zero value in the frequency range that is influenced by the current and potential distributions. Figure 9-11 shows that all the effect of the current and potential distribution appears in the global Ohmic impedance.

9.3 Experiments

The predictions made by the calculations can be compared to experimental observations. Vivier [39] conducted impedance measurements on a glassy carbon disk electrode to compare with the calculation results. Local impedance measurements were as well performed on a stainless steel disk to demonstrate that the inductive features predicted by the simulations are apparent in experiments.
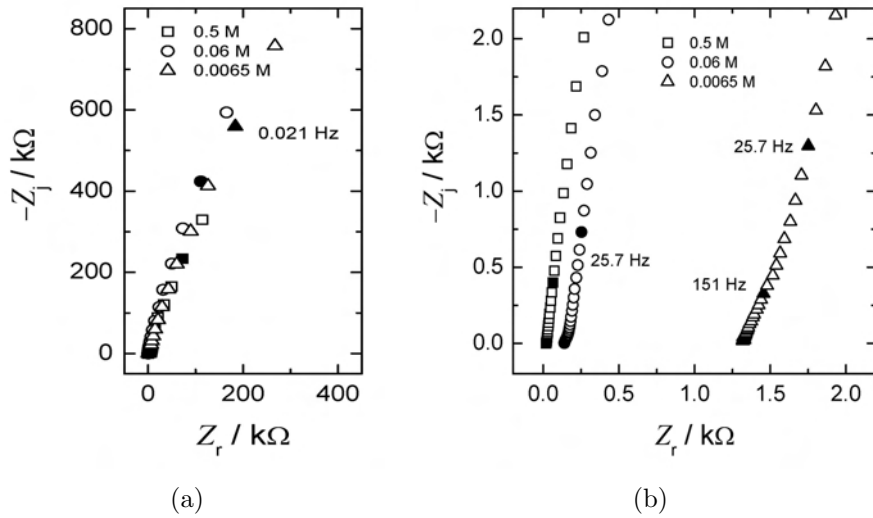
Figure 9-12. Complex-impedance-plane plots for the response of a glassy carbon disk in KCl electrolytes with concentration as a parameter. a) for frequency values between 100 kHz and 10 mHz; and b) zoomed region showing only high-frequency data.

9.3.1 Global Impedance of Glassy-Carbon Electrode

The global impedance measurements were made at three different concentrations of KCl. The results obtained in 0.5 M, 0.06 M and 0.0065 M KCl are presented in Figure 9-12 with concentration as a parameter. The differences among the results are most apparent at high frequencies, as shown in Figure 9-12(b). The results are consistent with a blocking, but not ideally polarized, electrode. The agreement also suggests that there is a local capacity dispersion on the glassy carbon disk electrode. A high-frequency feature is evident in Figure 9-12(b), and this feature appears at lower frequencies for the smaller concentration.

The dimensionless imaginary part of the impedance is presented in Figure 9-13(a) as a function of dimensionless frequency. The superposition of data for the three values of conductivity is in excellent agreement with the calculations (see Figure 9-2(b)), and the change in slope from a value of -1 appears at frequencies higher than $K = 1$.

The derivative of the logarithm of the dimensionless imaginary impedance with respect to the logarithm of dimensionless frequency is presented in Figure 9-13(b). The
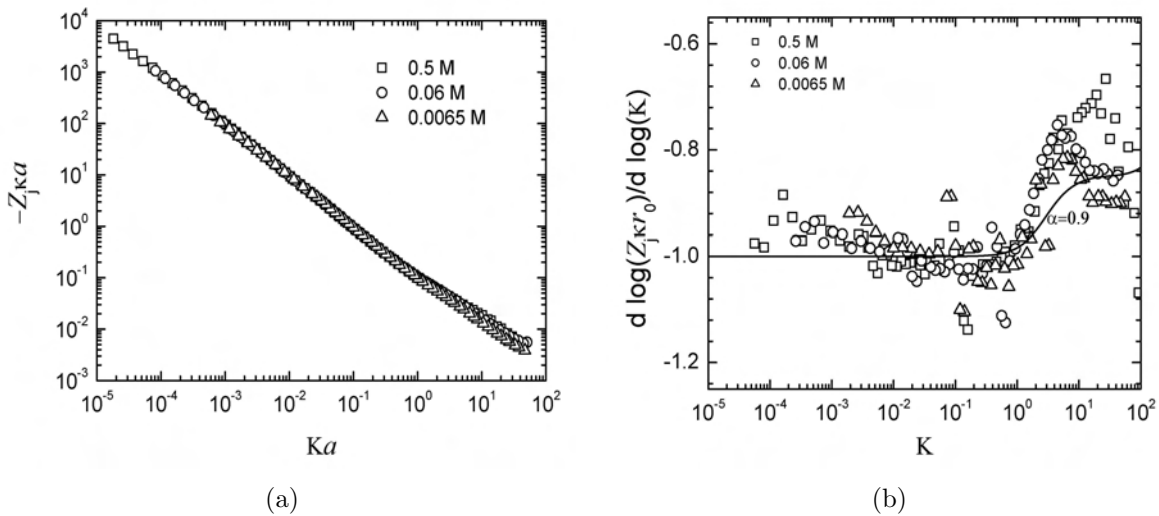
Figure 9-13. Dimensionless analysis for the impedance response of a graphite disk in KCl electrolytes with concentration as a parameter. a) Dimensionless imaginary part of the impedance as a function of dimensionless frequency (corresponding to Figure 9-2(b)); and b) Derivative of the logarithm of the dimensionless imaginary part of the impedance with respect to the logarithm of dimensionless frequency (corresponding to Figure 9-3).

dispersion of the data apparent in Figure 9-13(b) can be attributed to the fact that the derivative calculations were performed on experimental data. The superposition of data for the three values of conductivity is in excellent agreement with Figure 9-3 with $\alpha = 0.9$, and the transitional frequency between low and high-frequency response is in good agreement with the theoretical value of K = 1.

9.3.2 Local Impedance of Stainless Steel Electrode

The local impedance measurements were performed on a Fe-17Cr stainless steel disk electrode in 0.05 M KCl + 0.005 M Na_2SO_4 electrolyte. The local impedance and local interfacial obtained at the center of the disk ($r/r_0 = 0$) are presented in Figure 9-14. [93] As predicted from the calculations, the local impedance exhibits inductive loops at high frequency; whereas, the local interfacial impedance shows expected behavior for a local CPE within all frequency range. The characteristic transition frequency at which the geometry plays a role locates approximately at K=0.52, which is consistent with the theoretical prediction K=1. The local interfacial impedance exhibits an ideal local CPE
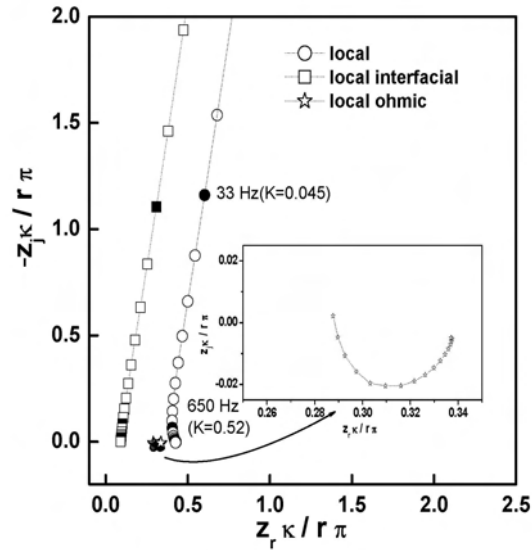
Figure 9-14. Experimental local impedance, local interfacial impedance, and local Ohmic impedance in Nyquist format of a stainless steel disk electrode at the center of the electrode ($r/r_0 = 0$). [93]

behavior, which agrees with the perdition from Figure 9-5. The local Ohmic impedance, the difference between the local and local interfacial impedance, is given in the rectangle box in the figure. The shape of the local impedance at $r/r_0=0$ is consistent with that seen in Figure 9-10.

The local impedance shows CPE behavior at low frequencies and a change in sign in the imaginary part of the impedance at high frequencies. This appearance of high-frequency inductive loops is consistent with the calculated local impedance presented in Figure 9-9(b). The agreement between the model presented here and the experimental results obtained from the steel electrode illustrates the utility of the model for describing features of systems that exhibit CPE behavior over a range of frequency.

CHAPTER 10
DISK ELECTRODE WITH SINGLE FARADAIC REACTION

The results presented in chapters 8 and 9 illustrate that the current and potential distributions associated with disk electrodes induce an apparent CPE behavior on the impedance of blocking electrodes. This chapter explores the influence of current distribution on impedance response of a disk electrode subject to a single Faradaic reaction. [31]

10.1 Theoretical Development

The mathematical development presented in this chapter followed those presented in Chapters 8 and 9. Lapace's equation written in the rotational elliptic coordinates (equations (8–5) and (8–6)) remained as the governing equations. The key difference between the present work and those described in the previous chapters was the boundary condition applied at the electrode surface.

The problem was solved for two kinetic regimes. Under linear kinetics, following Newman [42] and Nisancioglu [43, 44], the current density at the electrode surface was expressed as

$$i = C_0 \frac{\partial (V - \Phi_0)}{\partial t} + \frac{(\alpha_a + \alpha_c) i_0 F}{RT} \left(\bar{V} - \bar{\Phi}_0 \right) = -\kappa \left. \frac{\partial \Phi}{\partial y} \right|_{y=0} = -\frac{\kappa}{r_0 \eta} \left. \frac{\partial \Phi}{\partial \xi} \right|_{\xi=0} \qquad (10\text{–}1)$$

The assumption of linear kinetics applies for $\bar{\imath} << i_0$. Under assumption of Tafel kinetics, the current density at the electrode surface was expressed as

$$i = C_0 \frac{\partial (V - \Phi_0)}{\partial t} - i_0 \exp{-\left(\frac{\alpha_c F}{RT} \left(\bar{V} - \bar{\Phi}_0 \right) \right)} = -\kappa \left. \frac{\partial \Phi}{\partial y} \right|_{y=0} = -\frac{\kappa}{r_0 \eta} \left. \frac{\partial \Phi}{\partial \xi} \right|_{\xi=0} \qquad (10\text{–}2)$$

where the current in the Tafel regime was assumed to be cathodic. A similar expression can be developed under assumption of anodic currents. The results presented here are general because the impedance results do not depend on whether the current is anodic or cathodic.

The flux boundary conditions (10–1) or (10–2) apply at the electrode surface ($\xi = 0$). The boundary conditions (10–1) or (10–2) were written in frequency domain as

$$\mathrm{K}\tilde{\Phi}_j + J\left(\tilde{V}_r - \tilde{\Phi}_{0,r}\right) = -\frac{1}{\eta}\left.\frac{\partial\tilde{\Phi}_r}{\partial\xi}\right|_{\xi=0} \tag{10–3}$$

and

$$\mathrm{K}\left(\tilde{V}_r - \tilde{\Phi}_{0,r}\right) + J\tilde{\Phi}_{0,j} = -\frac{1}{\eta}\left.\frac{\partial\tilde{\Phi}_j}{\partial\xi}\right|_{\xi=0} \tag{10–4}$$

for real and imaginary components, respectively. Here $\tilde{V}_r$ represents the imposed perturbation in the electrode potential referenced to an electrode at infinity and K is the dimensionless frequency, defined as

$$\mathrm{K} = \frac{\omega C_0 r_0}{\kappa} \tag{10–5}$$

Under the assumption of linear kinetics, valid for $\bar{\imath} << i_0$, the parameter J was defined to be

$$J = \frac{(\alpha_a + \alpha_c)\,F i_0 r_0}{RT\kappa} \tag{10–6}$$

For Tafel kinetics, valid for $\bar{\imath} >> i_0$, the parameter J was defined to be a function of radial position on the electrode surface as

$$J(\eta) = \frac{\alpha_c F \bar{\imath}(\eta) r_0}{RT\kappa} \tag{10–7}$$

where $\bar{\imath}(\eta)$ was obtained from the steady-state solution as

$$\bar{\imath} = i_0 \exp\left(\frac{\alpha_c F}{RT}\left(\bar{V} - \bar{\Phi}_0\right)\right) \tag{10–8}$$

The local charge-transfer resistance for linear kinetics can be expressed in terms of parameters used in equation (10–6) as

$$R_t = \frac{RT}{i_0 F(\alpha_a + \alpha_c)} \tag{10–9}$$

123

The local charge-transfer resistance for Tafel kinetics can be expressed in terms of parameters used in equation (10–7) as

$$R_t = \frac{RT}{\bar{i}(\eta) F \alpha_c} \qquad (10\text{–}10)$$

For linear kinetics, R_t was independent of radial position, but, under Tafel kinetics, as shown in equation (10–10), R_t depended on radial position. From a mathematical perspective, the principle difference between the linear and Tafel cases was that J and R_t were held constant for the linear polarization; whereas, for the Tafel kinetics, J and R_t were functions of radial position determined by solution of the nonlinear steady-state problem.

The relationship between the parameter J and the charge-transfer and Ohmic resistances can be established using the high-frequency limit for the Ohmic resistance to a disk electrode obtained by Newman, [94] *i.e.*

$$R_e = \frac{\pi r_0}{4\kappa} \qquad (10\text{–}11)$$

where R_e has units of Ωcm^2. The parameter J can therefore be expressed in terms of the Ohmic resistance R_e and charge transfer resistance R_t as

$$J = \frac{4}{\pi} \frac{R_e}{R_t} \qquad (10\text{–}12)$$

Large values of J are seen when the Ohmic resistance is much larger than the charge-transfer resistance, and small values of J are seen when the charge-transfer resistance dominates.

The equations were solved under assumption of a uniform capacitance C_0 using the collocation package PDE2D developed by Sewell. [90] Calculations were performed for differing domain sizes, and the results reported here were obtained by extrapolation to an infinite domain size.
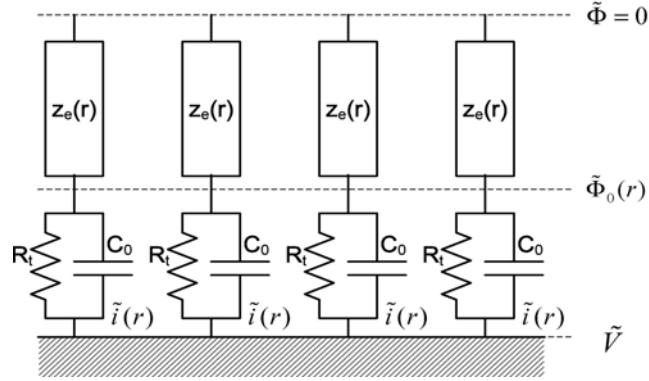
Figure 10-1. Schematic representation of an impedance distribution for a disk electrode where z_e represents the local Ohmic impedance, C_0 represents the interfacial capacitance, and R_t represents the charge-transfer resistance.

10.2   Results and Discussion

The nature of the metal-electrolyte interface of an electrode exhibiting a Faradaic reaction can be understood in the schematic representation given as Figure 10-1.   Under linear kinetics, both C_0 and R_t were independent of radial position; whereas, for Tafel kinetics, $1/R_t$ varied with radial position in accordance with the current distribution presented in Figure 7-6.

The calculated results for global, local, local interfacial, and local Ohmic impedances are presented in this section. A list of symbols for local and global impedances used is provided in Table 8-1.

10.2.1   Global Impedance

The calculated global impedance response is presented in Figure 10-2(a) for $J = 0.1$ and in Figure 10-2(b) for $J = 1.0$ with dimensionless frequency K as a parameter. The real and imaginary components are presented in dimensionless form to eliminate the influence of electrolyte conductivity κ and disk radius r_0. The impedance results for linear kinetics at $J = 0.1$ match closely with the impedance response

$$\frac{Z\kappa}{\pi r_0} = \frac{1}{4} + \frac{1}{\pi}\frac{1/J}{1 + j\mathrm{K}/J} \tag{10–13}$$
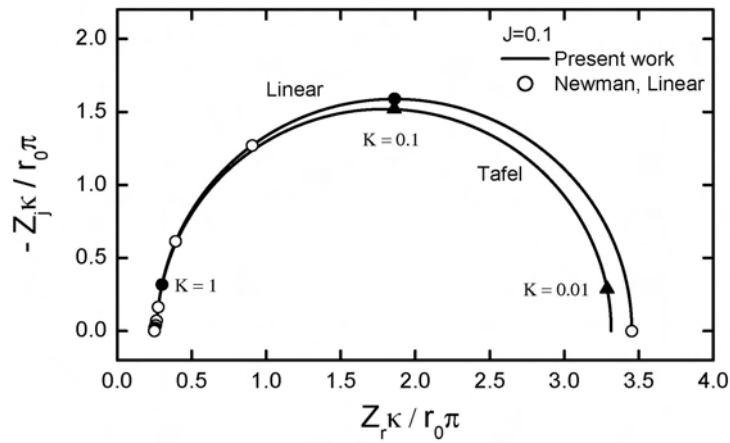
(a)
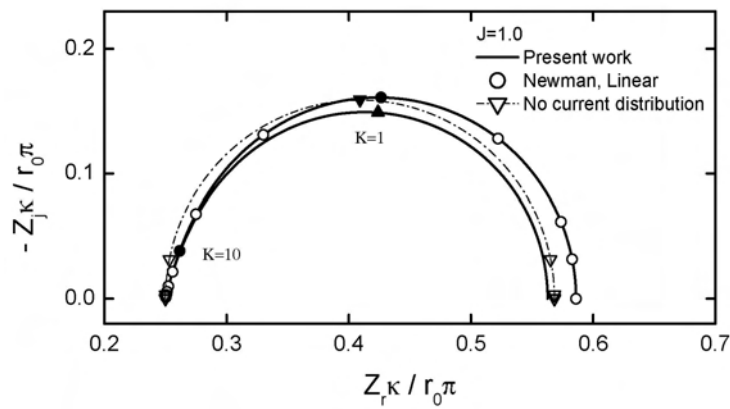
(b)

Figure 10-2. Calculated Nyquist representation of the impedance response for a disk electrode under assumptions of Tafel and linear kinetics. Open symbols represent the result calculated by Newman. [42] a) $J = 0.1$; and b) $J = 1.0$.
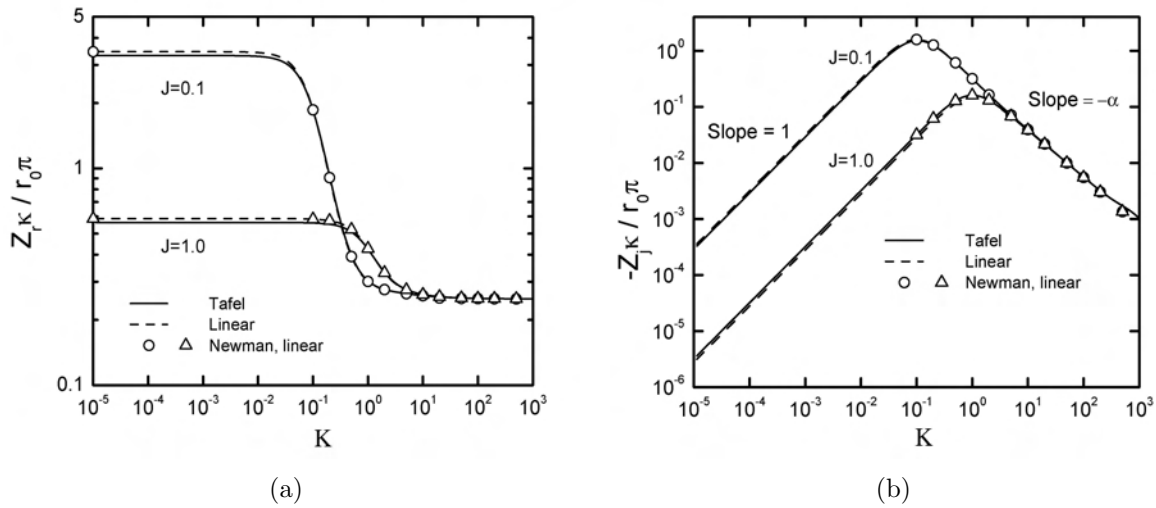
Figure 10-3. Calculated representation of the impedance response for a disk electrode under assumptions of Tafel and linear kinetics and with with J as a parameter. Open symbols represent the result calculated by Newman. [42] a) real part; and b) imaginary part.

derived in the absence of current distribution effects. The impedance response for Tafel kinetics differs because the charge-transfer resistance is a function of radial position. The comparison between the impedance for linear kinetics and equation (10–13) for $J = 1$ shows the distortion of the high-frequency impedance response associated with the influence of current and potential distributions.

The calculated results for linear kinetics in Figure 10-2 show good agreement to the corresponding numerical values obtained by Newman. [42] The comparison with Newman's calculations is seen more clearly in the representation of the real and imaginary parts of the impedance response shown in Figures 10-3(a) and 10-3(b), respectively. At low frequencies, values for the real part of the impedance differ for impedance calculated under the assumptions of linear and Tafel kinetics; whereas, the values of the imaginary impedance calculated under the assumptions of linear and Tafel kinetics are superposed for all frequencies. The slope of the lines presented in Figure 10-3(b) are equal to 1 at low frequencies but differ from −1 at high frequencies. As stated by Orazem et al. [78], the slope of these lines can be related to the exponent α used in models for CPE behavior.
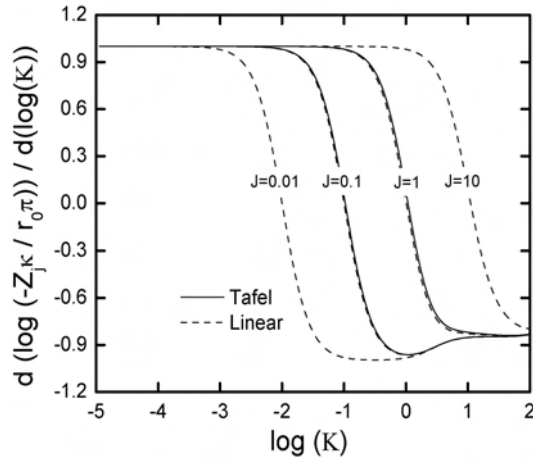
Figure 10-4. The calculated derivative of $\log(Z_j\kappa/r_0\pi)$ with respect to $\log(K)$ (taken from Figure 10-3(b)) as a function of K with J as a parameter.

The calculated derivative of $\log(Z_j\kappa/r_0\pi)$ with respect to $\log(K)$ is presented in Figure 10-4 as a function of K with J as a parameter. At large frequencies, the quantity $d\log(Z_j\kappa/r_0\pi)/d\log(K)$ can be considered to be equal to $-\alpha$ where α is the exponent used for models of CPE behavior. The characteristic frequency at which the value of slope deviates from unity increases with the dimensionless parameter J. The transition frequencies correspond to the inverse of the R_tC_0 time constant and overlap when given as a function of

$$\frac{K}{J} = \frac{\omega C_0 RT}{\bar{\imath}\alpha_c F} = \omega R_t C_0 \tag{10–14}$$

The functional dependence of $d\log(Z_j\kappa/r_0\pi)/d\log(K)$ was independent of assumption of either linear or Tafel kinetics.

When $d\log(Z_j\kappa/r_0\pi)/d\log(K)$ was plotted as a function of $\log(K/J)$, given in Figure 10-5, all the curves for K < 1 are superimposed. The characteristic frequency K/J=1 is associated with the R_tC_0 time constant for the Faradaic reaction and the characteristic frequency for the effect of the current and potential distributions at K=1 is associated with the capacitance and the Ohmic resistance.

128
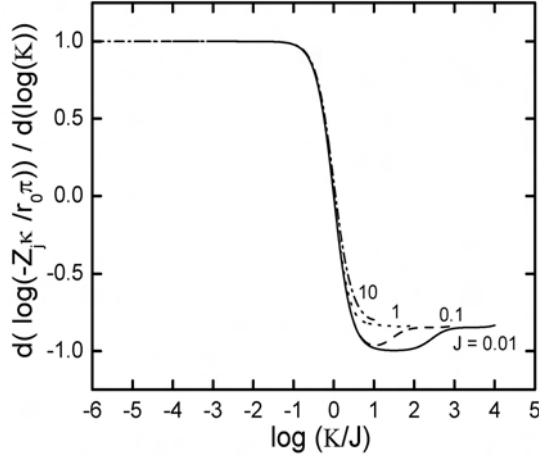
Figure 10-5. The calculated derivative of $\log(Z_j\kappa/r_0\pi)$ with respect to $\log(\mathrm{K}/J)$ (taken from Figure 10-3(b)) as a function of K with J as a parameter.

10.2.2 Local Interfacial Impedance

The calculated local interfacial impedance for Tafel kinetics with $J = 1$ is presented in Figure 10-6 as a function of frequency with normalized radial position as a parameter. At low frequencies, the local interfacial impedance, for both real and imaginary, is smallest at the periphery and largest at the center of the disk. The variation at low frequencies is less distinguishable for smaller values of J. All the curves in Figures 10-6(a) and 10-6(b) are superposed at frequencies K > 1.

For the linear kinetics calculation, where J is independent of radial position, the scaled real part of the local interfacial impedance follows

$$\frac{z_{0,r}\kappa}{r_0\pi} = \frac{J}{\pi(J^2 + \mathrm{K}^2)} \tag{10–15}$$

and the imaginary part of the local interfacial impedance follows

$$\frac{z_{0,j}\kappa}{r_0\pi} = \frac{-\mathrm{K}}{\pi(J^2 + \mathrm{K}^2)} \tag{10–16}$$

Plots similar to Figure 10-7 were obtained for the local interfacial impedance calculated under assumption of linear kinetics, but for linear kinetics the local interfacial impedance was independent of radial position.

129
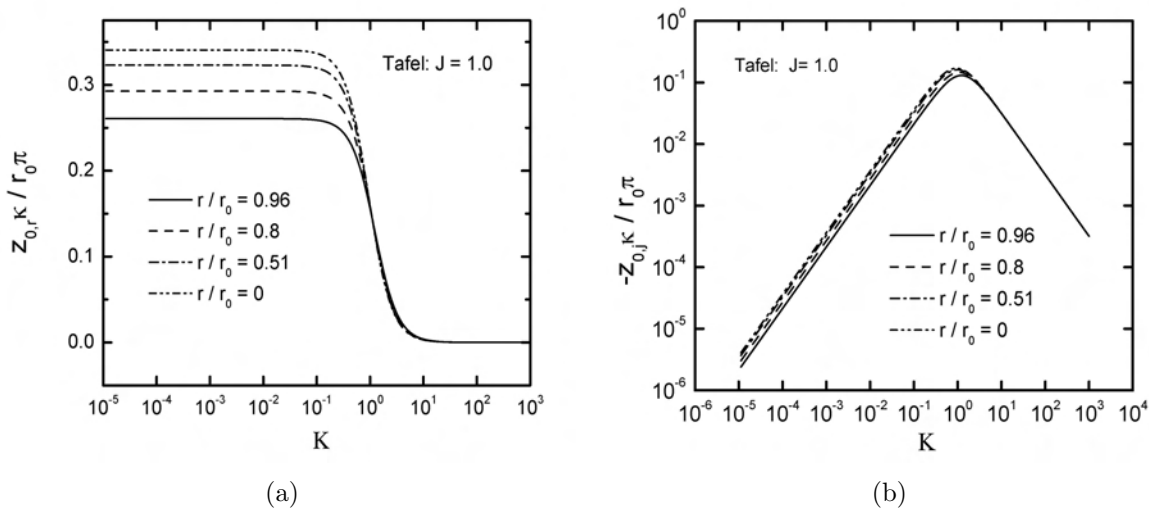
Figure 10-6. Calculated representation of the local interfacial impedance response for a disk electrode as a function of dimensionless frequency K under assumptions of Tafel kinetics with $J = 1.0$: a) real part; and b) imaginary part.

The local interfacial impedance for Tafel kinetics with $J = 1$ is presented in Figure 10-7 as a function of normalized radial position with dimensionless frequency as a parameter. Under the Tafel kinetics assumption that J is a function of radial position, as shown in Figure 10-7, the real and imaginary parts of the local interfacial impedance change around the values given in equations (10–15) and (10–16) and have minimum values at the periphery of the disk. The dependence of both real and imaginary of the local interfacial impedance is more evident at low frequency than high frequency.

10.2.3 Local Impedance

The calculated local impedance for Tafel and linear kinetics with $J = 1$ is presented in Figure 10-8 in Nyquist format with radial position as a parameter. In both cases, the impedance is largest at the center of the disk and smallest at the periphery, reflecting the greater accessibility of the periphery of the disk electrode. Similar results are also obtained for $J = 0.1$, but the differences between radial positions are much less significant. Inductive loops are observed at high frequencies and these are seen in both Tafel and linear calculations for $J = 0.1$ and $J = 1.0$.

130
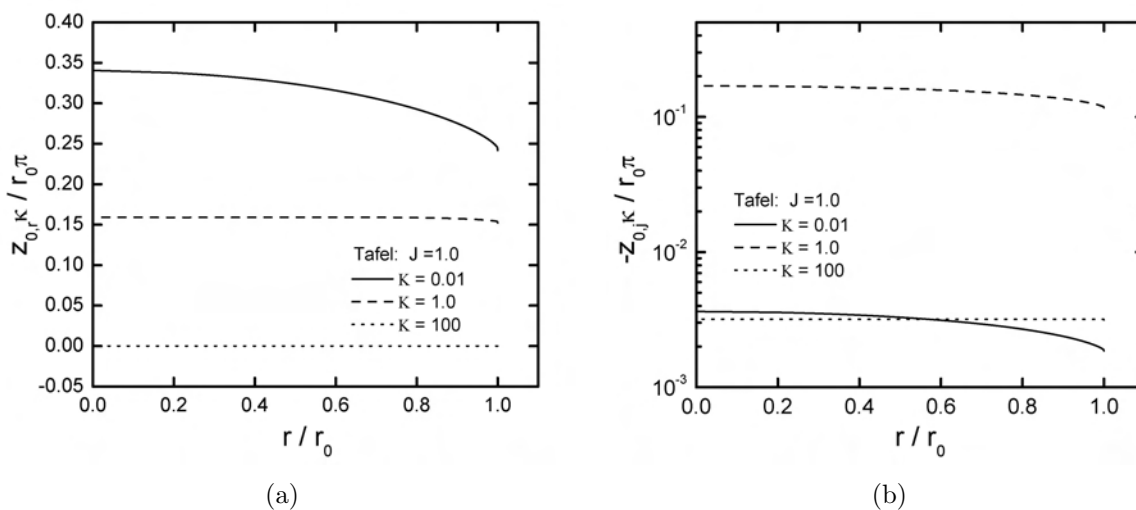
Figure 10-7. Calculated representation of the local interfacial impedance response for a disk electrode as a function of radial position under assumptions of Tafel kinetics with $J = 1.0$: a) real part; and b) imaginary part.

The real and imaginary parts of the local impedance for Tafel kinetics with $J = 1.0$ are presented in Figures 10-9(a) and 10-9(b), respectively. The real part of the local impedance presented in Figure 10-9(a) reaches asymptotic values at K $\rightarrow$ 0 and K $\rightarrow$ 100. The absolute value of the imaginary part presented in Figure 10-9(b) shows the change of sign associated with the inductive features seen in Figure 10-8(a). The changes in sign occur at frequencies below K=100, indicating that the inductive loop cannot be attributed to calculation artifacts.

10.2.4 Local Ohmic Impedance

The local Ohmic impedance z_e accounts for the difference between the local interfacial and the local impedances. The calculated Ohmic impedance for Tafel kinetics with $J = 1.0$ are presented in Figure 10-10 in Nyquist format with normalized radial position as a parameter. The results obtained here for the local Ohmic impedance are very similar to those reported for the ideally polarized electrode and for the blocking electrode with local CPE behavior. At the periphery of the electrode, two time constants (inductive
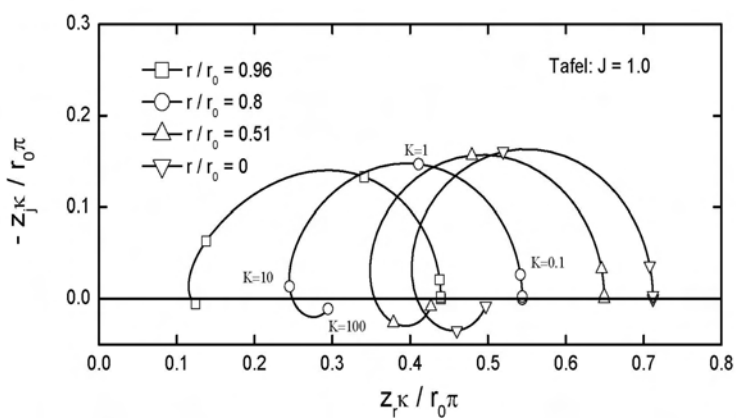
(a)
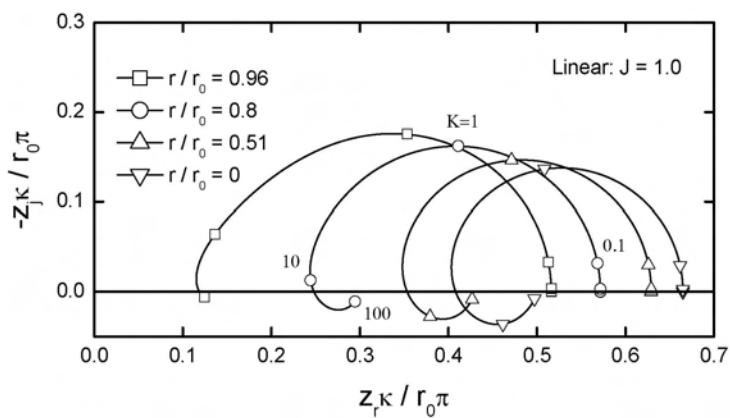
(b)

Figure 10-8. Calculated representation of the local impedance response for a disk electrode as a function of dimensionless frequency K under assumptions of Tafel kinetics with $J = 1.0$. a) Tafel kinetics; and b) linear kinetics.
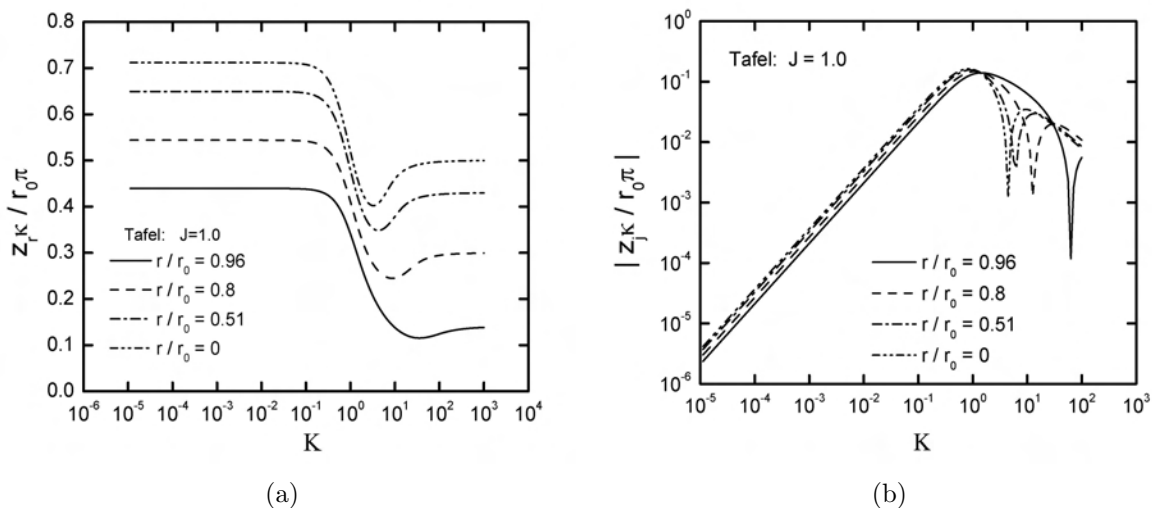
Figure 10-9. Calculated representation of the local impedance response for a disk electrode as a function of dimensionless frequency K with $J = 1.0$. a) real part; and b) imaginary part.
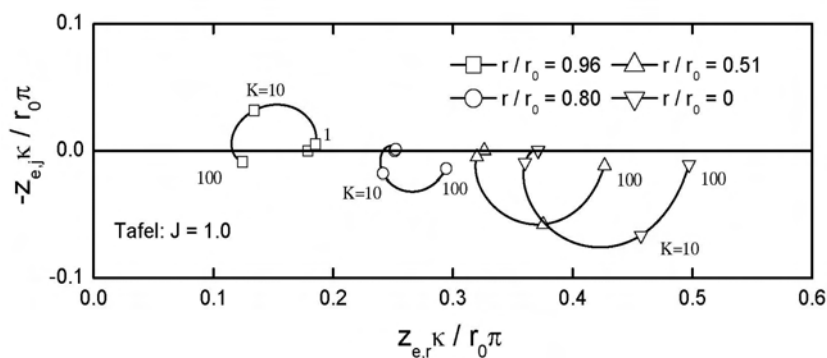
Figure 10-10. Calculated representation of the local Ohmic impedance response for a disk electrode as a function of dimensionless frequency K under assumptions of Tafel kinetics with $J = 1.0$
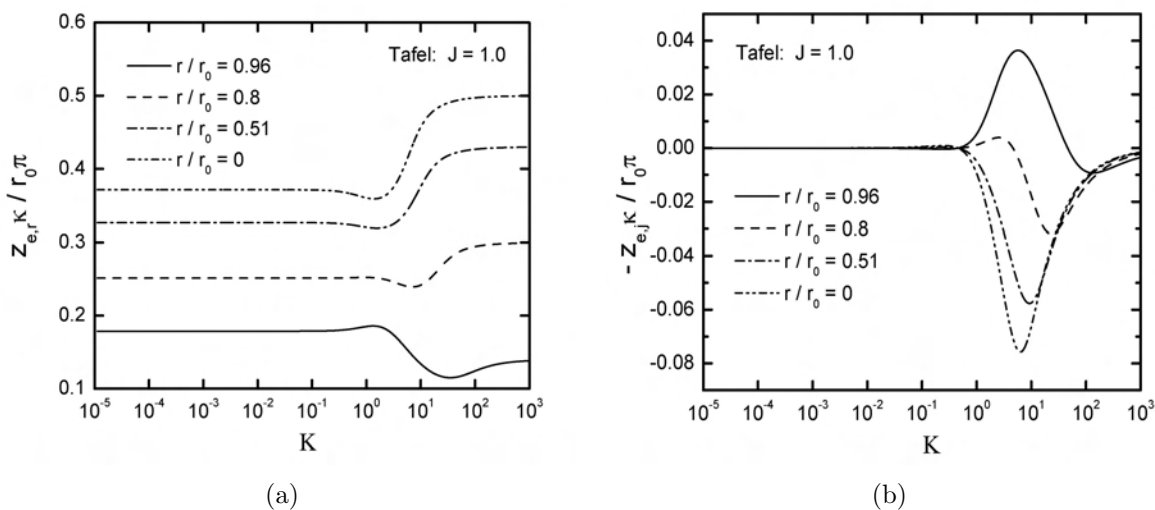
Figure 10-11. Calculated representation of the local Ohmic impedance response for a disk electrode as a function of dimensionless frequency K under assumptions of Tafel kinetics with $J = 1.0$. a) real part; and b) imaginary part.

and capacitive loops) are seen; whereas, at the electrode center only an inductive loop is evident. These loops are distributed around the asymptotic real value of $1/4$.

The calculated values for real and imaginary parts of the local Ohmic impedance are presented in Figures 10-11(a) and 10-11(b), respectively, as a function of frequency with radial position as a parameter. The local Ohmic impedance has only real values at K $\rightarrow 0$ and K $\rightarrow \infty$, but in the frequency range $10^{-2} <$ K < 100, z_e has both real and imaginary components. This range of dimensionless frequency was not dependent on the value of J. The local Ohmic impedance obtained for linear kinetics and for different J were similar to the results reported here.

The representation of an Ohmic impedance as a complex number represents a departure from standard practice. As shown in previous sections, the local impedance has inductive features that are not seen in the local interfacial impedance. These inductive features are implicit in the local Ohmic impedance. As similar results were obtained for ideally polarized and blocking electrodes with local CPE behavior, the result cannot be
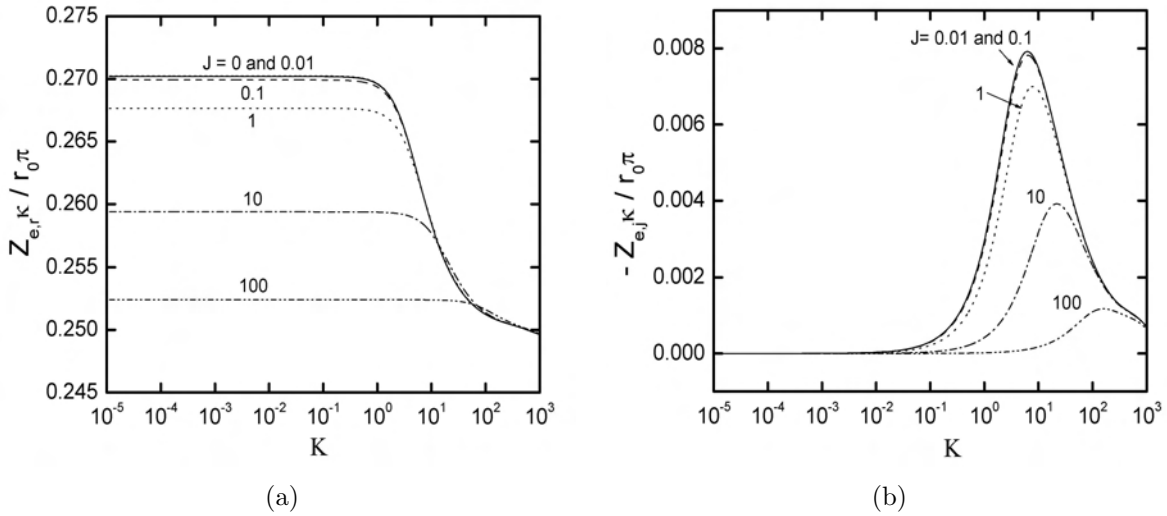
Figure 10-12. Calculated global Ohmic impedance response for a disk electrode as a function of dimensionless frequency for linear kinetics with J as a parameter. a) real part; and b) imaginary part.

attributed to Faradaic reactions and can be attributed only to the Ohmic contribution of the electrolyte.

10.2.5 Global Interfacial and Global Ohmic Impedance

The global interfacial impedance for linear kinetics is independent of radial position and is given by

$$Z_0 = \frac{R_t}{1 + j\omega C_0 R_t} \qquad (10\text{–}17)$$

The global Ohmic impedance Z_e is obtained from the global impedance Z by the expression

$$Z_e = Z - Z_0 \qquad (10\text{–}18)$$

The real part and imaginary parts of Z_e, obtained for linear kinetics are given in Figures 10-12(a) and 10-12(b), respectively, as functions of dimensionless frequency K with J as a parameter. In the low frequency range $Z_e \kappa / r_0 \pi$ is a pure resistance with numerical values that decreases with increasing J. All curves superimpose in the high frequency range toward asymptotic value of 1/4. The imaginary part of the global Ohmic impedance shows

a nonzero value in the frequency range that is influenced by the current and potential distributions.

At high and low frequency limits, the global Ohmic impedance defined in the present work is consistent with the accepted understanding of the Ohmic resistance to current flow to a disk electrode. The global Ohmic impedance approaches, at high frequencies, the primary resistance for a disk electrode (equation(10–11)) described by Newman. [94] This result was obtained as well for ideally polarized (Chapter 8) and blocking electrodes with local CPE behavior (Chapter 9). The complex nature of both global and local Ohmic impedances is seen at intermediate frequencies. This complex value is the origin of the inductive features seen in the local impedance and the origin of the CPE-like behavior found in the global impedance.

10.3   Interpretation of Impedance Results

Nisancioglu [43] estimated the error caused by frequency dispersion in evaluating physical properties such as charge transfer resistance and capacitance. A parallel analysis is presented here in terms of the commonly used CPE models.

10.3.1   Determination of Charge Transfer Resistance

The impedance response of a disk electrode in the absence of current distribution effects can be expressed by equation (10–13). The corresponding charge-transfer resistance evident at low frequencies is given by

$$\frac{R_t \kappa}{\pi r_0} = \frac{1}{\pi J} \tag{10–19}$$

The effective global charge-transfer resistance can be estimated from the calculated impedance according to

$$\frac{R_{\text{eff}} \kappa}{\pi r_0} = \left. \frac{Z_r \kappa}{\pi J} \right|_{\text{K}=0} - \frac{1}{4} \tag{10–20}$$

The value of R_{eff}/R_t is presented in Figure 10-13 as a function of J under the assumption of linear kinetics.   The results are full agreement with those presented in different format by Nisancioglu [43]. The influence of the frequency dispersion is greatest when J is large,
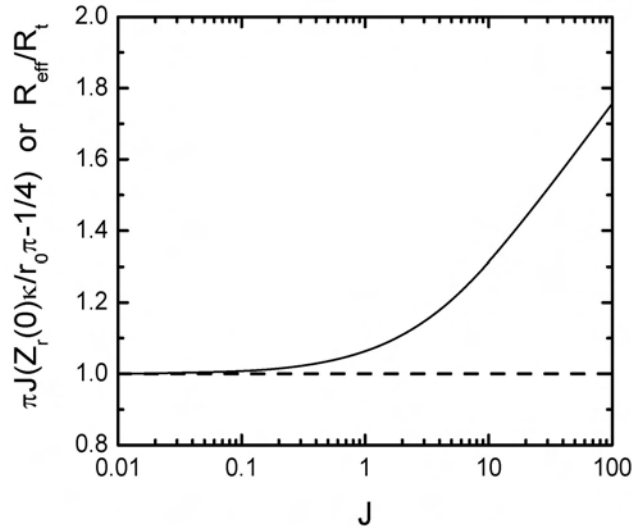
Figure 10-13. The apparent value of R_{eff}/R_t obtained from the calculated impedance response at low frequencies as a function of J.

i.e. when the Ohmic resistance dominates over the charge transfer resistance. At $J = 100$, an error of 75 percent is seen in the estimation of the charge-transfer resistance.

10.3.2 Determination of Capacitance

The evaluation of interfacial capacitance is perhaps better done in terms of the CPE. The values of α and 1-α obtained from Figure 10-4 are presented in Figure 10-14 as functions of J. The value of α ranges from 0.98 for $J = 0.01$ to 0.87 for $J = 10$, which demonstrates that nonuniform current and potential distributions on a disk electrode can yield high-frequency CPE-like behavior. As J becomes small, *i.e.* as the charge-transfer resistance dominates over the Ohmic resistance, α tends toward unity. It is significant that the calculated value of α shown in Figure 10-14 corresponds to a range of α that is frequently observed in experiments.

As shown in equation (9–9), the effective CPE coefficient Q_{eff} for electrochemical systems follows

$$Q_{\text{eff}} = \sin\left(\frac{\alpha\pi}{2}\right) \frac{-1}{Z_j(\omega)\omega^\alpha}$$
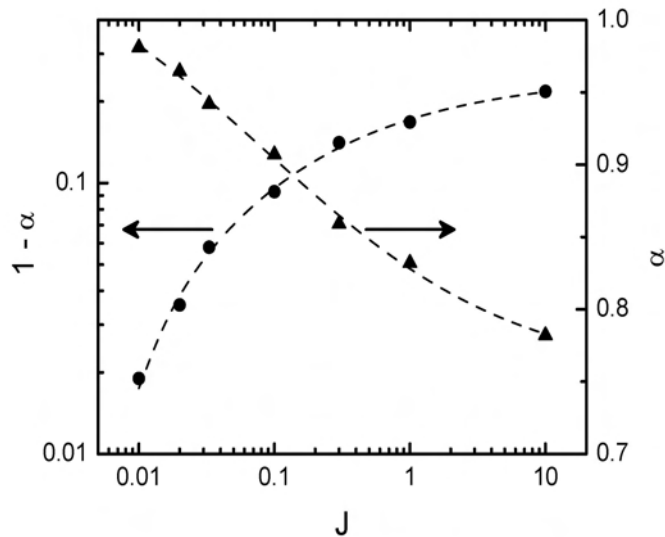
Figure 10-14. The apparent value of 1-α obtained from the calculated impedance response at high frequencies as a function of J.

The value of effective CPE coefficient, scaled by the interfacial capacitance, is presented in Figure 10-15 as a function of J. The frequencies reported in Figure 10-15 are limited to those that are one decade larger than the characteristic frequency because, in this frequency range, the value of α is well-defined. Figure 10-15 was developed taking into account the observation, seen in Figure 10-4, that the value of α is dependent on the frequency at which the slope is evaluated. Thus, the value of Q_{eff} reported is that corresponding to the value of α at a given frequency K.

While the dimensions are not exactly that of a capacitance, the CPE coefficient is often assumed to have approximately the same numerical value as the interfacial capacitance. The value of Q_{eff} presented in Figure 10-15 is a function of frequency. At high-frequencies, where frequency dispersion plays a significant role, the effective CPE coefficient Q_{eff} provides an inaccurate estimate for the interfacial capacitance, even for small values of J where α is close to unity. The errors in estimating the interfacial capacitance are on the order of 500 percent at K = 100.
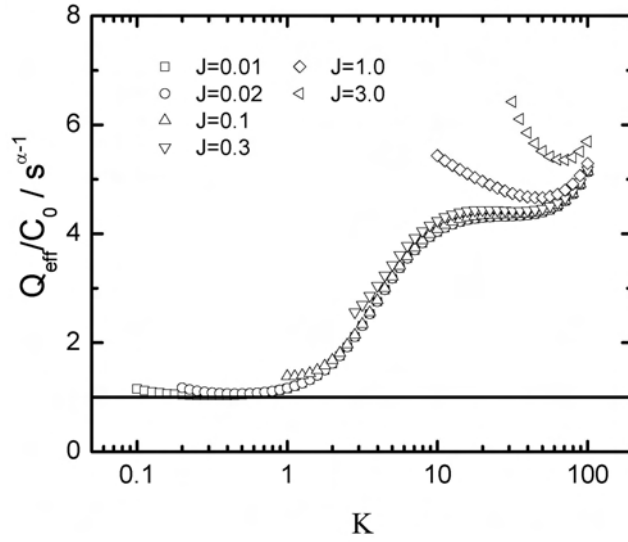
Figure 10-15. Effective CPE coefficient scaled by the interfacial capacitance as a function of J.

A number of researchers have explored the relationship between CPE parameters and the interfacial capacitance. Hsu and Mansfeld [95] proposed

$$C_{\text{eff}} = Q(\omega_{\max})^{\alpha-1} = Q \left(\frac{\kappa \text{K}}{C_0 r_0} \right)^{\alpha-1}_{\max} \tag{10–21}$$

where $\omega_{\max}$ (or $\text{K}_{\max}$) is the characteristic frequency at which the imaginary part of the impedance reaches its maximum value and C_{eff} is the estimated interfacial capacitance. Equation (10–21) is tested against the input value of interfacial capacitance in Figure 10-16 where C_0 is the known interfacial capacitance which was independent of radial position. As described above, Figure 10-16 was developed using local frequency-dependent values of α and Q_{eff}. The frequencies reported in Figure 10-16 are limited to those that are one decade larger than the characteristic frequency $\omega_{\max}$. While equation (10–21) represents an improvement as compared to direct use of the CPE coefficient Q_{eff}, the errors in estimating the interfacial capacitance depend on both J and K and range between -70 to $+100$ percent.
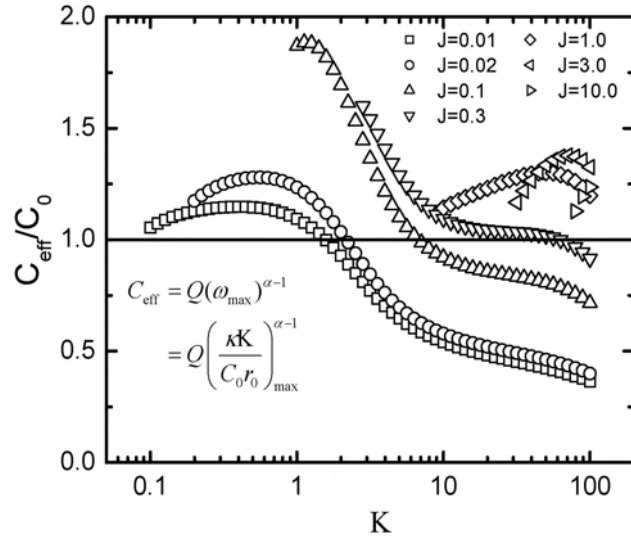
Figure 10-16. Effective capacitance calculated from equation (10–21) and normalized by the input interfacial capacitance for a disk electrode as a function of dimensionless frequency K with J as a parameter. (See Hsu and Mansfeld [95])

Brug et al. [30] developed a relationship for a blocking electrode between the interfacial capacitance and the CPE coefficient Q as

$$C_{\text{eff}} = \left[QR_e^{(1-\alpha)}\right]^{1/\alpha} \tag{10–22}$$

A similar relationship between the interfacial capacitance and the CPE coefficient Q was developed for a Faradaic system as

$$C_{\text{eff}} = \left[Q\left(\frac{1}{R_e} + \frac{1}{R_t}\right)^{(\alpha-1)}\right]^{1/\alpha} = \left[Q\left(\frac{1}{R_e}\left(1 + \frac{\pi J}{4}\right)\right)^{(\alpha-1)}\right]^{1/\alpha} \tag{10–23}$$

Equations (10–22) and (10–23) are compared to the expected value of interfacial capacitance in Figures 10-17(a) and 10-17(b), respectively. Figures 10-17(a) and 10-17(b) were developed using local frequency-dependent values of α and Q_{eff} over the same frequency range as is reported in Figures 10-15 and 10-16. The frequencies reported in Figure 10-17 are limited to those that are one decade larger than the characteristic frequency ω_{max}. The error in equation (10–22) is a function of both frequency K and

140
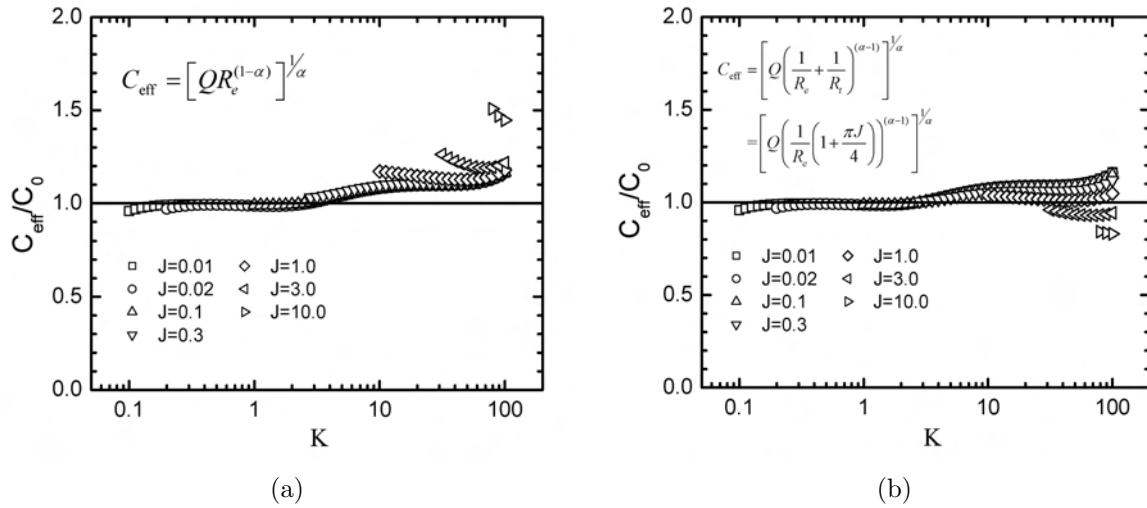
Figure 10-17. Normalized effective capacitance calculated from relationships presented by Brug et al. [30] for a disk electrode as a function of dimensionless frequency K with J as a parameter. a) with correction for Ohmic resistance R_e (equation (10–22)); and b) with correction for both Ohmic resistance R_e and charge-transfer resistance R_t (equation (10–23)).

J. The dependence on J is reduced significantly when both the Ohmic resistance R_e and charge-transfer resistance R_t are taken into account, and the errors in estimating interfacial capacitance are less than 20 percent. Of the relationships tested, equation (10–23) provides the best means for estimating interfacial capacitance when frequency dispersion is significant. The capacitance analysis presented here shows that, for determining interfacial capacitance, the influence of current and potential distributions on the impedance response cannot be neglected, even if the apparent CPE exponent α has values close to unity.

CHAPTER 11
CONCLUSION AND RECOMMENDATION

This dissertation covers two research topics that are important to corrosion of metal. The conclusion associated with the delamination model is presented in Section 11.1, and that associated with the impedance calculation is presented in Section 11.2.

11.1   Mathematical Models for Cathodic Delamination of Coated Metal

A one-dimensional, transient mathematical model was developed that simulates the delamination of polymeric coating from a zinc surface. The model included simultaneously multiple electrochemical reactions, homogeneous reactions, and formation of corrosion products. The calculation results are in agreement with the experimental observations reported by Stratmann et al. [9–11, 14–16] for coated steel and coated zinc. The consistency with experimental observations supports the hypotheses proposed by Allahar that the porosity and polarization kinetics can be treated as functions of pH.

The simulated results obtained using the equilibrium ε-pH relationship demonstrate that the overall delamination process is preliminary governed by the transport of the cations from the defect to the front region. The rate of the delamination depends on the mobility and the concentration of the cations. The anions, on the other hand, have no significant influence on the delamination rate.

The computational results obtained using a non-equilibrium ε-pH relationship indicate that, when the bond-breaking reactions take place at a sufficiently slow rate, the potential front and the porosity front become distinguishable. The movement of the potential front follows the change of pH along the metal-coating interface; whereas, the movement of the porosity front is limited by the bond-breaking reactions. The kinetic analysis of the non-equilibrium results also shows that the delamination mechanism shifts from a mass-controlled mechanism to a mixed controlled mechanism when the bond-braking reactions are sufficiently slow.

The mathematical model presented here provides a framework for advanced models in which complex parameters, such as coating property and surface treatments, can be included. The expansion of the one-dimensional model to a two-dimensional delaminated zone is recommended in the future. The influence of the expansion on delamination rate or delamination kinetics will be interesting.

A coupling of a two-dimensional defect with the delaminated zone is also recommended for a more sophisticated model. This combination will relax the boundary conditions at the location shared by the defect and the delaminated zone. The coupling will also account explicitly for the galvanic couple formed between anodic and cathodic sites. The development of the jointed model might be difficult because of the geometry of the system and the complex phenomena in the domain. A commercial program, such as COMSOL Multiphysics, is recommended for the development.

11.2   Influence of Geometry-Induced Current And Potential Distribution of Disk Electrodes on Impedance Response

The results presented from Chapters 8 to 10 have shown that the geometry-induced current and potential distributions induce a high-frequency dispersion that distorts the impedance response of a disk electrode. In all electrochemical systems under study, the local interfacial impedance exhibits the expected ideal behavior through all frequencies. The local impedance only shows ideal behavior at low frequency but non-ideal behavior at high frequency. The inductive loops observed in local impedance is influenced by local Ohmic impedance, which has imaginary component about the dimensionless frequency $K=1$. The complex value of the local Ohmic impedance is the origin of the inductive features in the local impedance and the origin of the CPE-like behavior in the global impedance.

The calculated results presented in Chapters 8 to 10 are compared with literature and experiments. For the ideally blocking electrode and electrode exhibiting Faradaic reactions, the calculated global impedance is in excellent agreement with those obtained

by Newman. The high-frequency dispersion seen in the global impedance has an appearance of a constant-phase element (CPE), but it can be considered to be only a quasi-CPE because the CPE exponent α is not independent of frequency. The impedance experiments performed on a glassy carbon disk and stainless steel disk electrode exhibit good consistency with the calculation results for a blocking electrode subject to coupled 2-D and 3-D distributions. The characteristic transition frequency at which the geometry plays a role is within experimental range. This geometry effect, however, could possibly be avoided by changing the size of the electrode or the concentration of the electrolyte.

The work explores the role of the current and potential distributions associated with a disk electrode on both local and global impedance. This is also the first work to express the geometric effect on impedance response in terms of CPE. The calculated results illustrate that the use of local impedance spectroscopy is able to distinguish CPE behavior that has an origin with a 3-D distribution from one that arises from a 2-D distribution.

The electrochemical systems investigated so far did not consider the influence of convective diffusion that enhances mass transfer in electrochemical systems. It will be interesting to explore the effect of current and potential distributions on the impedance response of a disk electrode in the presence of mass-transfer effects. Moreover, multiple heterogeneous reactions can be included in the calculation in the future. Surface coverage might need to be incorporated when multiple electrochemical reactions take place simultaneously. It will be interesting to investigate the relation between global and local impedances when the surface coverage plays a role in the calculation.

APPENDIX A
PROGRAM LISTING FOR THE CATHODIC DELAMINATION

This appendix presents the program listing for the cathodic delamination model. The program was developed using *Microsoft Visual Fortran, Version 9.0* with double precision accuracy.

A.1 Main Program Listing

```
  implicit double precision(a-h,o-z)
  implicit integer(i-n)
  common/ca/height,F,frt,vapp,tbetazn,excurzn,thick_gel,thickness,&
 &     total_time,t_step,z(9),diff(9),fzd(9),curolim,h,hh(2001),mm,rate_k
  common/cb/a(11,11),b(11,11),c(11,2001),d(11,23),g(11),x(11,11),y(11,11),n,nj
  common/cc/ii,conc(9,2001),phi(2001),por(2001),d_phi(2001),&
 &     dd_phi(2001),diff_phi(2001),d_c(9,2001),dd_c(9,2001),&
 &     d_flux(9,2001),flux(9,2001),curzn(2001),curo(2001),&
 &     c_aver(9,2001),g_eq(9,2001),c_ini(9,2001),d_aa(2001)
  common/cd/del_len,fro_len,sem_len,tac_len,c_ohdel,c_nadel,c_cldel,&
 &         c_ohfro,c_nafro,c_clfro,c_ohsem,c_nasem,c_clsem,c_ohint,&
 &         c_naint,c_clint,jdel,jfro,jsem,b1_pro,b2_pro,b3_pro,&
 &         b4_pro,b5_pro,b6_pro,b7_pro,b1_sur,b2_sur,b3_sur,b4_sur,&
 &         b5_sur,b6_sur,b7_sur,b1_blo,b2_blo,b3_blo,b4_blo,b5_blo,&
 &         b6_blo,b7_blo,b8_blo,b1_poi,b2_poi,b3_poi,b4_poi,b5_poi,&
 &         b6_poi,b7_poi,ph(2001),por_ini(2001),aa(2001),sur_cov(2001),&
 &         bb(2001),block(2001),poi(2001),b8,b9,b10,b11
  common/ce/flux_mig(9,2001),flux_dif(9,2001),curnet(2001),d_por(2001),&
 &         d_v(2001),total_current

!Read input data and discretize delamination zone
      call input
!Initialize the concentration distributions
      call initial(j)
      call setup(j)
!Time-stepping routine
      call cal_conc(j)

      stop
      end
```

A.2 Subroutine Program Listing

```
! subroutine that reads input data from input file
      subroutine input
      implicit double precision(a-h,o-z)
      implicit integer(i-n)
      common/ca/height,F,frt,vapp,tbetazn,excurzn,thick_gel,thickness,&
```

```
      &       total_time,t_step,rate_k,z_oh,z_na,z_cl,z_zn,z_h,z_znoh,&
      &       z_hzno2,z_zno2,z_znoh2,diff_oh,diff_na,diff_cl,diff_zn,&
      &       diff_h,diff_znoh,diff_hzno2,diff_zno2,diff_znoh2,z(9),&
      &       diff(9),fzd(9),curolim,h,hh(2001),mm
      common/cb/a(11,11),b(11,11),c(11,2001),d(11,23),g(11),x(11,11),&
      &       y(11,11),n,nj

       character name*40
       open(unit=101,file="input_cd_2.txt",status='unknown')
       rewind 101

       read(101,110)name,n                    ! # of variables
       read(101,110)name,nj                   ! # of mesh points
       read(101,120)name,height               ! length    cm
       read(101,130)name,F                     ! Faraday Constant
       read(101,130)name,frt                   ! F/(RT)   J/mole
       read(101,120)name,vapp                  ! metal potential V
       read(101,120)name,tbetazn               ! Tafel slope of Zn dissolution
       read(101,120)name,excurzn               ! exchange current density of Zn
       read(101,120)name,thick_gel             ! gel thickness
       read(101,120)name,thickness             ! coating thickness
       read(101,120)name,total_time            ! total time
       read(101,120)name,t_step                ! time step
       read(101,120)name,rate_k                ! rate constant of forming Zn(Oh)2
       read(101,120)name,z_oh                  ! charge number for OH-
       read(101,120)name,z_na                  ! charge number for Na+
       read(101,120)name,z_cl                  ! charge number for Cl-
       read(101,120)name,z_zn                  ! charge number for Zn2+
       read(101,120)name,z_h                   ! charge number for H+
       read(101,120)name,z_znoh                ! charge number for ZnOH+
       read(101,120)name,z_hzno2               ! charge number for HZnO2-
       read(101,120)name,z_zno2                ! charge number for ZnO22-
       read(101,120)name,z_znoh2               ! charge number for Zn(OH)2
       read(101,120)name,diff_oh               ! charge number for OH-
       read(101,120)name,diff_na               ! charge number for Na+
       read(101,120)name,diff_cl               ! charge number for Cl-
       read(101,120)name,diff_zn               ! charge number for Zn2+
       read(101,120)name,diff_h                ! charge number for H+
       read(101,120)name,diff_znoh             ! charge number for ZnOH+
       read(101,120)name,diff_hzno2            ! charge number for HZnO2-
       read(101,120)name,diff_zno2             ! charge number for ZnO22-
       read(101,120)name,diff_znoh2            ! charge number for Zn(OH)2

 110   format(a20,i6)
 120   format(a20,f12.10)
```

```fortran
 130  format(a20,f16.6)

! Limiting current density of oxygen reduction in a
! metal-electrolyte medium
      curolim=4*F*(1.9d-5)*(1.26d-6)
! Calculate grid size
      h=height/(nj-1)
! Calculate number of time loops
      mm=total_time/t_step

      do i= 1,n
        fzd(i)= frt*z(i)*diff(i)
      enddo
      do j=1,nj
        hh(j+1)=hh(j)+h
      enddo
      return
      end


! subroutine that calculates initial concentration and potential
! distributions
      subroutine initial(j)
      implicit double precision(a-h,o-z)
      implicit integer(i-n)
      common/cb/a(11,11),b(11,11),c(11,2001),d(11,23),g(11),x(11,11),&
     &      y(11,11),n,nj
      common/cd/del_len,fro_len,sem_len,tac_len,c_ohdel,c_nadel,c_cldel,&
     &          c_ohfro,c_nafro,c_clfro,c_ohsem,c_nasem,c_clsem,c_ohint,&
     &          c_naint,c_clint,jdel,jfro,jsem,b1_pro,b2_pro,b3_pro,&
     &          b4_pro,b5_pro,b6_pro,b7_pro,b1_sur,b2_sur,b3_sur,b4_sur,&
     &          b5_sur,b6_sur,b7_sur,b1_blo,b2_blo,b3_blo,b4_blo,b5_blo,&
     &          b6_blo,b7_blo,b8_blo,b1_poi,b2_poi,b3_poi,b4_poi,b5_poi,&
     &          b6_poi,b7_poi,ph(2001),por_ini(2001),aa(2001),sur_cov(2001),&
     &          bb(2001),block(2001),poi(2001),b8,b9,b10,b11

      character name*40
      open(unit=20,file="initial_cd_0.01M.txt",status='unknown')
      rewind 20

      open(unit=35,file='c_ini.text')
      open(unit=45,file='parameters_ini.text')

       read(20,210)name,del_len        ! length delaminated region
       read(20,210)name,fro_len        ! length front region
       read(20,210)name,sem_len        ! length semi-intact region
```

```
      read(20,210)name,tac_len          ! length fully-intact region
      read(20,210)name,c_ohdel          ! c_OH in the delaminated zone
      read(20,210)name,c_nadel          ! c_Na in the delaminated zone
      read(20,210)name,c_cldel          ! c_Cl in the delaminated zone
      read(20,210)name,c_ohfro          ! c_OH in the front region
      read(20,210)name,c_nafro          ! c_Na in the front region
      read(20,210)name,c_clfro          ! c_Cl in the front region
      read(20,210)name,c_ohsem          ! c_OH in the sem-intact region
      read(20,210)name,c_nasem          ! c_Na in the sem-intact region
      read(20,210)name,c_clsem          ! c_OH in the sem-intact region
      read(20,210)name,c_ohint          ! c_OH in the fully-intact region
      read(20,210)name,c_naint          ! c_Na in the fully-intact region
      read(20,210)name,c_clint          ! c_Cl in the fully-intact region
      read(20,210)name,b1_pro           ! parameter for porosity
      read(20,210)name,b2_pro           ! parameter for porosity
      read(20,210)name,b3_pro           ! parameter for porosity
      read(20,210)name,b4_pro           ! parameter for porosity
      read(20,210)name,b1_blo           ! parameter for blocking factor
      read(20,210)name,b2_blo           ! parameter for blocking factor
      read(20,210)name,b3_blo           ! parameter for blocking factor
      read(20,210)name,b4_blo           ! parameter for blocking factor
      read(20,210)name,b5_blo           ! parameter for blocking factor
      read(20,210)name,b6_blo           ! parameter for blocking factor
      read(20,210)name,b7_blo           ! parameter for blocking factor
      read(20,210)name,b1_poi           ! parameter for poisoning factor
      read(20,210)name,b2_poi           ! parameter for poisoning factor
      read(20,210)name,b3_poi           ! parameter for poisoning factor
      read(20,210)name,b4_poi           ! parameter for poisoning factor

210 format(a20,f16.6)
411 format(1x,i4,1x,e13.5,5e13.5)
412 format(1x,i4,e13.5,1x,4e13.5)
413 format(1x,a4,6x,a5,7x,a7,3(6x,a7),8x,a3)
414 format(1x,a4,6x,a5,7x,a7,4x,a10,3x,a9,5x,a7)

   jdel=(nj-1)/4       ! set length in the delaminated region
   jfro=(nj-1)*5/32    ! set length in the front
   jsem=(nj-1)*3/16    ! set length points in the semi-intact region

   cc=1/b4_blo
   b8= exp(b2_pro*(17-b3_pro))
   b9= b2_pro/2.3026d0
   b10=exp(b5_pro*(17-b6_pro))
   b11=b5_pro/2.3026d0
```

```fortran
! set nodal points in the domain
      do j=1,nj
        if(j.le.jdel) call cini_del(j)
        if((j.gt.jdel).and.(j.le.jfro)) call cini_fro(j)
        if((j.gt.jfro).and.(j.le.jsem)) call cini_sem(j)
        if(j.gt.jsem) call cini_int(j)
      enddo

      do j=1,nj
! Calculate assumed initial pH distribution
        ph(j)= -log10(1.0d-17/c_ini(1,j))
! Calculate assumed initial porosity distribution
        por_ini(j)=b1_pro/(1+exp(b2_pro*(ph(j)-b3_pro)))+&
       &          b4_pro/(1+exp(b5_pro*(ph(j)-b6_pro)))+b7_pro
        aa(j)= por_ini(j)**1.5
! Calculate assumed initial blocking factor distribution
        bb(j)=b1_blo*exp(-b2_blo*(ph(j)-b3_blo))
        block(j)=((bb(j)/(1+bb(j)))+b7_blo)*&
       &            ((1/(cc+exp(-b5_blo*(ph(j)-b6_blo))))+b8_blo)
! Calculate assumed initial poisoning factor distribution
        poi(j)=b1_poi/(1+exp(b2_poi*(ph(j)-b3_poi)))+&
       &          b4_poi/(1+exp(b5_poi*(ph(j)-b6_poi)))+b7_poi
      enddo
      return
      end

      subroutine cini_del(j)
      implicit double precision(a-h,o-z)
      implicit integer(i-n)
      common/cc/ii,conc(9,2001),phi(2001),por(2001),d_phi(2001),&
     &      dd_phi(2001),diff_phi(2001),d_c(9,2001),dd_c(9,2001),&
     &      d_flux(9,2001),flux(9,2001),curzn(2001),curo(2001),&
     &      c_aver(9,2001),g_eq(9,2001),c_ini(9,2001),d_aa(2001)
      common/cd/del_len,fro_len,sem_len,tac_len,c_ohdel,c_nadel,c_cldel,&
     &          c_ohfro,c_nafro,c_clfro,c_ohsem,c_nasem,c_clsem,c_ohint,&
     &          c_naint,c_clint,jdel,jfro,jsem,b1_pro,b2_pro,b3_pro,&
     &          b4_pro,b5_pro,b6_pro,b7_pro,b1_sur,b2_sur,b3_sur,b4_sur,&
     &          b5_sur,b6_sur,b7_sur,b1_blo,b2_blo,b3_blo,b4_blo,b5_blo,&
     &          b6_blo,b7_blo,b8_blo,b1_poi,b2_poi,b3_poi,b4_poi,b5_poi,&
     &          b6_poi,b7_poi,ph(2001),por_ini(2001),aa(2001),sur_cov(2001),&
     &          bb(2001),block(2001),poi(2001),b8,b9,b10,b11
! OH-
      c_ini(1,j)= c_ohdel+(c_ohfro-c_ohdel)*(j-1)*h/del_len
! Na+
      c_ini(2,j)= c_nadel+(c_nafro-c_nadel)*(j-1)*h/del_len
```

```fortran
! Cl-
      c_ini(3,j)= c_cldel+(c_clfro-c_cldel)*(j-1)*h/del_len
! Zn2+
      c_ini(4,j)=0.5*(c_ini(1,j)-c_ini(2,j)+c_ini(3,j))
! H+
      c_ini(5,j)= 0.0d0
! ZnOH+
      c_ini(6,j)= 0.0d0
! HZnO2-
      c_ini(7,j)= 0.0d0
! ZnO22-
      c_ini(8,j)= 0.0d0
! Zn(OH)2
      c_ini(9,j)= 0.0d0

      return
      end

      subroutine cini_fro(j)
      implicit double precision(a-h,o-z)
      implicit integer(i-n)
      common/cc/ii,conc(9,2001),phi(2001),por(2001),d_phi(2001),&
     &      dd_phi(2001),diff_phi(2001),d_c(9,2001),dd_c(9,2001),&
     &      d_flux(9,2001),flux(9,2001),curzn(2001),curo(2001),&
     &      c_aver(9,2001),g_eq(9,2001),c_ini(9,2001),d_aa(2001)
      common/cd/del_len,fro_len,sem_len,tac_len,c_ohdel,c_nadel,c_cldel,&
     &          c_ohfro,c_nafro,c_clfro,c_ohsem,c_nasem,c_clsem,c_ohint,&
     &          c_naint,c_clint,jdel,jfro,jsem,b1_pro,b2_pro,b3_pro,&
     &          b4_pro,b5_pro,b6_pro,b7_pro,b1_sur,b2_sur,b3_sur,b4_sur,&
     &          b5_sur,b6_sur,b7_sur,b1_blo,b2_blo,b3_blo,b4_blo,b5_blo,&
     &          b6_blo,b7_blo,b8_blo,b1_poi,b2_poi,b3_poi,b4_poi,b5_poi,&
     &          b6_poi,b7_poi,ph(2001),por_ini(2001),aa(2001),sur_cov(2001),&
     &          bb(2001),block(2001),poi(2001),b8,b9,b10,b11
! OH-
      c_ini(1,j)= c_ohfro*exp((hh(j)-del_len)*log(c_ohsem/c_ohfro)/fro_len)
! Na+
      c_ini(2,j)= c_nafro*exp((hh(j)-del_len)*log(c_nasem/c_nafro)/fro_len)
! Cl-
      c_ini(3,j)= c_clfro*exp((hh(j)-del_len)*log(c_clsem/c_clfro)/fro_len)
! Zn2+
      c_ini(4,j)=0.5*(c_ini(1,j)-c_ini(2,j)+c_ini(3,j))
! H+
      c_ini(5,j)= 0.0d0
! ZnOH+
      c_ini(6,j)= 0.0d0
```

```fortran
! HZnO2-
      c_ini(7,j)= 0.0d0
! ZnO22-
      c_ini(8,j)= 0.0d0
! Zn(OH)2
      c_ini(9,j)= 0.0d0
   return
   end

      subroutine cini_sem(j)
      implicit double precision(a-h,o-z)
      implicit integer(i-n)
      common/cc/ii,conc(9,2001),phi(2001),por(2001),d_phi(2001),&
     &       dd_phi(2001),diff_phi(2001),d_c(9,2001),dd_c(9,2001),&
     &       d_flux(9,2001),flux(9,2001),curzn(2001),curo(2001),&
     &       c_aver(9,2001),g_eq(9,2001),c_ini(9,2001),d_aa(2001)
      common/cd/del_len,fro_len,sem_len,tac_len,c_ohdel,c_nadel,c_cldel,&
     &          c_ohfro,c_nafro,c_clfro,c_ohsem,c_nasem,c_clsem,c_ohint,&
     &          c_naint,c_clint,jdel,jfro,jsem,b1_pro,b2_pro,b3_pro,&
     &          b4_pro,b5_pro,b6_pro,b7_pro,b1_sur,b2_sur,b3_sur,b4_sur,&
     &          b5_sur,b6_sur,b7_sur,b1_blo,b2_blo,b3_blo,b4_blo,b5_blo,&
     &          b6_blo,b7_blo,b8_blo,b1_poi,b2_poi,b3_poi,b4_poi,b5_poi,&
     &          b6_poi,b7_poi,ph(2001),por_ini(2001),aa(2001),sur_cov(2001),&
     &          bb(2001),block(2001),poi(2001),b8,b9,b10,b11
! OH-
      c_ini(1,j)= c_ohsem*exp((hh(j)-del_len-fro_len)*&
     &             log(c_ohint/c_ohsem)/sem_len)
! Na+
      c_ini(2,j)= c_nasem*exp((hh(j)-del_len-fro_len)*&
     &             log(c_naint/c_nasem)/sem_len)
! Cl-
      c_ini(3,j)= c_clsem*exp((hh(j)-del_len-fro_len)*&
     &             log(c_clint/c_clsem)/sem_len)
! Zn2+
      c_ini(4,j)=0.5*(c_ini(1,j)-c_ini(2,j)+c_ini(3,j))
! H+
      c_ini(5,j)= 0.0d0
! ZnOH+
      c_ini(6,j)= 0.0d0
! HZnO2-
      c_ini(7,j)= 0.0d0
! ZnO22-
      c_ini(8,j)= 0.0d0
! Zn(OH)2
      c_ini(9,j)= 0.0d0
```

```fortran
      return
      end

      subroutine cini_int(j)
      implicit double precision(a-h,o-z)
      implicit integer(i-n)
      common/cc/ii,conc(9,2001),phi(2001),por(2001),d_phi(2001),&
     &      dd_phi(2001),diff_phi(2001),d_c(9,2001),dd_c(9,2001),&
     &      d_flux(9,2001),flux(9,2001),curzn(2001),curo(2001),&
     &      c_aver(9,2001),g_eq(9,2001),c_ini(9,2001),d_aa(2001)
      common/cd/del_len,fro_len,sem_len,tac_len,c_ohdel,c_nadel,c_cldel,&
     &          c_ohfro,c_nafro,c_clfro,c_ohsem,c_nasem,c_clsem,c_ohint,&
     &          c_naint,c_clint,jdel,jfro,jsem,b1_pro,b2_pro,b3_pro,&
     &          b4_pro,b5_pro,b6_pro,b7_pro,b1_sur,b2_sur,b3_sur,b4_sur,&
     &          b5_sur,b6_sur,b7_sur,b1_blo,b2_blo,b3_blo,b4_blo,b5_blo,&
     &          b6_blo,b7_blo,b8_blo,b1_poi,b2_poi,b3_poi,b4_poi,b5_poi,&
     &          b6_poi,b7_poi,ph(2001),por_ini(2001),aa(2001),sur_cov(2001),&
     &          bb(2001),block(2001),poi(2001),b8,b9,b10,b11
!OH-
      c_ini(1,j)= c_ohint
!Na+
      c_ini(2,j)= c_naint
!Cl-
      c_ini(3,j)= c_clint
!Zn2+
      c_ini(4,j)=0.5*(c_ini(1,j)-c_ini(2,j)+c_ini(3,j))
!H+
      c_ini(5,j)= 0.0d0
!ZnOH+
      c_ini(6,j)= 0.0d0
!HZnO2-
      c_ini(7,j)= 0.0d0
!ZnO22-
      c_ini(8,j)= 0.0d0
!Zn(OH)2
      c_ini(9,j)= 0.0d0
      return
      end

!subroutine that records initial guesses
      subroutine setup(j)
      implicit double precision(a-h,o-z)
      implicit integer(i-n)
      common/cc/ii,conc(9,2001),phi(2001),por(2001),d_phi(2001),&
     &      dd_phi(2001),diff_phi(2001),d_c(9,2001),dd_c(9,2001),&
```

152

```fortran
     &        d_flux(9,2001),flux(9,2001),curzn(2001),curo(2001),&
     &        c_aver(9,2001),g_eq(9,2001),c_ini(9,2001),d_aa(2001)
      common/cd/del_len,fro_len,sem_len,tac_len,c_ohdel,c_nadel,c_cldel,&
     &          c_ohfro,c_nafro,c_clfro,c_ohsem,c_nasem,c_clsem,c_ohint,&
     &          c_naint,c_clint,jdel,jfro,jsem,b1_pro,b2_pro,b3_pro,&
     &          b4_pro,b5_pro,b6_pro,b7_pro,b1_sur,b2_sur,b3_sur,b4_sur,&
     &          b5_sur,b6_sur,b7_sur,b1_blo,b2_blo,b3_blo,b4_blo,b5_blo,&
     &          b6_blo,b7_blo,b8_blo,b1_poi,b2_poi,b3_poi,b4_poi,b5_poi,&
     &          b6_poi,b7_poi,ph(2001),por_ini(2001),aa(2001),sur_cov(2001),&
     &          bb(2001),block(2001),poi(2001),b8,b9,b10,b11

      do j=1,nj
        phi(j)=-0.05
        conc(1,j)=1.0d-4
        conc(2,j)=1.0d-6
        conc(3,j)=1.0d-6
        conc(4,j)=0.5d-4
        conc(5,j)=1.0d-16
        conc(6,j)=1.0d-20
        conc(7,j)=1.0d-25
        conc(8,j)=1.0d-30
        conc(9,j)=1.0d-20
        por(j)=0.1d0
      enddo
      return
      end

!subroutine for calculating conc. and solution potential
      subroutine cal_conc(j)
      implicit double precision(a-h,o-z)
      implicit integer(i-n)
      common/cb/a(11,11),b(11,11),c(11,2001),d(11,23),g(11),x(11,11),&
     &     y(11,11),n,nj
      common/ca/height,F,frt,vapp,tbetazn,excurzn,thick_gel,thickness,&
     &     total_time,t_step,rate_k,z_oh,z_na,z_cl,z_zn,z_h,z_znoh,&
     &     z_hzno2,z_zno2,z_znoh2,diff_oh,diff_na,diff_cl,diff_zn,&
     &     diff_h,diff_znoh,diff_hzno2,diff_zno2,diff_znoh2,z(9),&
     &     diff(9),fzd(9),curolim,h,hh(2001),mm
      common/cc/ii,conc(9,2001),phi(2001),por(2001),d_phi(2001),&
     &      dd_phi(2001),diff_phi(2001),d_c(9,2001),dd_c(9,2001),&
     &      d_flux(9,2001),flux(9,2001),curzn(2001),curo(2001),&
     &      c_aver(9,2001),g_eq(9,2001),c_ini(9,2001),d_aa(2001)
      common/cd/del_len,fro_len,sem_len,tac_len,c_ohdel,c_nadel,c_cldel,&
     &          c_ohfro,c_nafro,c_clfro,c_ohsem,c_nasem,c_clsem,c_ohint,&
     &          c_naint,c_clint,jdel,jfro,jsem,b1_pro,b2_pro,b3_pro,&
```

```
     &            b4_pro,b5_pro,b6_pro,b7_pro,b1_sur,b2_sur,b3_sur,b4_sur,&
     &            b5_sur,b6_sur,b7_sur,b1_blo,b2_blo,b3_blo,b4_blo,b5_blo,&
     &            b6_blo,b7_blo,b8_blo,b1_poi,b2_poi,b3_poi,b4_poi,b5_poi,&
     &            b6_poi,b7_poi,ph(2001),por_ini(2001),aa(2001),sur_cov(2001),&
     &            bb(2001),block(2001),poi(2001),b8,b9,b10,b11

     open(unit=102,file='g1.txt')
200  format(11(e10.2))
300  format(/,a7,i4)

     do ii=1,mm
       do i=1,n
        do k =1,n
          x(i,k)=0.0
          y(i,k)=0.0
        enddo
       enddo


       j=0
     do l=1,40
     if (ii.eq.mm) write(102,300) "jcount=", l
50   j=j+1
     do i=1,n
      g(i)=0.0d0
       do k=1,n
          a(i,k)=0.0d0
          b(i,k)=0.0d0
          d(i,k)=0.0d0
       enddo
     enddo

     if(j.eq.1) call bc_1(j)
     if((ii.eq.mm).and.(j.eq.1)) write(102,200) (g(k),k=1,n)
     if((j.gt.1).and.(j.lt.nj)) call body(j)
     if((ii.eq.mm).and.(j.eq.2)) write(102,200) (g(k),k=1,n)
     if((ii.eq.mm).and.(j.eq.(nj-1)/8)) write(102,200) (g(k),k=1,n)
     if((ii.eq.mm).and.(j.eq.(nj-1)/4)) write(102,200) (g(k),k=1,n)
     if((ii.eq.mm).and.(j.eq.nj-1)) write(102,200) (g(k),k=1,n)
     if(j.eq.nj) call bc_2(j)
     if((ii.eq.mm).and.(j.eq.nj)) write(102,200) (g(k),k=1,n)
     call band(j)

     if (j.ne.nj) go to 50

     do 100 j=1,nj
```

```fortran
! Set boundaries for values of concentrations and solution
! potential
        if (c(1,j).lt.-0.5) c(1,j)=-0.50d0
        if (c(1,j).gt.0.5)  c(1,j)=0.50d0
        if (c(2,j).lt.(-0.999*conc(1,j))) c(2,j)=-0.999*conc(1,j)
        if (c(2,j).gt.(1000.0*conc(1,j))) c(2,j)=1000.0*conc(1,j)
        if (c(3,j).lt.(-0.999*conc(2,j))) c(3,j)=-0.999*conc(2,j)
        if (c(3,j).gt.(1000.0*conc(2,j))) c(3,j)=1000.0*conc(2,j)
        if (c(4,j).lt.(-0.999*conc(3,j))) c(4,j)=-0.999*conc(3,j)
        if (c(4,j).gt.(1000.0*conc(3,j))) c(4,j)=1000.0*conc(3,j)
        if (c(5,j).lt.(-0.999*conc(4,j))) c(5,j)=-0.999*conc(4,j)
        if (c(5,j).gt.(1000.0*conc(4,j))) c(5,j)=1000.0*conc(4,j)
        if (c(6,j).lt.-0.5) c(6,j)=-0.50d0
        if (c(6,j).gt.0.5)  c(6,j)=0.50d0
        if (c(7,j).lt.(-0.999*conc(5,j))) c(7,j)=-0.999*conc(5,j)
        if (c(7,j).gt.(1000.0*conc(5,j))) c(7,j)=1000.0*conc(5,j)
        if (c(8,j).lt.(-0.999*conc(6,j))) c(8,j)=-0.999*conc(6,j)
        if (c(8,j).gt.(1000.0*conc(6,j))) c(8,j)=1000.0*conc(6,j)
        if (c(9,j).lt.(-0.999*conc(7,j))) c(9,j)=-0.999*conc(7,j)
        if (c(9,j).gt.(1000.0*conc(7,j))) c(9,j)=1000.0*conc(7,j)
        if(c(10,j).lt.(-0.999*conc(8,j))) c(10,j)=-0.999*conc(8,j)
        if(c(10,j).gt.(1000.0*conc(8,j))) c(10,j)=1000.0*conc(8,j)
        if(c(11,j).lt.(-0.999*conc(9,j))) c(11,j)=-0.999*conc(9,j)
        if(c(11,j).gt.(1000.0*conc(9,j))) c(11,j)=1000.0*conc(9,j)
! update new values
        phi(j) = phi(j)+c(1,j)
        conc(1,j) = conc(1,j)+c(2,j)
        conc(2,j) = conc(2,j)+c(3,j)
        conc(3,j) = conc(3,j)+c(4,j)
        conc(4,j) = conc(4,j)+c(5,j)
          por(j) = por(j)+c(6,j)
        conc(5,j) = conc(5,j)+c(7,j)
        conc(6,j) = conc(6,j)+c(8,j)
        conc(7,j) = conc(7,j)+c(9,j)
        conc(8,j) = conc(8,j)+c(10,j)
        conc(9,j) = conc(9,j)+c(11,j)
 100    continue
        call cal_porosity(j)    ! update the hypothesized parameters

        if(l.eq.40) then
          call cal_flux(j)      ! calculate flux and current values
          call results(j)       ! output files
        endif

        j=0
```

```fortran
        enddo
         do i=1,n-2
           do j=1,nj
            c_ini(i,j)=conc(i,j)
            por_ini(j)=por(j)
           enddo
          enddo

       enddo
       return
       end

!subroutine of BAND(J) algorithm
       SUBROUTINE BAND(J)
       IMPLICIT DOUBLE PRECISION(A-H,O-Z)
       IMPLICIT INTEGER (I-N)
       DOUBLE PRECISION E(11,12,2001)
       common/cb/a(11,11),b(11,11),c(11,2001),d(11,23),g(11),x(11,11),&
     &     y(11,11),n,nj

       SAVE E,NP1
 101   FORMAT (/15H DETERM=0 AT J=,I4)
       IF((J-2).LT.0) GO TO 1
       IF((J-2).EQ.0) GO TO 6
       IF((J-2).GT.0) GO TO 8
   1   NP1= N + 1
       DO 2 I=1,N
       D(I,2*N+1)= G(I)
       DO 2 L=1,N
       LPN= L + N
   2   D(I,LPN)= X(I,L)
       CALL MATINV (N,2*N+1,DETERM)
       IF (DETERM)  4,3,4
   3   PRINT 101, J
   4   DO 5 K=1,N
       E(K,NP1,1)= D(K,2*N+1)
       DO 5 L=1,N
       E(K,L,1)= - D(K,L)
       LPN= L + N
   5   X(K,L)= - D(K,LPN)
       RETURN
   6   DO 7 I=1,N
       DO 7 K=1,N
       DO 7 L=1,N
   7   D(I,K)= D(I,K) + A(I,L)*X(L,K)
```

```
 8  IF (J-NJ)  11,9,9
 9  DO 10 I=1,N
    DO 10 L=1,N
    G(I)= G(I) - Y(I,L)*E(L,NP1,J-2)
    DO 10 M=1,N
10  A(I,L)= A(I,L) + Y(I,M)*E(M,L,J-2)
11  DO 12 I=1,N
    D(I,NP1)= - G(I)
    DO 12 L=1,N
    D(I,NP1)= D(I,NP1) + A(I,L)*E(L,NP1,J-1)
    DO 12 K=1,N
12  B(I,K)= B(I,K) + A(I,L)*E(L,K,J-1)
    CALL MATINV (N,NP1,DETERM)
    IF (DETERM)  14,13,14
13  PRINT 101, J
14  DO 15 K=1,N
    DO 15 M=1,NP1
15  E(K,M,J)= - D(K,M)
    IF (J-NJ)  20,16,16
16  DO 17 K=1,N
17  C(K,J)= E(K,NP1,J)
    DO 18 JJ=2,NJ
    M= NJ - JJ + 1
    DO 18 K=1,N
    C(K,M)= E(K,NP1,M)
    DO 18 L=1,N
18  C(K,M)= C(K,M) + E(K,L,M)*C(L,M+1)
    DO 19 L=1,N
    DO 19 K=1,N
19  C(K,1)= C(K,1) + X(K,L)*C(L,3)
20  RETURN
    END
!*********************** MAtrix inverse*************************

    SUBROUTINE MATINV(N,M,DETERM)
    IMPLICIT DOUBLE PRECISION(A-H,O-Z)
    IMPLICIT INTEGER (I-N)
    common/cb/a(11,11),b(11,11),c(11,2001),d(11,23)

    INTEGER ID(6)
    DETERM=1.0d0
    DO 1 I=1,N
 1  ID(I)=0
    DO 18 NN=1,N
    BMAX=1.1
```

```
      DO 6 I=1,N
      IF(ID(I).NE.0) GO TO 6
      BNEXT=0.0
      BTRY=0.0
      DO 5 J=1,N
      IF(ID(J).NE.0) GO TO 5
      IF(ABS(B(I,J)).LE.BNEXT) GO TO 5
      BNEXT=ABS(B(I,J))
      IF(BNEXT.LE.BTRY) GO TO 5
      BNEXT=BTRY
      BTRY=ABS(B(I,J))
      JC=J
 5    CONTINUE
      IF(BNEXT.GE.BMAX*BTRY) GO TO 6
      BMAX=BNEXT/BTRY
      IROW=I
      JCOL=JC
 6    CONTINUE
      IF(ID(JC).EQ.0) GO TO 8
      DETERM=0.0
      RETURN
 8    ID(JCOL)=1
      IF(JCOL.EQ.IROW) GO TO 12
      DO 10 J=1,N
      SAVE=B(IROW,J)
      B(IROW,J)=B(JCOL,J)
10    B(JCOL,J)=SAVE
      DO 11 K=1,M
      SAVE=D(IROW,K)
      D(IROW,K)=D(JCOL,K)
11    D(JCOL,K)=SAVE
12    F=1.0/B(JCOL,JCOL)
      DO 13 J=1,N
13    B(JCOL,J)=B(JCOL,J)*F
      DO 14 K=1,M
14    D(JCOL,K)=D(JCOL,K)*F
      DO 18 I=1,N
      IF(I.EQ.JCOL) GO TO 18
      F=B(I,JCOL)
      DO 16 J=1,N
16    B(I,J)=B(I,J)-F*B(JCOL,J)
      DO 17 K=1,M
17    D(I,K)=D(I,K)-F*D(JCOL,K)
18    CONTINUE
      RETURN
```

```fortran
      END

! subroutine for the boundary sharing with defect
      subroutine bc_1(j)
      implicit double precision(a-h,o-z)
      implicit integer(i-n)
      common/ca/height,F,frt,vapp,tbetazn,excurzn,thick_gel,thickness,&
     &      total_time,t_step,rate_k,z_oh,z_na,z_cl,z_zn,z_h,z_znoh,&
     &      z_hzno2,z_zno2,z_znoh2,diff_oh,diff_na,diff_cl,diff_zn,&
     &      diff_h,diff_znoh,diff_hzno2,diff_zno2,diff_znoh2,z(9),&
     &      diff(9),fzd(9),curolim,h,hh(2001),mm
      common/cb/a(11,11),b(11,11),c(11,2001),d(11,23),g(11),x(11,11),&
     &      y(11,11),n,nj
      common/cc/ii,conc(9,2001),phi(2001),por(2001),d_phi(2001),&
     &      dd_phi(2001),diff_phi(2001),d_c(9,2001),dd_c(9,2001),&
     &      d_flux(9,2001),flux(9,2001),curzn(2001),curo(2001),&
     &      c_aver(9,2001),g_eq(9,2001),c_ini(9,2001),d_aa(2001)
      common/cd/del_len,fro_len,sem_len,tac_len,c_ohdel,c_nadel,c_cldel,&
     &          c_ohfro,c_nafro,c_clfro,c_ohsem,c_nasem,c_clsem,c_ohint,&
     &          c_naint,c_clint,jdel,jfro,jsem,b1_pro,b2_pro,b3_pro,&
     &          b4_pro,b5_pro,b6_pro,b7_pro,b1_sur,b2_sur,b3_sur,b4_sur,&
     &          b5_sur,b6_sur,b7_sur,b1_blo,b2_blo,b3_blo,b4_blo,b5_blo,&
     &          b6_blo,b7_blo,b8_blo,b1_poi,b2_poi,b3_poi,b4_poi,b5_poi,&
     &          b6_poi,b7_poi,ph(2001),por_ini(2001),aa(2001),sur_cov(2001),&
     &          bb(2001),block(2001),poi(2001),b8,b9,b10,b11
      common/ce/flux_mig(9,2001),flux_dif(9,2001),curnet(2001),d_por(2001),&
     &          d_v(2001),total_current


      ophi=0.402-tbetao*log10(excuro)
      znphi=-0.763-tbetazn*log10(excurzn)
      ff1=(por(j)*b7_pro)**1.5
      ff2=(por(j)**1.5)*thickness+(b7_pro**1.5)*thick_gel
      ff=ff1/ff2
      diff_phi(j)=vapp-phi(j)
! current density due to zinc dissolution
      curzn(j)=(10**((vapp-phi(j)-znphi)/tbetazn))*sur_cov(j)*poi(j)
! current density due to oxygen reduction
      curo(j)=-curolim*sur_cov(j)*block(j)*ff

      dd=b1_pro*b8*b9
      ee=b4_pro*b10*b11
! solution potential
      g(1)= phi(j)+0.1
      b(1,1)= -1.0d0
! OH-
```

```fortran
      g(2)= conc(1,j)-1.0d-3
      b(2,2)= -1.0d0
! Na+
      g(3)= conc(2,j)-1.0d-3
      b(3,3)= -1.0d0
! Cl-
      g(4)= conc(3,j)-5.0d-4
      b(4,4)= -1.0d0
! Zn2+
      g(5)= conc(4,j)-2.5d-4
      b(5,5)= -1.0d0
! porosity
      g(6)= por(j)-b1_pro/(1+b8*(conc(1,j)**b9))-&
      &              b4_pro/(1+b10*(conc(1,j)**b11))-b7_pro
      b(6,2)=-dd*(conc(1,j)**(b9-1))/((1+b8*(conc(1,j)**b9))**2)&
      &        -ee*(conc(1,j)**(b11-1))/((1+b10*(conc(1,j)**b11))**2)
      b(6,6)= -1.0d0
! H+   H2O --> OH+ +OH-
      g(7)=conc(1,j)*conc(5,j)-1.0d-20
      b(7,2)= -conc(5,j)
      b(7,7)= -conc(1,j)
! ZnOH+  Zn2+ + OH- --> ZnOH+
      g(8)= conc(6,j)-(10.0**1.33)*conc(1,j)*conc(4,j)
      b(8,2)= (10.0**1.33)*conc(4,j)
      b(8,5)= (10.0**1.33)*conc(1,j)
      b(8,8)= -1.0d0
! HZnO2-   ZnOH+ +2OH- --> HZnO2- + H2O
      g(9)= conc(7,j)-(10.0**4.03)*conc(6,j)*(conc(1,j)**2)
      b(9,2)= 2*(10.0**4.03)*conc(6,j)*conc(1,j)
      b(9,8)= (10.0**4.03)*(conc(1,j)**2)
      b(9,9)= -1.0d0
! ZnO22-   HZnO2- + OH- --> ZnO22- + H2O
      g(10)= conc(8,j)-(10.0**(-2.17))*conc(1,j)*conc(7,j)
      b(10,2)= (10.0**(-2.17))*conc(7,j)
      b(10,9)= (10.0**(-2.17))*conc(1,j)
      b(10,10)= -1.0d0
! Zn(OH)2  Zn2+ + 2OH- --> Zn(OH)2
      g(11)= (por(j)*conc(9,j)-por_ini(j)*c_ini(9,j))/t_step-&
      &        rate_k*(conc(1,j)*conc(1,j)*conc(4,j)-3.0d-26)
      b(11,2)= 2*rate_k*conc(1,j)*conc(4,j)
      b(11,5)= rate_k*conc(1,j)*conc(1,j)
      b(11,6)= -conc(9,j)/t_step
      b(11,11)= -por(j)/t_step
      return
      end
```

```
!subroutine for non-boundary points
      subroutine body(j)
      implicit double precision(a-h,o-z)
      implicit integer(i-n)
      common/ca/height,F,frt,vapp,tbetazn,excurzn,thick_gel,thickness,&
     &     total_time,t_step,rate_k,z_oh,z_na,z_cl,z_zn,z_h,z_znoh,&
     &     z_hzno2,z_zno2,z_znoh2,diff_oh,diff_na,diff_cl,diff_zn,&
     &     diff_h,diff_znoh,diff_hzno2,diff_zno2,diff_znoh2,z(9),&
     &     diff(9),fzd(9),curolim,h,hh(2001),mm
      common/cb/a(11,11),b(11,11),c(11,2001),d(11,23),g(11),x(11,11),&
     &     y(11,11),n,nj
      common/cc/ii,conc(9,2001),phi(2001),por(2001),d_phi(2001),&
     &     dd_phi(2001),diff_phi(2001),d_c(9,2001),dd_c(9,2001),&
     &     d_flux(9,2001),flux(9,2001),curzn(2001),curo(2001),&
     &     c_aver(9,2001),g_eq(9,2001),c_ini(9,2001),d_aa(2001)
      common/cd/del_len,fro_len,sem_len,tac_len,c_ohdel,c_nadel,c_cldel,&
     &         c_ohfro,c_nafro,c_clfro,c_ohsem,c_nasem,c_clsem,c_ohint,&
     &         c_naint,c_clint,jdel,jfro,jsem,b1_pro,b2_pro,b3_pro,&
     &         b4_pro,b5_pro,b6_pro,b7_pro,b1_sur,b2_sur,b3_sur,b4_sur,&
     &         b5_sur,b6_sur,b7_sur,b1_blo,b2_blo,b3_blo,b4_blo,b5_blo,&
     &         b6_blo,b7_blo,b8_blo,b1_poi,b2_poi,b3_poi,b4_poi,b5_poi,&
     &         b6_poi,b7_poi,ph(2001),por_ini(2001),aa(2001),sur_cov(2001),&
     &         bb(2001),block(2001),poi(2001),b8,b9,b10,b11
      common/ce/flux_mig(9,2001),flux_dif(9,2001),curnet(2001),d_por(2001),&
     &         d_v(2001),total_current

      dd=b1_pro*b8*b9
      ee=b4_pro*b10*b11
      d_aa(j)= (aa(j+1)-aa(j-1))/(2*h)
      d_phi(j)= (phi(j+1)-phi(j-1))/(2*h)
      dd_phi(j)= (phi(j+1)-2*phi(j)+phi(j-1))/(h*h)
      diff_phi(j)= vapp-phi(j)

      do i=1,n-2
        d_c(i,j)= (conc(i,j+1)-conc(i,j-1))/(2*h)
       dd_c(i,j)= (conc(i,j+1)-2*conc(i,j)+conc(i,j-1))/(h*h)
       d_flux(i,j)= (-fzd(i)*conc(i,j)*dd_phi(j)-fzd(i)*d_c(i,j)*&
     &           d_phi(j)-diff(i)*dd_c(i,j))*aa(j)+&
     &      d_aa(j)*(-fzd(i)*conc(i,j)*d_phi(j)-diff(i)*d_c(i,j))
       g_eq(i,j)= (conc(i,j)*por(j)-c_ini(i,j)*por_ini(j))/t_step+d_flux(i,j)
      enddo

      ophi=0.402-tbetao*log10(excuro)
      znphi=-0.763-tbetazn*log10(excurzn)
```

```fortran
        ff1=(por(j)*b7_pro)**1.5
        ff2=(por(j)**1.5)*thickness+(b7_pro**1.5)*thick_gel
        ff=ff1/ff2
! calculate current densities due to electrochemical reactions
        curzn(j)=(10**((diff_phi(j)-znphi)/tbetazn))*sur_cov(j)*poi(j)
        curo(j)=-curolim*sur_cov(j)*block(j)*ff
! solution potential(electroneutrality)
        g(1)= z(1)*conc(1,j)+z(2)*conc(2,j)+z(3)*conc(3,j)+z(4)*conc(4,j)+&
     &       z(5)*conc(5,j)+z(6)*conc(6,j)+z(7)*conc(7,j)+z(8)*conc(8,j)
        b(1,2)= -z(1)
        b(1,3)= -z(2)
        b(1,4)= -z(3)
        b(1,5)= -z(4)
        b(1,7)= -z(5)
        b(1,8)= -z(6)
        b(1,9)= -z(7)
        b(1,10)= -z(8)
! OH-
        g(2)=g_eq(1,j)+curo(j)/(F*thickness)-g_eq(5,j)-g_eq(4,j)+&
     &      curzn(j)/(2*F*thickness)+2*g_eq(7,j)+3*g_eq(8,j)-&
     &      (por(j)*conc(9,j)-por_ini(j)*c_ini(9,j))/t_step

        a(2,1)= (fzd(1)*conc(1,j)/(h*h)-fzd(1)*d_c(1,j)/(2*h))*aa(j)-&
     &         d_aa(j)*fzd(1)*conc(1,j)/(2*h)-&
     &         (fzd(5)*conc(5,j)/(h*h)-fzd(5)*d_c(5,j)/(2*h))*aa(j)+&
     &         d_aa(j)*fzd(5)*conc(5,j)/(2*h)-&
     &         (fzd(4)*conc(4,j)/(h*h)-fzd(4)*d_c(4,j)/(2*h))*aa(j)+&
     &         d_aa(j)*fzd(4)*conc(4,j)/(2*h)+&
     &        2*(fzd(7)*conc(7,j)/(h*h)-fzd(7)*d_c(7,j)/(2*h))*aa(j)-&
     &        2*d_aa(j)*fzd(7)*conc(7,j)/(2*h)+&
     &        3*(fzd(8)*conc(8,j)/(h*h)-fzd(8)*d_c(8,j)/(2*h))*aa(j)-&
     &        3*d_aa(j)*fzd(8)*conc(8,j)/(2*h)
        b(2,1)=-2*fzd(1)*conc(1,j)*aa(j)/(h*h)+&
     &         2*fzd(5)*conc(5,j)*aa(j)/(h*h)+&
     &         2*fzd(4)*conc(4,j)*aa(j)/(h*h)+&
     &        log(10.0)*curzn(j)/(2*F*tbetazn*thickness)-&
     &         4*fzd(7)*conc(7,j)*aa(j)/(h*h)-&
     &         6*fzd(8)*conc(8,j)*aa(j)/(h*h)
        d(2,1)= (fzd(1)*conc(1,j)/(h*h)+fzd(1)*d_c(1,j)/(2*h))*aa(j)+&
     &          d_aa(j)*fzd(1)*conc(1,j)/(2*h)-&
     &         (fzd(5)*conc(5,j)/(h*h)+fzd(5)*d_c(5,j)/(2*h))*aa(j)-&
     &          d_aa(j)*fzd(5)*conc(5,j)/(2*h)-&
     &         (fzd(4)*conc(4,j)/(h*h)+fzd(4)*d_c(4,j)/(2*h))*aa(j)-&
     &          d_aa(j)*fzd(4)*conc(4,j)/(2*h)+&
     &        2*(fzd(7)*conc(7,j)/(h*h)+fzd(7)*d_c(7,j)/(2*h))*aa(j)+&
```

```
&        2*d_aa(j)*fzd(7)*conc(7,j)/(2*h)+&
&        3*(fzd(8)*conc(8,j)/(h*h)+fzd(8)*d_c(8,j)/(2*h))*aa(j)+&
&        3*d_aa(j)*fzd(8)*conc(8,j)/(2*h)
 a(2,2)= (-fzd(1)*d_phi(j)/(2*h)+diff(1)/(h*h))*aa(j)-&
&         d_aa(j)*diff(1)/(2*h)
 b(2,2)= -por(j)/t_step+(fzd(1)*dd_phi(j)-2*diff(1)/(h*h))*aa(j)&
&        +d_aa(j)*fzd(1)*d_phi(j)
 d(2,2)= (fzd(1)*d_phi(j)/(2*h)+diff(1)/(h*h))*aa(j)+&
&         d_aa(j)*diff(1)/(2*h)
 a(2,5)= -(-fzd(4)*d_phi(j)/(2*h)+diff(4)/(h*h))*aa(j)+&
&         d_aa(j)*diff(4)/(2*h)
 b(2,5)=  por(j)/t_step-(fzd(4)*dd_phi(j)-2*diff(4)/(h*h))*aa(j)&
&         -d_aa(j)*fzd(4)*d_phi(j)
 d(2,5)= -(fzd(4)*d_phi(j)/(2*h)+diff(4)/(h*h))*aa(j)-&
&         d_aa(j)*diff(4)/(2*h)
 a(2,6)=(-fzd(1)*conc(1,j)*d_phi(j)-diff(1)*d_c(1,j))*&
&         (1.5d0*(por(j-1)**0.5d0))/(2*h)-&
&        (-fzd(5)*conc(5,j)*d_phi(j)-diff(5)*d_c(5,j))*&
&         (1.5d0*(por(j-1)**0.5d0))/(2*h)-&
&        (-fzd(4)*conc(4,j)*d_phi(j)-diff(4)*d_c(4,j))*&
&         (1.5d0*(por(j-1)**0.5d0))/(2*h)+&
&     2*(-fzd(7)*conc(7,j)*d_phi(j)-diff(7)*d_c(7,j))*&
&         (1.5d0*(por(j-1)**0.5d0))/(2*h)+&
&     3*(-fzd(8)*conc(8,j)*d_phi(j)-diff(8)*d_c(8,j))*&
&         (1.5d0*(por(j-1)**0.5d0))/(2*h)
 b(2,6)=-conc(1,j)/t_step-1.5*(por(j)**0.5)*(-fzd(1)*conc(1,j)*&
&         dd_phi(j)-fzd(1)*d_c(1,j)*d_phi(j)-diff(1)*dd_c(1,j))+&
&         (1.5d0*(por(j)**0.5)*(b7_pro**1.5))/ff2-&
&         ff1*1.5d0*(por(j)**0.5)*thickness/(ff2**2))*&
&         curolim/(F*thickness)+&
&         conc(5,j)/t_step+1.5*(por(j)**0.5)*(-fzd(5)*conc(5,j)*&
&         dd_phi(j)-fzd(5)*d_c(5,j)*d_phi(j)-diff(5)*dd_c(5,j))+&
&         conc(4,j)/t_step+1.5*(por(j)**0.5)*(-fzd(4)*conc(4,j)*&
&         dd_phi(j)-fzd(4)*d_c(4,j)*d_phi(j)-diff(4)*dd_c(4,j))-&
&       2*conc(7,j)/t_step-3.0*(por(j)**0.5)*(-fzd(7)*conc(7,j)*&
&         dd_phi(j)-fzd(7)*d_c(7,j)*d_phi(j)-diff(7)*dd_c(7,j))-&
&       3*conc(8,j)/t_step-4.5*(por(j)**0.5)*(-fzd(8)*conc(8,j)*&
&         dd_phi(j)-fzd(8)*d_c(8,j)*d_phi(j)-diff(8)*dd_c(8,j))+&
&         conc(9,j)/t_step
 d(2,6)=(-fzd(1)*conc(1,j)*d_phi(j)-diff(1)*d_c(1,j))*&
&         (-1.5d0*(por(j+1)**0.5d0))/(2*h)-&
&        (-fzd(5)*conc(5,j)*d_phi(j)-diff(5)*d_c(5,j))*&
&         (-1.5d0*(por(j+1)**0.5d0))/(2*h)-&
&        (-fzd(4)*conc(4,j)*d_phi(j)-diff(4)*d_c(4,j))*&
&         (-1.5d0*(por(j+1)**0.5d0))/(2*h)+&
```

```
     &      2*(-fzd(7)*conc(7,j)*d_phi(j)-diff(7)*d_c(7,j))*&
     &          (-1.5d0*(por(j+1)**0.5d0))/(2*h)+&
     &      3*(-fzd(8)*conc(8,j)*d_phi(j)-diff(8)*d_c(8,j))*&
     &          (-1.5d0*(por(j+1)**0.5d0))/(2*h)
      a(2,7)= -(-fzd(5)*d_phi(j)/(2*h)+diff(5)/(h*h))*aa(j)+&
     &           d_aa(j)*diff(5)/(2*h)
      b(2,7)=  por(j)/t_step-(fzd(5)*dd_phi(j)-2*diff(5)/(h*h))*aa(j)&
     &          -d_aa(j)*fzd(5)*d_phi(j)
      d(2,7)= -(fzd(5)*d_phi(j)/(2*h)+diff(5)/(h*h))*aa(j)-&
     &           d_aa(j)*diff(5)/(2*h)
      a(2,9)= 2*(-fzd(7)*d_phi(j)/(2*h)+diff(7)/(h*h))*aa(j)-&
     &          2*d_aa(j)*diff(7)/(2*h)
      b(2,9)= -2*por(j)/t_step+2*(fzd(7)*dd_phi(j)-2*diff(7)/(h*h))*aa(j)&
     &          +2*d_aa(j)*fzd(7)*d_phi(j)
      d(2,9)= 2*(fzd(7)*d_phi(j)/(2*h)+diff(7)/(h*h))*aa(j)+&
     &          2*d_aa(j)*diff(7)/(2*h)
      a(2,10)= 3*(-fzd(8)*d_phi(j)/(2*h)+diff(8)/(h*h))*aa(j)-&
     &           3*d_aa(j)*diff(8)/(2*h)
      b(2,10)= -3*por(j)/t_step+3*(fzd(8)*dd_phi(j)-2*diff(8)/(h*h))*aa(j)&
     &           +3*d_aa(j)*fzd(8)*d_phi(j)
      d(2,10)= 3*(fzd(8)*d_phi(j)/(2*h)+diff(8)/(h*h))*aa(j)+&
     &           3*d_aa(j)*diff(8)/(2*h)
      b(2,11)= por(j)/t_step
! Na+ and Cl-
      do i=2,3
        g(i+1)= g_eq(i,j)
        a(i+1,1)=(fzd(i)*conc(i,j)/(h*h)-fzd(i)*d_c(i,j)/(2*h))*aa(j)-&
     &           d_aa(j)*fzd(i)*conc(i,j)/(2*h)
        b(i+1,1)=-2*fzd(i)*conc(i,j)*aa(j)/(h*h)
        d(i+1,1)=(fzd(i)*conc(i,j)/(h*h)+fzd(i)*d_c(i,j)/(2*h))*aa(j)+&
     &           d_aa(j)*fzd(i)*conc(i,j)/(2*h)
        a(i+1,i+1)=(-fzd(i)*d_phi(j)/(2*h)+diff(i)/(h*h))*aa(j)-&
     &           d_aa(j)*diff(i)/(2*h)
        b(i+1,i+1)=-por(j)/t_step+(fzd(i)*dd_phi(j)-2*diff(i)/(h*h))*aa(j)&
     &             +d_aa(j)*fzd(i)*d_phi(j)
        d(i+1,i+1)=(fzd(i)*d_phi(j)/(2*h)+diff(i)/(h*h))*aa(j)+&
     &           d_aa(j)*diff(i)/(2*h)
        a(i+1,6)=(-fzd(i)*conc(i,j)*d_phi(j)-diff(i)*d_c(i,j))*&
     &          (1.5d0*(por(j-1)**0.5d0))/(2*h)
        b(i+1,6)=-conc(i,j)/t_step-1.5*(por(j)**0.5)*(-fzd(i)*conc(i,j)*&
     &          dd_phi(j)-fzd(i)*d_c(i,j)*d_phi(j)-diff(i)*dd_c(i,j))
        d(i+1,6)=(-fzd(i)*conc(i,j)*d_phi(j)-diff(i)*d_c(i,j))*&
     &          (-1.5d0*(por(j+1)**0.5d0))/(2*h)
      enddo
! Zn2+
```

```
  g(5)=g_eq(4,j)-curzn(j)/(2*F*thickness)+g_eq(6,j)+g_eq(7,j)+&
&      g_eq(8,j)-(por(j)*conc(9,j)-por_ini(j)*c_ini(9,j))/t_step

  a(5,1)= (fzd(4)*conc(4,j)/(h*h)-fzd(4)*d_c(4,j)/(2*h))*aa(j)-&
&          d_aa(j)*fzd(4)*conc(4,j)/(2*h)+&
&         (fzd(6)*conc(6,j)/(h*h)-fzd(6)*d_c(6,j)/(2*h))*aa(j)-&
&          d_aa(j)*fzd(6)*conc(6,j)/(2*h)+&
&         (fzd(7)*conc(7,j)/(h*h)-fzd(7)*d_c(7,j)/(2*h))*aa(j)-&
&          d_aa(j)*fzd(7)*conc(7,j)/(2*h)+&
&         (fzd(8)*conc(8,j)/(h*h)-fzd(8)*d_c(8,j)/(2*h))*aa(j)-&
&          d_aa(j)*fzd(8)*conc(8,j)/(2*h)
  b(5,1)= -2*fzd(4)*conc(4,j)*aa(j)/(h*h)&
&         -log(10.0)*curzn(j)/(2*F*tbetazn*thickness)&
&         -2*fzd(6)*conc(6,j)*aa(j)/(h*h)&
&         -2*fzd(7)*conc(7,j)*aa(j)/(h*h)&
&         -2*fzd(8)*conc(8,j)*aa(j)/(h*h)
  d(5,1)= (fzd(4)*conc(4,j)/(h*h)+fzd(4)*d_c(4,j)/(2*h))*aa(j)+&
&          d_aa(j)*fzd(4)*conc(4,j)/(2*h)+&
&         (fzd(6)*conc(6,j)/(h*h)+fzd(6)*d_c(6,j)/(2*h))*aa(j)+&
&          d_aa(j)*fzd(6)*conc(6,j)/(2*h)+&
&         (fzd(7)*conc(7,j)/(h*h)+fzd(7)*d_c(7,j)/(2*h))*aa(j)+&
&          d_aa(j)*fzd(7)*conc(7,j)/(2*h)+&
&         (fzd(8)*conc(8,j)/(h*h)+fzd(8)*d_c(8,j)/(2*h))*aa(j)+&
&          d_aa(j)*fzd(8)*conc(8,j)/(2*h)
  a(5,5)= (-fzd(4)*d_phi(j)/(2*h)+diff(4)/(h*h))*aa(j)-&
&          d_aa(j)*diff(4)/(2*h)
  b(5,5)= -por(j)/t_step+(fzd(4)*dd_phi(j)-2*diff(4)/(h*h))*aa(j)&
&          +d_aa(j)*fzd(4)*d_phi(j)
  d(5,5)= (fzd(4)*d_phi(j)/(2*h)+diff(4)/(h*h))*aa(j)+&
&          d_aa(j)*diff(4)/(2*h)
  a(5,6)=(-fzd(4)*conc(4,j)*d_phi(j)-diff(4)*d_c(4,j))*&
&         (1.5d0*(por(j-1)**0.5d0))/(2*h)+&
&        (-fzd(6)*conc(6,j)*d_phi(j)-diff(6)*d_c(6,j))*&
&         (1.5d0*(por(j-1)**0.5d0))/(2*h)+&
&        (-fzd(7)*conc(7,j)*d_phi(j)-diff(7)*d_c(7,j))*&
&         (1.5d0*(por(j-1)**0.5d0))/(2*h)+&
&        (-fzd(8)*conc(8,j)*d_phi(j)-diff(8)*d_c(8,j))*&
&         (1.5d0*(por(j-1)**0.5d0))/(2*h)
  b(5,6)=-conc(4,j)/t_step-1.5*(por(j)**0.5)*(-fzd(4)*conc(4,j)*&
&         dd_phi(j)-fzd(4)*d_c(4,j)*d_phi(j)-diff(4)*dd_c(4,j))-&
&         conc(6,j)/t_step-1.5*(por(j)**0.5)*(-fzd(6)*conc(6,j)*&
&         dd_phi(j)-fzd(6)*d_c(6,j)*d_phi(j)-diff(6)*dd_c(6,j))-&
&         conc(7,j)/t_step-1.5*(por(j)**0.5)*(-fzd(7)*conc(7,j)*&
&         dd_phi(j)-fzd(7)*d_c(7,j)*d_phi(j)-diff(7)*dd_c(7,j))-&
&         conc(8,j)/t_step-1.5*(por(j)**0.5)*(-fzd(8)*conc(8,j)*&
```

165

```fortran
     &          dd_phi(j)-fzd(8)*d_c(8,j)*d_phi(j)-diff(8)*dd_c(8,j))+&
     &          conc(9,j)/t_step
      d(5,6)=(-fzd(4)*conc(4,j)*d_phi(j)-diff(4)*d_c(4,j))*&
     &          (-1.5d0*(por(j+1)**0.5d0))/(2*h)+&
     &        (-fzd(6)*conc(6,j)*d_phi(j)-diff(6)*d_c(6,j))*&
     &          (-1.5d0*(por(j+1)**0.5d0))/(2*h)+&
     &        (-fzd(7)*conc(7,j)*d_phi(j)-diff(7)*d_c(7,j))*&
     &          (-1.5d0*(por(j+1)**0.5d0))/(2*h)+&
     &        (-fzd(8)*conc(8,j)*d_phi(j)-diff(8)*d_c(8,j))*&
     &          (-1.5d0*(por(j+1)**0.5d0))/(2*h)
      a(5,8)= (-fzd(6)*d_phi(j)/(2*h)+diff(6)/(h*h))*aa(j)-&
     &          d_aa(j)*diff(6)/(2*h)
      b(5,8)= -por(j)/t_step+(fzd(6)*dd_phi(j)-2*diff(6)/(h*h))*aa(j)&
     &           +d_aa(j)*fzd(6)*d_phi(j)
      d(5,8)= (fzd(6)*d_phi(j)/(2*h)+diff(6)/(h*h))*aa(j)+&
     &          d_aa(j)*diff(6)/(2*h)
      a(5,9)= (-fzd(7)*d_phi(j)/(2*h)+diff(7)/(h*h))*aa(j)-&
     &          d_aa(j)*diff(7)/(2*h)
      b(5,9)= -por(j)/t_step+(fzd(7)*dd_phi(j)-2*diff(7)/(h*h))*aa(j)&
     &           +d_aa(j)*fzd(7)*d_phi(j)
      d(5,9)= (fzd(7)*d_phi(j)/(2*h)+diff(7)/(h*h))*aa(j)+&
     &          d_aa(j)*diff(7)/(2*h)


      a(5,10)= (-fzd(8)*d_phi(j)/(2*h)+diff(8)/(h*h))*aa(j)-&
     &          d_aa(j)*diff(8)/(2*h)
      b(5,10)= -por(j)/t_step+(fzd(8)*dd_phi(j)-2*diff(8)/(h*h))*aa(j)&
     &           +d_aa(j)*fzd(8)*d_phi(j)
      d(5,10)= (fzd(8)*d_phi(j)/(2*h)+diff(8)/(h*h))*aa(j)+&
     &          d_aa(j)*diff(8)/(2*h)
      b(5,11)= por(j)/t_step
! Porosity
      g(6)= por(j)-b1_pro/(1+b8*(conc(1,j)**b9))-&
     &            b4_pro/(1+b10*(conc(1,j)**b11))-b7_pro
      b(6,2)= -dd*(conc(1,j)**(b9-1))/((1+b8*(conc(1,j)**b9))**2)&
     &       -ee*(conc(1,j)**(b11-1))/((1+b10*(conc(1,j)**b11))**2)
      b(6,6)= -1.0d0
! H+  H2O --> H+ +OH-
      g(7)=conc(1,j)*conc(5,j)-1.0d-20
      b(7,2)= -conc(5,j)
      b(7,7)= -conc(1,j)
! ZnOH+  Zn2+ +OH- --> ZnOH+
      g(8)= conc(6,j)-(10.0**1.33)*conc(1,j)*conc(4,j)
      b(8,2)= (10.0**1.33)*conc(4,j)
      b(8,5)= (10.0**1.33)*conc(1,j)
      b(8,8)= -1.0d0
```

```fortran
! HZnO2-   ZnOH+ +2OH- --> HZnO2- + H2O
      g(9)= conc(7,j)-(10.0**4.03)*conc(6,j)*(conc(1,j)**2)
      b(9,2)= 2*(10.0**4.03)*conc(6,j)*conc(1,j)
      b(9,8)= (10.0**4.03)*(conc(1,j)**2)
      b(9,9)= -1.0d0
! ZnO22-  HZnO2- + OH- --> ZnO22- + H2O
      g(10)= conc(8,j)-(10.0**(-2.17))*conc(1,j)*conc(7,j)
      b(10,2)= (10.0**(-2.17))*conc(7,j)
      b(10,9)= (10.0**(-2.17))*conc(1,j)
      b(10,10)= -1.0d0
! Zn(OH)2  Zn2+ + 2OH- --> Zn(OH)2
      g(11)= (por(j)*conc(9,j)-por_ini(j)*c_ini(9,j))/t_step-&
      &      rate_k*(conc(1,j)*conc(1,j)*conc(4,j)-3.0d-26)
      b(11,2)= 2*rate_k*conc(1,j)*conc(4,j)
      b(11,5)= rate_k*conc(1,j)*conc(1,j)
      b(11,6)= -conc(9,j)/t_step
      b(11,11)= -por(j)/t_step
      return
      end

! subroutine for the boundary in the fully-intact region
      subroutine bc_2(j)
      implicit double precision(a-h,o-z)
      implicit integer(i-n)
      common/ca/height,F,frt,vapp,tbetazn,excurzn,thick_gel,thickness,&
      &    total_time,t_step,rate_k,z_oh,z_na,z_cl,z_zn,z_h,z_znoh,&
      &    z_hzno2,z_zno2,z_znoh2,diff_oh,diff_na,diff_cl,diff_zn,&
      &    diff_h,diff_znoh,diff_hzno2,diff_zno2,diff_znoh2,z(9),&
      &    diff(9),fzd(9),curolim,h,hh(2001),mm
      common/cb/a(11,11),b(11,11),c(11,2001),d(11,23),g(11),x(11,11),&
      &    y(11,11),n,nj
      common/cc/ii,conc(9,2001),phi(2001),por(2001),d_phi(2001),&
      &    dd_phi(2001),diff_phi(2001),d_c(9,2001),dd_c(9,2001),&
      &    d_flux(9,2001),flux(9,2001),curzn(2001),curo(2001),&
      &    c_aver(9,2001),g_eq(9,2001),c_ini(9,2001),d_aa(2001)
      common/cd/del_len,fro_len,sem_len,tac_len,c_ohdel,c_nadel,c_cldel,&
      &       c_ohfro,c_nafro,c_clfro,c_ohsem,c_nasem,c_clsem,c_ohint,&
      &       c_naint,c_clint,jdel,jfro,jsem,b1_pro,b2_pro,b3_pro,&
      &       b4_pro,b5_pro,b6_pro,b7_pro,b1_sur,b2_sur,b3_sur,b4_sur,&
      &       b5_sur,b6_sur,b7_sur,b1_blo,b2_blo,b3_blo,b4_blo,b5_blo,&
      &       b6_blo,b7_blo,b8_blo,b1_poi,b2_poi,b3_poi,b4_poi,b5_poi,&
      &       b6_poi,b7_poi,ph(2001),por_ini(2001),aa(2001),sur_cov(2001),&
      &       bb(2001),block(2001),poi(2001),b8,b9,b10,b11
      common/ce/flux_mig(9,2001),flux_dif(9,2001),curnet(2001),d_por(2001),&
      &       d_v(2001),total_current
```

```
        dd=b1_pro*b8*b9
        ee=b4_pro*b10*b11
        d_aa(j)=(aa(j)-aa(j-1))/h
        d_phi(j)= (phi(j)-phi(j-1))/h
        diff_phi(j)=vapp-phi(j)

        ophi=0.402-tbetao*log10(excuro)
        znphi=-0.763-tbetazn*log10(excurzn)
        ff1=(por(j)*b7_pro)**1.5
        ff2=(por(j)**1.5)*thickness+(b7_pro**1.5)*thick_gel
        ff=ff1/ff2
! calculate current densities due to electrochemical reactions
        curzn(j)=(10**((vapp-phi(j)-znphi/tbetazn))*sur_cov(j)*poi(j)
        curo(j)=-curolim*sur_cov(j)*block(j)*ff

        do i=1,n-2
         c_aver(i,j)= (conc(i,j-1)+conc(i,j))/2
         d_c(i,j)= (conc(i,j)-conc(i,j-1))/h
         flux(i,j)= -fzd(i)*c_aver(i,j)*d_phi(j)-diff(i)*d_c(i,j)
         g_eq(i,j)= (conc(i,j)*por(j)-c_ini(i,j)*por_ini(j))/t_step-&
        &          aa(j)*2*flux(i,j)/h+flux(i,j)*d_aa(j)/2
        enddo
! solution potential (Electroneturality)
        g(1)= z(1)*conc(1,j)+z(2)*conc(2,j)+z(3)*conc(3,j)+z(4)*conc(4,j)+&
        &       z(5)*conc(5,j)+z(6)*conc(6,j)+z(7)*conc(7,j)+z(8)*conc(8,j)
        b(1,2)= -z(1)
        b(1,3)= -z(2)
        b(1,4)= -z(3)
        b(1,5)= -z(4)
        b(1,7)= -z(5)
        b(1,8)= -z(6)
        b(1,9)= -z(7)
        b(1,10)= -z(8)
! OH-
        g(2)= g_eq(1,j)-g_eq(5,j)-g_eq(4,j)+2*g_eq(7,j)+3*g_eq(8,j)-&
        &      (por(j)*conc(9,j)-por_ini(j)*c_ini(9,j))/t_step
         a(2,1)= fzd(1)*c_aver(1,j)*aa(j)*2/(h*h)-&
        &         fzd(1)*c_aver(1,j)*d_aa(j)/(2*h)-&
        &         fzd(5)*c_aver(5,j)*aa(j)*2/(h*h)+&
        &         fzd(5)*c_aver(5,j)*d_aa(j)/(2*h)-&
        &         fzd(4)*c_aver(4,j)*aa(j)*2/(h*h)+&
        &         fzd(4)*c_aver(4,j)*d_aa(j)/(2*h)+&
        &       2*fzd(7)*c_aver(7,j)*aa(j)*2/(h*h)-&
        &       2*fzd(7)*c_aver(7,j)*d_aa(j)/(2*h)+&
        &       3*fzd(8)*c_aver(8,j)*aa(j)*2/(h*h)-&
```

```
&        3*fzd(8)*c_aver(8,j)*d_aa(j)/(2*h)
 b(2,1)= -fzd(1)*c_aver(1,j)*aa(j)*2/(h*h)+&
&          fzd(1)*c_aver(1,j)*d_aa(j)/(2*h)+&
&          fzd(5)*c_aver(5,j)*aa(j)*2/(h*h)-&
&          fzd(5)*c_aver(5,j)*d_aa(j)/(2*h)+&
&          fzd(4)*c_aver(4,j)*aa(j)*2/(h*h)-&
&          fzd(4)*c_aver(4,j)*d_aa(j)/(2*h)-&
&        2*fzd(7)*c_aver(7,j)*aa(j)*2/(h*h)+&
&        2*fzd(7)*c_aver(7,j)*d_aa(j)/(2*h)-&
&        3*fzd(8)*c_aver(8,j)*aa(j)*2/(h*h)+&
&        3*fzd(8)*c_aver(8,j)*d_aa(j)/(2*h)
 a(2,2)= -(fzd(1)*d_phi(j)/2-diff(1)/h)*2*aa(j)/h+&
&          (fzd(1)*d_phi(j)/2-diff(1)/h)*d_aa(j)/2
 b(2,2)= -por(j)/t_step-(fzd(1)*d_phi(j)/2+diff(1)/h)*2*aa(j)/h+&
&          (fzd(1)*d_phi(j)/2+diff(1)/h)*d_aa(j)/2
 a(2,5)= (fzd(4)*d_phi(j)/2-diff(4)/h)*2*aa(j)/h-&
&          (fzd(4)*d_phi(j)/2-diff(4)/h)*d_aa(j)/2
 b(2,5)=  por(j)/t_step+(fzd(4)*d_phi(j)/2+diff(4)/h)*2*aa(j)/h-&
&          (fzd(4)*d_phi(j)/2+diff(4)/h)*d_aa(j)/2
 a(2,6)= flux(1,j)*1.5d0*(por(j-1)**0.5)/(2*h)-&
&          flux(5,j)*1.5d0*(por(j-1)**0.5)/(2*h)-&
&          flux(4,j)*1.5d0*(por(j-1)**0.5)/(2*h)+&
&        2*flux(7,j)*1.5d0*(por(j-1)**0.5)/(2*h)+&
&        3*flux(8,j)*1.5d0*(por(j-1)**0.5)/(2*h)
 b(2,6)= -conc(1,j)/t_step+2*1.5d0*flux(1,j)/h-&
&          flux(1,j)*1.5d0*(por(j)**0.5)/(2*h)+&
&          conc(5,j)/t_step-2*1.5d0*flux(5,j)/h+&
&          flux(5,j)*1.5d0*(por(j)**0.5)/(2*h)+&
&          conc(4,j)/t_step-2*1.5d0*flux(4,j)/h+&
&          flux(4,j)*1.5d0*(por(j)**0.5)/(2*h)-&
&        2*conc(7,j)/t_step+4*1.5d0*flux(7,j)/h-&
&        2*flux(7,j)*1.5d0*(por(j)**0.5)/(2*h)-&
&        3*conc(8,j)/t_step+6*1.5d0*flux(8,j)/h-&
&        3*flux(8,j)*1.5d0*(por(j)**0.5)/(2*h)+&
&          conc(9,j)/t_step
 a(2,7)= (fzd(5)*d_phi(j)/2-diff(5)/h)*2*aa(j)/h-&
&          (fzd(5)*d_phi(j)/2-diff(5)/h)*d_aa(j)/2
 b(2,7)=  por(j)/t_step+(fzd(5)*d_phi(j)/2+diff(5)/h)*2*aa(j)/h-&
&          (fzd(5)*d_phi(j)/2+diff(5)/h)*d_aa(j)/2
 a(2,9)= -2*(fzd(7)*d_phi(j)/2-diff(7)/h)*2*aa(j)/h+&
&          2*(fzd(7)*d_phi(j)/2-diff(7)/h)*d_aa(j)/2
 b(2,9)= -2*por(j)/t_step-2*(fzd(7)*d_phi(j)/2+diff(7)/h)*2*aa(j)/h+&
&          2*(fzd(7)*d_phi(j)/2+diff(7)/h)*d_aa(j)/2
 a(2,10)= -3*(fzd(8)*d_phi(j)/2-diff(8)/h)*2*aa(j)/h+&
&          3*(fzd(8)*d_phi(j)/2-diff(8)/h)*d_aa(j)/2
```

```fortran
      b(2,10)= -3*por(j)/t_step-2*(fzd(8)*d_phi(j)/2+diff(8)/h)*2*aa(j)/h+&
     &          3*(fzd(8)*d_phi(j)/2+diff(8)/h)*d_aa(j)/2
      b(2,11)= por(j)/t_step
! Na+ and Cl-
      do i=2,3
        g(i+1)= g_eq(i,j)
        a(i+1,1)= fzd(i)*c_aver(i,j)*aa(j)*2/(h*h)-&
     &          fzd(i)*c_aver(i,j)*d_aa(j)/(2*h)
        b(i+1,1)=-fzd(i)*c_aver(i,j)*aa(j)*2/(h*h)+&
     &          fzd(i)*c_aver(i,j)*d_aa(j)/(2*h)
        a(i+1,i+1)=-(fzd(i)*d_phi(j)/2-diff(i)/h)*2*aa(j)/h+&
     &           (fzd(i)*d_phi(j)/2-diff(i)/h)*d_aa(j)/2
        b(i+1,i+1)=-por(j)/t_step-(fzd(i)*d_phi(j)/2+diff(i)/h)*2*aa(j)/h+&
     &           (fzd(i)*d_phi(j)/2+diff(i)/h)*d_aa(j)/2
        a(i+1,6)= flux(i,j)*1.5d0*(por(j-1)**0.5)/(2*h)
        b(i+1,6)= -conc(i,j)/t_step+2*1.5d0*flux(i,j)/h-&
     &          flux(i,j)*1.5d0*(por(j)**0.5)/(2*h)
      enddo
! Zn2+
      g(5)= g_eq(4,j)+g_eq(6,j)+g_eq(7,j)+g_eq(8,j)-&
     &      (por(j)*conc(9,j)-por_ini(j)*c_ini(9,j))/t_step
      a(5,1)= fzd(4)*c_aver(4,j)*aa(j)*2/(h*h)-&
     &        fzd(4)*c_aver(4,j)*d_aa(j)/(2*h)+&
     &        fzd(6)*c_aver(6,j)*aa(j)*2/(h*h)-&
     &        fzd(6)*c_aver(6,j)*d_aa(j)/(2*h)+&
     &        fzd(7)*c_aver(7,j)*aa(j)*2/(h*h)-&
     &        fzd(7)*c_aver(7,j)*d_aa(j)/(2*h)+&
     &        fzd(8)*c_aver(8,j)*aa(j)*2/(h*h)-&
     &        fzd(8)*c_aver(8,j)*d_aa(j)/(2*h)
      b(5,1)= -fzd(4)*c_aver(4,j)*aa(j)*2/(h*h)+&
     &         fzd(4)*c_aver(4,j)*d_aa(j)/(2*h)-&
     &         fzd(6)*c_aver(6,j)*aa(j)*2/(h*h)+&
     &         fzd(6)*c_aver(6,j)*d_aa(j)/(2*h)-&
     &         fzd(7)*c_aver(7,j)*aa(j)*2/(h*h)+&
     &         fzd(7)*c_aver(7,j)*d_aa(j)/(2*h)-&
     &         fzd(8)*c_aver(8,j)*aa(j)*2/(h*h)+&
     &         fzd(8)*c_aver(8,j)*d_aa(j)/(2*h)
      a(5,5)= -(fzd(4)*d_phi(j)/2-diff(4)/h)*2*aa(j)/h+&
     &         (fzd(4)*d_phi(j)/2-diff(4)/h)*d_aa(j)/2
      b(5,5)= -por(j)/t_step-(fzd(4)*d_phi(j)/2+diff(4)/h)*2*aa(j)/h+&
     &         (fzd(4)*d_phi(j)/2+diff(4)/h)*d_aa(j)/2
      a(5,6)= flux(4,j)*1.5d0*(por(j-1)**0.5)/(2*h)+&
     &        flux(6,j)*1.5d0*(por(j-1)**0.5)/(2*h)+&
     &        flux(7,j)*1.5d0*(por(j-1)**0.5)/(2*h)+&
     &        flux(8,j)*1.5d0*(por(j-1)**0.5)/(2*h)
```

```fortran
      b(5,6)= -conc(4,j)/t_step+2*1.5d0*flux(4,j)/h-&
     &        flux(4,j)*1.5d0*(por(j)**0.5)/(2*h)-&
     &        conc(6,j)/t_step+2*1.5d0*flux(6,j)/h-&
     &        flux(6,j)*1.5d0*(por(j)**0.5)/(2*h)-&
     &        conc(7,j)/t_step+2*1.5d0*flux(7,j)/h-&
     &        flux(7,j)*1.5d0*(por(j)**0.5)/(2*h)-&
     &        conc(8,j)/t_step+2*1.5d0*flux(8,j)/h-&
     &        flux(8,j)*1.5d0*(por(j)**0.5)/(2*h)+&
     &        conc(9,j)/t_step
      a(5,8)= -(fzd(6)*d_phi(j)/2-diff(6)/h)*2*aa(j)/h+&
     &         (fzd(6)*d_phi(j)/2-diff(6)/h)*d_aa(j)/2
      b(5,8)= -por(j)/t_step-(fzd(6)*d_phi(j)/2+diff(6)/h)*2*aa(j)/h+&
     &         (fzd(6)*d_phi(j)/2+diff(6)/h)*d_aa(j)/2
      a(5,9)= -(fzd(7)*d_phi(j)/2-diff(7)/h)*2*aa(j)/h+&
     &         (fzd(7)*d_phi(j)/2-diff(7)/h)*d_aa(j)/2
      b(5,9)= -por(j)/t_step-(fzd(7)*d_phi(j)/2+diff(7)/h)*2*aa(j)/h+&
     &         (fzd(7)*d_phi(j)/2+diff(7)/h)*d_aa(j)/2
      a(5,10)= -(fzd(8)*d_phi(j)/2-diff(8)/h)*2*aa(j)/h+&
     &          (fzd(8)*d_phi(j)/2-diff(8)/h)*d_aa(j)/2
      b(5,10)= -por(j)/t_step-(fzd(8)*d_phi(j)/2+diff(8)/h)*2*aa(j)/h+&
     &          (fzd(8)*d_phi(j)/2+diff(8)/h)*d_aa(j)/2
      b(5,11)= por(j)/t_step
! Porosity
      g(6)= por(j)-b1_pro/(1+b8*(conc(1,j)**b9))-&
     &             b4_pro/(1+b10*(conc(1,j)**b11))-b7_pro
      b(6,2)= -dd*(conc(1,j)**(b9-1))/((1+b8*(conc(1,j)**b9))**2)&
     &        -ee*(conc(1,j)**(b11-1))/((1+b10*(conc(1,j)**b11))**2)
      b(6,6)= -1.0d0
! H+
      g(7)=conc(1,j)*conc(5,j)-1.0d-20
      b(7,2)= -conc(5,j)
      b(7,7)= -conc(1,j)
! ZnOH+  Zn2+ + OH- --> ZnOH+
      g(8)= conc(6,j)-(10.0**1.33)*conc(1,j)*conc(4,j)
      b(8,2)= (10.0**1.33)*conc(4,j)
      b(8,5)= (10.0**1.33)*conc(1,j)
      b(8,8)= -1.0d0
! HZnO2-   ZnOH+ +2OH- --> HZnO2- + H2O
      g(9)= conc(7,j)-(10.0**4.03)*conc(6,j)*(conc(1,j)**2)
      b(9,2)= 2*(10.0**4.03)*conc(6,j)*conc(1,j)
      b(9,8)= (10.0**4.03)*(conc(1,j)**2)
      b(9,9)= -1.0d0
! ZnO22-  HZnO2- + OH- --> ZnO22- + H2O
      g(10)= conc(8,j)-(10.0**(-2.17))*conc(1,j)*conc(7,j)
      b(10,2)= (10.0**(-2.17))*conc(7,j)
```

```
      b(10,9)= (10.0**(-2.17))*conc(1,j)
      b(10,10)= -1.0d0
! Zn(OH)2  Zn2+ + 2OH- --> Zn(OH)2
      g(11)= (por(j)*conc(9,j)-por_ini(j)*c_ini(9,j))/t_step-&
     &        rate_k*(conc(1,j)*conc(1,j)*conc(4,j)-3.0d-26)
      b(11,2)= 2*rate_k*conc(1,j)*conc(4,j)
      b(11,5)= rate_k*conc(1,j)*conc(1,j)
      b(11,6)= -conc(9,j)/t_step
      b(11,11)= -por(j)/t_step
      return
      end
```

APPENDIX B
PROGRAM LISTING FOR IMPEDANCE CALCULATIONS

The program listings for the impedance calculations presented in Chapters 8 to 10 are given in this appendix. The theoretical development for the cases of ideally-polarized electrodes (Chapter 8), electrodes with local CPE (Chapter 9), and electrodes exhibiting Faradaic reactions (Chapter 10) were similar. The key difference was the boundary condition applied on the electrode surface. The calculations were performed using the collocation package PDE2D developed by Sewell.[90]

B.1   Main Program Listing

```
C       * PDE2D 8.3 MAIN PROGRAM *
C       *** 2D PROBLEM SOLVED (COLLOCATION METHOD) ***
        implicit double precision (a-h,o-z)
        parameter (neqnmx=  99)
C       NXGRID = number of X-grid lines
        PARAMETER (NXGRID= 400)
C       NXGRID = number of X-grid lines
        PARAMETER (NYGRID = 50)
        PARAMETER (NEQN = 2)
        parameter (nzgrid = 1)
        PARAMETER (IRWK8Z=            1)
        PARAMETER (IIWK8Z=            1)
        PARAMETER (NXP8Z=201,NYP8Z=201,NZP8Z=2,KDEG8Z=1)
        common/parm8z/ pi,a,omega,ck,c,deltav,nprob,iprob,DJ,CPEalpha
        dimension xgrid(nxgrid),ygrid(nygrid),zgrid(nzgrid),xout8z(0:nx,0:
       &ny),yout8z(0:nx,0:ny),zout8z(0:nx,0:ny),xcross(100),ycross(100),to
       &ut8z(0:nsave),uout8z(0:nx,0:ny,4*neqn,0:nsave),xres8z(nxp8z),yres8
       &z(nyp8z),zres8z(nzp8z),ures8z(neqn,nxp8z,nyp8z,nzp8z)
        allocatable iwrk8z(:),rwrk8z(:)
        character*40 title
        logical linear,crankn,noupdt,nodist,fillin,evcmpx,adapt,plot,lsqfi
       &t,fdiff,solid,econ8z,ncon8z,restrt,gridid
        common/dtdp14/ sint8z(20),bint8z(20),slim8z(20),blim8z(20)
        common/dtdp15/ evlr8z,ev0r,evli8z,ev0i,evcmpx
        common/dtdp19/ toler(neqnmx),adapt
        common/dtdp30/ econ8z,ncon8z
        common/dtdp45/ perdc(neqnmx)
        common/dtdp46/ eps8z,cgtl8z,npmx8z
        common/dtdp52/ nxa8z,nya8z,nza8z,kd8z
        common/dtdp53/ work8z(nxp8z*nyp8z*nzp8z+9)
        common/dtdp64/ amin8z(4*neqnmx),amax8z(4*neqnmx)
```

```
        pi = 4.0*atan(1.d0)
        zr8z = 0.0
        nxa8z = nxp8z
        nya8z = nyp8z
        nza8z = nzp8z
        kd8z = kdeg8z
C
        nomega=160
        a=0.25
        ck=0.05
        c=3.0d-5
        deltav=0.01
        DJ=1.0
        CPEalpha=0.8
C
      do 78760 iomega=1,nomega
        omega=10**(-5+iprob*0.05)
C#############################################################################
C     A collocation finite element method is used, with bi-cubic Hermite   #
C     basis functions on the elements (small rectangles) defined by the grid #
C     points:                                                              #
C              XGRID(1),...,XGRID(NXGRID)                                   #
C              YGRID(1),...,YGRID(NYGRID)                                   #
C     You will first be prompted for NXGRID, the number of X-grid points,  #
C     then for XGRID(1),...,XGRID(NXGRID).  Any points defaulted will be   #
C     uniformly spaced between the points you define; the first and last   #
C     points cannot be defaulted.  Then you will be prompted similarly     #
C     for the number and values of the Y-grid points.  The rectangle over  #
C     which the PDE system is to be solved is then:                        #
C              XGRID(1) < X < XGRID(NXGRID)                                 #
C              YGRID(1) < Y < YGRID(NYGRID)                                 #
C                                                                          #
C#############################################################################
      call dtdpwx(xgrid,nxgrid,0)
      call dtdpwx(ygrid,nygrid,0)
      XGRID(1) = 0.0d0
      XGRID(NXGRID) = 200
      YGRID(1) = 0.0d0
      YGRID(NYGRID) = 1.0d0
C
      zgrid(1) = 0
      call dtdpwx(xgrid,nxgrid,1)
      call dtdpwx(ygrid,nygrid,1)
C#############################################################################
C     If you don't want to read the FINE PRINT, enter ISOLVE = 1.          #
```

```
C                                                                            #
C       ++++++++++++++ THE "FINE PRINT" (CAN USUALLY BE IGNORED) ++++++++++++++#
C       + The following linear system solvers are available:              +#
C       +                                                                 +#
C       + 1. Sparse direct method                                         +#
C       +                Harwell Library routine MA27 (used by permission) is  +#
C       +                used to solve the (positive definite) "normal"        +#
C       +                equations A**T*A*x = A**T*b.  The normal equations,   +#
C       +                which are essentially the equations which would result +#
C       +                if a least squares finite element method were used    +#
C       +                instead of a collocation method, are substantially    +#
C       +                more ill-conditioned than the original system Ax = b, +#
C       +                so it may be important to use high precision if this  +#
C       +                option is chosen.                                     +#
C#############################################################################
       ISOLVE =          1
C#############################################################################
C       Is this a linear problem? ("linear" means all differential equations   #
C       and all boundary conditions are linear)                                #
C#############################################################################
       LINEAR = .true.
C#############################################################################
C       Give an upper limit on the number of Newton's method iterations        #
C       (NSTEPS) to be allowed for this nonlinear problem.  NSTEPS defaults     #
C       to 15.                                                                  #
C#############################################################################
       NSTEPS = 15
C#############################################################################
C       The solution is saved on an NX+1 by NY+1 rectangular grid covering     #
C       the rectangle (XA,XB) x (YA,YB).  Enter values for XA,XB,YA,YB.        #
C       These variables are usually defaulted.                                 #
C                                                                              #
C       The defaults are XA = XGRID(1),  XB = XGRID(NXGRID)                     #
C                        YA = YGRID(1),  YB = YGRID(NYGRID)                     #
C                                                                              #
C#############################################################################
C          defaults for xa,xb,ya,yb
       xa = xgrid(1)
       xb = xgrid(nxgrid)
       ya = ygrid(1)
       yb = ygrid(nygrid)
       call dtdpx3(nx,ny,0,xa,xb,ya,yb,zr8z,zr8z,hx8z,hy8z,hz8z,xout8z,yo
     &ut8z,zout8z,npts8z)

       subroutine tran8z(itrans,x,y,z8z)
```

```
      implicit double precision (a-h,o-z)
      common /dtdp41/xcart(3),x1grad(3),x2grad(3),x3grad(3),x1hess(3,3),
     &x2hess(3,3),x3hess(3,3)
      common/parm8z/ pi,a,omega,ck,c,deltav,nprob,iprob,DJ,CPEalpha
C##############################################################################
C     If your region is rectangular, enter ITRANS=0, and you need not read    #
C     the FINE PRINT.                                                         #
C                                                                             #
C     + If X,Y represent polar or other non-Cartesian coordinates, you can   +#
C     + reference the Cartesian coordinates X1,X2 and derivatives of your    +#
C     + unknowns with respect to these coordinates, when you define your     +#
C     + PDE coefficients, boundary conditions, and volume and boundary       +#
C     + integrals, if you enter ITRANS .NE. 0.  Enter:                       +#
C     +   ITRANS = 1, if X,Y are polar coordinates, that is, if              +#
C     +                X=R, Y=Theta, where    X1 = R*cos(Theta)              +#
C     +                                       X2 = R*sin(Theta)              +#
C     +   ITRANS = -1, same as ITRANS=1, but X=Theta, Y=R                    +#
C     +   ITRANS = 3, to define your own coordinate transformation.  In      +#
C     +                this case, you will be prompted to define X1,X2 and   +#
C     +                their first and second derivatives in terms of X,Y.   +#
C     +   ITRANS = -3, same as ITRANS=3, but you will only be prompted to    +#
C     +                define XCART(*) = (X1,X2); their first and second     +#
C     +                derivatives will be approximated using finite         +#
C     +                differences.                                          +#
C     +   When ITRANS = -3 or 3, the first derivatives of X1,X2 must all     +#
C     +   be continuous.                                                     +#
C##############################################################################
      ITRANS =          -3
      XCART(1) = a*sqrt((1+x**2)*abs(1-y**2))
      XCART(2) = a*x*y
      xcart(3) = z8z
      x3grad(3) = 1
      return
      end
```

B.2   Subroutine Listing

```
      subroutine pdes8z(yd8z,i8z,j8z,kint8z,x,y,z8z,t,uu8z)
      implicit double precision (a-h,o-z)
      parameter (neqnmx=  99)
      common /dtdp5x/un8z(10,neqnmx)
      common /dtdp18/normx,normy,nz8z
      double precision normx,normy,nz8z,norm1,norm2,n38z
      dimension uu8z(10,neqnmx)
      common/parm8z/ pi,a,omega,ck,c,deltav,nprob,iprob,DJ,CPEalpha
      zr8z = 0.0
```

```fortran
      pr  = uu8z(1, 1)
      prx = uu8z(2, 1)
      pry = uu8z(3, 1)
      prxx= uu8z(5, 1)
      pryy= uu8z(6, 1)
      prxy= uu8z(8, 1)
      pryx= uu8z(8, 1)
      pii  = uu8z(1, 2)
      piix = uu8z(2, 2)
      piiy = uu8z(3, 2)
      piixx= uu8z(5, 2)
      piiyy= uu8z(6, 2)
      piixy= uu8z(8, 2)
      piiyx= uu8z(8, 2)
      call dtdpcd(x,y,z8z)
      call dtdpcb(x,y,z8z,normx,normy,nz8z,x1,x2,x38z,norm1,norm2,n38z,3)
      call dtdpcc(x,y,z8z,
     &          prx,pry,zr8z,prxx,pryy,zr8z,prxy,zr8z,zr8z,
     & x1,x2,x38z,pr1,pr2,u38z,pr11,pr22,u338z,pr12,u138z,u238z,
     & pr21,u318z,u328z,dvol,darc)
      call dtdpcc(x,y,z8z,
     &          piix,piiy,zr8z,piixx,piiyy,zr8z,piixy,zr8z,zr8z,
     & x1,x2,x38z,pii1,pii2,u38z,pii11,pii22,u338z,pii12,u138z,u238z,
     & pii21,u318z,u328z,dvol,darc)
                      if (i8z.eq.0) then
      yd8z = 0.0
C#############################################################################
C    Enter FORTRAN expressions to define the boundary condition functions,  #
C    which may be functions of                                              #
C            X,Y,pr,prx,pry,                                                 #
C                pii,piix,piiy                                               #
C#############################################################################
             if (j8z.eq.0) then
      yd8z = 0.0
C                                                       F1 DEFINED
      if (i8z.eq.    1) yd8z =
     & 2*x*prx+(1+x**2)*prxx-2*y*pry+(1-y**2)*pryy
C                                                       F2 DEFINED
      if (i8z.eq.    2) yd8z =
     & 2*x*piix+(1+x**2)*piixx-2*y*piiy+(1-y**2)*piiyy
             else
             endif
      return
      end
C
```

```fortran
      subroutine gb8z(gd8z,ifac8z,i8z,j8z,x,y,z8z,t,uu8z)
      implicit double precision (a-h,o-z)
      parameter (neqnmx=  99)
      dimension uu8z(10,neqnmx)
C        un8z(1,I),un8z(2,I),... hold the (rarely used) values
C        of UI,UIx,... from the previous iteration or time step
      common /dtdp5x/ un8z(10,neqnmx)
      common /dtdp18/normx,normy,nz8z
      double precision none,normx,normy,nz8z,norm1,norm2,n38z
      common/parm8z/ pi,a,omega,ck,c,deltav,nprob,iprob,DJ,CPEalpha
      none = dtdplx(2)
      zr8z = 0.0
      pr  = uu8z(1, 1)
      prx = uu8z(2, 1)
      pry = uu8z(3, 1)
      pii  = uu8z(1, 2)
      piix = uu8z(2, 2)
      piiy = uu8z(3, 2)
      call dtdpcd(x,y,z8z)
      call dtdpcb(x,y,z8z,normx,normy,nz8z,x1,x2,x38z,norm1,norm2,n38z,3
     &)
      call dtdpcb(
     & x,y,z8z,prx,pry,zr8z,x1,x2,x38z,pr1,pr2,u38z,2)
      call dtdpcb(
     & x,y,z8z,piix,piiy,zr8z,x1,x2,x38z,pii1,pii2,u38z,2)
      if (j8z.eq.0) gd8z = 0.0
C#############################################################################
C     Enter FORTRAN expressions to define the boundary condition functions,  #
C     which may be functions of                                              #
C                                                                            #
C              X,Y,pr,prx,pry,                                               #
C                   pii,piix,piiy and (if applicable) T                      #
C#############################################################################
            if (ifac8z.eq. 1) then
C#############################################################################
C                                                                            #
C     First define the boundary conditions on the face X = XGRID(1).         #
C#############################################################################
                     if (j8z.eq.0) then
C                                                 G1 DEFINED
      if (i8z.eq.    1) gd8z =
C For Ideally-Polarized Blocking Electrodes
     & omega*pii+prx/y
C For Blocking Electrodes with Local CPE
     & omega*((deltav-pr)*cos(CPEalpha*pi/2)+pii*sin(CPEalpha*pi/2))+prx/y
```

178

```fortran
C For Electrode Subject to a Faradaic Reaction
      & prx/y+omega*pii+(deltav-prs)*DJ


C                                                    G2 DEFINED
         if (i8z.eq.     2) gd8z =
C For Ideally-Polarized Blocking Electrode
      & omega*deltav-omega*pr+piix/y
C For Blocking Electrodes with Local CPE
      & omega*(deltav*sin(CPEalpha*pi/2)-pii*cos(CPEalpha*pi/2)-
      & pr*sin(CPEalpha*pi/2))+piix/y
C For Electrode Subject to a Faradaic Reaction
      & piix/y+omega*(deltav-pr)-pii*DJ


                              else
                              endif
                 endif
                 if (ifac8z.eq. 2) then
C##############################################################################
C     Now define the boundary conditions on the face X = XGRID(NXGRID).      #
C##############################################################################
                              if (j8z.eq.0) then
C                                                    G1 DEFINED
         if (i8z.eq.     1) gd8z = pr
C                                                    G2 DEFINED
         if (i8z.eq.     2) gd8z = pii
                              else
                              endif
                 endif
                 if (ifac8z.eq. 3) then
C##############################################################################
C     Now define the boundary conditions on the face Y = YGRID(1).          #
C##############################################################################
                              if (j8z.eq.0) then
C                                                    G1 DEFINED
         if (i8z.eq.     1) gd8z = pry
C                                                    G2 DEFINED
         if (i8z.eq.     2) gd8z = piiy
                              else
                              endif
                 endif
                 if (ifac8z.eq. 4) then
C##############################################################################
C     Now define the boundary conditions on the face Y = YGRID(NYGRID).      #
C##############################################################################
                              if (j8z.eq.0) then
```

```fortran
C                                                      G1 DEFINED
      if (i8z.eq.     1) gd8z = pry
C                                                      G2 DEFINED
      if (i8z.eq.     2) gd8z = piiy
                        else
                        endif
          endif
      return
      end
C
      subroutine postpr(tout,nsave,xout,yout,nx,ny,uout,neqn)
      implicit double precision (a-h,o-z)
      dimension xout(0:nx,0:ny),yout(0:nx,0:ny),zout(0:nx,0:ny),
     &rout(0:nx,0:ny),tout(0:nsave),phi_re(0:nx,0:ny),phi_im(0:nx,0:ny),
     & dprx(0:nx,0:ny),dpry(0:nx,0:ny),dpiix(0:nx,0:ny),
     & dpiiy(0:nx,0:ny),diff(0:nx,0:ny),trans(0:nx,0:ny)
      dimension cur_re(0:nx,0:ny),cur_im(0:nx,0:ny),cur(0:nx,0:ny),
     & subloc_re(0:nx,0:ny),subloc_im(0:nx,0:ny),ocal_re(0:nx,0:ny),
     & ocal_im(0:nx,0:ny),resis_re(0:nx,0:ny),resis_im(0:nx,0:ny),
     & gcur_re(0:ny),gcur_im(0:ny)
      dimension uout(0:nx,0:ny,4,neqn,0:nsave)
      common/parm8z/ pi,a,omega,ck,c,deltav,nprob,iprob,DJ,CPEalpha
      UOUT(I,J,1,IEQ,L) = U-sub-IEQ
      UOUT(I,J,2,IEQ,L) = UX-sub-IEQ
      UOUT(I,J,3,IEQ,L) = UY-sub-IEQ

         open (unit=33,file='data_1.sav')
         open (unit=34,file='loc_1.txt')
         open (unit=35,file='global.txt')

  9      format (10E17.8)
 10      format (12E20.12)
 11      format (10E17.8)
 13      format (7E17.8)

         DO I=0,NX
         DO J=0,NY
          zout(i,j)= a*xout(i,j)*yout(i,j)
          trans(i,j)= sqrt((1+xout(i,j)**2)*abs(1-yout(i,j)**2))
          rout(i,j)=a*trans(i,j)
          phi_re(i,j)=uout(i,j,1,1,1)
          phi_im(i,j)=uout(i,j,1,2,1)
          dprx(i,j)= UOUT(I,J,2,1,1)
          dpry(i,j)= UOUT(I,J,3,1,1)
          dpiix(i,j)=UOUT(I,J,2,2,1)
```

```fortran
      dpiiy(i,j)=UOUT(I,J,3,2,1)
      z8z = 0.0
      call dtdpcd(x,y,z8z)
      call dtdpcb(x,y,z8z,z18z,z28z,z38z,x1,x2,x38z,
   &  d18z,d28z,d38z,1)
      write(33,9)  xout(i,j),yout(i,j),zout(i,j),rout(i,j),
   &  phi_re(i,j),phi_im(i,j),dprx(i,j),dpry(i,j),dpiix(i,j),
   &  dpiiy(i,j)
     END DO
     END DO

      do i=0,nx
      do j=0,ny
       diff(i,j)=deltav-phi_re(i,j)
       cur_re(i,j)=-ck*dprx(i,j)/(a*yout(i,j))
       cur_im(i,j)=-ck*dpiix(i,j)/(a*yout(i,j))
       cur(i,j)=cur_re(i,j)**2+cur_im(i,j)**2
       subloc_re(i,j)=deltav*cur_re(i,j)/cur(i,j)
       subloc_im(i,j)=-deltav*cur_im(i,j)/cur(i,j)
       ocal_re(i,j)= (cur_re(i,j)*diff(i,j)-phi_im(i,j)*cur_im(i,j))/
   &   cur(i,j)
       ocal_im(i,j)=-(cur_im(i,j)*(deltav-phi_re(i,j))+
   &   phi_im(i,j)*cur_re(i,j))/cur(i,j)
       resis_re(i,j)=(phi_re(i,j)*cur_re(i,j)+phi_im(i,j)*
   &                 cur_im(i,j))/cur(i,j)
       resis_im(i,j)=-(phi_re(i,j)*cur_im(i,j)-phi_im(i,j)*
   &                 cur_re(i,j))/cur(i,j)
     write(34,10) xout(i,j),yout(i,j),zout(i,j),rout(i,j),
   & cur_re(i,j),cur_im(i,j),subloc_re(i,j),subloc_im(i,j),
   & ocal_re(i,j),ocal_im(i,j),resis_re(i,j),resis_im(i,j)
      enddo
      enddo
C
      ttcur_re=0.0d0
      ttcur_im=0.0d0
     do j=0,ny
      if ((j.eq.0).or.(j.eq.ny)) then
         gcur_re(j)=etacur_re(0,j)
         gcur_im(j)=etacur_im(0,j)
       else if (mod(j,2).eq.1) then
         gcur_re(j)=4*etacur_re(0,j)
         gcur_im(j)=4*etacur_im(0,j)
       else if (mod(j,2).eq.0) then
         gcur_re(j)=2*etacur_re(0,j)
         gcur_im(j)=2*etacur_im(0,j)
```

```
          endif
          enddo
C Integrate current density on the electrode surface
          do j=0,ny
           value_re= gcur_re(j)
           value_im= gcur_im(j)
c          value_re=(gcur_re(j)+gcur_re(j+1))*(rout(0,j+1)-rout(0,j))/2
           ttcur_re=ttcur_re+value_re
           ttcur_im=ttcur_im+value_im
          enddo
C Calculate Global Impedance
           tcur_re=ttcur_re*0.02/3
           tcur_im=ttcur_im*0.02/3
           globalim_re=deltav*tcur_re/(tcur_re**2+tcur_im**2)
           globalim_im=deltav*tcur_im/(tcur_re**2+tcur_im**2)
           dimenim_re=globalim_re*ck*a
           dimenim_im=globalim_im*ck*a
           Reff=4*dimenim_re
           c_ceff=dimenim_im*omega*pi

          write(35,11) omega,tcur_re,tcur_im,globalim_re,globalim_im,
     &    dimenim_re,dimenim_im,Reff,c_ceff
       return
       end
```

APPENDIX C
MATHEMATICAL MODEL FOR A DISSOLUTION OF ZINC ROTATING DISK ELECTRODE

As a preliminary step towards development of the model for the cathodic delamination, a one-dimensional, transient model was developed for the dissolution and passivation of a rotating zinc disk in a dilute solution of NaCl. The model treated explicitly the coupling of mass transport phenomena, electrochemical reactions and homogeneous reactions.

C.1 Model Development

The advantages of using a rotating disk electrode system are that the hydrodynamics conditions are well understood and the fluid mechanics associated within the system is well studied. A schematic illustration of the flow field generated by a rotating disk is presented in Figure where z is the direction perpendicular to the disk and r is direction along the disk electrode. The rotation of the disk causes a spiral movement of the fluid resulting in a net velocity toward the disk and in the radial direction.

C.1.1 Mass Transfer

The mass transfer of a species i in an electrochemical system is governed by equation (2–1) where the flux of a species i is given in equation (2–2). Combination with the Nernst-Einstein equation (equation (2–4)), under the assumptions of a steady-state condition and an incompressible electrolyte, the governing equation for c_i can be rewritten as

$$0 = z_i F \frac{D_i}{RT} c_i \nabla \cdot (c_i \nabla \Phi) + D_i \nabla^2 c_i - v \nabla c_i + R_i \qquad \text{(C–1)}$$

where the terms on the right side represent the contribution of migration, diffusion, convection, and production by homogeneous reactions, respectively.

The steady flow created by an infinite disk rotating at a constant angular velocity in a fluid with constant physical properties was presented by Newman.[46] Under the assumption that the velocities in r and θ direction are negligible, the velocity normal to
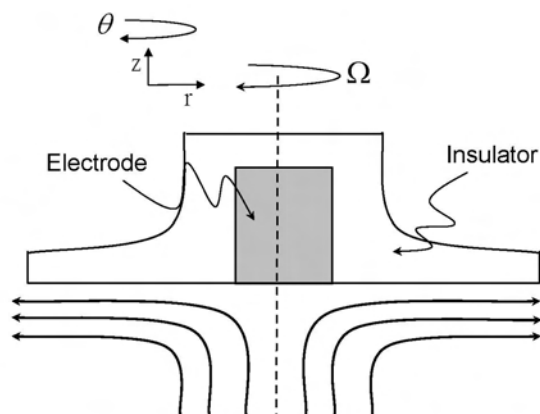
Figure C-1. Schematic representation of a rotating disk electrode system in which a disk electrode is embedded in a large insulator.

the disks that brings reactants to the surface is expected to follow

$$v_z = \sqrt{\nu\Omega} H\left(z\sqrt{\frac{\Omega}{\nu}}\right) \qquad (C\text{--}2)$$

where ν is the kinematic viscosity and Ω. Near the electrode surface, the dimensionless velocity H in equation (C–2) can be expressed as a power series

$$H = -a\left(z\sqrt{\frac{\Omega}{\nu}}\right)^2 + \frac{1}{3}\left(z\sqrt{\frac{\Omega}{\nu}}\right)^3 + \frac{b}{6}\left(z\sqrt{\frac{\Omega}{\nu}}\right)^4 + \dots \qquad (C\text{--}3)$$

where the coefficients a and b have values of 0.51023 and -0.616, respectively.

C.1.2 Electrode Kinetics

The electrochemical reactions of interest in the present model involved zinc dissolution (4–6) and oxygen reduction (4–7). Under the assumption that the electrochemical reaction considered are irreversible, the current densities due to zinc dissolution followed the Bulter-Volmer expression. The oxygen reduction was assumed to be mass-transfer-limited; thus, the limiting current density, shown in equation (2–39), depends on the concentration of oxygen in the bulk. The thickness of the diffusion layer x seen in equation (2–39), in a

cylindrical coordinate, is a function of rotation speed by

$$\delta = \left(\frac{1}{aSc}\right)^{1/3} \left(\frac{\nu}{\Omega}\right)^{1/2} \Gamma\left(\frac{1}{3}\right) \tag{C–4}$$

where Sc is Schmidt number and $\Gamma\left(\frac{1}{3}\right)$ is the gamma function of $1/3$.

C.1.3 Homogeneous Reactions

The oxygen reduction taking place underneath the coating results in an increase of pH in the interfacial degraded layer. For zinc, a series of chemical reactions associated with Zn^{2+} hydrolysis is possible in alkaline solutions.[66, 67] In the presented model, multiple homogeneous reactions, including water dissociation and a series of reactions associated with Zn^{2+} hydrolysis, were considered. The mechanisms and equilibrium conditions of these chemical reactions are summarized in Table 4-2.[67]

C.1.4 Boundary Condition

At the far boundary condition, the concentrations and solution potential were fixed at bulk conditions $c_{i,\infty}= 1.26 \times 10^{-3}$ M and $\Phi_\infty=0$. On the boundary of the metal surface the zero-flux condition was used for the chemically inert species Na^+ and Cl^-. The concentration of oxygen was set as zero because the oxygen reduction reaction was assumed to be mass-transfer limited. The boundary conditions at the metal surface for Zn^{2+} and OH^- were obtained by relating their fluxes with the current densities due to the electrochemical reactions on the metal surface. The equilibrium conditions listed in Table 4-2 were treated as boundary conditions for H^+, $ZnOH^+$, $HZnO_2^-$, and ZnO_2^{2-}.

C.1.5 Solution Method

The system of coupled, non-linear, partial differential equations required an iterative method to converge on a solution starting from an initial guess. A tri-diagonal method, BAND algorithm, was chosen to calculate the distribution of c_i and Φ. The mathematical model was developed using *Microsoft Visual Fortran, Version 9.0* with double precision accuracy.[74]
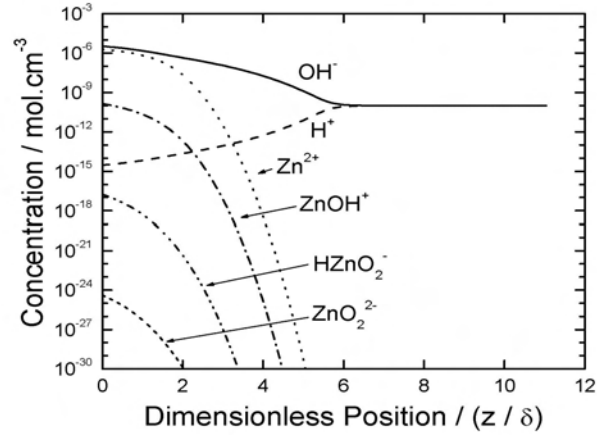
Figure C-2. Calculated concentration distributions of species of OH^-, Zn^{2+}, H^+, $ZnOH^+$, $HZnO_2^-$, and ZnO_2^{2-} on electrode surface.

C.2   Results and Discussion

The calculated distributions satisfied the coupled phenomena of species mass transport and electronutrality. The domain length was 0.2 cm, the rotating speed was Ω =50 rad/s, the thickness of the diffusion layer was $x = 0.018$ cm, and the metal potential was chosen to be $\Psi = -0.77$ V.

The concentration distributions of the chemical species are presented in Figure C-2 as a function of dimensionless position. Due to the electrochemical reactions occurring on the electrode surface, the concentrations of OH^- and Zn^{2+} have a maximum near the surface. The concentrations of the species produced in the homogeneous reactions (H^+, $ZnOH^+$, $HZnO_2^-$, and ZnO_2^{2-}) are largest near the surface and decrease with increasing distance away from the electrode.

At steady state, based on the mass balance equation, the homogenous rate for species R_i can be written by

$$R_i = \nabla \cdot N_i \tag{C-5}$$

Thus, the rate for each of the homogeneous reactions can be expressed as follows:

$$R_1 = \nabla \cdot N_{H^+} \tag{C-6}$$
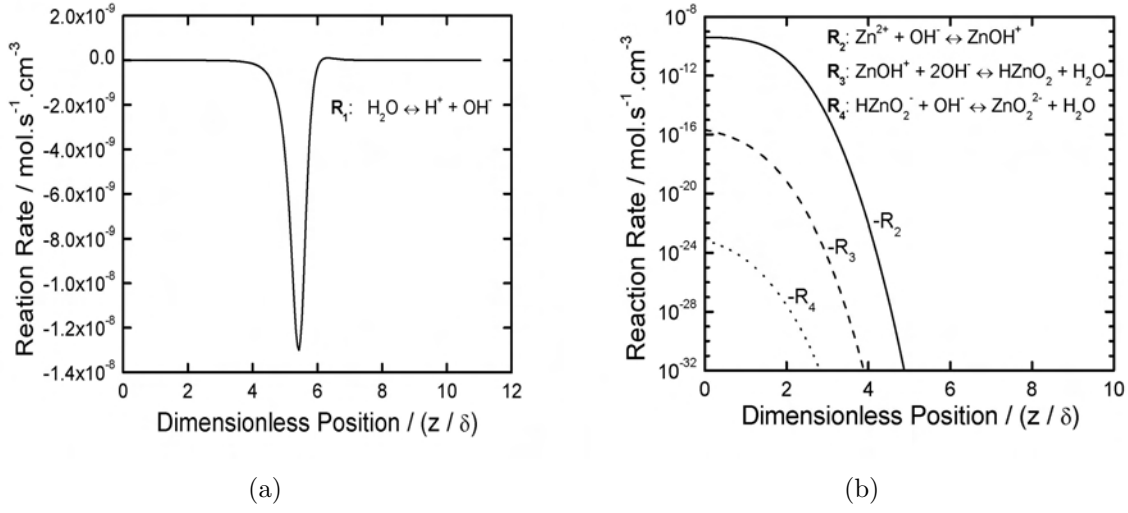
Figure C-3. Calculated rate of the homogeneous reactions included in the model. a) Water disassociation reaction; and b) Zinc hydrolysis reactions.

$$R_2 = -\nabla \cdot N_{Zn^{2+}} \tag{C–7}$$

$$R_3 = \nabla \cdot N_{HZnO_2^-} + \nabla \cdot N_{ZnO_2^{2-}} \tag{C–8}$$

and

$$R_4 = \nabla \cdot N_{ZnO_2^{2-}} \tag{C–9}$$

The rate of water dissociation is plotted in Figure C-3(a) as a function of dimensionless position. The OH^- ions generated near the electrode surface combine with H^+ ions in the solution to form water molecular. Due to the constraint of the equilibrium condition, the concentration of H^+ ions is small near the electrode; consequently, the rate of this reaction is approximately zero near the surface. When z/δ approaches 5.4, the concentrations of OH^- ions becomes close to that of H^+ ions, leading to the sharp increase in Figure C-3(a).

The rates of the zinc hydrolysis are presented in Figure C-3(b) as a function of dimensionless position. The negative value of R_2 indicates that $ZnOH^+$ ions dissociate into Zn^{2+} and OH^- ions. This implies that, after the Zn^{2+} and OH^- ions are formed, the $ZnOH^+$ ions were immediately produced near the surface. This can also be used to explain the negative rates of reactions 3 and 4.

C.3 Conclusion

A mathematical model for one-dimensional, steady-state rotating disk electrode system was developed. In this model, multiple heterogeneous reactions and equilibrated homogeneous reactions were coupled with mass transport due to migration, diffusion and convection. The calculated results demonstrates that after corrosion reaction occurs the pH value of the electrolyte has been changed significantly due to the formation of OH^- ions. The results also show the coupling among the multiple homogeneous reactions that take place simultaneously in the system.

APPENDIX D
MATHEMATICAL MODEL FOR GALVANIC COUPLING IN A 2-D CELL

As a step toward the development of comprehensive model for cathodic delamination, a two-dimensional model was developed that calculated the distributions of concentrations and potential associated with cut-edge corrosion. Within the present model, the Zn electrode serves as the local anode and steel as the local cathode. The purpose of the model was to understand the set up of the galvanic couple by starting from uniform distributions of all reactive species. The uniform initial conditions permit the concentration and potential gradients appearing later due to the electrochemical reactions. Within the model, multiple homogeneous reactions, including water dissociation and a series of reactions associated with hydrolysis were assumed to occur simultaneously in the solution phase.

D.1   Model Development

A schematic representation of the Zn-Fe model is given in Figure D-1 where Zn acts as an anode, Fe acts as a cathode, and NaCl serves as the electrolyte. An insulator is inserted between the two electrodes and the two vertical walls are composed of insulators as well. Zinc dissolution was assumed to take place on the anode, whereas oxygen reduction and hydrogen evolution were both assumed to occur on the cathode. No iron dissolution was considered on the steel.
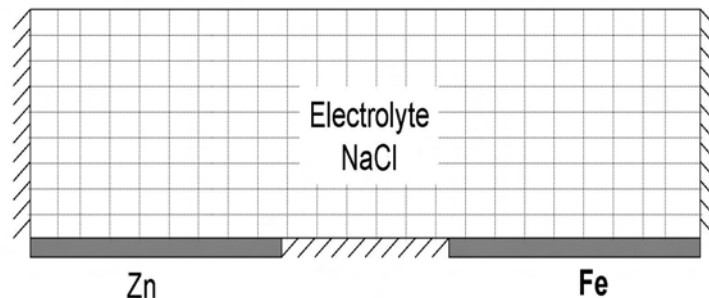
Figure D-1. Schematic representation of a two electrode cell in which Zn serves a local anode and Fe as a local cathode.

The development of the present model is similar to that presented in Appendix C. The key differences were that the governing equations were expanded in a two-dimensional form and different boundary conditions were applied on the anode, cathode and insulator. In this model, the anodic and cathodic current expression are applied on the Zn ($0<x<0.016$ cm) and Fe ($0.024<x<0.04$ cm) electrodes, respectively. On the region where the insulator is inserted ($0.016<x<0.024$ cm), a zero-flux condition was employed for all species.

D.2   Solution Method

The calculations by Allahar show that the accuracy of applied numerical technique plays an important role on determining whether the equilibrium relations that describe the homogeneous reactions can or cannot be incorporated.[21, 22] As a result, a numerical technique with high-order accuracy is extremely crucial for this particular development.

In the development of the present model, a commercial program based upon collocation method, PDE2D, was chosen. The use of the collocation method yields approximations that are of high-order accuracy even when coupled nonlinear partial differential equations are solved in a multidimensional domain. With this PDE2D program, all homogeneous reaction can be included simultaneously and the discontinuity at the bottom boundary can be handled without numerical difficulties.

D.3   Results and Discussion

The dimension of the domain was set to be 0.04 cm in the direction along the electrodes and 0.02 cm in the direction away from the electrodes. At the bottom boundary, $0<x<0.016$ cm is the region where anodic reaction is dominant, and $0.024<x<0.04$ cm is the region where cathodic reactions are more important. The potential on the metal was chosen as $V=-1.1$ V_{SHE}. The polarization parameters for zinc dissolution included $\beta_{\text{Zn}}=0.08$ $V/decade$, $i_{0,\text{Zn}}=12$ mA/cm^2, $E_{0,\text{Zn}}=-0.763$ V_{SHE}, $\beta_{\text{H}_2}=0.18$ $V/decade$, $i_{0,\text{H}_2}=10^{-5}mA/cm^2$, and $E_{0,\text{H}_2}=-0.828$ V_{SHE}.
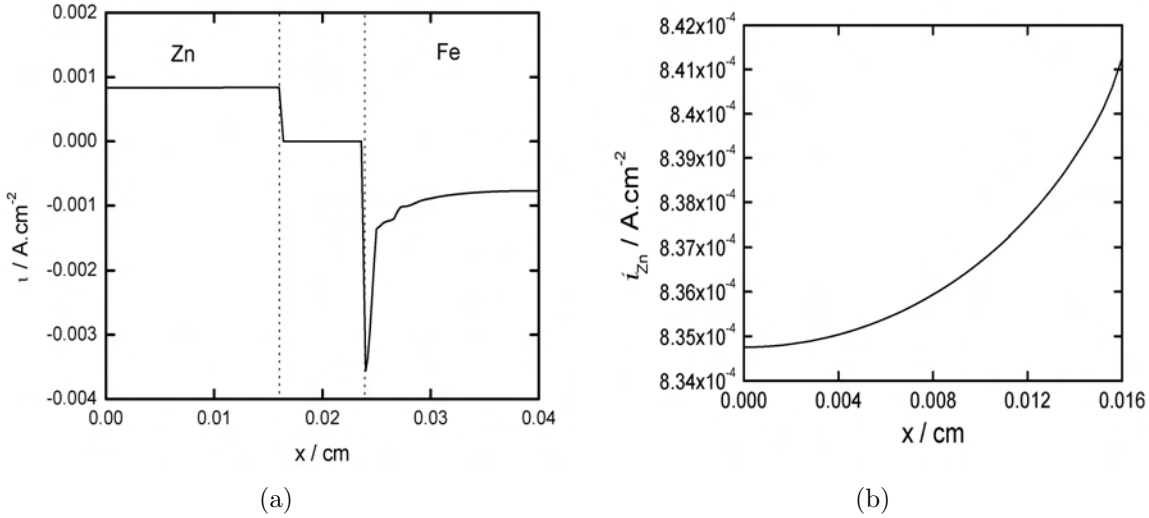
Figure D-2. Calculated current density distributions along the x axis. a) $0 < x < 0.04$ cm; and b) $0 < x < 0.016$ cm.

The overall current density distribution along the x axis is given in Figure D-2(a) where the anodic current density is displayed within $0 < x < 0.016$ cm, and the cathodic current density is within $0.024 < x < 0.04$ cm. The current density drops to zero between 0.016 cm and 0.024 cm, corresponding to the position of the insulator. The distribution of the anodic current density on the Zn electrode is presented in Figure D-2(b). It is clear in Figure D-2(b) that the anodic current density increases when approaching the edge of the electrode. Both Figures D-2(a) and D-2(b) confirm that the geometry of the electrodes constrain the distributions of current density in a way such that the periphery of the disk has a greater accessibility. The distributions given in Figure D-2 also show that the applied collocation method is able to handle the discontinuous transition from the insulator to the two electrodes.

The concentration distributions of Zn^{2+} and OH^- ions in units of mole/cm^3 are presented in Figure D-3 in contour format. Due to the local anodic reaction, the concentration of Zn^{2+} ions has a largest around the Zn electrode and decreases with increasing distance away from the local anode. A similar behavior was observed in the concentration distribution of OH^- ions.
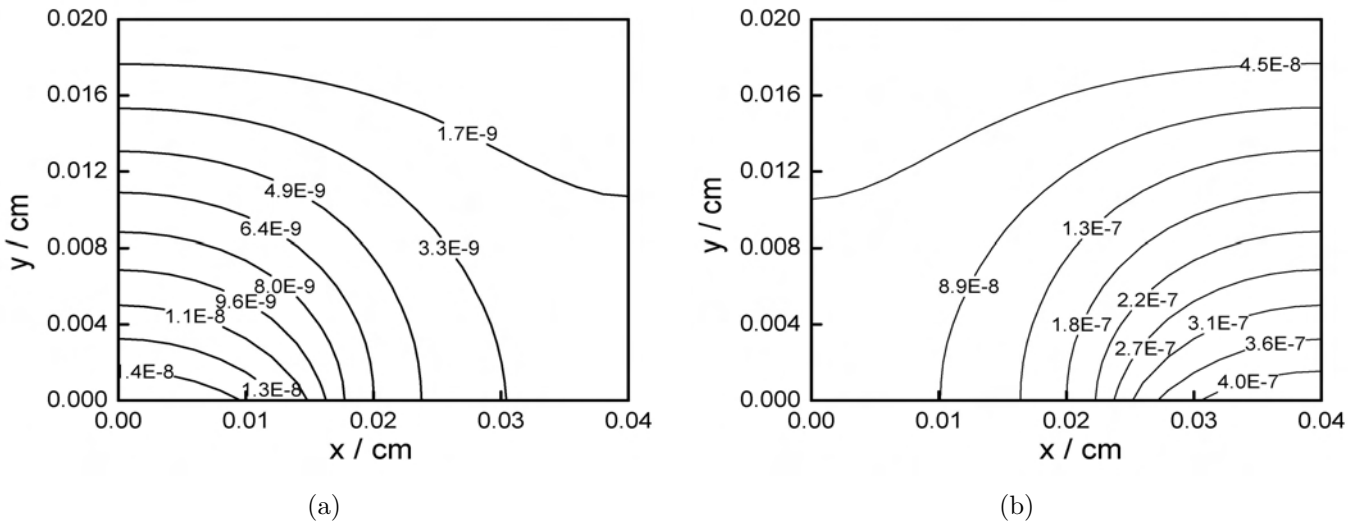
Figure D-3. Calculated distributions of concentration in a unit of mole/cm^3. a) Zn^{2+} ions; and b) OH^- ions.
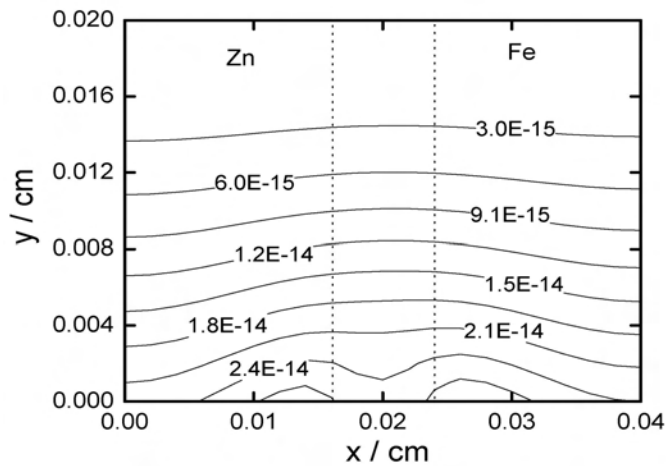
Figure D-4. Calculated distribution of ratio of $\frac{c_{Zn^{2+}} \cdot c^2_{OH^-}}{K_{sp}}$ where K_{sp} is the standard solubility product of $Zn(OH)_{2(s)}$.

The calculated concentrations of Zn^{2+} and OH^- ions can be used to predict the formation of corrosion product $Zn(OH)_{2(s)}$. The predicted distribution of precipitated $Zn(OH)_{2(s)}$ is presented in Figure D-4. The magnitude in Figure D-4 is estimated by $\frac{c_{Zn^{2+}} \cdot c^2_{OH^-}}{K_{sp}}$ where K_{sp} is the standard solubility product of $Zn(OH)_{2(s)}$ with a value of 3×10^{-17} (mol/liter)^3 at room temperature.[10] The value of $\frac{c_{Zn^{2+}} \cdot c^2_{OH^-}}{K_{sp}}$, which reflects the driving force of forming $Zn(OH)_{2(s)}$, is largest near the local cathode and decreases with the distance away from the electrode.

D.4   Conclusion

The presented work serves as a preliminary approach for modeling the two-dimensional cathodic delamination system. The uniform initial concentration distributions applied in the model allowed us to simulate the natural establishment of the galvanic element. The computational results indicate that the numerical difficulties associated with including homogeneous reactions in a two spatial dimension and with the discontinuous region at the boundary have been overcome in a steady-state model. The results also showed that the unique configuration of the delamination system led to an interesting distribution pattern of the species produced in the homogeneous reactions. The employed numerical technique will be tested later for treating precipitation of $Zn(OH)_2$ in a transient model.

APPENDIX E
PARAMETER SENSITIVITY ANALYSIS

Due to the use of porosity-pH, poisoning-pH and blocking-pH relations, there are several fitting parameters used in the cathodic delamination program. It is important to explore the sensitivities of these parameters on the simulation results. The sensitivity analysis is presented in this appendix. In the report, each fitting parameter were analyzed using three different values. The velocity of the moving fronts and the kinetic analysis were checked to determine the sensitivity.

E.1   Porosity

There are four fitting parameters used in the construction of the equilibrated porosity-pH relation (see Figure 4-2). The fitting parameter $b_{\varepsilon,1}$ is associated with the constant value seen at the high pH region. The fitting parameter $b_{\varepsilon,2}$ governs the slope of the curve that increases from low pH to high pH regions. The deflection point located in the middle of the increasing curve is controlled by the fitting parameter $b_{\varepsilon,3}$. The constant value seen at the low pH region is governed by the fitting parameter $b_{\varepsilon,4}$.

E.1.1 $b_{\varepsilon,1}$

The sensitivity analysis for the fitting parameter $b_{\varepsilon,1}$ is summarized in Table E-1. When the fitting parameter $b_{\varepsilon,1}$ that governs the porosity at high pH increases from 0.01 to 0.1, the rate of the delamination determined by both potential front and porosity front increase by approximately 60 percent. It is observed that when $b_{\varepsilon,1}$ is equal 0.1, the interfacial potential in the intact region increases with delamination time. The change of $b_{\varepsilon,1}$ from 0.01 to 0.001 decreases the moving velocities by approximately 40 percent. The reaction order, however, is not influenced by the change to the fitting parameter $b_{\varepsilon,1}$.

Table E-1. Sensitivity analysis for $b_{\varepsilon,1}$

	$b_{\varepsilon,1} = 0.001$	$b_{\varepsilon,1} = 0.01$	$b_{\varepsilon,1} = 0.1$
Potential Front Velocity	1.33	2.19	3.58
Porosity Front Velocity	1.09	1.63	3.27
Reaction Order for Potential Front	0.54	0.55	0.56
Reaction Order for Porosity Front	0.59	0.6	0.6

Table E-2. Sensitivity analysis for $b_{\varepsilon,2}$

	$b_{\varepsilon,2} = -5$	$b_{\varepsilon,2} = -3$	$b_{\varepsilon,2} = -2$
Potential Front Velocity	2.26	2.19	1.98
Porosity Front Velocity	2.20	1.63	1.18
Reaction Order for Potential Front	0.56	0.55	0.55
Reaction Order for Porosity Front	0.63	0.6	0.6
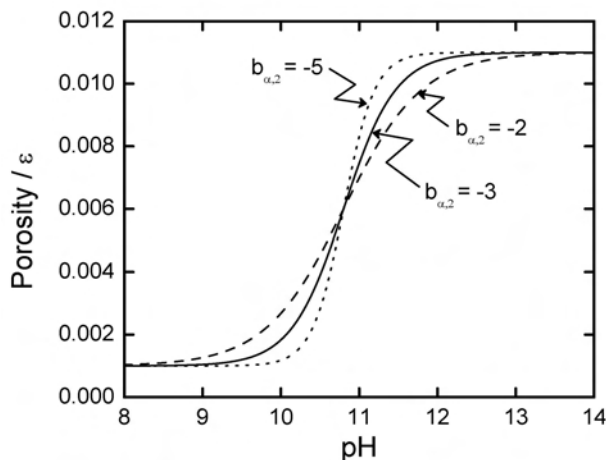
Figure E-1. The sensitivity of the slope of the increasing curve to $b_{\varepsilon,2}$.

E.1.2 $b_{\varepsilon,2}$

The sensitivity analysis for the fitting parameter $b_{\varepsilon,2}$ is summarized in Table E-2. As illustrated in Figure E-1, the slope of the increasing curve in Figure 6-6 becomes steeper when the fitting parameter $b_{\varepsilon,2}$ changes from -2 to -5. The increase in the slope results in a sight increase in the velocities of both potential front and porosity front. The other observed feature is that the rates of the two fronts are approximately equal when the slope is steep. It is also observed that the shape of the resulting potential distributions (see Figure 6-6) is also influenced by this parameter. The reaction order, however, is not influenced by the change in $b_{\varepsilon,2}$.

E.1.3 $b_{\varepsilon,3}$

The sensitivity analysis for the fitting parameter $b_{\varepsilon,3}$ is summarized in Table E-3. The deflection point of the increasing curve seen in Figure 4-2 shifts from left to right when the fitting parameter $b_{\varepsilon,3}$ increases from 9.8 to 11.8. When the deflection point is

Table E-3. Sensitivity analysis for $b_{\varepsilon,3}$

	$b_{\varepsilon,3} = 9.8$	$b_{\varepsilon,3} = 10.8$	$b_{\varepsilon,3} = 11.8$
Potential Front Velocity	2.73	2.19	1.73
Porosity Front Velocity	2.27	1.63	0.5
Reaction Order for Potential Front	0.53	0.55	0.56
Reaction Order for Porosity Front	0.54	0.6	1.1

Table E-4. Sensitivity analysis for $b_{\varepsilon,4}$

	$b_{\varepsilon,4} = 10^{-4}$	$b_{\varepsilon,4} = 10^{-3}$	$b_{\varepsilon,4} = 10^{-2}$
Potential Front Velocity	1.94	2.19	3.66
Porosity Front Velocity	1.62	1.63	2.98
Reaction Order for Potential Front	0.56	0.55	0.56
Reaction Order for Porosity Front	0.61	0.6	0.72

pushed to high pH region, the velocities of the fronts decrease. For $b_{\varepsilon,3} = 11.8$, the velocity of the porosity front decreases to 0.5 mm/hr and the reaction order analysis shows a kinetic-controlled mechanism for the porosity front.

E.1.4 $b_{\varepsilon,4}$

The sensitivity analysis for the fitting parameter $b_{\varepsilon,4}$ is summarized in Table E-4. The fitting parameter $b_{\varepsilon,4}$ controls the constant value seen at the low pH region in Figure 4-2. As shown in Table E-4, the decrease in this fitting parameter does not have strong impact on the rate or the mechanism of the delamination. However, when $b_{\varepsilon,4}$ increases to 0.01, the movements of both potential and porosity fronts increase dramatically. For $b_{\varepsilon,4}$=0.01, the mechanism of the delamination remains mass-transfer controlled for the potential front, but changes to a mixed-controlled mechanism for the porosity front.

E.2 Poisoning Factor

Four fitting parameters were used in the construction of the poisoning factor-pH relation (see Figure 4-3(b)). The fitting parameter $b_{\zeta,1}$ influences the constant value at the high pH region. The fitting parameter $b_{\zeta,2}$ governs the slope of the transition from low pH to high pH regions. The deflection point seen in the middle of the increasing curve changes with the fitting parameter $b_{\zeta,3}$. The constant value seen at the low pH region is related to the fitting parameter $b_{\zeta,4}$.

Table E-5. Sensitivity analysis for $b_{\zeta,1}$

	$b_{\zeta,1} = 3.5$	$b_{\zeta,1} = 4.5$	$b_{\zeta,1} = 5.5$
Potential Front Velocity	2.18	2.19	2.16
Porosity Front Velocity	1.6	1.63	1.6
Reaction Order for Potential Front	0.55	0.55	0.56
Reaction Order for Porosity Front	0.62	0.6	0.61

Table E-6. Sensitivity analysis for $b_{\zeta,2}$

	$b_{\zeta,2} = -1.3$	$b_{\zeta,2} = -3.3$	$b_{\zeta,2} = -5.3$
Potential Front Velocity	2.1	2.19	2.2
Porosity Front Velocity	1.35	1.63	1.75
Reaction Order for Potential Front	0.55	0.55	0.55
Reaction Order for Porosity Front	0.62	0.6	0.62

E.2.1 $b_{\zeta,1}$

The sensitivity analysis for the fitting parameter $b_{\zeta,1}$ is summarized in Table E-5. When the high-pH value in Figure 4-3(b) increases by two orders ($b_{\zeta,1}$ changes from 3.5 to 5.5), the rate of the delamination remains approximately the same. The reaction orders determined based upon the potential front and the porosity front are not influenced much by the fitting parameter $b_{\zeta,1}$.

E.2.2 $b_{\zeta,2}$

The sensitivity analysis for the fitting parameter $b_{\zeta,2}$ is summarized in Table E-6. The slope of the increasing curve in Figure 4-3(b) becomes steeper when the fitting parameter $b_{\zeta,2}$ changes from -1.3 to -5.3. The change in $b_{\zeta,2}$ does not influence the rate determined by the potential front, but has a slight impact on that determined by the porosity front. For the values that have been tested, the kinetic analysis indicates that the change in $b_{\zeta,2}$ has no significant impact on the delamination mechanism.

E.2.3 $b_{\zeta,3}$

The sensitivity analysis for the fitting parameter $b_{\zeta,3}$ is summarized in Table E-7. The deflection point of the increasing curve seen in Figure 4-3(b) shifts from left to right when the fitting parameter $b_{\zeta,3}$ changes from 9.4 to 11.4. The simulation results do not change much when $b_{\zeta,3}$ changes from 9.4 to 10.4, but the velocities of both fronts

Table E-7. Sensitivity analysis for $b_{\zeta,3}$

	$b_{\zeta,3} = 9.4$	$b_{\zeta,3} = 10.4$	$b_{\zeta,3} = 11.4$
Potential Front Velocity	2.15	2.19	2.06
Porosity Front Velocity	1.62	1.63	1.33
Reaction Order for Potential Front	0.55	0.55	0.55
Reaction Order for Porosity Front	0.62	0.6	0.62

Table E-8. Sensitivity analysis for $b_{\zeta,4}$

	$b_{\zeta,4} = -15$	$b_{\zeta,4} = -16$	$b_{\zeta,4} = -17$
Potential Front Velocity	2.20	2.19	2.16
Porosity Front Velocity	1.68	1.63	1.65
Reaction Order for Potential Front	0.56	0.55	0.56
Reaction Order for Porosity Front	0.63	0.6	0.62

decrease slightly when $b_{\zeta,3}$ changes from 10.4 to 11.4. For the values that have been tested, the kinetic analysis shows that the change in $b_{\zeta,3}$ has no significant impact on the delamination mechanism.

E.2.4 $b_{\zeta,4}$

The sensitivity analysis for the fitting parameter $b_{\zeta,4}$ is summarized in Table E-8. The computational results remain approximately the same when $b_{\zeta,4}$ changes from -15, -16 to -17. For the values that have been tested, the simulation results are insensitive to this fitting parameter.

E.3 Blocking Factor

The blocking factor was used in the cathodic current density expression. In order to characterize an enhanced electrochemical reactivity for oxygen reduction in the front region, a slight increase was assigned in pH range 10 to 11 in Figure 4-4(b). Seven fitting parameters were used in the construction of Figure 4-4(b). The fitting parameter $b_{\alpha,1}$ is related to the constant value seen at the low pH region. The fitting parameter $b_{\alpha,2}$ is associated with the slope of the curve at the low pH region. The deflection point at low-pH curve is controlled by the fitting parameter $b_{\alpha,3}$. The fitting parameter $b_{\alpha,4}$ is associated with the constant value at the high pH region. The fitting parameter $b_{\alpha,5}$ is related to the slope of the short curve seen at high pH. The length of the constant region

Table E-9. Sensitivity analysis for $b_{\alpha,1}$

	$b_{\alpha,1} = 6.5$	$b_{\alpha,1} = 7.5$	$b_{\alpha,1} = 8.5$
Potential Front Velocity	2.0	2.19	2.52
Porosity Front Velocity	1.60	1.63	2.29
Reaction Order for Potential Front	0.56	0.55	0.57
Reaction Order for Porosity Front	0.62	0.6	0.65

Table E-10. Sensitivity analysis for $b_{\alpha,2}$

	$b_{\alpha,2} = -10$	$b_{\alpha,2} = -7$	$b_{\alpha,2} = -4$
Potential Front Velocity	2.29	2.19	2.07
Porosity Front Velocity	1.78	1.63	1.45
Reaction Order for Potential Front	0.55	0.55	0.55
Reaction Order for Porosity Front	0.62	0.6	0.62

in the middle range of pH is characterized by $b_{\alpha,6}$ and the magnitude of the constant seen at the front region is governed by the fitting parameter $b_{\alpha,7}$.

E.3.1 $b_{\alpha,1}$

The sensitivity analysis for the fitting parameter $b_{\alpha,1}$ is summarized in Table E-9. When the fitting parameter $b_{\alpha,1}$ changes from 6.5 to 7.5, the computational results in terms of delamination rate and mechanism do not change much. However, when $b_{\alpha,1}$ changes from 7.5 to 8.5, corresponding to an increase in the blocking factor at low pH, the rates and kinetic order determined by both potential front and porosity front show increasing tendency.

E.3.2 $b_{\alpha,2}$

The sensitivity analysis for the fitting parameter $b_{\alpha,2}$ is summarized in Table E-10. The slope of the increasing curve at low pH in Figure 4-4(b) becomes steeper when the fitting parameter $b_{\alpha,2}$ changes from -4 to -10. The increase in the slope results in an increase in the velocities of both potential front and porosity front. For the values that have been tested, the kinetic analysis indicates that the change in $b_{\alpha,2}$ has no significant impact on the delamination mechanism.

Table E-11. Sensitivity analysis for $b_{\alpha,3}$

	$b_{\alpha,3} = 8.8$	$b_{\alpha,3} = 9.8$	$b_{\alpha,3} = 10.8$
Potential Front Velocity	2.51	2.19	2.0
Porosity Front Velocity	1.71	1.63	1.5
Reaction Order for Potential Front	0.58	0.55	0.55
Reaction Order for Porosity Front	0.59	0.6	0.61

Table E-12. Sensitivity analysis for $b_{\alpha,4}$

	$b_{\alpha,4} = -2.5$	$b_{\alpha,4} = -1.5$	$b_{\alpha,4} = -0.5$
Potential Front Velocity	2.11	2.19	2.26
Porosity Front Velocity	1.18	1.63	1.78
Reaction Order for Potential Front	0.55	0.55	0.55
Reaction Order for Porosity Front	0.62	0.62	0.6

E.3.3 $b_{\alpha,3}$

The sensitivity analysis for the fitting parameter $b_{\alpha,3}$ is summarized in Table E-11. The deflection point of the increasing curve at low pH in Figure 4-3(b) shifts from left to right when the fitting parameter $b_{\alpha,3}$ changes from 8.8 to 10.8. When the deflection point is pushed to high pH region, the velocities of the fronts decrease. For $b_{\alpha,3} = 10.8$, the velocity of the porosity front decreases to 1.5 mm/hr, but the reaction order based upon the porosity front does not change with $b_{\alpha,3}$.

E.3.4 $b_{\alpha,4}$

The sensitivity analysis for the fitting parameter $b_{\alpha,4}$ is summarized in Table E-12. The fitting parameter $b_{\alpha,4}$ is associated with the constant value seen at the high pH region in Figure 4-3(b). When $b_{\alpha,4}$ changes from -2.5 to -0.5, the blocking factor at high pH increases from 10^{-5} to 10^{-3}; thus, the delamination rates increase with $b_{\alpha,4}$. The delamination mechanism is not influenced significantly by $b_{\alpha,4}$.

E.3.5 $b_{\alpha,5}$

The sensitivity analysis for the fitting parameter $b_{\alpha,5}$ is summarized in Table E-13. The fitting parameter $b_{\alpha,5}$ is related to the slope of the short curve seen at high pH in Figure 4-4(b). When the fitting parameter $b_{\alpha,5}$ increases from -60 to -40, the slope of the curve becomes more gradual. The computational results remain approximately the same

Table E-13. Sensitivity analysis for $b_{\alpha,5}$

	$b_{\alpha,5} = -60$	$b_{\alpha,5} = -50$	$b_{\alpha,5} = -40$
Potential Front Velocity	2.20	2.19	2.23
Porosity Front Velocity	1.66	1.63	1.63
Reaction Order for Potential Front	0.55	0.55	0.55
Reaction Order for Porosity Front	0.62	0.6	0.62

Table E-14. Sensitivity analysis for $b_{\alpha,6}$

	$b_{\alpha,6} = 10.1$	$b_{\alpha,6} = 11.1$	$b_{\alpha,6} = 12.1$
Potential Front Velocity	2.15	2.19	2.15
Porosity Front Velocity	1.6	1.63	1.66
Reaction Order for Potential Front	0.55	0.55	0.55
Reaction Order for Porosity Front	0.61	0.6	0.62

for three values of $b_{\alpha,5}$. For the values that have been tested, the simulation results are insensitive to this fitting parameter.

E.3.6 $b_{\alpha,6}$

The sensitivity analysis for the fitting parameter $b_{\alpha,6}$ is summarized in Table E-14. In Figure 4-4(b), the length of the constant region in the middle range of pH increases with the fitting parameter $b_{\alpha,6}$. The computational results remain approximately the same when $b_{\alpha,6}$ increases from 10.1 to 12.1. For the values that have been tested, the simulation results are insensitive to this fitting parameter.

E.3.7 $b_{\alpha,7}$

The sensitivity analysis for the fitting parameter $b_{\alpha,7}$ is summarized in Table E-15. In Figure 4-4(b), the magnitude of the constant in the middle range of pH increases from 10^{-4} to 10^{-2} when $b_{\alpha,6}$ changes from -11.1 to -9.1. The increase in the blocking factor leads to a increase in the delamination rates. The kinetic analysis for -11.1 and -10.1

Table E-15. Sensitivity analysis for $b_{\alpha,7}$

	$b_{\alpha,7} = -11$	$b_{\alpha,7} = -10$	$b_{\alpha,7} = -9$
Potential Front Velocity	1.96	2.19	2.36
Porosity Front Velocity	1.47	1.63	1.77
Reaction Order for Potential Front	0.55	0.55	0.57
Reaction Order for Porosity Front	0.59	0.6	0.68

shows the same delamination mechanism, but shows a mixed-controlled mechanism for the porosity front when $b_{\alpha,6}$ is equal to 12.1.

The sensitivity analysis presented above indicates that the parameters used in the construction of the porosity-pH relation ($b_{\varepsilon,1}$ to $b_{\varepsilon,4}$) are most sensitive ones in the simulations. The fitting parameter $b_{\varepsilon,1}$ that governs the porosity at high pH influences up to 60 percent of the delamination rate. The shape of the resulting potential distributions is also influenced by that of the equilibrated porosity-pH relation. The the parameters used in the construction of the poisoning factor-pH relation ($b_{\zeta,1}$ to $b_{\zeta,4}$) and blocking factor-pH relation ($b_{\alpha,1}$ to $b_{\alpha,7}$) are, in general, less sensitive. However, the increase in the cathodic current density at the front region results in an increase in delamination rate and a shift in delamination kinetics.

REFERENCES

[1] G. K. V. D. Wel and O. C. Adan, "Moisture in organic coatings - a review," *Progress in Organic Coatings*, *37*, (1999), p. 1.

[2] T. Sugama, R. Kawase, C. C. Berndt, and H. Herman, "An evaluation of methacrylic acid-modified poly(ethylene) coatings applied by flame spray technology," *Progress in Organic Coatings*, *25*, (1995), p. 2015.

[3] E. R. George and J. Reimer, "Flamesprayed thermoplastic powder coatings," *Polymer Engineering and Science*, *31*, (1991), p. 789.

[4] W. . J. H. Leidheiser, H Jr; Wang and W. Wang, "Some substrate and environmental influences on the cathodic delamination of organic coatings," *Journal of Coating Technology*, *53*, (1981), p. 77.

[5] H. Leidheiser, W. Wang, and L. Igetoft, "The mechanism for the cathodic delamination of organic coatings from a metal surface," *Progress in Organic Coatings*, *11*, (1983), p. 19.

[6] T. Nguyen, D. Bentz, and E. Byrd, "A sudy of water at the organic coating/substrate interface," *Journal of Coatings Technology*, *66*, (1994), p. 39.

[7] H. Yasuda and V. Stannett, "Permeation, solution, and diffusion of water in some high polymers," *Journal of Polymer Science*, *57*, (1962), p. 907.

[8] J. S. Hammond, J. W. Holubka, J. E. deVries, and R. A. Dickie, "The application of x-ray photo-electron spectroscopy to a study of interfacial composition in corrosion-induced paint de-adhesion," *Corrosion Science*, *21*, (1981), p. 187.

[9] W. Furbeth and M. Stratmann, "The delamination of polymeric coatings from electrogalvanised steel - a mechanistic approach. part1: delamination from a defect with intact zinc layer," *Corrosion Science*, *43*, (2001), p. 207.

[10] W. Furbeth and M. Stratmann, "The delamination of polymeric coatings from electrogalvanized steel - a mechanistic approach. part 3: delamination kinetics and influence of co2," *Corrosion Science*, *43*, (2001), p. 243.

[11] W. Furbeth and M. Stratmann, "The delamination of polymeric coatings from electroglanized steel - a mechanistic approach. part 2: delamination from adefect down to steel," *Corrosion Science*, *43*, (2001), p. 229.

[12] G. Grundmeier, C. Reinartz, M. Rohwerder, and M. Stratmann, "Corrosion properties of chemically modified metal surfaces," *Electrochimica Acta*, *43*, (1998), p. 165.

[13] G. Grundmeier, W. Schmidt, and M. Stratmann, "Corrosion protection by organic coatings: electrochemical mechanism amd novel method investigation," *Electrochimica Acta*, *45*, (2000), p. 2515.

[14] A. Leng, H. Streckel, K. Hofmann, and M. Stratmann, "The delamination of polymeric coatings from steel part3: Effect of the oxygen partial pressure on the delamination reaction and current distribution at the metal/polymer interface," *Corrosion Science*, *41*, (1999), p. 599.

[15] A. Leng, H. Streckel, and M. Stratmann, "The delamination of polymeric coatings from steel. part 2: First stage of delamination, effect of type and concentration of cations on delamination, chemical analysis of the interface," *Corrosion Science*, *41*, (1999), p. 579.

[16] A. Leng, H. Strekel, and M. Stratmann, "The delamination of polymerica coatings from steel part 1: Calibration of the kelvinprobe and basic delaminatio mechanism," *Corrosion Science*, *41*, (1999), p. 547.

[17] M. Stratmann, R. Feser, and A. Leng, "Corrosion protection by organic films," *Electrochimica Acta*, *39*, (1994), p. 1207.

[18] M. Stratmann, A. Leng, W. Furbeth, H. Streckel, H. Gehmecker, and K.-H. Grobe-Brinkhaus, "The scanning kevin probe; a new technique for the in situ analysis of the delamination of organic coatings," *Progress in Organic Coatings*, *27*, (1996), p. 261.

[19] K. Ogle, S. Morel, and N. Meddahi, "An electrochemical study of the delamination of polymer coatings on galvanized steel," *Corrosion Science*, *47*, (2004), p. 2034.

[20] K. Ogle, A. Tomandl, N. Meddahi, and M. Wolpers, "The alkaline stability of phosphate coatings i: Icp atomic emission spectroelectrochemistry," *Corrosion Science*, *46*, (2004), p. 979.

[21] K. Allahar, M. Orazem, and K. Ogle, "Mathematical model for cathodic delamination using a porosity-ph relationship," *Corrosion Science*, *49*, (2007), p. 3638.

[22] K. N. Allahar,

Mathematical Modeling of Disbonded Coating and Cathodic Delamination Systems, Ph.D. dissertation, University of Florida, Gainesville, Florida, 2003.

[23] M. Ciureanu and H. Wang, "Electrochemical impedance study of electrode-membrane assemblies in pem fuel cells i. electro-oxidation of h2 and h2/co mixtures on pt-based gas-diffusion electrodes," *Journal of the Electrochemical Society*, *46*, (1999), p. 4031.

[24] W. Zhang, M. P. S. Kumar, S. Srinivasan, and H. J. Ploehn, "Ac-impedance studies on metal hydride electrodes," *Journal of the Electrochemical Society*, *142*, (1995), p. 2935.

[25] E. Barsukov and J. R. Macdonald, *Impedance Spectroscopy Theory, Experiment, and Applications*, Wiley, 2005.

[26] B. N. Popov, M. A. Alwohaibi, and R. E. White, "Using electrochemical impedance spectroscopy as a tool for organic coating solute saturation monitoring," *Journal of the Electrochemical Society*, *140*, (1993), p. 947.

[27] M. E. Orazem, P. Agarwal, and L. H. García-Rubio, "Critical issues associated with interpretation of impedance spectra," *Journal of Electroanalytical Chemistry and Interfacial Electrochemistry*, *378*, (1994), p. 51.

[28] A. J. Bard and L. R. Faulkner, *Electrochemical Methods: Fundamentals and Applications*, Wiley, New York, 1980.

[29] J. R. Macdonald, *Impedance Spectroscopy: Emphasizing Solid Materials and Systems*, Wiley, 1987.

[30] G. J. Brug, A. L. G. van den Eeden, M. Sluyters-Rehbach, and J. H. Sluyters, "The analysis of electrode impedances complicated by the presence of a constant phase element," *Journal of Electroanalytical Chemistry*, *176*, (1984), p. 275.

[31] V. M.-W. Huang, V. Vivier, M. E. Orazem, N. Pebere, and B. Tribollet, "The apparent constant-phase-element behavior of a disk electrode with faradaic reactions global and local impedance analysis," *Journal of the Electrochemical Society*, *154*, (2007), p. C99.

[32] V. M.-W. Huang, V. Vivier, M. E. Orazem, N. Pebere, and B. Tribollet, "The apparent constant-phase-element behavior of an ideally polarized blocking electrode a global and local impedance analysis," *Journal of the Electrochemical Society*, *154*, (2007), p. C81.

[33] Z. Lukacs, "The numerical evaluation of the distortion of eis data due to the distribution of parameters," *Journal of Electroanalytical Chemistry*, *432*, (1997), p. 79.

[34] Z. Lukacs, "Evaluation of model and dispersion parameters and their effects on the formation of constant-phase elements in equivalent circuits," *Journal of Electroanalytical Chemistry*, *464*, (1999), p. 68.

[35] C. A. Schiller and W. Strunz, "The evaluation of experimental dielectric data of barrier coatings by means of different models," *Electrochimica Acta*, *46*, (2001), p. 3619.

[36] L. Young, "Anodic oxide films part 4: The interpretation of impedance measurements on oxide coated electrodes on niobium," *Transactions of the Faraday Society*, *51*, (1955), p. 1250.

[37] R. Jurczakowski, C. Hitz, and A. Lasia, "Impedance of porous au based electrodes," *Journal of Electroanalytical Chemistry*, *572*, (2004), p. 355.

[38] T. Pajkossy, "Impedance spectroscopy at interfaces of metals and aqueous solutions - surface roughness, cpe and related issues," *Solid State Ionics*, *176*, (2005), p. 1997.

[39] V. M.-W. Huang, V. Vivier, M. E. Orazem, I. Frateur, and B. Tribollet, "The global and local impedance response of a blocking disk electrode with local constant-phase-element behavior," *Journal of the Electrochemical Society*, *154*, (2007), p. C89.

[40] J. Jorcin, M. Orazem, N. Pebere, and B. Tribollet, "Cpe analysis by local electrochemical impedance spectroscpy," *Electrochimica Acta*, *51*, (2006), p. 1473.

[41] J. Newman, "Current distribution on a rotating disk below the limiting current," *Journal of the Electrochemical Society*, *113*, (1966), p. 1235.

[42] J. Newman, "Frequency dispersion in capacity measurements at a disk electrode," *Journal of the Electrochemical Society*, *117*, (1970), p. 198.

[43] K. Nisançiöglu, "The error in polarization resistance and capacitance measurements resulting from nonuniform ohmic potential drop to flush-mounted probes," *Corrosion*, *43*, (1987), p. 258.

[44] K. Nisançiöglu, "Theoretical problems related to ohmic resistance compensation," in *The Measurement and Correction of Electrolyte Resistance in Electrochemical Tests*, L. L. Scribner and S. R. Taylor, Eds., Philadelphia, PA, 1990, number 1056, p. 61, American Society for Testing and Materials.

[45] K. Nisançiöglu and J. Newman, "Transient convective diffusion to a disk electrode," *Journal of Electroanalytical Chemistry*, *50*, (1974), p. 23.

[46] J. S. Newman, *Electrochemical Engineering*, Prentice-Hall, Englewood Cliffs, New Jersey, 2 edition, 1991.

[47] M. Orazem, J. Esteban, K. Kenelley, and R. Degerstedt, "Mathematical models for cathodic protection of an underground pipeline with coating holidays: Part 1 - theoretical development," *Corrosion*, *53*, (1997), p. 264.

[48] D. A. Jones, *Principles and Prevention of Corrosion*, Prentice Hall, Upper Saddle River, NJ, 1996.

[49] K. Wapner, B. Schoenberger, M. Stratmann, and G. Grundmeier, "Height-regulating scanning kelvin probe for simultaneous measurement of surface topology and electrode potentials at buried polymer/metal interfaces," *Journal of the Electrochemical Society*, *152*, (2005), p. E114.

[50] G. Williams and H. N. McMurray, "Chromate inhibition of corrosion-driven organic coating delamination studied using a scanning kelvin probe technique," *Journal of the Electrochemical Society*, *148*, (2001), p. B377.

[51] G. Williams, H. N. McMurray, and D. A. Worsley, "Cerium inhibition of corrosion-driven organic coating delamination studied using a scanning kelvin probe technique," *Journal of the Electrochemical Society*, *149*, (2002), p. B154.

[52] T. Nguyen, E. Byrd, D. Bentz, and C. Lin, "In situ measurements of water at the organic coating/substrate interface," *Progress in Organic Coatings*, *27*, (1996), p. 181.

[53] K. Wapner, M. Stratmann, and G. Grundmeier, "In situ infrared spectroscopic and scanning kelvin probe measurements of water and ion transport at polymer/metal interfaces," *Electrochimica Acta*, *51*, (2006), p. 3303.

[54] J. B. Jorcin, E. Aragon, C. Merlatti, and N. Pebere, "Delaminated areas beneath organic coating: A local electrochemical impedance approach," *Corrosion Science*, *148*, (2006), p. 1779.

[55] G. Grundmeier and M. Stratmann, "Plasma polymerization - a new and promising way for the corrosion protection of steel," *Materials and Corrosion*, *49*, (1998), p. 150.

[56] K. Wapner and G. Grundmeier, "Scanning kelvin probe measurements of the stabilitt of adhesvie/ metal interfaces in corrosive environments," *Advanced Engineering Materials*, *6*, (2004), p. 163.

[57] M. A. Hernandez, F. Galliano, and D. Landolt, "Mechansim of cathodic delamination control of znic-aluminum phosphate pigment in waterbrone coatings," *Corrosion Science*, *46*, (2004), p. 2281.

[58] S. M. Shardland, "A mathematical model of the initiation of crevice corrosion in metals," *Corrosion Science*, *33*, (1992), p. 183.

[59] S. M. Sharland, "A mathematical model of crevice and pitting corrosion-ii. the mathematical solution," *Corrosion Science*, *28*, (1988), p. 621.

[60] S. M. Sharland, C. P. Jackson, and A. J. Diver, "A finite-element model of the propagation of corrosion crevices and pits," *Corrosion Science*, *29*, (1989), p. 1149.

[61] S. M. Sharland and P. W. Tasker, "A mathematical model of crevice and pitting corrosion-i. the physical model," *Corrosion Science*, *28*, (1988), p. 603.

[62] D. T. Chin and G. M. Sabde, "Modeling transport process and current distribution in a cathodically protected crevice," *Corrosion Science*, *56*, (2000), p. 783.

[63] N. Sridhar, D. S. Dunn, and M. Seth, "Application of a general reactive transport model to predict environment under disbonded coatings," *Corrosion*, *57*, (2001), p. 598.

[64] A. C. West, "Comparison of modeling approaches for a porous salt film," *Journal of the Electrochemical Society*, *140*, (1993), p. 403.

[65] M. G. Fontana, *Corrosion Engineering*, McGraw-Hill, New York, New York, 1986.

[66] M. Pourbaix, *Atlas of Electrochemical Equilibria in Aqueous Solutions*, NACE International: The Corrosion Society, Houston, Texas, USA, 1974.

[67] G. Zhang, *Corrosion and Electrochemistry of Zinc*, Plenum Press, New York, 1996.

[68] D. H. J. Newman and K. Vetter, "Potential distribution in a corroding pit," *Electrochimica Acta*, *22*, (1977), p. 829.

[69] M. Watson and J. Postlethwaite, "Numerical simulation of crevice corrosion of stainless steels and nickel alloys in chloride solutions," *Corrosion*, *46*, (1990), p. 522.

[70] D. R. Lide, *Handbook of Chemistry and Physics*, CRC Press, Cleveland, Ohio, 82nd edition, 2001-2002.

[71] B. Beverskog and I. Puigdomenech, "Revised pourbaix diagrams for zin at 25-300 c," *Corrosion Science*, *1*, (1997), p. 107.

[72] H. Dafydd, D. A. Worsley, and H. N. McMurray, "The kinetics and mechanism of cathodic oxygen reduction on zinc and zinc-aluminium alloy galvanized coatingi," *Corrosion Science*, *47*, (2005), p. 3006.

[73] K. E. Atkinson, *An Introduction to Numerical Analysis*, John Willey, 2nd edition, 1989.

[74] W. H. Press, S. A. Teukolsky, W. T. Vetterling, and B. P. Flannery, *Numerical Recipes in Fortran 77*, Press Syndicate of the University of Cambridge, Cambridge, Uk, 2nd edition, 1992.

[75] D. R. Lide, *Handbook of Chemistry and Physics*, CRC Press, 84th edition, 2003-2004.

[76] E. Tada, keiichi Sugawara, and H. Kaneko, "Distribution of ph during galvanic corrosion of a zn/steel couple," *Electrochimica Acta*, *49*, (2004), p. 1019.

[77] I. Annergren, D. Thierry, and F. Zou, "Localized electrochemical impedance spectroscopy for studying pitting corrosion on stainless steels," *Journal of the Electrochemical Society*, *144*, (1997), p. 1208.

[78] M. E. Orazem, N. Pebere, and B. Tribollet, "Enhanced graphical representation of electrochemical data," *Journal of the Electrochemical Society*, *153*, (2006), p. B129.

[79] Z. Kerner and T. Pajkossy, "Impedance of rough capacitive electrodes: The role of surface disorder," *Journal of Electroanalytical Chemistry*, *448*, (1998), p. 139.

[80] R. de Levie, "On porous electrodes in electrolyte solutions-iv," *Electrochimica Acta*, *9*, (1964), p. 1231.

[81] R. de Levie, "The influence of surface roughness of solid electrodes on electrochemical measurements," *Electrochimica Acta*, *10*, (1965), p. 113.

[82] A. Lasia, "Impedance of porous electrodes," *Journal of Electroanalytical Chemistry*, *397*, (1995), p. 27.

[83] H. K. Song, H. Y. Hwang, K. H. Lee, and L. H. Dao, "The effect of pore size distribution on the frequency dispersion of porous electrodes," *Electrochimica Acta*, *45*, (2000), p. 2241.

[84] N. V. Huong, C. C. Hinnen, J. Dalbera, and R. Parsons, "Adsorption of ethyl ether on polycrystal and the (110) single crystal face of gold by admittance measurements and modulated reflection spectroscopy," *Journal of Electroanalytical Chemistry*, *125*, (1981), p. 177.

[85] V. D. Jovic, R. Parsons, and B. M. Jovic, "Anion absorption on the (111) face of silver," *Journal of Electroanalytical Chemistry*, *339*, (1992), p. 327.

[86] J. Lipkowski, C. N. V. Huong, C. Hinnen, R. Parsons, and J. Chevalet, "Adsorption of diethylether on single-crystal gold electrodes: Calculation of adsorption parameters," *Journal of Electroanalytical Chemistry*, *143*, (1983), p. 375.

[87] T. Pajkossy, T. Wandlowski, and D. M. Kolb, "Impedance aspects of anion adsorption on gold single crystal electrodes," *Journal of Electroanalytical Chemistry*, *414*, (1996), p. 209.

[88] D. Landolt, "Electrochemical and materials science aspects of alloy deposition," *Electrochimica Acta*, *39*, (1994), p. 1075.

[89] M. Datta and D. Landolt, "Fundamental aspects and applications of electrochemical microfabrication," *Electrochimica Acta*, *45*, (2000), p. 15.

[90] G. Sewell, *The Numerical Solution of Ordinary and Partial Differential Equations*, Wiley, 2005.

[91] R. S. Lillard, P. J. Moran, and H. Isaacs, "A novel method for generating quantitative local electrochemical impedance spectroscopy," *Journal of the Electrochemical Society*, *139*, (1992), p. 1007.

[92] F. Zou, D. Thietty, and H. S. Isaacs, "A high-resolution probe for localized electrochemical impedance spectroscopy measurements," *Journal of the Electrochemical Society*, *144*, (1997), p. 1957.

[93] I. Frateur, V. M.-W. Huang, M. E. Orazem, B. Tribollet, and V. Vivier, "Experimental issues associated with measurement of local electrochemical impedance," *Journal of the Electrochemical Society*, Submitted 2007.

[94] J. Newman, "Resistance for flow of current to a rotating disk," *Journal of the Electrochemical Society*, *113*, (1966), p. 501.

[95] C. H. Hsu and F. Manfeld, "Technical note: Concerning the conversion of the constant phase element parameter y-0 into a capacitance," *Corrosion*, *57*, (2001), p. 747.

BIOGRAPHICAL SKETCH

Mei-Wen Huang grew up in Tainan, Taiwan. She received her bachelor of science degree from the Chemical Engineering Department at the National Chung-Hsiang University in Taiwan in June, 2002. She began her graduate studies at the University of Florida in August 2002 to pursue a master of science degree. After the completion of the degree requirements, she joined Professor Mark E. Orazems electrochemical engineering research group in 2003 to pursue a doctor of philosophy degree. She graduated in the summer of 2007 after spending four years being educated in chemical and electrochemical engineering.